

Material, acoustic, and mechanical properties of mosquito and midge antennae

Brian D. Saltin

Department of Electronic and Electrical Engineering

University of Strathclyde

A thesis submitted for the degree of

Doctor of Philosophy

January 2020

Copyright

This thesis is the result of the author's original research. It has been composed by the author and has not been previously submitted for examination which has led to the award of a degree.

The copyright of this thesis belongs to the author under the terms of the United Kingdom Copyright Acts as qualified by University of Strathclyde Regulation 3.50. Due acknowledgement must always be made of the use of any material contained in, or derived from, this thesis.

Signed:

Date:

Nothing in Biology Makes Sense Except in
the Light of Evolution

Theodosius Dobzhansky

Acknowledgements

I would like to thank both my supervisors, Dr. Joseph C. Jackson and Prof Dr. James F. C. Windmill, for their support and counsel throughout my PhD, as well as for many a fruitful academic debate. Especially my first supervisor I thank for hours of productive meetings and help with abstracts, travel grant applications and countless other things.

I thank all my family and friends for their support, especially my father Jochen P. and my mother Gisela M. Saltin, who from early on encouraged my journey into science and Luise Loges for countless hours of proofreading my work and stylistic advice. Furthermore, I owe thanks to Elizabeth Klenschi and Dr. Jeremy Gibson for their advice and expert LDV training when I started my journey at Strathclyde. The latter also invested a lot of effort in his role as lab manager keeping facilities safe and tidy and in general good working condition. I owe thanks to CUE's longstanding technicians Grant Smillie and Walter Galbraith for help in procuring and maintaining lab equipment – here also Dr. Jose Guerreiro bears mentioning. Moreover, I want to thank all my other colleagues in CUE who got involved in small ways.

I am grateful to Dr. Francesco Baldini (Vector Biology and Disease Group, University of Glasgow) for providing *Anopheles* specimens, Shahida Begum (London School of Hygiene and Tropical Medicine) for the provision of *T. brevipalpis* and Dr. Carla Lorenz as well as Prof. Dr. Heinz R. Köhler (University of Tübingen) for the provision of *C. riparius*. Finally, I thank my collaborators at Kiel University, Prof. Dr. Stanislav Gorb and Dr. Yoko Matsumura.

Abstract

The aim of this PhD is to contribute to the understanding of antennal hearing in insects. To this end, Confocal Laser Scanning Microscopy (CLSM), Finite Element Modelling (FEM) and Laser Doppler Vibrometry (LDV) were employed.

The combination of the first two allows, in absence of prior knowledge of the material properties of mosquito or midge antennae, to assess the material structure and to gauge which impact this distribution can have on the antenna's mechanical behaviour in response to sound. It was revealed that, rather than a simple beam of uniform cuticle, the antennae of the insects studied had patterns and distributions of hard and soft ring elements along the length of their antennae. These properties were simulated with FEM and showed that they can strongly influence the resonant frequency of the antennae. Further investigations were done on the vibrational behaviour of these insects with LDV.

The males of *T. brevipalpis*, *An. arabiensis* and *An. gambiae* demonstrated strong self-oscillation with high Q-factors. Unlike the mosquitoes, vibrometry of *C. riparius* showed no relevant self-oscillation of the antenna. Female *T. brevipalpis* produced self-oscillation but weaker than the male. The three-dimensional pattern of self-oscillation in all investigated mosquito species follows a distorted elliptical path. When stimulated with sound, the self-oscillating antennae exhibited classic nonlinear behaviour such as entrainment and down-modulation. Taken together, this thesis highlights the complex mechanics of acoustic reception in mosquitoes and midges, both mechanically and structurally.

Table of Contents

	Title	Page
1	Aims of this study	1
1	Introduction	2
1.1	Topic Overview	2
1.2	What is hearing?	8
1.3	A brief history of the investigation of mosquito hearing	12
1.4	Hearing in <i>Toxorhynchites brevipalpis</i> , <i>Anopheles arabiensis</i> , and <i>Anopheles gambiae</i>	23
1.4.1	<i>Toxorhynchites brevipalpis</i>	24
1.4.2	<i>Anopheles arabiensis</i>	26
1.4.3	<i>Anopheles gambiae</i>	26
1.5	An even briefer history of the investigation of midge hearing	27
1.6	The synergy of interacting research scientific fields	28
1.7	What makes antennal hearing special?	29
1.8	Chordotonal organs	32
1.9	Recent technology developments in insect audition science	36
1.9.1	The Doppler effect and how it is used for laser vibrometry	36
1.9.2	The LDV device used for experiments in this study.	39
1.9.3	How does Confocal Laser Scanning Microscopy (CLSM) work?	39
1.9.4	How does Finite Element Modelling (FEM) work?	41
2	Material and Techniques	44
2.1	Animal culture maintenance	44
2.2	Laser Doppler Vibrometry (3D)	45
2.2.1	Specimen preparation	45
2.2.2	Laser Doppler Vibrometry Experiments	46
2.2.3	Measurement errors	52
2.2.4	Microphone calibration	53
2.2.5	Experimental procedures to record the movement in time and space	54

	Title	Page
2.2.6	Data Analysis	57
2.2.6.1	Considerations on filtering the data	58
2.2.6.2	How data were filtered	59
2.2.6.3	Converting from velocity type data to displacement data	60
2.2.6.4	List and brief description of individual MatLAB scripts used	60
	- Visual inspection script	
	- 3D movement plotter script	
	- Short windowed FFT auxiliary plot	
	- Smoothed individual and species average plot generation	
2.3	Preparation for and operation of Confocal Laser Scanning Microscopy (CLSM) 3D laser vibrometer function.	66
2.3.1	Specimen preparation	67
2.3.2	CLSM operation	67
2.3.3	How to read CLSM images – image colour coding	68
2.3.4	CLSM images – analysis and extraction of information for FEM	70
2.3.5	3D reconstruction	71
2.4	Finite Element Modelling (FEM)	72
2.4.1	CAD model generation	72
2.4.2	COMSOL settings	77
2.5	Other Techniques	81
2.5.1	Electrophysiology	81
2.5.2	Scanning Electron Microscopy (SEM)	82
2.5.3	Wingbeat recordings and real wingbeat signals presented to experimental animal	82
3	Results of Confocal Laser Scanning Microscopy (CLSM) investigations	83
3.1	<i>Toxorhynchites brevipalpis</i> male	84
3.2	<i>Toxorhynchites brevipalpis</i> female	93
3.3	Male to female comparison <i>Toxorhynchites brevipalpis</i>	95
3.4	<i>Anopheles arabiensis</i> male	97
3.5	<i>Chironomus riparius</i> male	101
3.6	<i>Chironomus riparius</i> female	104

	Title	Page
3.7	<i>Chironomus riparius</i> male to female comparison	107
3.8	<i>Toxorhynchites brevipalpis</i> and <i>Chironomus riparius</i> female comparison	107
3.9	<i>Toxorhynchites brevipalpis</i> and <i>Anopheles arabiensis</i> male comparison	108
3.10	Concluding remarks on results and outstanding comments	111
3.11	Discussion of CLSM results male	112
4	Finite Element Modelling (FEM)	116
4.1	FE modelling of the antenna	117
4.1.1	Background for the antenna simulations – the simple harmonic oscillator	118
4.1.2	The simulated geometry	120
4.2	The effect of “basal stiffness” on the antenna vibration	121
4.3	The effect of adding small subelements with differing stiffness to a uniform beam	123
4.4	The effect of the Poisson ratio	124
4.5	Qualitative analysis of the <i>Toxorhynchites brevipalpis</i> and <i>Anopheles arabiensis</i> antenna stiffness distribution	127
4.6	Qualitative analysis of the <i>Chironomus riparius</i> or the effect of position	129
4.7	The effect of straight beam vs. cone shape	132
4.8	Concluding remarks	133
4.9	Discussion of the FEM modelling of the male antenna of the three species	134
4.9.1	Combining CLSM observations and FEM	137
5	Results of 3D Laser Doppler Vibrometry investigation of antenna self-oscillation	140
5.1	Antenna self-oscillation frequency	140
5.2	Self-oscillation of the <i>Toxorhynchites brevipalpis</i> male	141
5.2.1	Fourier domain data analysis of the <i>Toxorhynchites brevipalpis</i> male	141
5.2.1.1	Note: Is age a factor in the self-oscillation frequency?	143

	Title	Page
5.2.2	Power spectrograms of self-oscillation in the <i>Toxorhynchites brevipalpis</i> male	144
5.2.3	3D-patterns of self-oscillation in the <i>Toxorhynchites brevipalpis</i> male	148
5.2.4	Male antennal reception of a directly presented female in <i>Toxorhynchites brevipalpis</i>	151
5.3	Self-oscillation in <i>Toxorhynchites brevipalpis</i> female	155
5.3.1	Wingbeat frequency recordings	155
5.4	<i>Anopheles arabiensis</i> male	157
5.4.1	Fourier domain data analysis of <i>Anopheles arabiensis</i> male	157
5.4.2	3D patterns in <i>Anopheles arabiensis</i> males	160
5.4.3	Pulsing of the self-oscillation in <i>Anopheles arabiensis</i> males	160
5.5	Comparing three-dimensional movements in <i>Anopheles arabiensis</i> and <i>Toxorhynchites brevipalpis</i>	164
5.6	Side note: <i>Anopheles gambiae</i> male – approximate values	165
5.7	<i>Chironomus riparius</i> male and female	168
5.8	Further controls on the principle of self-oscillation experiments	169
5.8.1	Electrophysiology control: pedicel potential vs. flight muscle potential	169
5.8.2	Decapitation control	171
5.9	Concluding remarks on the self-oscillation vibrometry	173
5.10	Standalone discussion of self-oscillation vibrometry	174
5.10.1	On the meaning of the Quality factor in <i>Anopheles arabiensis</i> and <i>Toxorhynchites brevipalpis</i>	174
5.10.2	On the meaning of the results in <i>Anopheles gambiae</i>	176
5.10.3	Comparing the self-oscillation in male and female <i>Toxorhynchites</i>	177
6	Results in <i>Toxorhynchites brevipalpis</i> when adding sound to self-oscillation	178
6.1	Response to imposed pure-tone sine waves	178
6.1.1	Entrainment by close-by frequency in 3D	179

	Title	Page
6.1.2	Sustained self-oscillation despite close frequency being played, resulting in two movements with little intermodulation	182
6.1.3	Difference tone vibration	184
6.1.4	Down-modulation of entraining frequency	186
6.2	Reception of a directly presented female	188
6.3	Concluding remarks and discussion	192
6.3.1	Male antenna stimulated with a sine wave sound	192
6.3.2	Male <i>Toxorhynchites brevipalpis</i> antenna response to the female wingbeat	193
6.3.3	Last notes on the addition of sound to self-oscillation	194
7	General discussion	195
7.1	Comparing the results with the aims	195
7.2	Reflection on the meaning of CLSM and COMSOL results	196
7.3	Reflection on the meaning of 3D LDV results	197
7.4	What does antenna self-oscillation mean for hearing?	197
7.5	What makes it move?	199
7.6	General observations	200
7.6.1	Movement of the antenna and resonant frequency of the scolopidia	200
7.6.2	Behavioural implications of mosquito hearing range	202
7.7	The evolutionary perspective	205
7.8	Concluding Remarks	208
8	Reference List	209
9	Appendix	221
9.1	Speaker Characterisation	221
9.2	Diptera Phylogeny	222
9.3	Paper	223

Table of Figures

Figure number	Title	Page
1.1	different hearing principles	3
1.2	Mosquito Image	4
1.3	Also Fig. 3.3: SEM overview of the female (a) and male (b) antenna anatomy of <i>Toxorhynchites brevipalpis</i> .	11
1.4	This figure shows in gray the experimental data for a male <i>Aedes aegypti</i> from Jackson (2006) and in black the simple harmonic oscillator fitting performed by Jackson.	14
1.5	The mammalian inner ear	17
1.6	This figure shows schematically the generalised anatomical difference between the Johnston's organs of male and female mosquitoes. Reproduced from Hart et al. (2011).	22
1.7	This figure is modified from Gibson and Russel (2006). It shows the wingbeat frequency adaptation in opposite (a) and same-sex pairings, (b) male and male, c) female and female), of tethered <i>Toxorhynchites brevipalpis</i> mosquitoes.	24
1.8	This figure shows the location and schematic, generalised, of the Johnston's organ. Reproduced from Saltin et al. (2019) based on Yack (2004).	33
1.9	This figure is reproduced from Yack, 2004. It illustrates three different types of scolopidia.	35
1.10	This figure shows a 3D laser vibrometer function schematics. Slightly modified from Domingo-Roca (2018) based on the Polytec manual.	38
2.1	Experimental setup.	48
2.2	Experimental setup overview.	49
2.3	3D laser vibrometer function.	51
2.4	CAD model of the simplified beam.	75
3.1	Direct comparison of the 2 nd segment of male and female of <i>Toxorhynchites brevipalpis</i> in maximum intensity projections.	85

3.2	Male <i>Toxorhynchites brevipalpis</i> in maximum intensity projections.	86
3.3	SEM overview of the female and male antenna of <i>Toxorhynchites brevipalpis</i> .	88
3.4	Detail of the male <i>Toxorhynchites brevipalpis</i> antenna. a)-b) Maximum intensity projections, c) SEM.	90
3.5	Details of the male pedicellus of <i>Toxorhynchites brevipalpis</i> .	91-92
3.6	Comparison images between females of <i>Toxorhynchites brevipalpis</i> (right) and <i>Chironomus riparius</i> antenna (left), brightness increased. b) female <i>Toxorhynchites brevipalpis</i> detail image of the 4 th antennal segment.	94
3.7	Comparison images between the male 2 nd segment of <i>Toxorhynchites brevipalpis</i> (left) and the 4 th to 8 th segment of the <i>Anopheles arabiensis</i> antenna (right) – brightness increased maximum intensity projections.	96
3.8	Full antenna of <i>Anopheles arabiensis</i> male – maximum intensity projection.	98-99
3.9	Detail of <i>Anopheles arabiensis</i> male.	100
3.10	<i>Chironomus riparius</i> male antenna.	101-102
3.11	Opened male pedicel of <i>Chironomus riparius</i> – maximum intensity projection.	104
3.12	Overview of the <i>Chironomus riparius</i> female antenna.	104-105
3.13	<i>Chironomus riparius</i> female pedicel – optical section.	106
3.14	Comparison images between the male 2 nd segment of <i>Toxorhynchites brevipalpis</i> (left) and the 4 th to 8 th segment of the <i>Anopheles arabiensis</i> antenna (right) – brightness increased optical cross section.	110
3.15	Male <i>Anopheles arabiensis</i> pedicel – optical section	111
4.1	Frequency response of a simple harmonic oscillator.	119
4.2	Reproduction of Fig. 2.4: CAD model of the simplified beam.	120
4.3	The effect of “basal stiffness” on the frequency response of the beam/flagellum.	122
4.4	The effect of adding hard or soft elements to a uniform beam on the frequency response.	124
4.5	The effect of the Poisson ratio on the frequency response of the beam/flagellum.	126-127

4.6	Comparison of a <i>Toxorhynchites</i> -type model with either uniform stiffness beam the addition of hard and soft elements.	128
4.7	Comparison of the <i>Anopheles</i> -type model with either uniform stiffness or the addition of hard elements	129
4.8	The effect of position on the frequency response of the beam/flagellum.	131
4.9	The effect of straight beam vs. conical shape on the frequency response of the beam/flagellum.	132
5.1	Average frequency overview of self-oscillation in <i>Toxorhynchites brevipalpis</i> males.	142
5.2	Age difference in <i>Toxorhynchites brevipalpis</i> male.	143
5.3	Example of the antenna in a male <i>Toxorhynchites brevipalpis</i> self-oscillating at one stable frequency.	145
5.4	Example of the antenna in a male <i>Toxorhynchites brevipalpis</i> self-oscillating featuring two independent frequencies.	146
5.5	Example of the antenna in a male <i>Toxorhynchites brevipalpis</i> self-oscillating at one stable frequency and its harmonics.	147
5.6	Overview of potential 3D-movement patterns observed in individual recordings of <i>Toxorhynchites brevipalpis</i> males.	149
5.7	Figure showing the self-oscillation of one <i>Toxorhynchites brevipalpis</i> male, labelled animal 08, in multiple viewing planes.	150
5.8	Shows a male <i>Toxorhynchites brevipalpis</i> in response to three recordings of one <i>Toxorhynchites brevipalpis</i> female, labelled animal 1.	152
5.9	Shows a male <i>Toxorhynchites brevipalpis</i> in response to three recordings of one <i>Toxorhynchites brevipalpis</i> female, labelled animal 2.	153
5.10	Shows a male <i>Toxorhynchites brevipalpis</i> in response to three recordings of one <i>Toxorhynchites brevipalpis</i> female, labelled animal 3.	154
5.11	This figure shows three recordings of <i>Toxorhynchites brevipalpis</i> female animal 1.	156
5.12	This figure shows three recordings of <i>Toxorhynchites brevipalpis</i> female animal 2.	156
5.13	This figure shows three recordings of <i>Toxorhynchites brevipalpis</i> female animal 3.	157

5.14	Average frequency overview of self-oscillation in <i>Anopheles arabiensis</i> males.	159
5.15	This figure shows the self-oscillation of one <i>Anopheles arabiensis</i> male, animal 26, in multiple viewing planes.	161
5.16	This figure shows an example of the antenna in a male <i>Anopheles arabiensis</i> self-oscillating, featuring non-constant oscillation.	162
5.17	This figure shows the two observed phase behaviours in <i>Anopheles arabiensis</i> .	163
5.18	This figure shows the Fourier domain representation of the self-oscillation observed in <i>Anopheles gambiae</i> .	166
5.19	This figure shows the self-oscillation of the antenna of one male <i>Anopheles gambiae</i> .	167
5.20	This figure shows <i>Chironomus riparius</i> female self-oscillation.	168
5.21	This figure shows nerve impulse recorded from <i>Toxorhynchites brevipalpis</i> .	170
5.22	This figure shows the two clearest cases, in which the antenna of a male <i>Toxorhynchites brevipalpis</i> still shows self-oscillation after the head was removed.	172
5.23	Addition of two sine waves.	175
6.1	This figure shows the state of complete entrainment of a male <i>Toxorhynchites brevipalpis</i> antenna.	180
6.2	This figure shows the 3D-movement patterns of the <i>Toxorhynchites brevipalpis</i> male antenna in complete entrainment.	181
6.3	This figure shows the state of two frequencies being presented in the antenna vibration in <i>Toxorhynchites brevipalpis</i> male	183
6.4	This figure shows the state of the antenna where a difference tone emerges in <i>Toxorhynchites brevipalpis</i> male.	185
6.5	This figure shows down-regulation of self-oscillation in <i>Toxorhynchites brevipalpis</i> male.	187
6.6	This figure shows a male <i>Toxorhynchites brevipalpis</i> , labelled animal 5, in response to three recordings of one <i>Toxorhynchites brevipalpis</i> female, labelled animal 1. Reproduction of 5.8	189

6.7	This figure shows a male <i>Toxorhynchites brevipalpis</i> , labelled animal 5, in response to three recordings of one <i>Toxorhynchites brevipalpis</i> female, labelled animal 2. Reproduction of 5.9	190
6.8	This figure shows a male <i>Toxorhynchites brevipalpis</i> (labelled animal 5) in response to three recordings of one <i>Toxorhynchites brevipalpis</i> female, labelled animal 3. Reproduction of 5.10	191
A1	Speaker Chracterisation	221
A2	Diptera Phylogeny	222

List of Tables

Table number	Title	Page
2.1	This table shows the positioning errors of the laser.	52
2.2	Signal types used.	54
2.3	Excitation, filter, corresponding image colour. Based on methods by Michels et al. (2012) .	69
2.4	CAD geometry and meshing	78
4.1	Reproduction of Table 2.4 CAD geometry and meshing	117
4.2	Amplitude of the first resonant frequency of beams with different Poisson ratios.	125
5.1	<i>Toxorhynchites brevipalpis</i> male frequency, directional Q-factor and displacement.	143
5.2	<i>Toxorhynchites brevipalpis</i> female frequency, directional Q-factor and displacement.	155
5.3	<i>Anopheles arabiensis</i> male frequency, directional Q-factor and displacement with averaged recording.	158
5.4	<i>Anopheles arabiensis</i> male frequency, directional Q-factor and displacement.	158
5.5	<i>Anopheles gambiae</i> male frequency, directional Q-factor and displacement.	165

List of Equations

Equation number	Title	Page
(1)	Doppler effect	36
(1b)	Doppler effect	36
(1c)	Doppler effect	37
(2)	Minimum field equation	42
(2b)	Minimum field equation	42
(3)	Acoustic impedance	54
(4)	Quality factor	63
(5)	COMSOL Solver equation	79
(5b)	COMSOL Solver equation	79
(6)	Substitute force equation	79
(5c)	COMSOL Solver equation	79
(7)	Resonant frequency of a mechanical simple harmonic oscillator	118
(7b)	Resonant frequency of a mechanical simple harmonic oscillator	135
(7c)	Resonant frequency of a mechanical simple harmonic oscillator	135
(8)	Volume of a cylinder	135
(9)	Area of a rectangle with the height and diameter of the cylinder	135
(7d)	Resonant frequency of a mechanical simple harmonic oscillator	135

Aims of this study

Before setting the stage by explaining the historic background of hearing research in the different investigated species and of the methods used, I want to set out what is to be achieved by the present study. Beginning with the notice that mechanical baseline data of the antenna of the species under investigation are missing, the three aims are as follows:

- 1) To identify the general pattern of material distribution in insect antennae. This should be done comparatively between species and sexes by one single study and experimenter (Section 3).
- 2) To employ computer simulations to verify the effect of the geometric distributions on beam vibration (Section 4).
- 3) To deliver comparable LDV measurements of the self-oscillation of more than one mosquito species and characterise the three-dimensional movements of the flagellum (Sections 5 & 6).

It has been suggested by previous works that the flagellar movement is at least in plane (Albert et al., 2016) or even three-dimensional. However, most existing experiments and measurements with LDV so far do not cover three dimensions.

The combined insight gained by objectives 1-3) should broaden and expand the general view of antennal hearing in terms of phenomena and distribution in species further than the existing single-species works imply (Section 7).

1. Introduction

1.1 Topic Overview

At the beginning of this thesis, I want to introduce my research. The first step is to lay out why the hearing of Culicidae and Chironomidae is a rewarding research topic. Secondly, it will be explained what the three techniques used - CLSM, FEM, and 3D LDV – are, and what each of them can contribute to this field. The third point will be a sketch of the contribution to knowledge of this doctoral thesis.

Why is the hearing of Culicidae and Chironomidae a relevant research field? While all insects are small, and some are even smaller than the species investigated here, the Diptera used are a good compromise in terms of size and handling. Their antennae are acute natural sensors that solve some problems of scale compared to wavelength of communication and, by the fact that antennal hearing is based on sound velocity perception, they are inherently directional. These three points are what make their hearing system interesting from a biomimetics aspect.

A phylogenetic tree of the Diptera can be found in Appendix 2.

Furthermore, at least Culicidae are a worldwide health hazard with 219 million cases of Malaria in 2018 alone (see also WHO, 2018 for malaria case numbers and death toll), which makes their mating behaviour – which depends heavily on acoustics – an important research topic for human and animal health. On a more positive note, while when emerging en masse, a potential nuisance, the larvae of Chironomidae and many other Diptera play a relevant role in the maintenance of aquatic ecosystems (Berg et al., 1992, Broza, 2008).

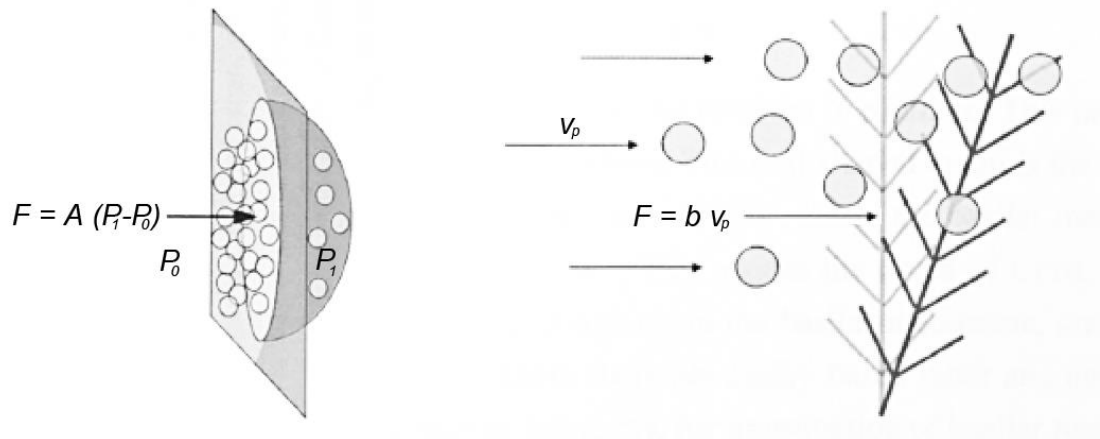


Fig. 1.1: This figure schematically illustrates the two different hearing principles of pressure-based hearing and sound particle velocity-based hearing. It is adapted and slightly modified from Jackson (2006).

P : pressure, v_p : particle velocity, b : viscous drag, A : area, F : force acting on the receiver, which in the case of pressure-based hearing depends on the difference between outer pressure P_1 and inner pressure P_0 .

Another matter again is a relative of the Chironomidae, *Culicoides impunctatus*, i.e. the Highland midge, implicated in the spread of the bluetongue disease (Jennings et al., 1987, Carpenter et al., 2009) – all of which, while not affecting humans directly, has a huge economic impact. Another point is that, with these species' hearing systems being external, they are easy to access. The species chosen are also relatively easy to keep and source. Some were procured from the London School of Tropical Medicine, some from the University of Glasgow's Vector Biology and Disease Group – *Chironomus* was sourced from the University of Tübingen. The Fig. 1.2 shows a *Toxorhynchites* sp. male on the left and a copulating pair of *Anopheles* sp. On the right, with the female – distinguishable by its translucent, blood-filled body (abdomen) and the non-plumose antennae – being the rightmost animal.



Fig. 1.2: On the left: *Toxorhynchites* sp. male (Graham Wise, CC BY 2.0). On the right: Copulating pair of *Anopheles* (Sam Cotton/University College London). The sexual dimorphism includes but is not limited to the plumose (hairy/featherlike) antennae of the male mosquito. The depicted female is also distinguished by its abdomen being translucent and enlarged from a recent blood meal. The images are not to scale.

Toxorhynchites, due to being non-biting, large and robust, is a staple species of acoustic mosquito research. Species of this group have been discussed as a measure of mosquito control, as their ferociously predatory larvae feed on a large number of other mosquito larvae. *Anopheles*, on the other hand, is a notorious transmitter of multiple diseases. These mosquitoes, opposed to *Toxorhynchites*, generally show swarming behaviour. Both mosquito species show pronounced acoustic behaviour.

Why use confocal laser scanning microscopy (CLSM)?

CLSM is a technique that, compared to direct mechanical measurements, is easy to use and quick to apply. It is not an absolute measurement, but it allows for comparative measurements of material stiffness distribution – which later could be used for more informed mechanical tests. As CLSM is a confocal microscopy technique, it provides the user with image stacks that allow to reconstruct the whole structure under investigation as if it were in whole depth in focus plane of the microscope. This is achieved by recombining the individual slices of the image stack. As each of the slices strictly only contains in-focus light, this results in a perfectly

sharp representation of the imaged object. In the present study, four different laser wavelengths were used for the excitation of the cuticle. It is thereby also possible to map the likely material distribution. The present work will follow a colour code introduced by Michels et al. (2012). In the used colour code, resilin-dominated, and therefore soft, structures are shown in blue, medium hard ones in green, and structures shown in red are in tendency sclerotized, that is, hard.

Therefore, CLSM can contribute more than structural information. In the case of *Toxorhynchites brevipalpis* and *Anopheles arabiensis*, the CLSM approach revealed an almost mirrored material distribution along the antenna. The *T. brevipalpis* antenna consists of a relatively hard beam with small softer and harder bands, while the *An. arabiensis* antenna is generally soft and interspaced by hard bands.

Why use the Finite Element Modelling method? The above-described alteration of hard and soft bands observed in CLSM led to the question: could this structuring affect the function of the antenna as an acoustic receiver?

To solve this question, Finite Element Modelling (FEM) was used as it is much easier to manipulate antenna structure in the digital world of FEM than to identify – if those even exist – or genetically engineer a mosquito which has an unbanded antenna. In FEM, a variety of situations can be tested relatively easily in a shorter time frame than breeding experiments for mosquitoes with different antenna substructure would be able to. This approach therefore allows to quickly assess whether a structural variation can have an effect. To this end, a simplified beam structure representing the mosquito antenna was drawn in COMSOL.

The model consists of a subdivided beam structure. For the two mosquito species, there were 13 evenly spread bands along the beam, for *Chironomus* only 11 bands, all evenly spread in the lowest part of the antenna beam.

The main message from FEM is that, although it is only small parts of the antenna that have different material properties, once soft elements are added to a uniform beam, the resonant frequency decreases, in the case of *T. brevipalpis* by about half. The addition of hard elements, on the other hand, has a stronger effect on the softer model of *An. arabiensis* than on the already more rigid *T. brevipalpis* model.

Three-dimensional Laser Doppler Vibrometry (LDV) measurements of the antenna motion on the native undisturbed antenna system and in response to sound were also conducted. When no sound is played, LDV allows to assess – if the system is moving – the active properties of the antenna. It is a suitably sensitive and non-contact measurement method to characterise this type of system.

The point that LDV is a non-contact measurement method is important, as a small and light system like a mosquito antenna would otherwise be influenced by the measurement device. The recorded vibrational data deliver a frequency spectrum from which, among other things, the resonant frequency and instantaneous frequency of the antenna motion can be extracted – always in comparison to a reference recording with a microphone. A further perk is, as the LDV is a measurement device with multiple sensors, it is possible to track the 3D motion of the antenna in space in real time – which has not been recorded before. In *An. arabiensis*, the resonant frequency is converging around 360Hz in all three directions and in *An. gambiae* approximately around 400Hz.

In *T. brevipalpis*, however, while individual frequency peaks are at least as sharp as in *Anopheles*, they do not converge on one frequency. Nonetheless, the average frequency in *T. brevipalpis* is 477Hz. The 3D-motions in both species resemble – depending on the viewing plane – a more or less distorted ellipsoid path. This was partly expected, as the antenna rests in a ball-socket joint at its base.

Contribution to Knowledge: It was possible to demonstrate that the antenna vibration, at least in some aspects, is less clear and simple than the situation seen in a simple rocking beam. Also, the material structure is more sophisticated and acoustic properties, while similar, vary between different species – this, in combination with the fact that more species than previously known show self-oscillation points to the potential that antenna hearing might have evolved multiple times – as is the case for tympanal hearing in insects.

This idea is further corroborated by two factors. The first of these is that the motor proteins in *Drosophila* and mosquitoes appear to be different ones, as results of another group suggest (Warren et al., 2010). The second, additional point in favour of multiple evolutionary origins is that acoustic sensory organs are present in a range of different Diptera Phyla, which are not necessarily closely related to each other (a Phylogeny can be found in Appendix 2). However, opposed to tympanal hearing, it is as yet unknown how many times antennal hearing might have evolved.

1.2 What is hearing?

Animal senses have been a marvel to human observers for a long time, so it is no surprise that the exquisite sensitivity of animal hearing organs has been extensively commented on (Johnston, 1855, Albert et al., 2016) – not least in insects (Göpfert et al., 1999, Nadrowski et al., 2010, Malkin et al., 2014, Greenfield, 2016). From a biomimetics perspective, insects are also interesting, as their sensory organs are very small. One of those well-known examples is the highly sensitive particle velocity sensor, the mosquito antenna, shown in Fig. 1.3. A flagellar insect antenna like the mosquito antenna consists of three parts: The scape (not shown in Fig. 1.3), the pedicel, and the flagellum, which is organised in segments and joints (Fig. 1.3). Inside the pedicel, a chordotonal organ specialised for acoustic perception can be found, which is named Johnston's organ. Without getting philosophical, one does, however, have to ask what is meant by the term “hearing” – and what is necessary to “hear”. The present study will adopt as the definition of “hearing” a combination of arguments made by Göpfert (et. al., 1999) and Yack (2004).

That is hearing needs a suitably efficient transduction and neuronal encoding, followed by a behavioural response. Therefore, hearing can be defined as the sum of perceiving an acoustic stimulus and displaying behaviour upon it (Göpfert et al., 1999). In order to accomplish this complex task, an individual needs a receiving structure (e.g. tympanum or antenna), that enables the animal to show a behavioural response to an auditory signal (Yack, 2004). Enabling is used in this context in the sense that ears make hearing possible and thereby are an essential prerequisite for an animal to act upon a sound signal. Logically speaking this means having the ability to sense something is a necessary condition to display a response – the specific

response itself can depend on other capabilities and factors e.g. the situation the animal is in. Returning to the works of Yack, contrary to this first part, she more implicitly than explicitly states that for a receiving structure to be effective, it needs a suitable transduction, and a neuronal encoding, mechanism – in the special case of the Johnston's organ both are at least partially located in the chordotonal organ (Yack, 2004). There is a large variety of insect hearing organs capable of this, based on the fact that hearing evolved at least 15-20 times within insects (Kirstensen, 1981, Robert, 2007, Strauß et al., 2015) – and that's not even counting the target of this study, the antenna, as it is unclear how often antennal hearing might have evolved independently.

Considering this range of variation in dipteran auditory sensors, it is no wonder that not all mechanisms of hearing have been thoroughly investigated yet. That being said, the focus in insect acoustics tends to edge towards tympanal ears (Yack, 2004), leaving the whole class of sound velocity receptors (like the antennae of Culicidae or Chironomidae and to a lesser extent even *Drosophila*) understudied.

Notwithstanding that, the acoustic behaviour of especially mosquitoes – but also midges – is of large ecological importance both in their function as part of the food chain and as vectors of “insect-borne diseases”, for example malaria. Therefore, it has a huge impact on global health. Regarding parasitology, only with a good understanding of the ecology of a transmitting vector can efficient controls be implemented (e.g. Sawadogo et al., 2013), and swarming is an important part of these insects' ecology (Butail et al., 2013). In most species of mosquitoes and midges, the localisation of females entering the male swarm is a critical point in their mating behaviour (Downes, 1969).

This can be achieved optically, as for example in Simuliidae (Wenk, 1965), or by acoustic means, as in most Culicidae and presumably some Chironomidae (Downes, 1969). Another reason why the study of antennal hearing is significant is that it has been shown that the transduction mechanism in hearing could be very similar between invertebrates and vertebrates (Nadrowski et al., 2009). This makes invertebrates an interesting and promising alternative research model in the use of laboratory animals – especially in the context of the “three Rs” (reduce, refine and replace). Using invertebrates as test animals has the additional advantage that they have short generation times and are cheaper in maintenance.

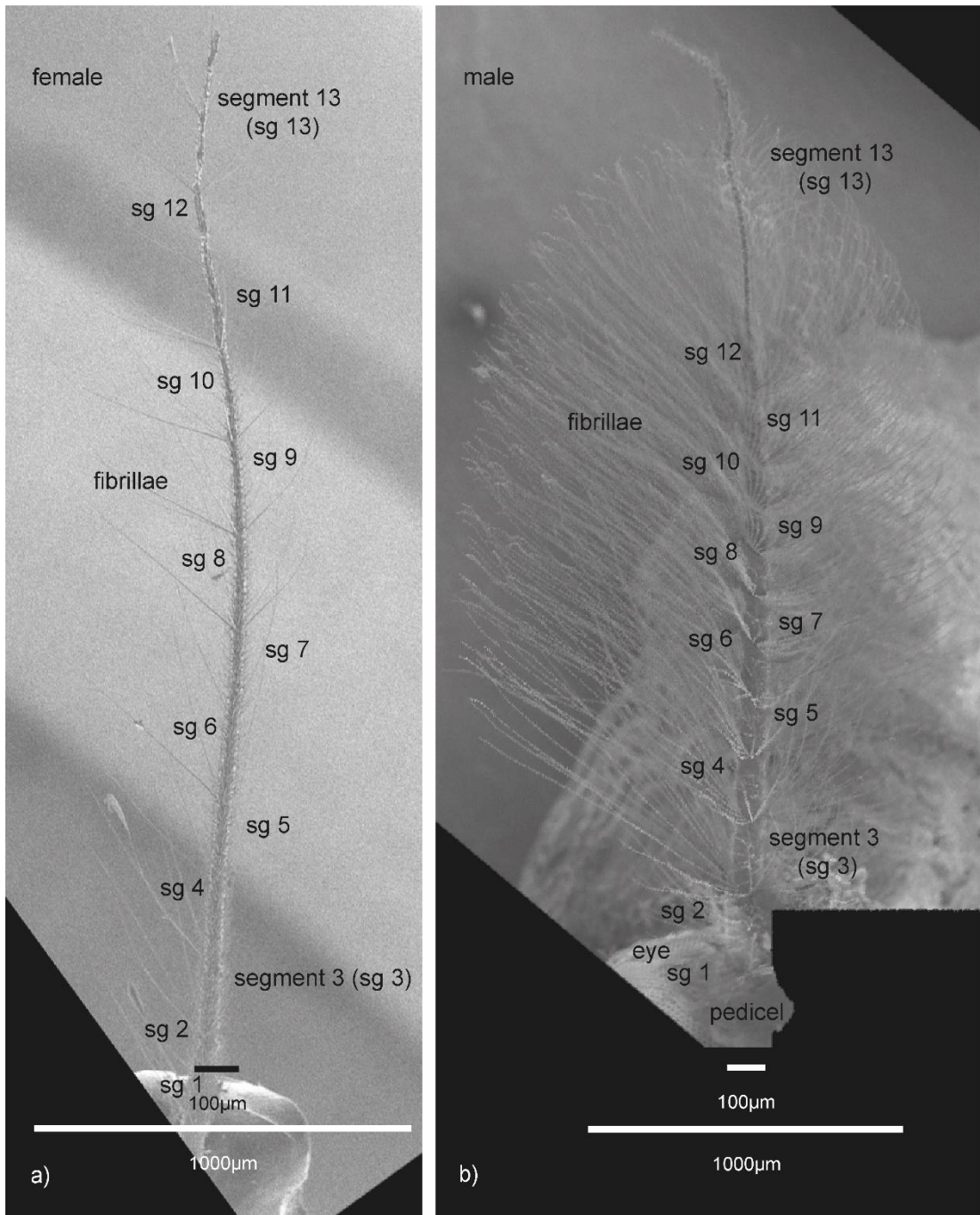


Fig. 1.3: also Fig. 3.3: SEM overview of the female (a) and male (b) antenna anatomy of *T. brevipalpis*, sexual dimorphism is typical in mosquito antennae. The antenna consists of three parts: The scape (not shown), the pedicel, and the flagellum). The flagellum of both sexes features 13 segments (sg) and a crest of hair-like structures known as fibrillae. The female antenna is markedly more slender than that of the male – fibrillae are potentially equally numerous, but shorter. For a more detailed description refer to Fig. 3.3.

1.3 A brief history of the investigation of mosquito hearing

Interest in how antennae work as sensory organs even predates Johnston's description of the auditory apparatus of the *Culex* mosquito, in 1855.

This is particularly noteworthy as the first experimental evidence for pressure-based hearing in insects was by Regen, over 50 years later in 1913. Insect hearing has been a topic of not only academic curiosity but also public concern ever since the works of Ronald Ross and his competitor Battista Grassi between 1896 and 1900 established the connection between mosquito bites and the transmission of malaria (Manson, 1900, Capanna, 2006). An example for a mosquito-transmitted disease discovered earlier is filariasis, e.g. *Wuchereria bancrofti*, which was described by the Scottish physician Sir Patrick Manson in 1879 (Capanna, 2006). The discovery of malaria transmission by mosquitoes was deemed so important that Ross was awarded the Nobel Prize for Physiology and Medicine in 1902 – after disputes over who deserved the credit were temporally settled by Robert Koch's decree. According to Capanna (2006), science historians nowadays attribute equal merit to both of them.

The huge economic burden of mosquito-borne diseases and their relevance to human and animal health is recognized even today (Cator et al., 2009, Mhatre, 2015, Benelli, 2016, Spitzen et al., 2018). The World Health Organization (WHO) reported an estimate of 219 million malaria cases worldwide in 2018, as opposed to 217 million in 2017, but the long-term trend since 2010 is downwards. About 50% of the cases worldwide 2017 were reported from Nigeria (25%), Democratic Republic of the Congo (11%), Mozambique (5%), India (4%), and Uganda (4%). The most burdened countries in Africa reported an increase of cases not a decline (WHO, 2018).

While a world free of mosquitoes or at least mosquito-borne diseases – if this was even at all desirable considering the whole ecological food web – is surely dreamed of by many tourists and not least NGOs and healthcare professionals, this is not only outside the scope of this but of any current research (Cator et al., 2009, Benelli, 2016, Spitzen et al., 2018). This, however, does not mean that an increase in understanding of the involved insect species' biology could not contribute to effective and efficient control measures in critical species (Sawadogo et al., 2013, Benelli et al., 2016). Many generations of researchers have added bit by bit to what we know about mosquitoes nowadays.

An excellent starting point for what was the stage of acoustic sensory science in the mid-1970s is Belton's analysis of direction-finding in male mosquitoes (Belton, 1974). As can be appreciated for example in Figure 1.3, the male antenna is densely covered in long hair-like structures named fibrillae and therefore called plumose, while the female antenna is not. In both sexes, a Johnston's organ is present in the second antenna part, the pedicel. The Johnston's organ was posthumously named after Christopher Johnston who first described it in 1855. It is a highly specialised mechano-sensor and a subtype of chordotonal organs, which generally innervate insect hearing organs (Yack, 2004). Referring back to Clement (1963), Belton supports the argument that the lesser sensitivity of the female Johnston's organ is due to lower mechanical/acoustic impedance compared to the male structure.

While the exact vibration mechanism of the flagellum was not known to him, Belton further proposes the following key points of antennal hearing:

- 1) That chordotonal organs respond to stretching as well as to slacking. This was based on the work of Whitear who had observed this in crustaceans (Whitear, 1960).

Outside of the chronological order, Yack, following Michelsen and Larsen, states that functionally, Johnston's organs are specialised chordotonal organs and a very common type of mechanical hearing organs among insects (Michelsen et al., 1985, Yack, 2004).

2) Male Johnston's organs are tuned to the female wingbeat. See Fig. 1.2 for a typical male mechanical antenna response. While intricate acoustic interactions based on wingbeat are observed (Gibson et al., 2006, Cator et al., 2009, 2010, 2011), in principle, the sound emitted during flight is a by-product of the flight in many species. The acoustic field of a flying mosquito can be described as a dipole (Jackson, 2006, Fig. 1.4).

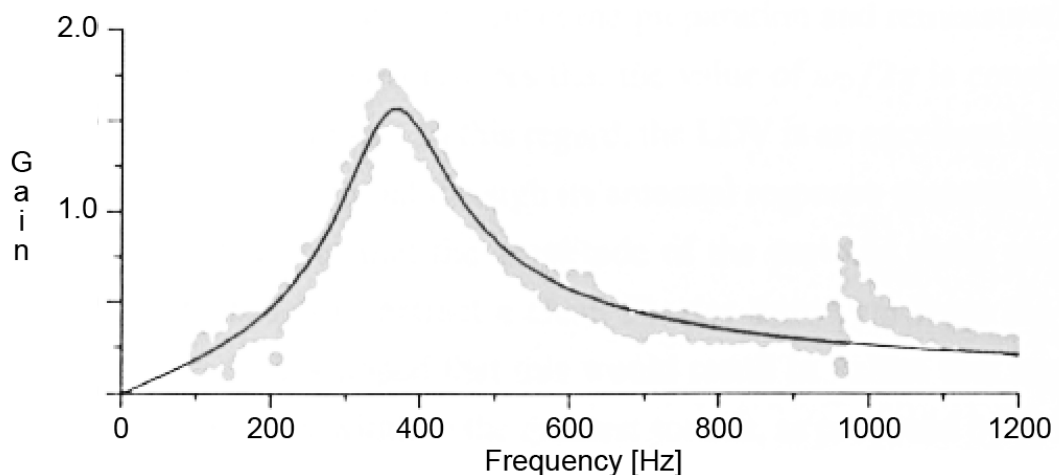


Fig. 1.4: This figure shows in gray the experimental data for a male *Aedes aegypti* from Jackson (2006) and in black the simple harmonic oscillator fitting performed by Jackson. This is deemed a typical male mosquito frequency response – peak values would, however, vary with species.

3) The basal plate and its connection (meaning the “articulation” of the flagellum), according to Keppler (1958), strongly contribute to the flagellum mechanics. Similarly, as the resonant frequency is dropping after removal of part of the flagellum, hydraulic pressure might play a part in the flagellum mechanics.

4) All investigations report frequency doubling in neural response possibly due to two sets of responding cells, which – albeit in different geometric relation as Belton and his contemporaries thought – is corroborated by much more recent works (Lapshin et al., 2019 and Windmill et al., 2019).

5) A comparatively massive electrode inserted in a pedicel will disturb the system, making Keppler's Klirrfaktor Hypothesis (Keppler, 1958) too simple (Belton, 1974) as at least a) the mechanical response of flagellum and Johnston's organ and b) electrical summation combined are involved in resolving harmonic components (Belton, 1974).

6) The previous point is also based on Belton's assumption that the complex mechanics might be influenced by the need to reject the flying mosquito's own wingbeat in addition to detecting conspecifics. This rejection of the own wingbeat combined with more modern results on neuronal feedback and control systems in the mosquito ear (Andres et al., 2016) could, given the possibility of feeding back neuronal signals to the ear, also be solved independently of antenna mechanics.

7) Belton, himself using glass instead of metal electrodes for single-cell electrophysiology, observed that individual scolopidia either respond to pull or push, not both. Belton's results in this point have to be refined down to cellular level. In the meantime, Boo & Richards' fine structure studies showed that each scolopidium consists of 2-3 neuronal cells (Boo et al., 1975).

The individual cells constituting a scolopidium only respond to pushing or pulling, not both, but the scolopidium as a whole, as demonstrated by a more recent and sophisticated approach, is capable of responding twice per stimulation and does so in antiphase (Lapshin et al., 2019). If one cell responds to the prong it attaches to by

mediating that the flagellum is pushed backwards by a (sound) stimulus, its partner cell – of the same scolopidium – responds to the restoration of the initial prong movement by the flagellum pulling the prong in the opposite direction. Broadly rephrasing Lapshin (et al., 2019), this means that scolopidia could be enabled to respond to both push and pull on the prong, while the individual cells only respond to one movement direction.

8) While mosquitoes can triangulate the source of sound with one or two antennae using the plane of vibration, they do not respond to non-divergent sound sources (Wishart et al., 1959). This has been challenged by experiments of Menda et al. (2019), as they report at least *Aedes aegypti* responding at a distance far beyond the near field to a loudspeaker. Even before Belton (1974), Von Békésy had clearly demonstrated that mosquitoes are tuned to 300-400Hz sounds (Von Békésy, 1969). The mechanism, although in effect comparable, is as of 2019 believed to be different from the one of the mammalian cochlea amplifier (Warren et al., 2010, Mhatre, 2015). The cochlea amplifier was first discovered by the combined work of Kemp and Rhode, both in 1978, who did not yet understand the underlying mechanism (Kemp et al., 1978, Rhode et al., 1978).

About two decades later it was revealed that a myosin-based adaptive motor in the outer hair cells and the transduction mechanism of the mechanically coupled inner hair cells are involved in the mammalian cochlea amplifier (Hudspeth et al., 1997, Martin et al., 2000, Warren et al., 2010). The situation in the mammalian inner ear is shown in Fig. 1.5. In contrast to the mammalian morphology, in the mosquito antenna, transduction and amplification are decoupled (Warren et al., 2010).

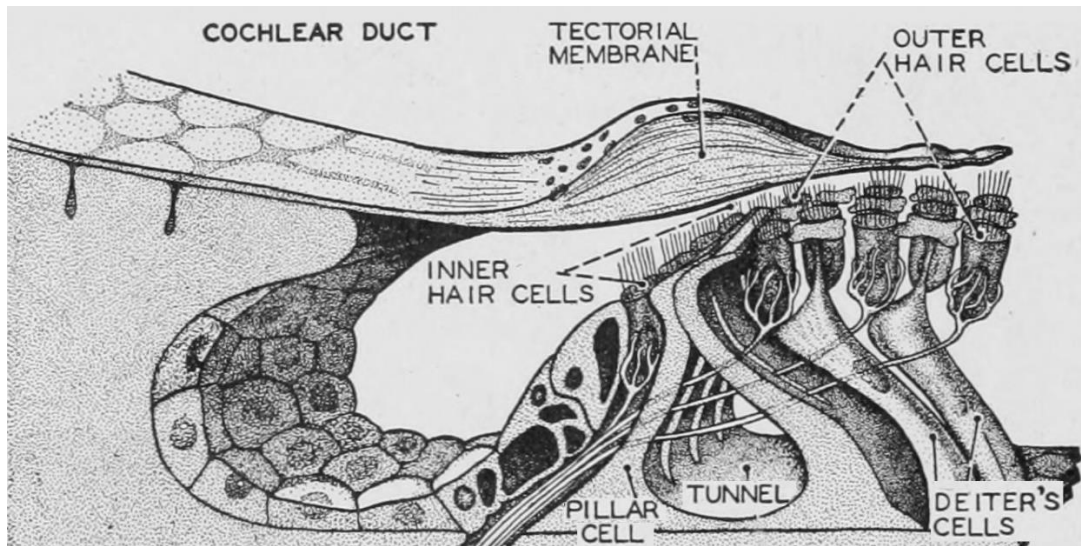


Fig. 1.5: The mammalian inner ear. This figure illustrates how morphologically different the hearing with an external antenna as e. g. in mosquitoes (Fig. 1.4, Fig. 1.8) is from the mammalian. It has to be highlighted, however, that similar but not same mechanisms are involved nonetheless, and that the insect antenna could in approximation be seen as an equivalent structure to a single hair cell, as both are sensors for viscous drag. Figure modified from Neal (et al., 1936).

The motor protein that the amplification in the mosquito is based on, is instead of myosin as in vertebrates, likely dynein (Warren et al., 2010). More recently, Göpfert and Robert just on the turn of the 21st century discovered a whole new layer of complexity when demonstrating that active processes are involved in mosquito audition in a series of excellent papers culminating in their 2001 publication using *Toxorhynchites brevivalpis* (Göpfert et al., 1999, 2000, 2001). Göpfert et al. also demonstrated in the Culicid *Aedes aegypti* distinct resonant modes and stiff coupling between the fibrillae and the flagellum of male animals (Göpfert et al., 1999). With the male flagellum being tuned towards $383 \pm 28\text{Hz}$ in this *Aedes* species and the fibrillae to 2600 or 3100Hz, the fibrillae act as surface extension to the flagellum if driven close to the flagellum's resonant frequency. The female antenna, showing by comparison no fibrillae, resonates at $227 \pm 17\text{Hz}$ (Göpfert et al., 1999).

In this study already they also propose the astonishing nm deflection sensitivity, which they report as 7nm for males and 23nm for females (Göpfert et al., 2000). In addition, Göpfert et al., 2001 gave the basis for works by Jackson and Robert (Jackson et al., 2006), which already changed the previous perception, for example by Bennet-Clark, 1971, that mosquitoes should only be able to perceive sound in a couple of millimetres distance at best (Hoy, 2006). This boundary has become the target of further scrutiny with the works of Menda (et al., 2019), extending male mosquito perception to maybe 10 metres and to at least around 1,5 metres in females (Feugère et al., 2019).

Hoy debates whether the male mosquito's active hearing is – as suggested by Jackson et al. (2006) – mainly an improvement of the male's search strategy or might also play a role as means for selective attention (Hoy, 2006). While the range of hearing in both sexes of mosquitoes remains a surprising field, Gibson and Russell (2006) as well as Cator et al. (2009, 2011), have shown acoustic courtship behaviour in both sexes. This involves converging wingbeat frequencies between the sexes. In fact, the opposite sex wingbeat is considered the main signal antennal hearing is tuned to (Nadrowski et al., 2010), with but a few exceptions (Bernard et al., 2006, Menda et al., 2019, Virgo et al., 2019). These include, but are not limited to, frog-biting midges (Cortellidae), where acoustics plays a part in foraging (Bernard et al., 2006, de Silva et al., 2015, Menda et al., 2019, Virgo et al., 2019).

Around 2010 the quest for what makes the scolopidia move was still very much open (Lu et al., 2009, Nadrowski et al., 2010). While remarkable works for example by Warren (et al., 2010) have approached this issue in mosquitoes, for the study of the phenomenon of antennal hearing and its relevance it ultimately does not matter what

the source of the compressive nonlinearity is, be it active (e.g. Warren et al., 2010) or passive mechanisms (e.g. cubic stiffness (Nadrowski et al., 2010)).

With the exception of the works of Thurm (1965), the following two paragraphs are based on the work of Warren (et al., 2010) who put forward dynein-tubulin as motor in mosquito antennae after experiments in *Culex* mosquitoes, on the grounds that the measured activation energy matches the activation energy of dynein-tubulin and older reports of dynein being the only motor present along the whole cilium (Thurm, 1965). In the case of the dynein-tubulin motor, those would be independent processes. Here it bears mentioning that with the involvement of dynein as motor in self-oscillation, there are still at least two ways the dynein-tubulin complex could be involved in self-oscillation. The first of these would be a conserved functionality from primarily sensory but still motile cilia, while the other would be an analogue to the role of myosin in vertebrate hearing. In that second case, dynein would be acting as an adaptive motor (Warren et al., 2010).

At this point, two theories – harmonic convergence, demonstrated in *Aedes* and *Toxorhynchites* (Gibson et al., 2006, Cator et al., 2009), and difference tone perception, seen in *Culex* (Warren et al., 2009) – were debated. More recently, Simoes (et al., 2016, 2018) reconciled or unified both theories by proposing that the presence of harmonics in the system could be part of the difference tone perception, based among others on the fact that for artificial stimulation of the hearing system signals without harmonics have been shown to be sufficient, for example by the same authors and Jackson (2006). On the matter of what is the ultimate source of motility, it bears mentioning that as recent as 2015 a review by Mhatre (2015) lists five potential sources of dividing models found in literature in classes.

They are as follows: A prestin-like system, deemed unlikely, and the adaptive motor-type models, the dynein motor explanation, the ion-channel feedback models, and the integrate and twitch approach. Another point to be made here is that antennae are multimodal sense organs. Their other sensory modalities are heat (Schadova et al., 2009), windspeed, gravity, humidity (Pielou, 1940) and olfaction, are associated with the antenna (e.g. Nadrowski et al. 2010, Matsuo et al., 2013). Modalities tend to show distinct neuronal representation (Kamikouchi et al., 2009). This work, however, will only focus on acoustic aspects. Hearing, in some species preceded by their acute sight (Wenk, 1965), in others yet maybe by other senses, is at least in many mosquito species critical for the mating display (Downes, 1969, Cator et al., 2009, Cator et al., 2011, Gibson et al., 2006). Despite all of this, the exact mechanism behind the amplification has so far remained elusive and finding it is not the aim of this thesis either. A relatively recent review of the broad competing model classes was done by Mhatre (2015).

Given that it is expressly not the aim of the thesis to find the ultimate cause of movement, the five broad classes discussed are listed here but will not be elaborated upon further. Briefly, the existing model classes are: electromotility, adaptation motor, dynein motor, ion channel feedback and integrate and twitch. While the first one is unlikely for the present case, as no comparable protein to prestin exist in insect hearing organs, all other four have merits of their own and it is yet undecided which best represents the actual situation. The integrate and twitch model is singled out by the fact that it describes the active aspect of hearing as an emergence of the system instead of locating it in the hair bundles (vertebrate ear) or cilia (insect ear). In all cases models must be held accountable for their degree of explanatory power, which

has two aspects: Firstly, whether they allow for mathematical reproduction of the natural situation – so far all do – and how much they actually describe nature. In other words, can we identify all necessary parts in the natural system to decide which model actually represents it (Ouellette, 2015)? The latter so far is impossible in the case of active hearing for vertebrates and invertebrates alike (Mhatre, 2015). In the earlier years of 21st century Göpfert’s findings (Göpfert et al., 1999, 2000, 2001) were shortly followed by studies by Jackson (et al., 2006), further illuminating the remarkable abilities of the antenna as hearing organ. Also very much worth mentioning are excellent works by Lapshin and Vorontsov, which now with lamentable delay – as originally not published in English – find their way into the wider audience (e.g. Lapshin et al., 2019). Among the most recent remarkable additions to the picture are Andres et al. (2016), demonstrating, similar to the situation in halteres (Heisenberg et al., 1988, Chan et al., 1996, Bender et al., 2006, Bartussek et al., 2018), the presence of an afferent control previously thought to be absent in insect antennae – for example, no afferent control was found in the antenna of *Drosophila* (Kamikouchi et al., 2010). While the exact mechanism of how the flagellum vibrates is neither known nor a target of the present study, given that all authors agree on the existence of twice-frequency forcing, but not necessarily on its function (Jackson et al., 2009, Warren et al., 2010, Lapshin, 2015, Windmill et al., 2018), it seems to warrant some further consideration. This phenomenon in principle describes that the pedicel activity in the presented context is of double i.e. twice the frequency as the stimulus. If hearing in all these animals depends on the twice-frequency forcing (Jackson et al., 2009, Warren et al., 2010, Windmill et al., 2018), and the real meaningful movement is not at lower frequencies (e.g. suggested by

Lapshin, 2015), the self-oscillation could be beneficial to hearing in itself. Windmill et al. (2018), performing atomic force microscopy on the scolopidia, showed again the twice-frequency forcing, which, while known for a comparatively long time, is one of the remaining mysteries and is now shown to be already visible at cellular levels. While it does not solve the question who reported it first, to reiterate that twice-frequency forcing has been known for quite some time, I quote Belton (1974): “Frequency doubling has been observed by all previous investigators”. He continues that Wishart (et al., 1959) and Tischner (1954) not only knew the phenomenon but speculated upon its cause. It is remarkable to note that in 1984, Risler already identified four classes of scolopidia (see Fig. 1.6), and like Clements (1963) rejected the notion of type C and D being involved in hearing (Hart et al., 2011). According to Hart et al. (2011), Risler hypothesised that the more numerous types give the males a higher sensitivity even prior to the knowledge of self-oscillation. Hart and colleagues, who published Risler’s initial results 25 years later, turned this observation around, given that both sexes hear.

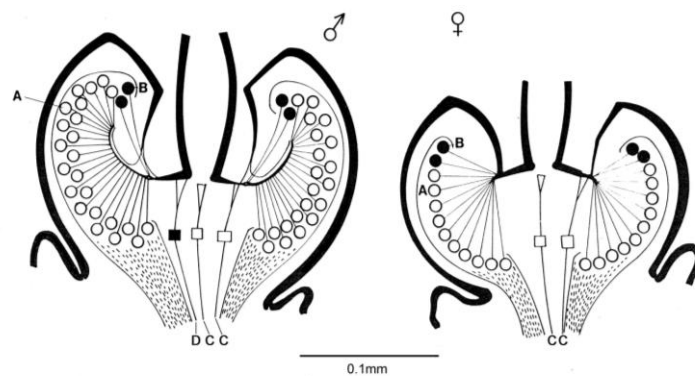


Fig. 1.6: This figure shows schematically the generalised anatomical difference between the Johnston’s organs of male and female mosquitoes. Taken from Hart et al. (2011). The letters A-D indicate the position of the four different scolopidia types.

Another development is the remarkable expansion of the range of sound velocity hearing according to Menda et al. (2019) from some mm (Bennet-Clark 1971, cited by Hoy, 2006, Albert et al., 2018) over ca. 2-10cm (Jackson et al., 2006) to 10m or more (Menda et al., 2019). This range has implications for the use of acoustic traps. While acoustic trapping of mosquitoes has been successfully performed for example on *Anopheles albimanus* as early as the 1950s, it, however, never was marketed with any success except in the sense of financial gain of the vendors. One of the reasons for this is that the sound signals would need to be species-specific, which limits the usefulness of the technique except if they are specifically tuned for a limited area and time targeting a known and numerous species. The new approach of Dieng et al. (2019) with mating disruption might be less specific, however, the involved environmental disturbance by a loud frequency blast would need to be evaluated in more scientific detail and weight against its systemic costs.

Less direct, but also less problematic, is the simply detection-based approach of Salim et al. (2017) allowing to confirm with a certain reliability the presence of known potentially dangerous mosquito species through acoustic means.

1.4 Hearing in *Toxorhynchites brevipalpis*, *Anopheles arabiensis*, and *Anopheles gambiae*

Before going into the specifics and peculiarities known for each of the investigated species (a Phylogeny can be found in Appendix 2), a general case for the importance of hearing in mosquito mating has to be made. The account of the rich history of research on swarm mating for the purpose of this study starts with Downes' (1969) classic work on the mating of Diptera – he was by far not the first to notice the

importance of hearing for many species in swarm mating, but presents a good starting point – and is not ending with Gibson (2006) and Cator (2009). The latter works coined the term “harmonic convergence” for an aerial mating display at least observed in *Aedes* species – Fig. 1.7 illustrates this frequency behaviour. As reproduction success is one key value to determine fitness (Darwin, 1859, Kuzenkov et al., 2019), the importance of hearing for many mosquito species is extremely high.

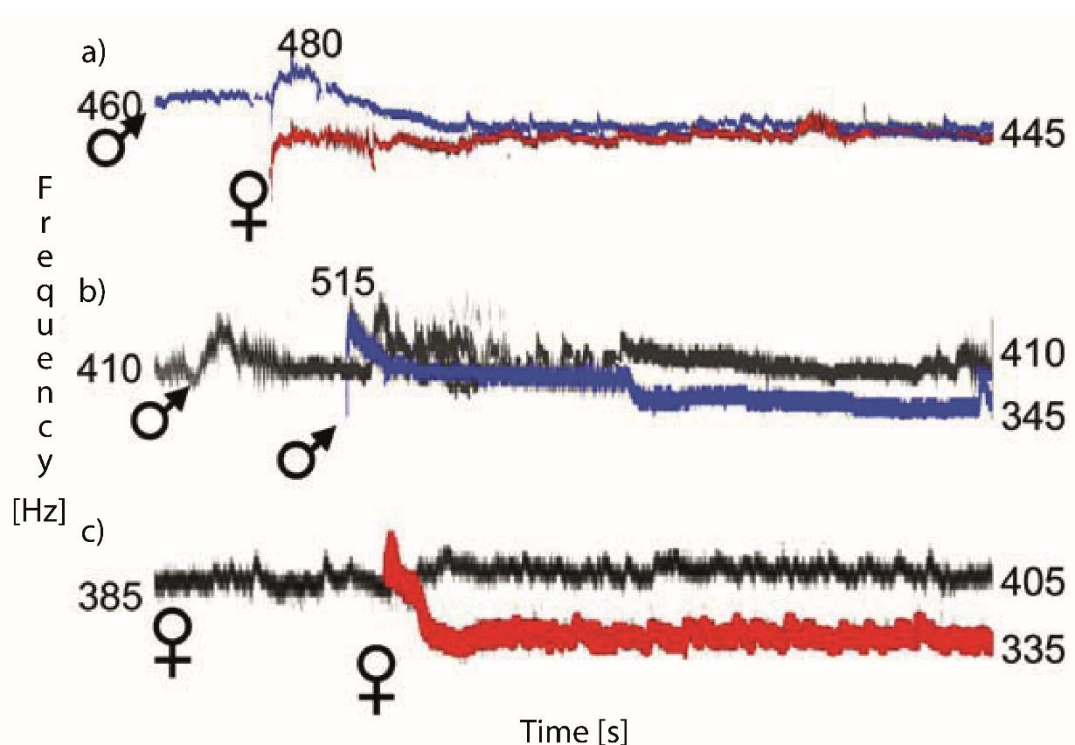


Fig 1.7: This figure is modified from Gibson and Russel (2006). It shows the wingbeat frequency adaptation in a) opposite-sex, b) male and male, and c) female and female pairings of tethered *Toxorhynchites brevipalpis* mosquitoes.

1.4.1 *Toxorhynchites brevipalpis*

For its robustness and ease of experimental handling, both due to its size and the fact that the species is non-biting, *T. brevipalpis* has a history as amenable test species in insect sensory research (Nijhout, 1977, McIver et al., 1978), especially hearing

research (Göpfert et al., 2000, 2001). *Toxorhynchites* species also have been considered for biological mosquito control, as their predatory larvae consume a large number of other mosquito larvae (especially *Culex* and *Aedes*) during development (Steffan et al., 1981) – for example, in *Toxorhynchites splendens* each larva feeds approximately on up to 81-131 mosquito larvae in the course of its four consecutive larval stages (Chochote et al., 2002).

Next to the possibly best studied and most universally used lab animal, *Drosophila*, *Toxorhynchites brevialpis* has the most well-explored antennal hearing system so far. They can detect at least $\pm 7\text{nm}$ deflections (equivalent to $1/10$ millidegree) and are known to show prolonged autogenous movement of up to 400nm (Robert et al., 2002). Furthermore, Jackson showed hysteresis of the tuning – that is, once engaged tuning charges persist beyond the stimulus time and depend on whether the signal was declining or ascending in intensity when last observed (Jackson, 2006 and Jackson et al., 2006). Their wingbeat has been measured multiple times as $426 \pm 43\text{Hz}$ in males and $405.7 \pm 43.5\text{Hz}$ in females (Jackson et al., 2006) – in another study $415 \pm 36\text{Hz}$ in females (Gibson et al., 2006).

The best frequencies vary between different species, as it depends on the length of the oscillator and biological factors. These parameters vary between different species as antenna and wings have an allometric relation to each other and the animal size (Cator et al., 2010, Sawadogo et al., 2013). Mosquito antennae have been observed to be capable of fulfilling all the criteria for active hearing detailed in section 1.6: compressive non-linearity, frequency specificity, self-sustained mechanical oscillation, and power gain (Göpfert et al., 2001, Jackson et al., 2006, Mhatre, 2015).

1.4.2 *Anopheles arabiensis*

While other species, like those of the *gambiae* complex, which is touched upon later, are even more prolific in the transmission of diseases than *Anopheles arabiensis*, little needs to be said on the devastating effect the genus *Anopheles* has worldwide. The present work among other things aims to establish a connection between earlier and present findings in *T. brevipalpis* and their relevance to vector species like *An. arabiensis* by demonstrating the presence of similar effects in them, which is in the spirit of concluding remarks by Hoy (2006): “These studies were done on a nonbiting mosquito, *T. brevipalpis*, but the deservedly infamous ones, including the malarial mosquito *Anopheles gambiae* and the yellow fever mosquito *Aedes aegypti*, warrant similar investigation.”

1.4.3 *Anopheles gambiae*

This is a particular case, as the species *An. gambiae* does not exist. It has been resolved as a number of so-called cryptic species that historically were subsumed into one (Brodgon, 1998). This is since the late 1970s to 80s known as the “*gambiae*”-complex. The individuals used for the present study were taken from a colony which was established before the cryptic species were separated in the early 1980s. For that very reason equally important and difficult to work with, it is hard to estimate historic works on what is and used to be called *An. gambiae*. In the following paragraphs some general historic findings of the female wingbeat and the role of acoustics will be referred to, nonetheless. One has to bear in mind that the main reason for the inclusion of the species complex is to demonstrate the wider

reach and spread of the acoustic phenomena observed, whatever the current Linnéan binominal or status as crypto species might be. The male and female flight frequency of *An. gambiae* have been measured to be $707.1 \pm 15.6\text{Hz}$ in males and $457.8 \pm 8.2\text{Hz}$ in females (Cator et al., 2010) or M males $704 \pm 25\text{Hz}$, S males, $682 \pm 27\text{Hz}$, and M females, $467 \pm 31\text{Hz}$, S females, $460 \pm 26\text{Hz}$ (Pennetier, 2010).

Another factor for many *Anopheles* species could be the presence of movable antenna hairs (Gibson et al., 2010), the influence of which is not yet fully understood, despite early investigations quoted by Hart et al. (2011) done by Wishart (1962) who demonstrated that the electric activity of the antenna is not diminished by the removal of up to 50% of the antennal hairs.

1.5 An even briefer history of the investigation of midge hearing

The situation in *Chironomidae* is less well studied (a Phylogeny can be found in Appendix 2). Although similar to mosquitoes their ability to respond to sound is well-known since at least Downes (1969), due to their less important worldwide impact, reports on midges' hearing organs are rarer.

Outside the related and fascinating group of frog-biting midges (Corethrellidae), which locate hosts acoustically and use acoustic mating signals (Bernal et al., 2006, de Silva et al., 2015), some sand flies (Psychodidae) (Vigoder et al., 2011), and of course *Drosophila* (Kerman et al., 1994, Eberl et al., 1997, 2000, Göpfert et al., 2001, Todi et al., 2004, Boekhoff-Falk, 2005, Lu et al., 2009, Kamikouchi et al., 2010), the research on antennal hearing in Diptera is scarce. The more species are investigated, however, the clearer it becomes that acoustic behaviour in Diptera, while not omnipresent, is more widespread than previously thought.

For this very reason the swarming and harmless species *Chironomus riparius*, which is a commonly used species for ecotoxicology test and whose larvae have a huge role in the ecosystem, was studied parallel to the mosquitoes.

While works of Lapshin et al. (2015) on captured *C. plumosus* (Linnaeus, 1758) specimens have shown that the neuronal capacities for acoustic behaviour does exist in Chironomidae, neither the acoustic properties of their antenna receivers nor their swarming behaviour has been fully characterised. Their life cycle and ecology is to some extent similar to that of the mosquitoes, which have been studied more.

The above-cited work by Lapshin (2015) has shown by electrophysiological methods that males have receptors with three different sensitivity maxima, 180Hz, 221Hz, and 264Hz. Their field of perception differs between the three frequencies, giving it a directional component (Lapshin et al., 2015). Furthermore, while acoustic data are scarce, anatomical studies have shown for a different midge species (*Fleuria lacustris*, Kieff 1924), which shows no swarming behaviour, that the pedicel is reduced in size. Swarming midges by comparison possess 1.33 times as many antenna fibrillae and 21 times more A-Type chordotonal sensillae leading to an estimatedly 70 times lower sensitivity in *F. lacustris* (Fedorova et al., 2009) than in *C. plumosus* (Fedorova et al., 2009, quoting Zhantiev et al., 1999). So far, no measurements of the mechanical properties of the antenna are available.

1.6 The synergy of interacting research scientific fields

Different methodological approaches have contributed to our understanding of antennal hearing, from ecology to behaviour to genetics, spanning neurology, taxonomy, even computer science and mathematics. In the present work, the emphasis will be on vibrometry and to a lesser extent on microscopy-based material science, feeding into basic simulation approaches. Electrophysiology will be lightly touched upon in support. The focus remains the broader mechanical behaviour of the front level of acoustic perception, the flagellum itself.

The flagellum – the main beam of the insect antenna – is moved by the viscous drag of passing air particles constituting the acoustic waves observed by the animals.

1.7 What makes antennal hearing special?

As in section 1.5, the mosquito antenna and the antennae of some other insects do not respond to acoustic pressure differences, but to sound velocity. For a schematic figure of sound pressure and sound velocity sensors, see Fig. 1.1. This is very different to what is commonly thought of as hearing. Excitingly, the vectorial nature of sound velocity also provides the potential for inherent directionality (Michelsen, 1998, Bennet-Clark, 1998). In some cases, this directionality is even achieved with only a single sensor. In fact, this has been shown as early as 1948. Roth experimented with ablations on mosquito antennae, leaving the mosquitoes with only one and they could still navigate towards the source of a sound, as reported by Belton (1974). The ability of acoustic navigation with one ear has been reported for crickets as well. While inherent directionality might play a role in cricket hearing (Lankheet et al., 2017, Michelsen et al., 1994, 1995) the question remains what is meant by this.

The contribution of inherent ipsilateral (same side) directionality to the overall directionality, compared to the crosstalk between the coupled ipsilateral and contralateral tympana and the neuronal contralateral inhibition remains a matter of debate, as Lankheet (et al. 2017) point out. They argue the way Michelsen (et al., 1994, 1995) processed their results overemphasised the component of contralateral cancellation over ipsilateral input. For mosquitoes, the flight paths seen were, however, somewhat more erratic after the loss of one antenna (Belton, 1974).

From today's point of view, this could be caused by more prominent questing behaviour compensating for the partial loss of function. Before delving further into antennal hearing, I would like to quote Nadrowski's 2010 review: "... antennal hearing organs clearly constitute attractive systems for studying fundamental aspects of hearing and for comparative hearing research. Beyond this, the mere fact that antennal hearing plays crucial roles in economically, scientifically, and medically important animals such as bees, flies, and mosquitoes, seems a quite compelling reason to look closely at their ears." Hopefully, this clearly sets the stage for the importance and relevance of understanding antennal hearing systems. Over the years, evidence has accumulated that antennal hearing might feature qualities of active hearing processes (e.g. Göpfert et al., 1999, 2001b, 2003, Robert et al., 2002, Mhatre, 2015, Jackson et al., 2006). Moreover, under the assumption that in antennal hearing active processes are involved, it is possible to look upon four criteria for a hearing process to be characterised as active, each in itself energy dependent.

These are 1) a compressive non-linearity, 2) frequency-specific amplification, 3) self-sustained mechanical oscillation/spontaneous otoacoustic emission, and 4) power gain (e.g. Göpfert et al., 1999, 2001b, 2003, Robert et al., 2002, Mhatre, 2015, Jackson et al., 2006). These criteria were originally developed in the study of vertebrate ears and in a different order (e.g. Hudspeth et al., 2000, Hudspeth, 2008). They are deemed suitable to test for active hearing in other animals as well (Göpfert et al., 2001, Mhatre et al., 2013, Mhatre, 2015, Manley, 2000).

With the small size of insects also come a range of issues. For one, interaural intensity difference and interaural time difference become really small and therefore make, if not hearing in general, then at least directional hearing, very difficult (Robert et al., 2002). Another one is that small insects are weak sound transmitters due to size factors (Bennet-Clark, 1998). Göpfert et al. (2000) measured the wingbeat frequency to be 415Hz – this corresponds to a wavelength of roughly 80cm. If one were to apply the optimal ratio between wavelength and sender or receiver, respectively, for dipole sounds, which Bennet-Clark (1998) found to be 1/4, the result would be 20cm. Since many insects are much smaller than that (<2cm) this ratio is not met and instead they use lower frequencies with larger wavelengths to reduce acoustic refraction and increase available muscle power (Bennet-Clark, 1998).

As an aggravating factor, for location and directionality it has to be pointed out that even if all these problems are resolved, the intensity of sound velocity falls with the cube opposed to the square of distance from the source for sound pressure in the near field (Hoy, 2006). To illustrate that in human scale, the difference in sound pressure at doubled distance is 1/4, but 1/8 for sound velocity.

This 50% difference might not yet be sufficiently convincing, however, with increasing distance values the difference only increases further to 25% at 4m etc. This makes recent findings by Menda et al. (2019) that extend the mosquito hearing range to 10m particularly remarkable. In addition, a confounding factor, which, while demonstrated primarily in midges, affects all investigated species is that a strong correlation between insect age and/or temperature and wingbeat frequency was observed with changes of up to 10Hz per 1°C (Ogawa et al., 1993). In order to fully appreciate antennal hearing, a further detour into insect mechano-sensors is necessary. All insect mechano-sensors described so far – and at the bottom of it, antennal and tympanal hearing (in all its 15-20 independently involved lineages Kirstensen, 1981, Robert et al., 2002, Robert, 2007, Strauß et al., 2015) – utilise mechano-sensors the insects already had (Yack, 2004). These mechano-sensors are the subject of the following section.

1.8 Chordotonal organs

While insect ears evolved numerous times (Robert et al., 2007, Strauß et al., 2015) the underlying mechano-receptors, called chordotonal organs, are universal in insects (Yack 2004, Strauß et al., 2015). While not all employ them for acoustic perception, the majority of insects have Johnston's organs, a specialised form of chordotonal organ located in the insect antenna (Kristensen, 1981). Chordotonal organs are very versatile in their ability to detect mechanical stimuli of different origin and are almost exclusively the go-to solution for innervation of insect ears (Nadrowski et al., 2010).

Before delving deeper into the function and organisation of the Johnston's organ, Fig. 1.8 is meant to introduce the morphology and terminology as well as its location inside the pedicel. The number of scolopidia varies largely between species – for example, *Drosophila* has 230-240 (Nadrowski et al., 2010) and mosquitoes up to 7000 (Boo et al., 1975). These units are formed by 2-3 primary mechano-receptor cells (Boo et al., 1975, Todi et al., 2004), the scolopale cell (creating the endolymph space) and a cap cell (connecting to the third antennal segment, the flagellum) attached by a ligament cell. Their neurons, which are attached to the second antennal segment (pedicel) cuticle, are of the bipolar type, with – at least in *Drosophila* and mosquitoes – a 9x2+0 axonemal structure (Uga et al., 1965, Boo et al., 1975).

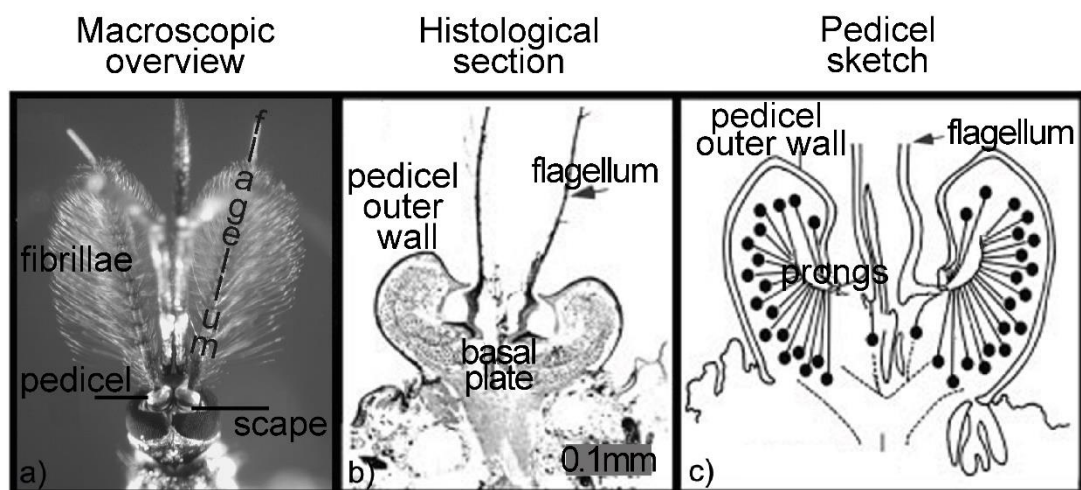


Fig. 1.8: This figure shows the location and schematic organisation of the Johnston's organ. It is simplified and reproduced from Yack (2004) in a modified version from the one already used in Saltin (et al., 2019). Panel a) shows the head of a *T. brevipalpis* male. Panel b) shows a cross-section of the pedicel, scale bar 0.1 mm, and panel c) a schematic of the inside of the pedicel.

As with the so far unsuccessful location of the motor protein, it is curious that an axoneme lacking the two central microtubuli is of the generally sensory type. Warren et al. (2010) demonstrated that in the sensory cilia of mosquitoes at least, dynein

could be the motor-protein. They do so based on works by Wiederhold (1976) and Mitchell (2007), who illustrate that the distinction between sensory and motile cilia does not have to imply that sensory cilia are immotile. Chordotonal organs generally consist of type I mechano-receptors, see also Fig. 1.9 ab (Yack, 2004). The Johnston's organ, which is the organ critically involved in antennal hearing, consists of scolopidia that proximally connect a radial array of cuticle diversifications known as prongs (see Fig. 1.8). The antennal shaft brought into oscillation by an external stimulus vibrates, thereby moving those prongs. This vibration then is thought to convey stretching and relaxation on the scolopidia which is transduced to neuronal signals in a hitherto unknown way (Yack, 2004).

Scolopidia, at least in *Aedes aegypti*, can be classed into four types (A-D). All of them are Type I mechano-receptors, two of which (A (ca. 97%) and B (3%)) make up the vast majority of scolopidia with Type C and D being neglectable in terms of numbers (Yack, 2004). A and B are the ones most likely involved in hearing. While it is not entirely clear that referring to the same subset of five respectively four scolopidia classes, Matsuo (2013) was able to locate different fields of scolopidia genetically within the Johnston's organ of *Drosophila*, which lends support to the idea of a specialisation and typological differentiation of scolopidia towards different functions. More recently in a sophisticated – not yet peer-reviewed – electrophysiological experiment, Laphsin et al. (2019) could demonstrate in male *Culex* mosquitoes that it is highly likely that twice-frequency forcing originates from neuron triplets/doublets inside the Johnston' organ. This would also align with findings by Windmill et al. (2018) demonstrating twice-frequency forcing on the cellular level with atomic force microscopy.

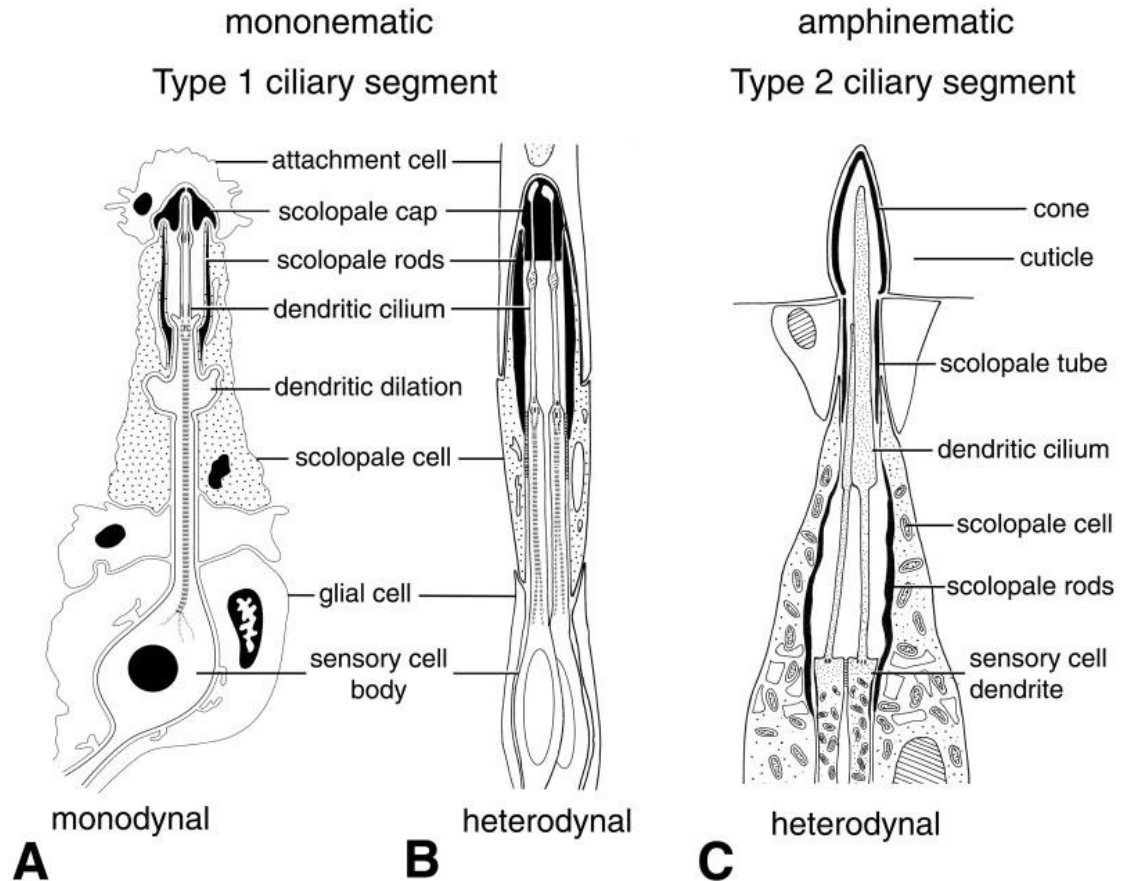


Fig. 1.9: This figure is reproduced from Yack, 2004, this figure illustrates three different types of scolopidia. “A: A mononematic, monodynal scolopidium from the tympanal ear of *Locusta migratoria*. B: A mononematic, heterodynal scolopidium from the femoral chordotonal organ of an adult lacewing, *Chrysoperla carnea*. C: An amphinematic, heterodynal scolopidium from the mouthparts of a beetle larva, *Speophyes lucidulus*. A is reproduced from Yack and Hoy (2003; after Gray [1960]) with permission of the publisher. B and C are redrawn from Lipovsek et al. (1999) and Corbière-Tichané (1971), respectively.” Monodynal scolopidia have only one neuron and cilium – in contrast heterodynal scolopidia, which have two to three cilia. Unaffected by cilia number, scolopidia can be classed as mononematic if their cap is subepidermal, while amphinematic ones lack a cap structure but instead have tube shaped sheaths and might protrude into the cuticle layer. Type I consists of bipolar sensor neurons and type 2 of multiple neurons, which are non-ciliated. All definitions of terminology given here are taken from Fields (et al., 1998).

1.9 Recent technology developments in insect audition science

1.9.1 The Doppler effect and how it is used for laser vibrometry

The Doppler effect describes how the movement of source or receiver affects the measured frequency. In the most general case of a wave – which, like sound, travels within a medium – both movements affect the measurement result inversely. The frequency relation is given by

$$f = f_0 \frac{(1 \pm \frac{v_o}{v_{ph}})}{(1 \mp \frac{v_s}{v_{ph}})} \quad (1)$$

where f is the frequency, f_0 the frequency if neither source nor sender move, v_{ph} the phase velocity of the wave, v_o the velocity of the observer and v_s the velocity of the source. It is important to note that in terms of the sign direction +/- and -/+ if source and receiver are moving towards each other the upper signs apply and vice versa if they move away from each other. To use one of the most common and instructive examples, if source and receiver move towards each other (e.g. an approaching ambulance) the frequency increases, while once the source passes the observer, the frequency drops appreciably as the signs now are inverted and the speed of the source reduces the perceived frequency. For scientific purposes, in the case of Laser Doppler Vibrometry (LDV), we can eliminate the effect of the observer moving, as we keep the laser emitter and the detector in relation to the sample (the source) constant in space over time. With that ($v_o=0$) the above formula becomes:

$$f = f_0 \frac{(1 \pm \frac{0}{v_{ph}})}{(1 \mp \frac{v_s}{v_{ph}})} \quad (1b)$$

which equates to

$$f = f_0 \frac{1}{\left(1 \mp \frac{v_s}{v_{ph}}\right)} \quad (1c)$$

In this case again, the upper sign denotes movement towards the receiver and the lower case away from the receiver. In practice, however, only the frequency difference is detected, which means that the measurement system cannot without further information tell the direction of movement. This is where the design of the measurement device (described in Methods) becomes important. The design of the device can also help to resolve the issue that even with relatively high frequency mechanical movements, the frequency differences are very small compared to the frequencies of light, by introducing a known artificial phase shift. Without going into the technical details of the system specification, which are described in Methods, how does LDV use the Doppler effect to record sample movement, velocity and acceleration? The technique started being used in 1964, just four years after laser technology was developed (Rothberg et al., 2016).

It capitalises on the Doppler shift introduced by sample movement during illumination with a laser beam (Rothberg et al., 2016). The main advantage being that the technique is non-contact, and therefore does not or only minimally interfere with the object's natural vibration (Rothberg et al., 2016). As the above general formula for the Doppler shift relates, the shift is directly related to the velocity of the sample movement. It does, however, require some technicalities to also extract the direction of movement. In the earlier days the technique was mainly focused with fluid-flow measurements, and only gradually escalated first into solid surface

science, and much later with the advent of scanning laser vibrometers in 1980, into engineering. There it has become a staple of structural health monitoring (Rothberg et al., 2016). Finally, in 1981, the first in vivo experimental work on a biological hearing system was published by Buunen et al. (1981, Rothberg et al., 2016). As the technique is very susceptible to noise, acoustic and mechanical isolation is key to its successful implementation in low amplitude vibrations systems (Buunen et al., 1981).

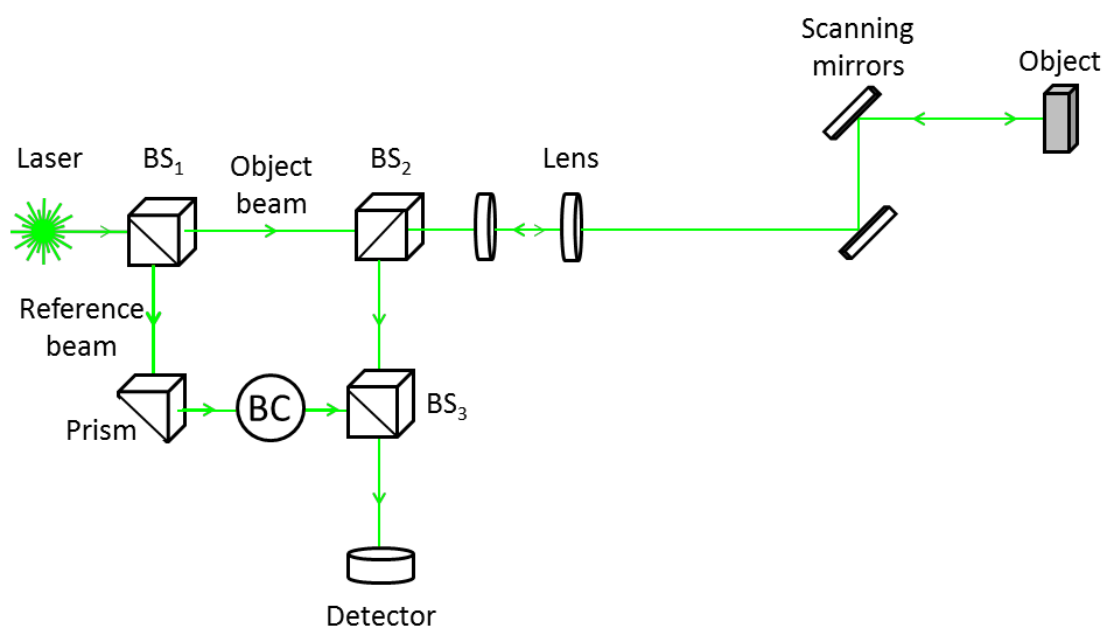


Fig. 1.10: This figure shows a 3D laser vibrometer function schematics. Slightly modified from Domingo-Roca (2018) based on the Polytec manual. The schematic illustrates how a laser is directed from source (left) through a first beam splitter (BS1), dividing it into an object beam and a reference beam. The reference beam is redirected by a prism and a comparative large frequency shift is introduced to it by a Bragg Cell (BC). The object beam, however, is split again. One part is going back to the detector and the other one is focused by two lenses and twice redirected by mirrors onto the investigated object. The reflection of this object beam then is redirected two more times, focused and redirected again. In the detector, the three beams then are registered simultaneously. The first is the reference beam, shifted by the Bragg Cell (after 1st split). The second is the beam portion taken from the object beam before it left the system (2nd split of the object beam). This one remains unchanged. The third is the reflected backscatter of the object beam.

Multi-channel devices of either multiple lasers or detectors have made 3D scans possible without the need to arrange multiple (costly) vibrometers as well (Rothberg et al., 2016). A schematic function of the device is reproduced modified from Domingo-Roca (2018, who based it on the Polytec manual) as Fig. 1.10.

1.9.2 The LDV device used for experiments in this study

In the used 3D LDV (Polytec MSA-100-3D), which has one beam and three detectors, there are two off-axis (X and Y) and one on-axis (Z) independent interferometers. This configuration allows to read out X, Y, Z velocity for each scan point of 3-5 μm size independently by a velocity-decoded voltage range 0-10V, using software adjustable to the expected movement range. Given the transient nature of antenna vibrations in combination with the fineness of the structure, manual focusing proved to be the best solution, albeit time-consuming and difficult. Therefore, to adequately capture the antenna – as subsequent scan points would not be on the same set of oscillations – only single measurement points were taken and at least in *T. brevipalpis* consequently without averaging in order to allow for capturing the instantaneous movement dynamics.

1.9.3 How does Confocal Laser Scanning Microscopy (CLSM) work?

CLSM is derived from fluorescence microscopy, which like conventional light microscopy has an issue with spatial resolution, as light enters the object or parts thereof uncontrolled and therefore the image is composed of in and out of focus-plane light rays – leading to blurring of contours and details.

Since its beginning, improving the resolution was the drive for the development of the fluorescence microscope and its predecessor, the ultramicroscope by Siedentopf in 1903 (Masters, 2010). Early on this was achieved simply by the use of smaller wavelengths, that is, higher light frequencies. The fluorescence microscope of today is based on either the Carl Zeiss fluorescence microscope or the competing Carl Reichert machine. Both were transmission mode microscopes, which only varied in the used condenser that were marketed around 1913 (Masters, 2010). Another milestone was the “illumination from above” developed by Brumberg in 1948. It uses a beam splitter (dichroic mirror) to allow epifluorescence microscopy where illumination and detection can take place from the same side as the reflected excitatory light does not pass through to the detector. Confocal microscopy was first addressed by Marvin Minsky who, predating laser technology, came up with the idea to use a point light source in combination with a pinhole apparatus to reject out-of-focus light (Minsky, 1961). The resulting rejection of out-of-focus light and applying a focused light beam point by point to the sample, thereby scanning the reflected intensity of each sample point in two or later three dimensions allowed a drastically increased detail resolution, generating perfectly sharp image planes. Later, in 1982, this technique was combined with laser-based fluorescence microscopy, eventually becoming Confocal Laser Scanning Microscopy using artificial fluorophores or the specimen’s autofluorescence in response to the laser excitation to image an object (Masters, 2010). Autofluorescence is the naturally occurring fluorescence without the application of a fluorescence dye to the specimen and originally was seen as a contrast hindrance for the ultramicroscope in 1903 (Masters, 2010).

Today it is, amongst others, used in the study of insect cuticle surface structures and, as it makes the addition of fluorophores unnecessary, allows the imaging of quasi-natural structures (Neff et al., 2000, Michels et al., 2012, Matsumura et al., 2017, Bergmann et al., 2018).

1.9.4 How does Finite Element Modelling (FEM) work?

FEM was originally developed in 1909 to help with the deformation of solids by Ritz (Ritz et al., 1909). However, it greatly benefitted from the advancements in computer science. Nowadays it is possible to solve a variety of field problems for example, thermal or electric conductivity, fluid dynamics or acoustic fields in a similar manner (Reid, 2017). The theory behind it has not changed since the technique was devised over a hundred years ago. In principle, FEM breaks down a physical situation, e.g. beam bending, into a series of smaller subelements, thereby allowing to solve the governing equations on a more limited and geometrically simpler entities (Reid, 2017). This is done by A) converting any given (complex) geometry into a set of simple symmetrical domains later called a mesh, by a program-embedded meshing algorithm and B) by shifting from the given strong-form equation, which as underdefined has no close-form solution to the weak-form equation.

The boundary condition can either be a “Dirichlet boundary” (boundary values are known and the resulting changes inside the investigated volume realm are calculated accordingly) or a “von Neumann boundary” (where the derivative of the boundary condition is defined and therefore known).

The exact theory behind this can be found (e.g. Mackie, 2015), but should not be of particular concern as the aim is not to improve or evaluate FEM methods but to apply said methods to a very specific biological problem. The combination thereof allows – in absence of an analytical solution for the whole problem – to utilise the Lagrange minimal work principle to find local minima using the minimum field equation,

$$f = -\Delta u + cv \quad (2)$$

where u = the unknown scalar, c = a constant, and v = shape-dependent for the function f . Furthermore, using Green's first identity, this can be transformed to

$$\int_{\Omega} (\Delta u) v + \int_{\Omega} \Delta u \cdot \Delta v = \int_{\Gamma} (\partial_n u) v \quad (2b)$$

as the Green identity (Riemann, 1851) shows that integrating over the boundary of an area equivalently solves integrating over the area itself. That is, with u being the situation under investigation and v a shape function.

The shape function is in this context for all practical purposes equivalent to the geometry defined mesh of the COMSOL simulation. The point here is that by subdividing the boundary, additionally, due to boundary condition, known points are defined allowing to expand the equation system, thereby making it sufficiently defined, once the known number of points equal the number of unknown variables. From this point on it becomes possible to solve the equations for the unknown points and thereby providing an estimate solution for the analytically unattainable situation. When discretizing a problem like this, attention has to be paid to size of the mesh elements as they need to be smaller than the shortest investigated wavelength (Reid, 2017).

This limitation, however, rarely becomes an issue with small structures like insect antennae, as the element size is also limited by the shortest dimension inside the volume. This can easily be as low as $100\mu\text{m}$, while the wavelengths for frequencies of interest are safely in cm range. Even for the upper frequency limit used (2.2kHz) the wavelength is 15.5cm. The real limit, especially with long and thin structures (unfavourable aspect ratios, leading to very small element sizes) becomes the computation time. By recombining the solutions for all subelements, an approximate solution for the situation under investigation is gained.

2. Material and Techniques

2.1 Animal culture maintenance

For this thesis, four species of non-Brachyceran flies, *Anopheles arabiensis*, *An. gambiae*, *Chironomus riparius*, and *Toxorhynchites brevipalpis*, were kept in the laboratory. Adults of all these species can be kept on 5% sucrose solution, provided on paper or cotton pads, refreshed every 2-3 days. To keep the necessary humidity (60-80%) and temperature (20-30°), a climate chamber was used (Brisea OVA-Easy, Advance from the Incubator Shop, TMM Direct Ltd., Beverley East Riding of Yorkshire, United Kingdom).

Toxorhynchites brevipalpis was bought in pupal stage from Shahida Begum at the Faculty of Infectious & Tropical Diseases (Disease Control Department, London School of Hygiene & Tropical Medicine, London, United Kingdom). Upon arrival, pupae were transferred to shallow water cups and placed in standard mosquito cages. *Anopheles arabiensis* and *gambiae* males were provided by Dr. Francesco Baldini of the Vector Biology and Disease Group (University of Glasgow) and kept alive on a diet of 5% sucrose solution in standard mosquito cages.

As *An. arabiensis* females are vectors competent for multiple mosquito-borne diseases, they had to be excluded from the investigation to comply with health and safety regulations more easily.

Chironomus riparius, after initially sharing some difficulties with *Chironomus plumosus*, whose culturing attempts have been terminated in an early stage of the study, later proved easier to keep in full culture. Their culturing was loosely based on McLachlan (1977) and Habashy (2005).

Modifications were made either based on experience or according to advice given by Dr. C. Lorenz of the Animal Physiology Ecology group at the University of Tuebingen (personal communication, 2015), who kindly provided eggs of *C. riparius*. Larvae of *C. riparius* were kept on a diet of commercial fish food (TetraMin, TetraMin GmbH, Herrenteich D-7849324) residing in plastic bowls (of 15cm depth), in which the water column was 7-9cm over a 3-5cm thick sand layer. The water was changed partially every three weeks and fully every two months. Water was kept oxygenised and in motion by a low-level pressurised air flow into each bowl. The sand, despite being particularly intended for use with animals (Thomas Hyne, fine grained bird sand, Glasgow) needed repeated thorough washing and watering for maintaining a healthy insect culture.

Both basins were placed in the lower of two layers of a custom-built, 1m x 1m x 2m flight cage covered in insect netting, to ensure sufficient space for swarming. Swarming is essential for mating to take place in *C. riparius*. Later tests with smaller enclosures also produced some offspring, but to a much lesser extent.

2.2 Laser Doppler Vibrometry (3D)

2.2.1 Specimen preparation

Animals, within a tube, were carefully anaesthetised with CO₂. Then, using a soldering iron, animals were placed between two sheets of dental wax (Kemdent, Dental Products Ltd, Purton, Swindon, SN5 4HT United Kingdom) with only the head protruding. After confirmation of animal health, the wax block was labelled

with specimen number before proceeding to glue the animal's head to its thorax and its pedicel to its head to prevent large scale movements.

The glue was applied to the animal using stainless steel insect pins (size 00). After a brief resting period inside the acoustic booth experiments were commenced.

2.2.2 Laser Doppler Vibrometry Experiments

In order to understand how the sample – in the present context the mosquito antenna – moves (in 3D space), Laser Doppler Vibrometry (LDV) is a suitably accurate non-contact measurement method. LDV is an excellent tool for this kind of research, opposed to human perception, as insect antenna movements are too small (pm to nm range) and too fast (shorter than 40ms, which equates to 25Hz, for example the human critical flicker frequency) to be resolved with unaided vision. While the possible frequency resolution of the device goes up to 2MHz, the movements of interest to the mosquito – and thereby the present study – are below 1kHz. That the technique is non-contact is important to the question of mosquito antenna movement for three reasons. Firstly, a thin and tiny structure like a mosquito antenna could easily be damaged by a contact measurement. Secondly even a very small and light measurement device would be comparatively heavy and therefore influence the observed motion, and thirdly a non-contact technique allows in principle for all natural degrees of freedom. The latter point is important to the present study as by using the three built-in sensors it is possible to execute three-dimensional tracking of the antenna in real time. LDV relies on the Doppler shift (Doppler, 1842). For the case of vibrometrical assessment of insect hearing organs this means, under the assumption that the sensor (antenna) and detector (LDV) positions remain constant

relative to each other, and combined with the fact that the initial qualities of the laser beam are known, that any shift in frequency of the reflected laser beam can be attributed to the animal's movement.

The potential for motion is further narrowed down by the experimental setup (see Fig. 2.1 and Fig. 2.2). It allows for antennal, but not for body motion. The signal provided by the internal signal generator or a playback via NI-DAQ-Box (National Instruments Data Acquisition Box) is played by a speaker after amplification (depicted in Fig. 2.1). The trigger of the internal signal generator is either looped back directly, so the signal generator automatically triggers the LDV measurement, or triggering is done manually, in the case of experiments in which the signal is started and stopped during the data recording. In the case of a DAQ-box playback, the trigger-out of the DAQ is connected to the trigger-in of the 3D LDV instead. The used DAQ consisting of NI BMC 2110 and NI USB 6251, with 16 input channels, 16 bit and a 1.25 MS/s (National Instruments Corporation, 11500 N MoPac Expwy, Austin, Texas, USA).

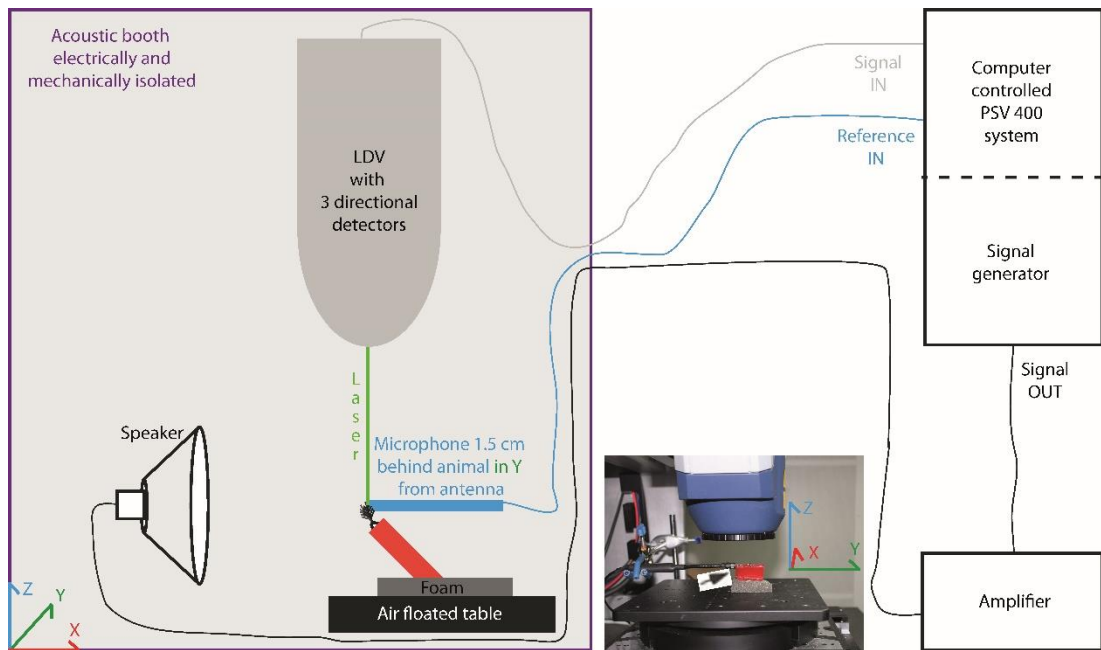


Fig. 2.1: Schematic of the experimental setup.

The figure shows from left to right, in purple the acoustic booth, in the lower left corner of which the coordinate axes of the laser system are indicated. The speaker is mechanically decoupled from the air-floating table (black, not to scale), on which the animal is positioned (inside the red box, representing the dental wax). The reference microphone is depicted in blue. In green the object beam of the LDV (which is outlined in gray) pointed on the insect's antenna protruding from the wax. Outside the booth there are the computer control system of the LDV (upper right corner), signal generator, and the acoustic amplifier (lower right corner). The photograph in the middle shows the animal setup as the setup faces the speaker. The image is taken from just above the speaker position. In the given viewing plain of the main schematics the X axis aligns with the experimental X axis while the Y axis of the view provided is the experimental Z axis. The image from above the speaker is rotated by 90° clockwise in relation to the schematics. Black arrow on white ground indicates where microphone and animal are aligned.

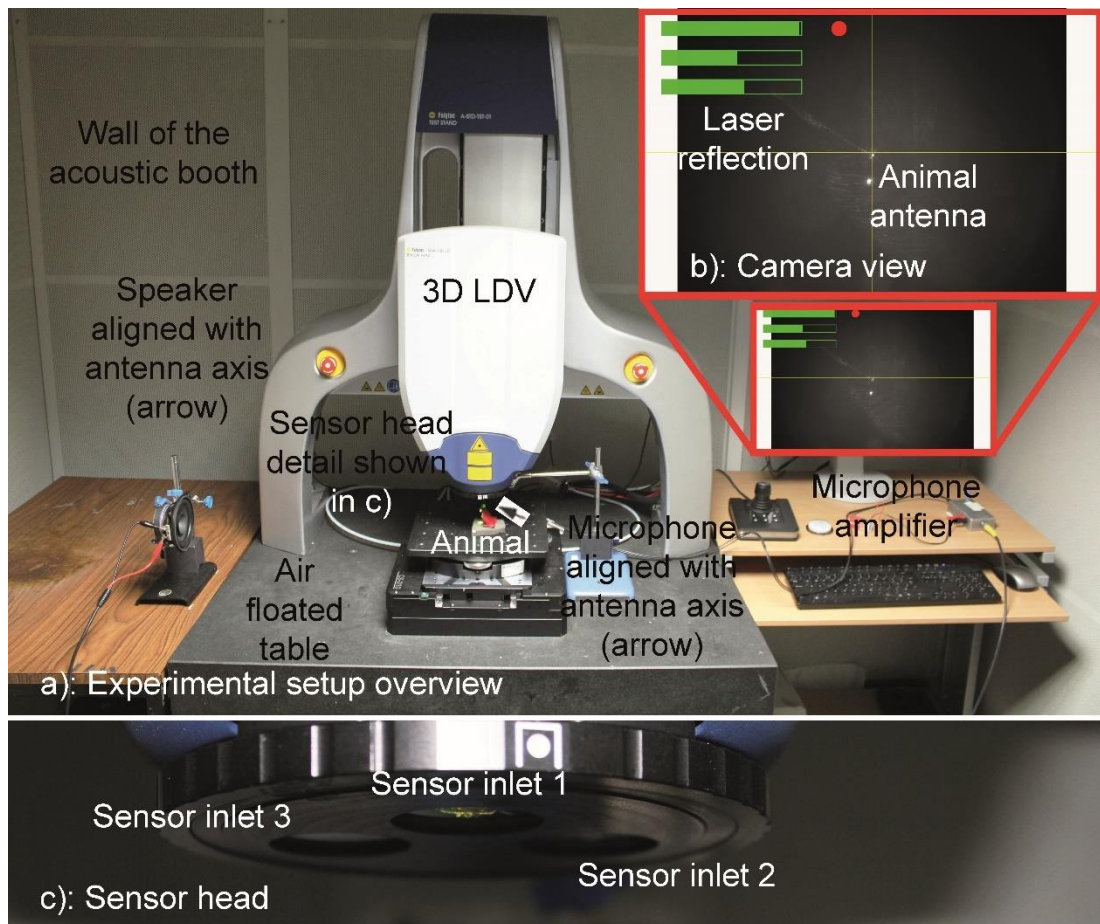


Fig. 2.2: a) Experimental setup overview. Speaker to the left and microphone amplifier to the right (gray box) on independent tables to avoid mechanical coupling of speaker drive and animal or microphone. b) Contrast improved setup image of the insect antenna with focused laser beam on last flagellomere. c) Sensor head of the 3D LDV, where the image shows the active laser and the three sensor inlets, one for each direction. Black arrow on white ground (just below the middle of panel a)) indicates where microphone, speaker and animal are aligned.

After capturing the laser frequency and amplitude with three directional sensors within the sensor head (see Fig. 2.2c) and 3D LDV (Fig. 2.3), the object beam is compared to the previously generated reference beam (including the known frequency shift by the Bragg cell) to calculate the movement of the test sample in time and 3D space, which is the basis of the frequency shift. For a more in-depth description see Introduction or the Polytec User manual (Polytec, 2008).

Furthermore, the general procedure of laser vibrometry on insects or even their hearing organs has been described elaborately and extensively manifold in the past two decades, not least by Warren, Jackson, and multiple recent PhDs and post-docs in the University of Strathclyde's Bioacoustics group (Hoy, 2006, Jackson, 2006, Jackson et al., 2006, Albert et al., 2007, Kössl et al., 2007, Göpfert et al., 2008, Nadrowski et al., 2008, 2010, Warren, 2010, Montealegre-Z et al., 2012, Mhatre et al., 2013, Mackie, 2015, Reid, 2017, Su et al., 2018). For this reason, only the specialties of the performed experiments on mosquito antennae will be reported in the following experimental procedures.

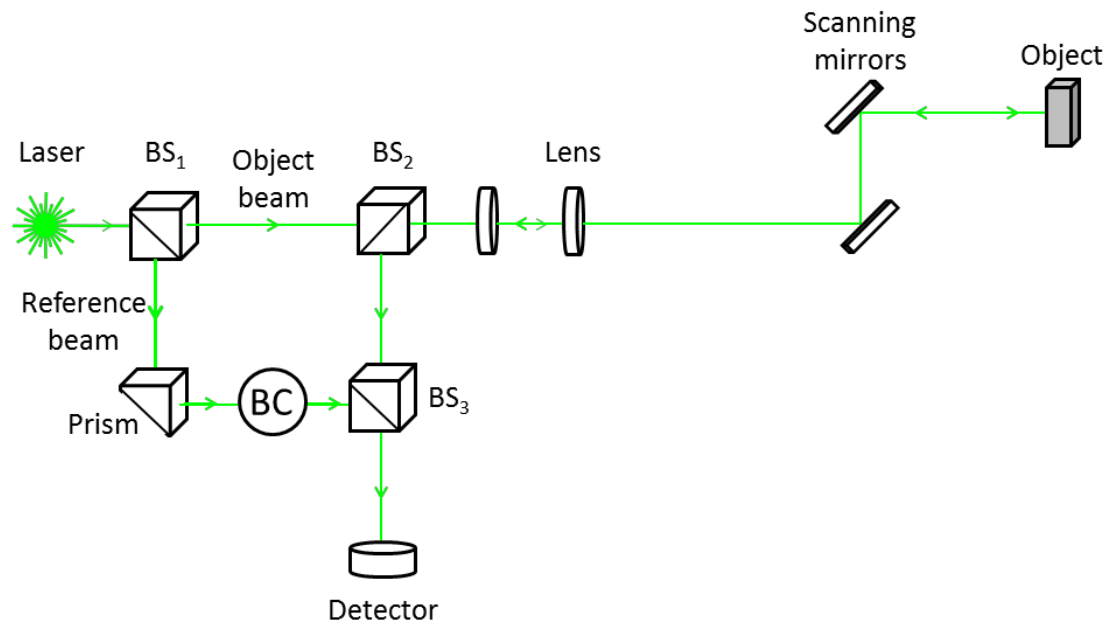


Fig. 2.3: 3D laser vibrometer function schematics. Slightly modified from Domingo-Roca (2018) based on the Polytec Manual. The schematic illustrates how a laser is directed from source (left) through a first beam splitter (BS1), dividing it into an object beam and a reference beam. The reference beam is redirected by a prism and a comparative large frequency shift is introduced to it by a Bragg Cell. The object beam, however, is split again. One part is going back to the detector and the other one is focused by two lenses and twice redirected by mirrors onto the investigated object. The reflection of this object beam then is redirected two more times, focused and redirected again. In the detector, the three beams then are registered simultaneously. The first is the reference beam, shifted by the Bragg Cell (after 1st split). The second is the beam portion taken from the object beam before it left the system (2nd split of the object beam). This one remains unchanged. The third is the reflected backscatter of the object beam. While in theory an unchanged beam and the backscatter would suffice to calculate the object movement, in praxis the frequencies of light are too high and the object movement frequencies too low – this is the reason the third beam with a huge frequency shift compared to the original one is used as well. Given that all original states (e.g. positions, wavelength and movement – except the movement of the object to investigate – are known, the measured introduced frequency shifts can be attributed to the objects movement.

2.2.3 Measurement errors

While not all measurement variation – investigating a biological sample – is due to measurement errors, it is important to judge how large the effect of measurement errors in a given case can be. There can be many sources of uncertainties including but not limited to animal positioning, physiological state, signal generator and amplifier reliability. The focus of this section is the precision and repeatability of the laser positioning. To estimate the influence of potentially varying positioning of the laser focus point, a marked spot on the vibrometer table was consecutively focused twelve times. The positioning errors are provided in row two of Table 2.1 for each direction independently as standard error of the mean absolute and in percent of the mean in parentheses. In line two as comparison the median absolute deviation (MAD) is given also as absolute followed by percent of median in parentheses. The length of twelve randomly picked antennae varies by mean = 53.5 μm (1.5%), median = 53.7 μm (1.5%). When comparing the position errors in Table 2.1 with these values, errors are small. Here it has to be pointed out that while it is used as a benchmark, the length variation between animals – influencing beam frequency by its very nature – is by no means considered an error source.

Table 2.1: shows the positioning errors of the laser beam for each direction independently. MAD means median absolute deviation, percentages are in relation to the mean (line 2) or median (line 3)

Positioning of the laser beam	X direction (left and right)	Y direction (back and forth)	Z direction (up and down)
Standard error of the mean	X:5.2 μm (0.1%)	Y:4.3 μm (0.02%)	Z:7.5 μm (<0.01%)
MAD	X:5.2 μm (0.1%)	Y:4.4 μm (0.02%)	Z:7.7 μm (<0.01%)

On the contrary, it is one of the investigated and otherwise little studied parameters. The fact that those lengths do vary more than ten times as much as the laser positioning, however, ensures that the precision of pointing the laser is so accurate as not to contribute in any meaningful way to the overall error of measurements – hence it can be excluded from considerations.

2.2.4 Microphone calibration

A further consideration is how to keep the reference channel consistent and comparable over the lifetime of the microphone, as particle velocity microphones are prone to changes of characteristics, for example due to settling of dust upon the sensor or changes in humidity. To mitigate this effect, a calibration against a known microphone was performed. The B & K microphone type 2670 (No 3018086) UA 100 (Brüel & Kjær, Engineering company, DK-2850 Nærum, Denmark) was manufacture calibrated in 2014, it was used with a Nexus conditioning amplifier (Brüel & Kjær, Engineering company, DK-2850 Nærum, Denmark) with the transducer supply set to auto and the polarity kept at 200V. The experimental velocity microphone was a Knowles (Knowles 25624 2308 W1 (Knowles, 1151 Maplewood Drive Itasca, Illinois, USA)) it was connected to a Low Noise Dual PreAmplifier (LM 387/LM387A up to 104dB gain (Texas Instruments Incorporated, P.O: Box 660199, Dallas, Texas 75266, USA formerly National Semiconductor Corporation)). The calibration of the velocity microphone was done by recording with both microphones (detail of the calibration microphone above) the same signal – a sine wave of 338Hz (approximately the middle of the relevant frequency range).

With 420 Ray's being the specific acoustic impedance of air it is possible by using the ratio between the recorded read-out voltage for both microphones and converting to sound velocity – based on the relationship between pressure (P [Pa]), sound velocity (V_s [m/s]), and the specific acoustic impedance (Z [Pa*s/m]),

$$P = Z(t) V \quad (3)$$

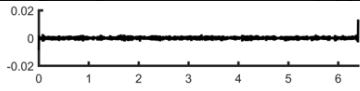
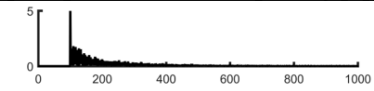
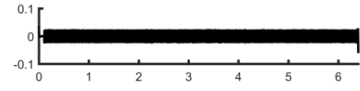
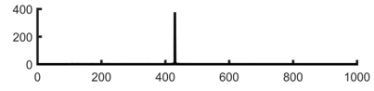
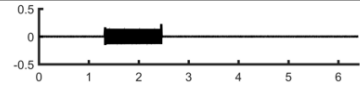
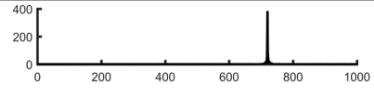
- to find a calibration factor. In the used setup this factor is 12.65.

Given that both microphones are considered approximately flat in response in the frequency range of interest, a one-point calibration was deemed sufficient.

2.2.5 Experimental procedures to record the movement in time and space

In order to be able to understand how a system behaves, a method that allows for accurately measuring it needs to be found. As discussed in section 2.2.2, LDV is very well suited to the task of making small scale fast movement observable. This section will detail how the experiments were arranged.

Table 2.2: This table shows the signal types used. Left column: signal types used. Middle column: time traces, amplitude over the 6.4 seconds recording period. Right column: Fourier domain representation of the same signal's frequency vs. amplitude. Time and FFT representations are filtered for below 100Hz noise.

Signal Types	Time Trace [Amplitude vs. Time [s]]	Fourier Domain [Amplitude vs. Frequency[s]]
No signal		
Sine wave		
Short time burst Sine wave		

Laser vibrometry is a non-contact vibrational measurement, recording the velocity of system motion. The presented experiments were performed without any averaging as systems states shift unpredictably. Hence, averaging would reduce the information content of the recordings as the documentation of the instantaneous movement is the focus of interest in this investigation. This being said, it has to be stated that an exception to the no average recording rule was made for *An. gambiae*, as clean recordings were difficult to obtain and supply was limited. This precludes investigation of movement patterns and instantaneous frequency for this species. It does, however, allow for frequency evaluation and while values need to be interpreted with caution for displacement (likely underestimated due to averaging) and Q factor (likely overestimated). The performed frequency evaluations are robust enough to provide a ball-park figure for this species and allow comparison with the other species.

A similar issue – albeit to a lesser extent – is present in *An. arabiensis*. Here the majority of the recordings was also done with magnitude averaging. The five recordings used for three-dimensional pattern analysis, however, were done without any averaging and fall within a similar value range, thereby validating the averaged recordings further. This even lends some further credibility to the averaged recordings in *An. gambiae*. In the more reliably available and dramatically more robust *T. brevipalpis* there was no need for averaged recordings. There were no averaged recordings performed for either *T. brevipalpis* or *C. riparius*.

The two main types of experiments (see Table 2.2) were, a) recording of self-oscillation of the animal in absence of an acoustic stimulus, and b) adding a sine wave tone immediately at full volume – generated by the built-in Polytec Signal generator. In the case of the DAQ playback the DAQ was triggered via one input channel by the internal LDV control PC (e.g. a₀₁) to put out a predefined signal in one of its output channels (e.g. a₀₀). As reference a calibrated (see section 2.2.4) sound velocity microphone was used.

For both the experimental measurement of self-oscillation and the addition of a sine wave stimulus, the animal and speaker position (see Fig. 2.1 and Fig. 2.2) were the same. The speaker used was a Riesen Special Performance Car Speaker (L20AT, 80 watt, 93mm membrane, speaker impedance 4 Ohm, response range 110Hz to 20kHz, sensitivity 86dB) connected to either the internal signal generator (see 3D LDV below) or the previously mentioned DAQ system via an integrated amplifier (either Sony Spontaneous twin drive Super Legato Linear TA-FE 370 (Sony, 1-7-1 Konan Minato-ku, Tokyo 108-0075, JAPAN) or an Onkyo Instant Amplifier A9010 (Onkyo, Kitahama Chuo Bldg. 2-2-22 Kitahama 541-0041)). See Appendix for a basic speaker characterisation.

The laser beam was focused on the lower end of the 13th segment of the antenna, taking care to have a compromise between good reflection and to use the minimal laser power, to avoid localized heating of the antenna. Typically, single point laser measurements were taken, as the amount of time available for experiments during which animals are in a good experimental state and remain static enough for manual focusing in three dimensions is limited.

For further equipment specification see below. A microphone was placed close to the right of the animal with a distance of ca. 1.5cm and perpendicular to the speaker facing the sound source the same way as the animal's antenna does (see Fig. 2.1). By aligning microphone (as indicated by black arrow on white ground in Fig. 2.1 and Fig. 2.2) and sample in this matter it is ensured that the recorded reference channel (microphone output) is exposed to the same stimulus or general acoustic environment as the animal. Data recording was performed with 5kHz sampling frequency as the relevant signals are below 1kHz yielding sufficient data point per oscillation cycle. The choice of 5kHz sampling rate and 12800 FFT bins – each 0.15625Hz – sets the recording duration to 6.4sec.

The 3D LDV system used is a custom-built Polytec prototype. It consists of an axis controller (Polytec A CTR-100), vibrometer front end (Polytec MSA-100-3D), Data Management System (Polytec DMS), a sensor head (Polytec MSA-100-3D) containing 3 heads (1st MSA-I-100, firmware 1.00, 2nd MSA-I-120, firmware 1.00, MSA-I-120, firmware 1.07), an acquisition board spectrum (M2i.4961), vibrometer controller (PSV-F-500-3D, firmware 1.07), decoder (DV-505, firmware 1.10) and a function generator (M2i 60xx).

2.2.6 Data Analysis

With the data acquired, interpretation of the recorded 3D motions of male and female animals is the next step. The raw time data are difficult to read for multiple reasons including, but not limited to, electric 50 & 100Hz noise, the amount of the included positional data, aggravated by the fact that with the base of the antenna fixed in space, subsequent movement cycles are plotted in the same space.

One way to deal with this issue is reducing the datasets to key metrics, for example mean frequency, median, standard deviation (StD), median absolute deviation (MAD), amplitude at mean frequency, and quality factor. While those metrics are undeniably useful and will be given where indicated, they also suffer from noise, do not convey any three-dimensional information and are unable to adequately describe more complicated situations, for example where a stimulus frequency and self-oscillation are both driving the system at the same time.

At this point visualisation of the instantaneous movement becomes key to understanding the system's behaviour. This visualisation and, where applicable, filtering were conducted with custom-built MATLAB code. A high-pass filter value was adjusted depending on species and was generally 120Hz for *Anopheles* sp. and 200Hz for *T. brevipalpis*.

In all the following procedures the sampling frequency (5000Hz) and the duration of the recordings (6.4s) were taken into account – different functionalities were pursued with independent pieces of code.

2.2.6.1 Considerations on filtering the data

An issue common to all pieces of code is filtering, as it is difficult to completely exclude low frequency noise. Hence, it will be addressed here prior to going into details of the specific aspects investigated. The presence of low-frequency mechanical (e.g. building vibrations) and electrical noise (mainly from the power grid) led to the filtering of these low frequencies (<120Hz) being the most common data processing step.

In principle there are two end goals to data analysis in this work. In some cases, the visualisation of the data in 3D space was the target, in others automation of data analysis. Each of these two goals demanded an individual and at times contradictory approach to filtering. In the case of visualisation, one wants the filter to have the minimal as possible impact on data representation meaning a low-pass filter should be as low as possible for the given experiment and species in these cases. For more analytical purposes, this can be reversed as the smaller the filtering window is the more noise is excluded. This enables a more reliable automated peak identification, with less need for direct optical inspection. With the data volume involved, this was highly desirable.

2.2.6.2 How data were filtered

To achieve a reasonable filtering result, the frequencies in questions were symmetrically set to zero in the Fourier domain of the data before reconvertng back to the time domain. While this effective application of a high pass rectangular window as a FFT- or frequency selective filtering comes with the usual faults of rectangular windowing, this was deemed the most suitable approach.

The most prominent flaws are leakage and an increasing error if the tested signal is explicitly between frequency bins of over 30% – which is hard to avoid as the exact vibration frequency is unknown prior to investigation. Given that the main interest is the identification of closely spaced frequencies that can transiently change due to self-oscillation despite high Q factors and that the signal to noise ratio is unfavourable, other approaches could also or even more distort the signals (Wickramarachi, 2003). If higher cut-off frequencies are used it will be stated in the

specific program. One might argue that this approach is rather heavy-handed. It does however have the advantage of not creating artificial phase information in the zeroed frequency band or the area of transition between filter and no filter signal.

2.2.6.3 Converting from velocity type data to displacement data

The LDV records object velocity. In some cases, however, the interest is rather the amount of displacement than the velocity with which this displacement is reached. To this end omega statistics (Mercer, 2006) is used to convert the Fourier domain raw or filtered velocity data into displacement data. To match the displacement amplitudes with the ones seen in the direct Polytec readout, the data furthermore needed to be scaled by a factor equal to half the number of FFT points.

As this is only relevant to questions of amplitude, not to questions of frequency the conversion was not used in all scripts. Still, usage was common enough to warrant being described here, rather than for all individual instances.

2.2.6.4 List and brief description of individual MATLAB scripts used

Q factor estimation:

The following paragraph addresses the special case of a self-oscillating system and the Q factor of self-oscillation. One of the above-mentioned MATLAB scripts is used to calculate the Q factor of the antenna in self-oscillation.

The Q factor of an actively driven system is expected to be $\gg 1$, as energy dissipation and input are balanced with each other.

This is because the Q factor describes for how many oscillatory circles after initial forcing the motion stays – at least relatively – constant and recognizable before decaying through energy loss or disturbance caused by noise and other inputs. The extent to which the Q factor of a self-oscillating system exceeds 1 is a measure of the coherence of forcing and oscillation of the observed self-oscillatory movement. Coherence in this context is used as used by Jackson (2006) and refers to the synchronisation of the neurons in the pedicel exerting force. If a large enough proportion of neurons acts in phase with each other and the external stimulus instead of randomly, they are thought to be capable of a net force input to the flagellum oscillation (Jackson, 2006). As this script plots the data at the same time, it had to be limited to ten data sets at a time. The graphical representation of the plotted data is necessary to allow for optical inspection, gauging whether the right frequency peak has been used for the calculation.

This limitation to 10 data sets meant that the script had to be run multiple times to process all the recordings. As with all following MATLAB programs the first step is to define the X, Y, and Z matrices, by splitting up the X, Y, and Z component of each individual recording and recombine all X direction data in one matrix, all Y direction data in another and the same for the Z direction. As this work step requires the identification and selection of individual data fields, each containing one recording, it was not dynamically automated, but indices were manually coded for each sex and species at a time. Following forward from this reorganisation of the data values, the processing can be semi-automated.

Data are filtered as described in section 2.2.6.2, the respective cut-off frequencies depended on the low-frequency noise level. Therefore, in *T. brevipalpis*, the lower cut-off frequency was 200Hz, in *An. arabiensis* it was lowered to 150Hz.

Amplitudes were scaled as described in section 2.2.6.3.

For optical inspection of goodness of fit, absolute values of the Fourier domain data is plotted at this stage, to if necessary (e.g. *T. brevipalpis* males labelled animals 21, 34, and 16) adjust the cut-off frequency to 250Hz or for the latter even 375Hz.

The rationale behind this step is that, while visually clear peaks can be present at higher frequency noise, if amplitudes, especially at low frequencies, are higher than the transient investigated signal and therefore would prevent an algorithm from recognizing the correct frequency peak. Noise in this setup could stem from electric fields, the experimental setup and unrelated animal movements. Measures to control for animal movement are described in section 2.2.1 specimen preparation.

Finding this defined maximum is essential for the Q-factor calculation and further consideration, for example plotting the three-dimensional movement at the self-oscillation frequency. As the frequency values (X) are unambiguously connected to the amplitude values (Y), the frequency of maximum amplitude is identified by the same index as the amplitude maximum. For the 50% maximum values, one has to consider that by using the first data point smaller than 50%, a small inaccuracy is introduced. This is because even with compared to the investigated frequencies of hundreds of Hz small frequency steps of 0.15625Hz, there is a deviation between exactly 50% and just below 50%. Due to the direct nature of measurement points, it would, however, be highly unlikely that each recording features an exact match for a 50% value.

To calculate the bandwidth the lower 50% frequency is simply subtracted from the upper 50% frequency. With peak frequency and bandwidth known the Q factor is:

$$Q = \frac{f}{b} \quad (4)$$

with Q = Quality factor, f = frequency of the signal, and b = bandwidth of the signal.

If anything, this approach rather under- than overestimates the Q factor and a conservative estimate is preferable to a slightly too high one.

Visual inspection script

Another MATLAB program developed had the purpose of plotting an overview of the different ways to look at the recorded vibrational data. The main purpose here is to allow for a quick assessment of the various aspects of the recorded data.

The script at first glance presents the time traces, individual spectrograms for each of the three Cartesian directions recorded and the reference (including the microphone calibration factor 12,6534 – see section 2.2.4, for an example image refer to Fig. 5.3). This allows to easily spot noise contamination or whether an experiment did not work. In row one the time signal is shown, from left to right, X, Y, and Z direction, followed by reference microphone. Additionally, in row two, the instantaneous frequencies in the X, Y, and Z directions are plotted with the same colour code that is used throughout: X (red), Y (green), Z (blue). Depending on the filtering settings, they either provide redundancy (with spectrograms) or allow to access small transient frequency changes, which otherwise would be inaccessible due to the FFT's time-windowing and the resolution of the spectrograms.

The instantaneous frequency was obtained via the Hilbert transform of the individual vibrational directions scaled from radians to frequency by dividing by 2π .

Finally, in the last image row an overview FFT with two y axes, one for all three directions, and one to compare with the reference measured in mPa converted to m/sec. As with most of my written code, filtering and conversion to displacement are included as described respectively in 2.2.6.2 and 2.2.6.3.

This script was meant to be easily adaptable in terms of cut-off frequency for filtering. Furthermore, in principle the spectrogram windowing can be changed. If not mentioned otherwise, however, a window of 200 datapoints with 75% overlap was used for image generation. If higher-resolution images than the automated ones were required, the relevant subset of plot functions was executed manually.

3D movement plotter script

To better understand the antenna's movement dynamics, illustrating the instantaneous movement was of interest. To achieve this, it was necessary to break down the large amount of data points, as the antenna, which is naturally fixed in one point, would move multiple times across its own path otherwise. To avoid this layering of movement cycles over one another, which would render the resulting image incomprehensible, the following was done:

The 32000 data points per recording were split into 2000 sets of 16 data points. To cut down image number, three of those sets, equivalent to 0,0096 seconds were then plotted – each in an individual colour in one image. These 48 points (3 x 16) correspond with the duration of the time data shown in line one.

In line three, which was added for orientation, the overall data the Z direction component of the whole recording is shown. The colour code of the 3D movement plots allowed to distinguish the temporal order of movement cycles at this level. This, however, still meant 666.7 image per recording, which with over 10 animals per species and four species indicated a strong demand for automation even after four such plots were collated into one. In short, the program displays four recordings in time trace line 1 and in 3D plot line 2. Filtering, scaling and conversion to displacement are performed as described above (2.2.6.2 and 2.2.6.3).

In addition to this, to better access frequency specific motion a second filtering option was added allowing to narrow the 3D plotted frequency band by applying a low-pass filter, if needed. Files were saved as pdf and combined to make video assessment as easy as possible. To ensure the show movement shapes – in varying plot rotations – are independent from the 90° setup under the LDV an Z and Y axis rotation to align antenna orientation with the Z axis were performed. This was only done as spot checks on selected recordings.

Short windowed FFT auxiliary plot

Mirroring the approach to the 3D movement plotter above, a script that shows short windowed movement amplitude in FFT was devised. This script was used to compare the FFT over the whole recording to FFTs performed on small time windows, as it had become apparent that the motion is highly changeable in shape and frequency over time – and the instantaneous frequency does not give amplitude information. In doing this, care has to be taken as by looking at a shorter time window, one loses frequency resolution. This poses a fundamental and not trivial

trade-off, as knowing amplitude and frequency of a signal shifting over time is important, a compromise was necessary between the two.

Smoothed individual and species average plot generation

In order to visualise the frequency variation and therefore distribution in each species, another piece of code was used to plot the XYZ normalised movement (and if applicable the amplitude of the reference signal) independently.

Therefore, after filtering the low frequency but high amplitude noise as of 2.2.6.2, normalisation was performed with an auxiliary script that divided independently the three directions by their respective maximum. This is useful as amplitudes of oscillation vary greatly and to be able to see all animals at once, data needed to be normalised. In this purpose data were not only filtered for low frequency noise but subjected to a running average with ± 24 data points to smooth the signal. A sample average over the individuals shown in FFT is also displayed in bold for each direction individually.

2.3 Preparation for and operation of Confocal Laser Scanning Microscopy (CLSM)

Confocal Laser Scanning Microscopy (CLSM) is a relative method to not only image morphology but also to gauge stiffness of cuticular structures – which in turn will influence mechanical behaviour. To image animals, they need to be dissected and suspended in glycerine between object slide and cover glass, to make subsequent imaging with four lasers possible.

Following a colour code described below, it is possible to describe structures as relatively hard or soft, which allows to test the potential for influencing mechanical bending of the imaged structure.

2.3.1 Specimen preparation

Prior to decapitation, animals were deeply anaesthetised with CO₂. Subsequent dissection with micro scissors, preparation needle, razor blade fragments and size 0 to 000 insect pins was conducted in phosphate PBS (Carl Roth GmbH & Co KG, Karlsruhe, Germany). After dissection, if necessary, for example with plumose antennae (for definition see section 1.2), the specimens were treated with the surfactant Triton X-100 (Sigma-Aldrich Chemie GmbH, Steinheim, Germany). This was done to guarantee the wetting of the complete surface of the antenna before it was transferred into glycerine (Carl Roth GmbH & Co KG, Karlsruhe, Germany). In between, the surfactant was washed out in multiple PBS steps to avoid carrying over any residue to the glycerine, as Triton X could theoretically alter the autofluorescence and the refractive index of the mixture. Glycerine is very well suited for CLSM or microscopy, as its optical refractive index is very close to the refractive index of glass (Michels et al., 2012).

2.3.2 CLSM operation

The CLSM of the type Zeiss LSM 700 (Carl Zeiss Microscopy GmbH, Jena, Germany) is semi-automated. Once excitation levels are set, it independently collects a Z-stack of the sample with predefined slice thickness between start and end point

of the scan. Additional individuals were observed under a Zeiss Axioplan fluorescence microscope (Carl Zeiss Microscopy GmbH, Jena Germany) to confirm that the imaged structures are typical for the investigated species.

A standardised method how to best configure the CLSM for analysis of insect cuticle properties has been established by Michels et al. (2012) and was followed for data collection. In principle the epifluorescence/autofluorescence of chitin varies depending on the composition of the chitin.

Resilin, a particularly flexible rubber-like protein, for example, autofluoresces if excited at a wavelength of 405nm (Michels et al., 2012). Specimens were sequentially exposed to the four excitatory wavelengths of 405, 488, 555, and 639 nm. The light emitted from the specimens was subjected to a band pass filter 420-480nm for 405nm excitation, or a long-pass filter of ≥ 490 , ≥ 560 , and ≥ 640 nm for the other three wavelengths. See the table 2.2 in the following section on colour coding. For an as faithful as possible representation of material properties samples were only imaged once, otherwise bleaching of autofluorescence could skew visualisation as different material components might not be similarly susceptible to bleaching. While this effect often can be neglected, in our case with relatively high laser powers (max. 30%) pronounced bleaching can occur (Michels et al., 2012).

2.3.3 How to read CLSM images – image colour coding

In order to better compare detected autofluorescences and their mixture, the sequentially independently acquired images for each of the four lasers are translated into colour channels and combined to an RGB image. The relatively comparable results of the 555nm and 639nm excitation are combined to the red channel.

As with CLSM settings the colour coding was done according to Michels and Gorb (Michels et al., 2012) and is summarized in the table 2.3 below. Important to notice is that both red colours were set to 50% saturation and combined in the red channel. This colour scheme leads to the following visualisation: well-sclerotized structures are represented in red, tough flexible structures are yellow-green, while more flexible parts containing a relatively high proportion of resilin are shown in light-blue, and resilin-dominated areas in blue colour.

Table 2.3: Excitation, filter, corresponding image colour. Based on methods by Michels et al. (2012).

Excitation wavelength	Filter bands used on autofluorescence	Display colour in Zeiss software	Display colour channel RGB	Meaning for material properties
405 nm Pinhole Size 28 [μm]	BP 420-480 nm	Blue	Blue channel	Blue: resilin-dominated areas
				Light blue: Likely relatively flexible high proportion of resilin
488 nm Pinhole Size 31 [μm]	LP \geq 490 nm	Green	Green channel	Yellow-green: Tough flexible
555 nm Pinhole Size 35 [μm]	LP \geq 560 nm	50% red	Red channel	Red: well-sclerotized
639 nm Pinhole Size 40 [μm]	LP \geq 640 nm	50% red	Red channel	

2.3.4 CLSM images – analysis and extraction of information for FEM

CLSM offers a relative method of material composition comparison, not absolute values. Hence, only images taken with the same settings or preferably structures imaged in the same scan can be compared. Beyond the taken and partially reproduced CLSM micrographs, observations of corresponding samples using a stereo fluorescence microscope informed the description of material distribution in the antenna of *An. arabiensis*, *C. riparius* and *T. brevipalpis*. In the case of intensity comparison between male and female *T. brevipalpis* the software program ImageJ was used to evaluate intensity of a corresponding area in both sexes.

Thereby informed about the dominating material in different antennal parts, values for the Young's modulus of the respective parts were deduced using stiffness range measurements conducted by Wegst et al. (2004) and Vincent et al. (2004). Therefore, using medium values of the ranges given, structures in blue range from 0.001 to 1MPa structures in green from 100-500MPa and structures in red from 1 to 10GP. Furthermore, using Amira 6.3/6.4(6.4. co-developed by Zuse Institute Berlin and Thermo Fisher Scientific (Thermo Fisher Scientific, 168 Third Avenue, Waltham, MA USA 02451)), 3D models of scanned specimens were created for visualisation and measurement. This process required exportation from the Zeiss microscope software, which handles the four channels independently, but only allows for export of three channels. To circumvent this limitation stacks of all four channels were exported separately as grayscale images and recombined using ImageJ to one stack, which then does not convey material information but holds all the structural information and can be read into the commercial software program Amira.

This program allows to semi-automatically follow the “intensity borders” of each image plane. This process is called segmentation. After an image set is segmented into individual images, it is possible to compute a 3D model of the structures depicted. To identify separate materials, it is necessary to refer to the CLSM maximum intensity projections as Amira only takes gray-scale input for 3D reconstruction.

2.3.5 3D reconstruction

To inform the models and simulations that are detailed in chapter 2.4, and for visualisation reasons, 3D-reconstructions of the morphological structures were made. The 3D models were chiefly informed by CLSM scans as above and Scanning Electron Microscopy observations detailed in section 2.5.3. A further source of information were exported CLSM Z-stacks followed by 3D reconstruction with Amira. Each of the four channels used by ZEISS were independently exported, with merge channels using ImageJ (Schneider et al., 2012), combined, converted to RGB, converted to 8-bit grayscale, and saved. Using CtAn the data was re-saved as an image stack and read into Amira. Area selection in Amira was based on overall intensity and correction by visual inspection and comparison to maximum intensity projection images. Following the segmentation, a surface was generated and exported or saved as image.

2.4 Finite Element Modelling (FEM)

As physical experiments are limited by the availability and accessibility of varying antenna systems and the sequence of elements in natural antennae cannot be changed easily, FEM can be a helpful tool for understanding the mechanical behaviour of the systems. To characterise the theoretical vibrational properties of the antennae, FEM in the frequency domain with COMSOL 5.3a (Comsol Inc., Stockholm, Sweden) was conducted. Contrary to the highly variable elasticity, there is a very limited amount of variation in density between the configurations (Vincent et al., 2004), and therefore density is considered constant in simulations. For simulations to be meaningful, it is necessary to correctly capture the geometry as well as the involved physics. The following two subsections will deal with geometries (2.4.1 CAD model generation) and physics settings (2.4.2 COMSOL settings) independently to better address those two fields.

2.4.1 CAD model generation

In an ideal world, a model would use all parameters of the original system. However, as real-world systems can be overly complex and difficult to capture in all aspects, it is necessary to introduce simplification in order to address the system in an adequate time frame. This is where CAD models come in. Even though simulated geometries are not imported 3D models of imaged or scanned antenna models, they are informed by the results of CLSM regarding geometry, material and material properties. However, not to exceed the time scope for computation, rather drastic simplifications were necessary.

Even the simplified models regularly needed more computational power than a desktop work station can provide. This is why the ARCHIE-WeSt supercomputer centre was used (ARCHIE-WeSt, 2020). The model which is believed to sufficiently capture the geometry of the system is composed as follows (Fig. 2.4., section 2.4.2): The flagellum is represented by a beam of uniform thickness, with regularly spaced bands of varying material properties. *C. riparius* is different from the uniformly distributed 12 joints and 13 elements used for the other two species, as in this species the whole pattern of varying stiffness is happening in a rapid sequence in the lower third of the flagellum.

The beam is made up of an inner cylinder (90% volume fraction) of tissue matter of assumed low uniform stiffness (1 kPa), within a hollow cylinder (10% volume fraction) that represents the cuticle. The rationale behind this low stiffness for the inner cylinder is that the higher values provided in literature for tissue assemblages refer to the resistance in direction of maximum resistance.

Literature values, while not limited to this range, include 730kPa (porcine aorta) (Ebenstein et al., 2002) and hundredths to tenths of MPa for soft tissue (Akhtar et al., 2011). As mentioned before, however, those are values for load-bearing, relatively stiff tissue. The human brain exhibits a range of 0.1kPa to 1kPa according to Liu et al. (2015), which is substantially lower. As not unlike the vertebrate brain, most cells in the Johnston's organ and all sensilla projections in the antenna are neuronal cells, the upper end of this elasticity range was used.

Beyond the aforementioned areas of varying stiffness representing the segment joints (or in *T. brevipalpis*, split-segment joints) between the thirteen flagellomeres no further details of the flagellum were taken into account for our beam model.

The dimensions for each of the thirteen subunits were defined by dividing the length of the antenna by the number of flagellomeres. In *T. brevipalpis* this is a length of 3.3mm/13 and in *An. arabiensis* 1.7mm/13. The corresponding flagellum diameter in *T. brevipalpis* was 120 μ m and in *An. arabiensis* 15 μ m. *Chironomus riparius* has a length of 1.4 mm and a diameter of 60 μ m tapering to 40 μ m. We did not simulate the large amount of fibrillae that cover the flagellum.

This is considered a valid step as the intent was to investigate whether a non-uniform distribution of stiffness as observed along the flagellum can have an influence on the effective stiffness of a beam. As for a sound velocity sensor, friction and damping are considered the driving force – which is represented in the model but as acting directly upon the beam. It has been shown for the mechanical behaviour that the fibrillae apparently are, in the biologically relevant frequency range for mosquitoes at least, stiffly coupled to the flagellum (Göpfert et al., 1999). This allows force transmission from the fibrillae to the flagellum. Therefore, to keep the model as simple as possible, it seems an acceptable step to combine the acting forces and let them act directly on the flagellum. Fibrillae do not add a relevant amount of mass to the system. By adding damping they would broaden but not shift the resonant frequency peaks. For similar reasons, as the fibrillae were classed as negligible in terms of mass and frequency, the only small density variations observable in chitin (e.g. Vincent et al., 2004) were also not investigated.

The effect of the Poisson's ratio was investigated. As resilin is rubber-like, it would be close to the ideal Poisson's ratio of 0.5. However, the present investigation is not concerned with the actual amplitude of excitation but merely with the resonant frequency of the beam structure.

Furthermore, the articulation of the flagellum is considered in a simplified way as well, primarily because complexity drastically increased computation time and secondarily because disentangling a host of factors contributing to the overall stiffness of the articulation based on CLSM alone would be very difficult, if at all possible. For that reason a basal disc, allometrically related to the flagellum length (3.3 mm in *T. brevipalpis*, 1.7 mm in *An. arabiensis*, and 1.4 mm in *C. riparius*) and diameter, was introduced – which should not be confused with the actual basal plate of the flagellum. For simulation purposes this disc is a stand-in for the combined effects of the articulation which pertains to but are not limited to the following elements involved: base plate, prongs, scolopidia, and soft surrounding tissues, joint friction.

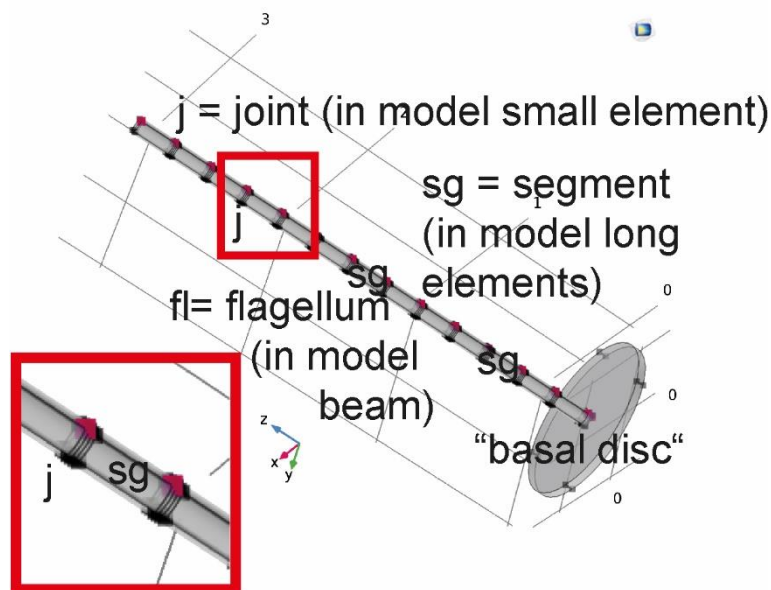


Fig.2.4: Layout of the simplified beam, based on antenna morphology used for COMSOL simulations. It is comprised of 13 large elements with 12 smaller elements representing segment joints. Joints were assembled, as seen in *T. brevipalpis*, out of three thin discs, or more precisely, ring elements. The beam is medially attached to a basal disc, which conveys the aforementioned basal stiffness, not to be confused with the actual basal plate but rather a compound quality, see main text.

The outline of material distribution differs between the three species and was implemented accordingly. The antenna of *T. brevipalpis* is a sequence of relatively hard elements, interspersed by two harder rings in between which a flexible ring is located (see Figs. 3.1-4, 3.4). Antennae of *Anopheles* have no medium-hard structures but instead the large elements are soft and a single small hard disc is separating each of the main elements from its more distal segment (see Figs. 3.7-3.9). To represent *C. riparius* (see Fig. 3.10), more adjustments were necessary. Here soft, medium, and hard elements – reminiscent of *T. brevipalpis* are present but located all in the lower third or half of the antenna (Fig. 3.10). To keep simulations comparable to investigate the effect of location of elements size differences were ignored and also that *C. riparius* actually only has 10, not 12, joints.

Red points in Fig. 2.4 show the data points recorded. The topmost point was used for displacement graphs in Figures 4.3-4.9. An impinging sound field was simulated by applying mechanical load perpendicular to the YZ plane in +X direction on the surface of the artificial flagellum on all elements. Except in the case of the *C. riparius* type model and the comparison of beam shape between a straight beam or alternatively a cone, the CAD models were kept the same. This does not include that the model for *Anopheles* was scaled down to match the smaller natural structure.

For the comparing the cylindrical beam generally used with a cone shaped version it was necessary to generate a new cone-shaped CAD model, with otherwise the same dimensions as the uniform straight beam.

2.4.2 COMSOL settings

The frequency domain simulations were conducted using the Solid Mechanics module, applying a pressure field of 0.1N/m^2 in +X direction perpendicular to the YZ plane, over the frequency range (20-2720Hz in 10Hz steps, except for *C. riparius* where steps were 5Hz, and straight beam vs. cone comparison where frequency steps were reduced to every 25Hz). In the graphs shown in Figs. 4.3-4.9 only the first 2000Hz are shown. The applied pressure field of 0.1N/m^2 approximately translate to a force of 21 pN for the large antenna and 2.1 pN for the small antenna. The Poisson's ratio, which is unknown for the specific chitin configurations in question, was set to 0.35 a value which is reasonably close to the observed Poisson's ratio range in various artificial compound polymer materials.

Variations of chitin density are considered to be in a similar range to each other, hence are simulated as having a constant density of 1183Kg/m^3 . This variation compared to the clearly different density of the tissue volume of 1059Kg/m^3 is considered small. This is validated by the fact that, contrary to the highly variable elasticity, there is a very limited amount of variation in density between chitin configurations (Vincent et al., 2004). COMSOL furthermore employs an explicit solver taking the influence of all other points on each point into account. This delivers more accurate representation of the physical world, it does, however, come at the cost of longer computation times. The issue of computation time is further aggravated by the fact that both the geometry, see Fig. 2.4.1, and the wavelength of the frequency, whose influence on the investigated structure is to be determined, limit the upper element size, as elements must be considerably smaller than both. The smaller the element the more elements are needed for the geometry.

For used elements see Table 2.4. The more elements, the more individual points need to be solved for with equation (5), the longer the computation time becomes.

Table 2.4: This table summarises the geometry and meshing settings used in all three species.

Antenna Model	Overall size [mm]	Number of elements	Average element quality	Minimum element quality	Large parts mesh: fine [10^{-4} m]	Small parts setting [$m 10^{-5}$]
<i>Toxorhynchites brevipalpis</i>	3.3	47707	0.455	0.009789	0.33-2.65	Finer 1.32-18.2
<i>Anopheles arabiensis</i>	1.7	249915	0.5763	0.001367	0.17-1.37	Extra fine 0.26-5.99
<i>Chironomus riparius</i>	1.2	85709	0.5694	0.05336	0.14-1.14	Extremely fine 0.03-2.85

Table 2.4 also illustrates that at least the average element quality is in an acceptable range. Independent of species and size, the large parts of the simplified beam structure representing the flagellomeres could be meshed with the same setting (Fine). In all simulations they vary by about the factor 8 between minimum and maximum, and are approximately normally distributed except in the largest species, *T. brevipalpis*, in which a second peak of lower quality elements exist (see also minimum element quality Table 2.4). The reason for varying mesh size between the small beam parts (Fig. 2.4) is the overall size difference, which while not affecting the large part, made using the same setting for the thinner parts impractical. In *C. riparius*, the species with the shortest antenna overall, this issue was exacerbated by the small elements all following quickly upon each other.

The Solver equation used by the solid mechanics module in the frequency domain is:

$$-\rho\omega^2u = \nabla \cdot S + Fve^{i\phi}, -k_z = \lambda \quad (5)$$

where ρ : is density, ω : angular frequency, u : displacement field, S : strain field, F : force field, v : velocity, ϕ : Phase, k_z : wavenumber (defined as ω /speed of sound), and λ : wavelength.

The equation can be simplified, as in the given situation ϕ : Phase =0; $\Rightarrow e^{i\phi} = 1$

$$-\rho\omega^2u = \nabla \cdot S + Fv, -k_z = \lambda \quad (5b)$$

Substituting that F can also be defined by formulae (2b)

$$F = S n \quad (6)$$

equation 1b can be simplified further to

$$-\rho\omega^2u = \nabla \cdot S + S n v, \quad (5c)$$

Structural transient behaviour included inertial terms. The discretisation of the displacement field was handled as quadratic serendipity to reduce computation time. The stiffness used for modelling the disc was derived from prong diameter and an approximation of their stiffness leading to a compound quality later on referred to as “basal stiffness”. The allometric relation between disc and flagellum ensures that the disc stays constant relative to the different model sizes.

The circumference of the disc was set to zero displacement in XY plane by a prescribed displacement boundary condition.

Effectively, our model is only concerned with the strongest mechanical response, however, the stiffness of the disc served as compliant clamp. This makes it possible to treat the beam boundary conditions as an intermediate between a free end and clamped, which is called a compliantly clamped beam. Otherwise the beam base and top were treated as free. Dimension of elements was kept the same except where noted otherwise. Control simulations of simple cylinders were done. The Euler-Bernoulli beam theory allows one to compare the simulated results with expected resonant frequencies at least for a clamped beam. This was done to confirm the models were well-behaved.

While Young's moduli were inferred by CLSM based on Wegst et al. (2004) and Vincent et al. (2004) to be as follows: hard areas are typically 5 GPa, medium-hard stiffness configuration are about 0.5GPa, and soft material is around 1MPa (average value for resilin). It has to be clarified, however, that really only the ratio of Young's moduli between materials matters for simulations when keeping values in the natural range. With the same model of the large beam and the same beam stiffness settings (except that base stiffness was set to 5kPa, a middle value between the 1kPa and 10kPa simulations) the effect of Poisson's Ratio from 0.25 over 0.3, 0.32, 0.35 to 0.38 and a more cone shaped beam (with the exact same settings) was simulated.

2.5 Other Techniques

This chapter gives a summary of the additional experimental techniques that were used, which mainly served as auxiliary or implicit control for the main experiments. Electrophysiological measurements were used as additional checks of the presence and source of self-oscillation. Scanning Electron Microscopy was used to confirm structural findings made by CLSM.

2.5.1 Electrophysiology

The aim of this approach was to supplement 3D LDV experiments with data of correlation between flight muscle activity and antenna movement. For this purpose, two electrodes of sharpened and isolation striped 99.99% pure silver Tungsten wire with a starting diameter of 0.125mm (Goodfellows, Cambridge Limited, Huntingdon PE29 6WR, England) were inserted in the insect body using micromanipulators (Märzhauser GmbH & CoKG, In der Murch 15, Wetzlar D-35579, Germany). Electric signals were recorded as the reference channel in self-oscillation experiments. Electrodes were inserted while casting the animal into wax as described in section 2.4. One electrode was inserted into the thorax, while the other was inserted into the abdomen. Pre-processing was done with a differential amplifier (DAM 50 Differential Amplifier, World Precision Instruments, 175 Sarasota Center Blvd., Sarasota, FL 34240). Following the conclusion of recordings with the 3D LDV, animals were decapitated and recorded again.

2.5.2 Scanning Electron Microscopy (SEM)

To improve understanding of general anatomical organisation of the investigated animals Scanning Electron Microscopy (SEM) images of the antennae were taken. Specimens were dried and brought into the SEM without sputter coating. With comparatively low magnification, this is possible without losing too much clarity of the imaged structure. The SEM used is a Hitachi S-3000 SEM with tungsten filament source (installed 2004, ca.14 years old and moderately used, Hitachi high-technology Canada, Inc, 89 Galaxy Blvd., Suite 14 Toronto, Ontario M9W 6A4 CANADA), and was operated together with Dr. Gordon Brown (Strathclyde University).

2.5.3 Wingbeat recordings and real wingbeat signals presented to experimental animal

Using the same experimental setup and equipment as for 3D LDV, the wingbeat frequency of a small number of females (N=3) and one male were recorded within a plastic tube. The purpose of this approach was to assess the properties of the wingbeat and to use females in a tube covered with insect netting as stimulus to the male mosquito.

3 Results of Confocal Laser Scanning Microscopy (CLSM) investigations

Given the objective to show and better understand the three-dimensional movement of the self-oscillating and sound-driven antenna, a closer look on the mechanical properties of the antenna is helpful. The purely mechanical behaviour then can serve as a base line for experiments in the noisy and less well-controlled animal system. Here Confocal Laser Scanning Microscopy (CLSM) can provide helpful insight as it enables the correlation of gross softness and hardness of cuticular structures. The resulting understanding of distribution can be used in manifold ways including but not limited to informing computer simulations (Section 5), serving as a road map for more precise material property tests. Parts of the following chapter are based on “Material stiffness variation in mosquito antennae”, published in Royal Society Interface (Saltin et al., 2019) in collaboration with the University of Kiel, Germany. For the sake of clarity, brightness-increased versions of the Confocal Laser Scanning Microscopy (CLSM) images are shown, but colour analysis was performed on unaltered images. As in the case of 3D LDV and simulations, CLSM results are first presented individually for each species and sex, followed by highlighting the differences and similarities between antennal structure and material composition between sexes and species where such a comparison is possible. The colour scheme used is following the established method of Michels et al. (2012) (detailed in Materials and Techniques). As stated earlier, likely resilin-dominated structures will be shown as blue-light-blue indicates relatively soft structures – tough but partially flexible structures are yellow-green and structures appearing orange-brown to deep red are considered to be sclerotized and therefore hard.

3.1 *Toxorhynchites brevipalpis* male

The male antenna is densely covered in fibrillae – hair-like structures, also called setae – and therefore called plumose. It is subdivided into 13 segments or flagellomeres. The 1st flagellomere articulates directly inside the pedicel, making direct observation of the lowest part of the flagellomere impossible. All subsequent flagellomeres start with a flexible ring (blue, ca. 15 µm across in Fig. 3.1), followed by a sclerotized coronal structure (yellow-reddish) interspaced with low-green fluorescent chitin. After the coronal structure, the segment continues for most of its length in low-green fluorescent chitin (Fig. 3.1 and Fig. 3.2 or Fig. 3.3) until the again somewhat sclerotized (yellow-reddish) ring (Fig. 3.1 and Fig. 3.4). After that, the next segment begins shown in Fig. 3.1 and Fig. 3.2 or Fig. 3.3).

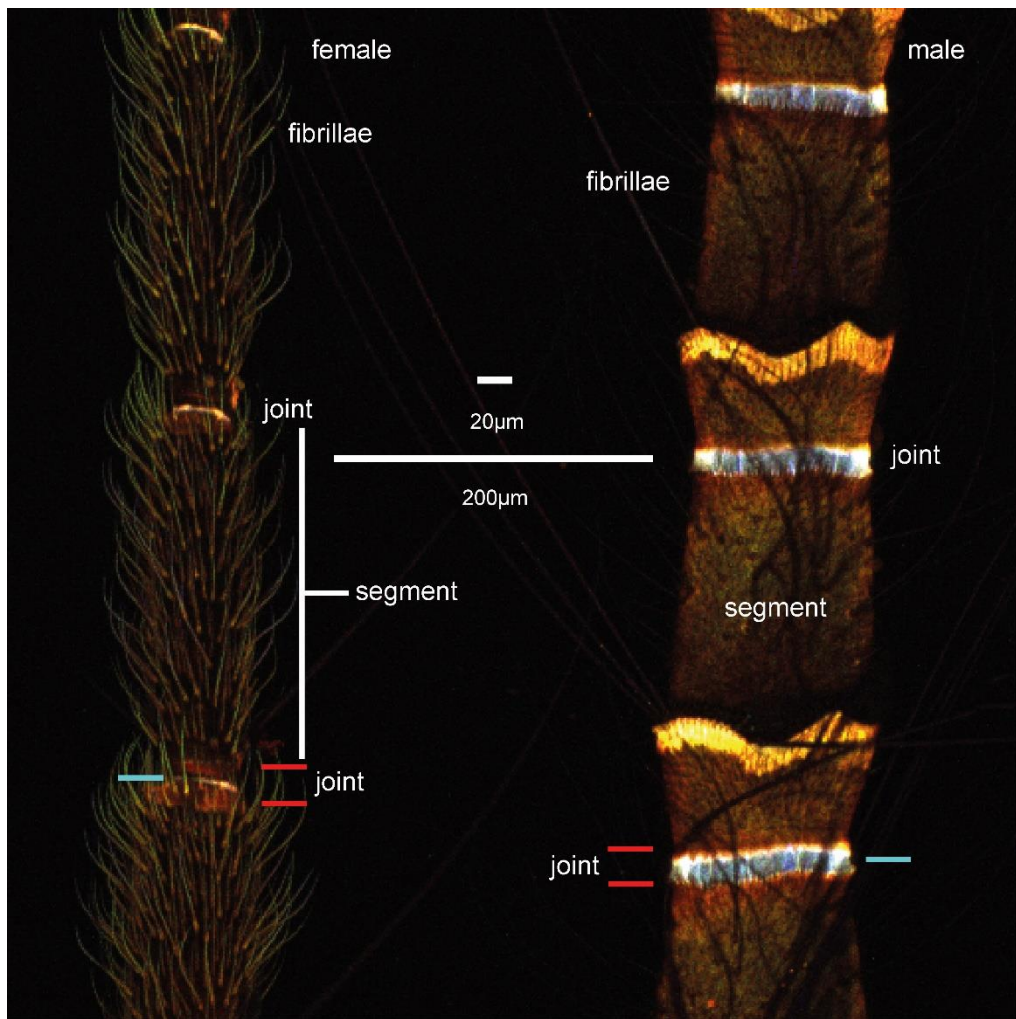


Fig. 3.1: This figure allows one to directly compare the 2nd segment of male and female of *T. brevipalpis* in maximum intensity projections. Lengths are similar but the diameter of the male antenna – right in this figure – is larger and the male antenna features fewer but longer fibrillae. Red or blue bars respectively indicate the hard-soft-hard 3-ring structure present in both sexes.

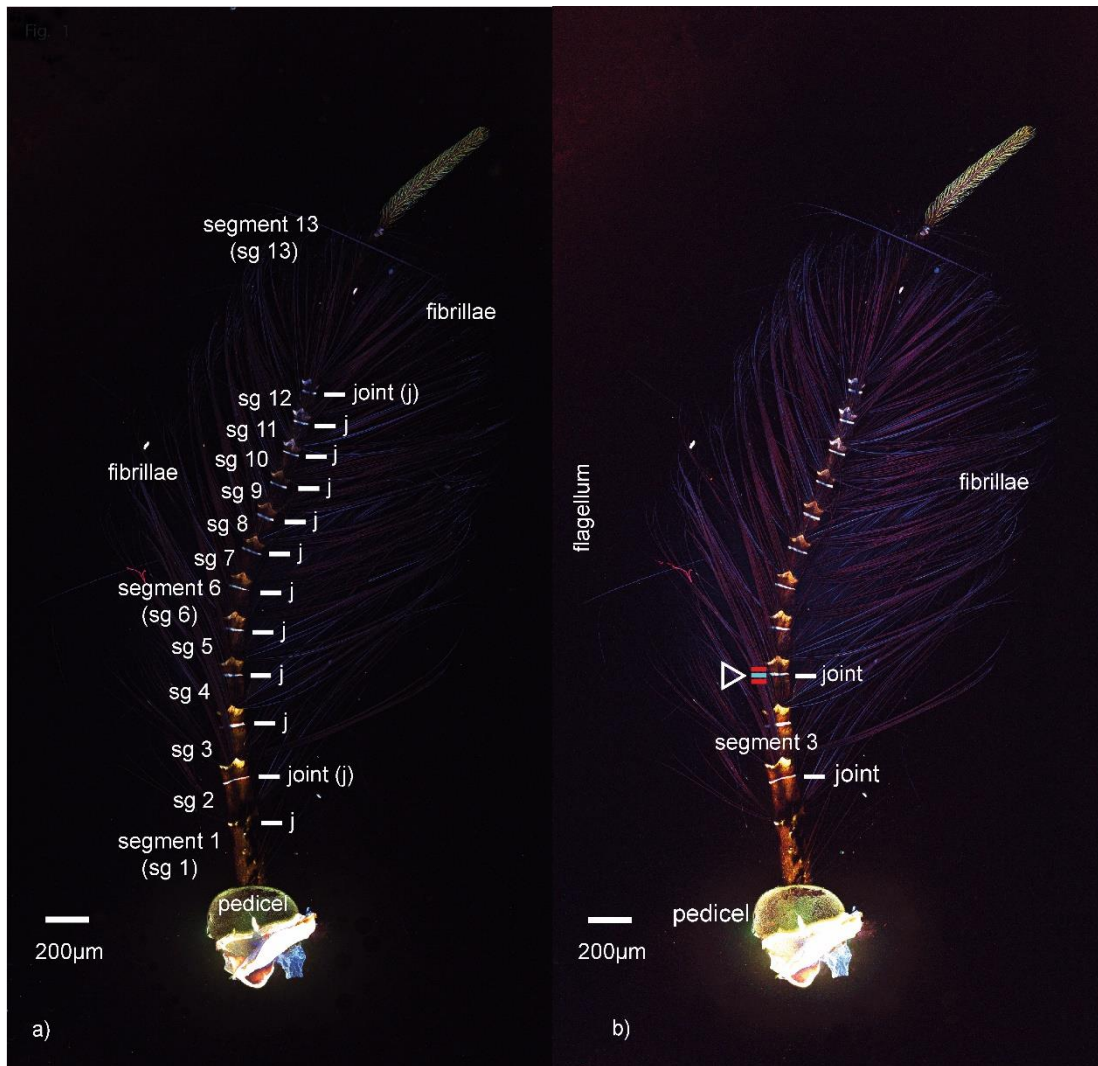


Fig. 3.2: Male *T. brevipalpis* antenna – maximum intensity projection. a) Increased brightness to b) high brightness. The antenna is constituted of twelve more or less regular subunits which follow one another, a large medium hard element that becomes harder at its most distal extension, followed by a soft blue band and an even harder structure upon which crests of uniform fibrillae insert.

The next element then is for most of its length medium-hard.

The 13th element differs from that pattern as it is filamentous and has no long fibrillae. The 3-ring structure referred to in FEM is indicated in b) by matching colour bars and an arrowhead. b) While some caution needs to be applied as images have been altered uniformly in intensity and contrast for illustrative reasons, a membranous (blue) area just under the most distal tip is visible and it appears that the disc elements have a gradient from harder (more red), proximal, to softer (more blue) autofluorescence towards distal. This, however, is also the case for the first four elements in the unaltered image. At the upper corners of the coronal structure, fibrillae emerge in a wave pattern.

The more detailed Fig. 3.4 also shows the singular fibrillae sockets, which are of similar hardness as the coronal structure they emerge from in the male of this species. From proximal to distal, the length and diameter of the antenna segments decrease. The 13th segment is more drastically different from the other segments: It is five to six times as long and more filamentous and shows almost no tapering along its length. The absence of long fibrillae, which cover all other segments densely, makes the flagellum here more accessible and give it a somewhat rounded appearance as layer upon layer of fibrillae comes to an end along the last segment (Fig. 3.2 and Fig. 3.3). This is being said to avoid the false impression that the last segment has no fibrillae (see Fig. 3.2), it has short ones. Somewhat puzzling is the presence of a tiny flexible area (blue in Fig. 3.2b) within the last segment.

In the pedicel, the outer wall of the pedicel is divided into two areas – the upper, sclerotized ridge (orange) – and the rest, which shows no further variation in material and is of uniform green fluorescence (Fig. 3.2 and Fig. 3.5). The centrally attaching prongs are clearly visible from the inside (Fig. 3.5). In CLSM, they appear uniform, both in material composition (all show evenly spread greenish autofluorescence) and geometry. Their continuously green fluorescence indicates they are made up of tough-flexible, but not overly sclerotized chitin.

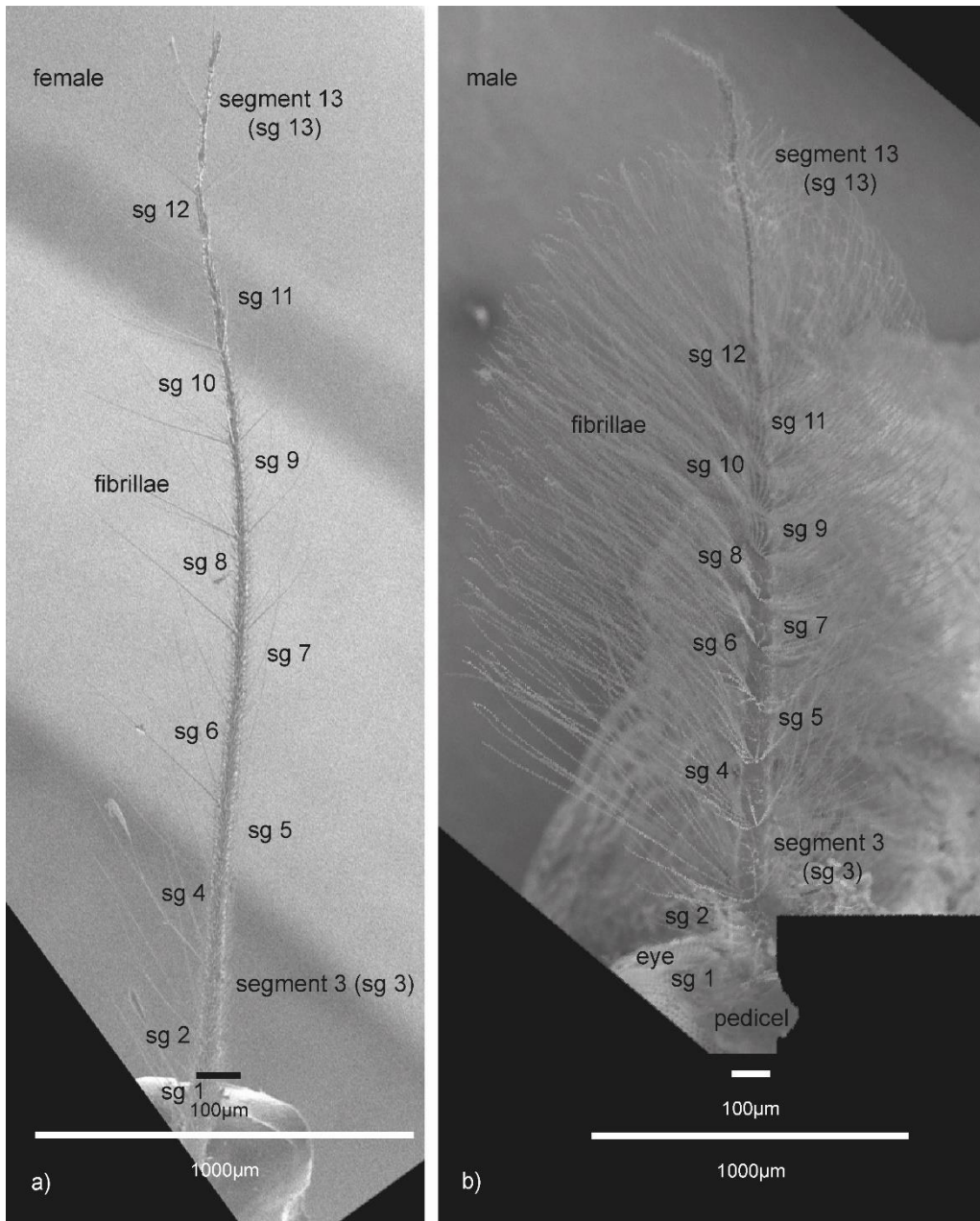


Fig. 3.3: SEM overview of the female (a) and male (b) antenna anatomy of *T. brevipalpis*. Both feature the familiar 13 segments and fibrillae crest. The female structure is markedly more slender than the male – fibrillae are potentially as numerous, but shorter.

This all being said, across individuals there seems to be some variation due to the relative nature of CLSM observations. A direct comparison is precluded as images are not taken with the same settings. This can be seen clearly in Fig. 3.5 a-c) which show different pedicels. Fig. 3.5 b), c) even illustrate how much the imaging result depends on microscope settings, as both are the left and the right pedicel, respectively, of the same individual.

Internally and externally, the area of the pedicel wall where the flagellum attaches appears as a stiff and sclerotized ring (red) within each image.

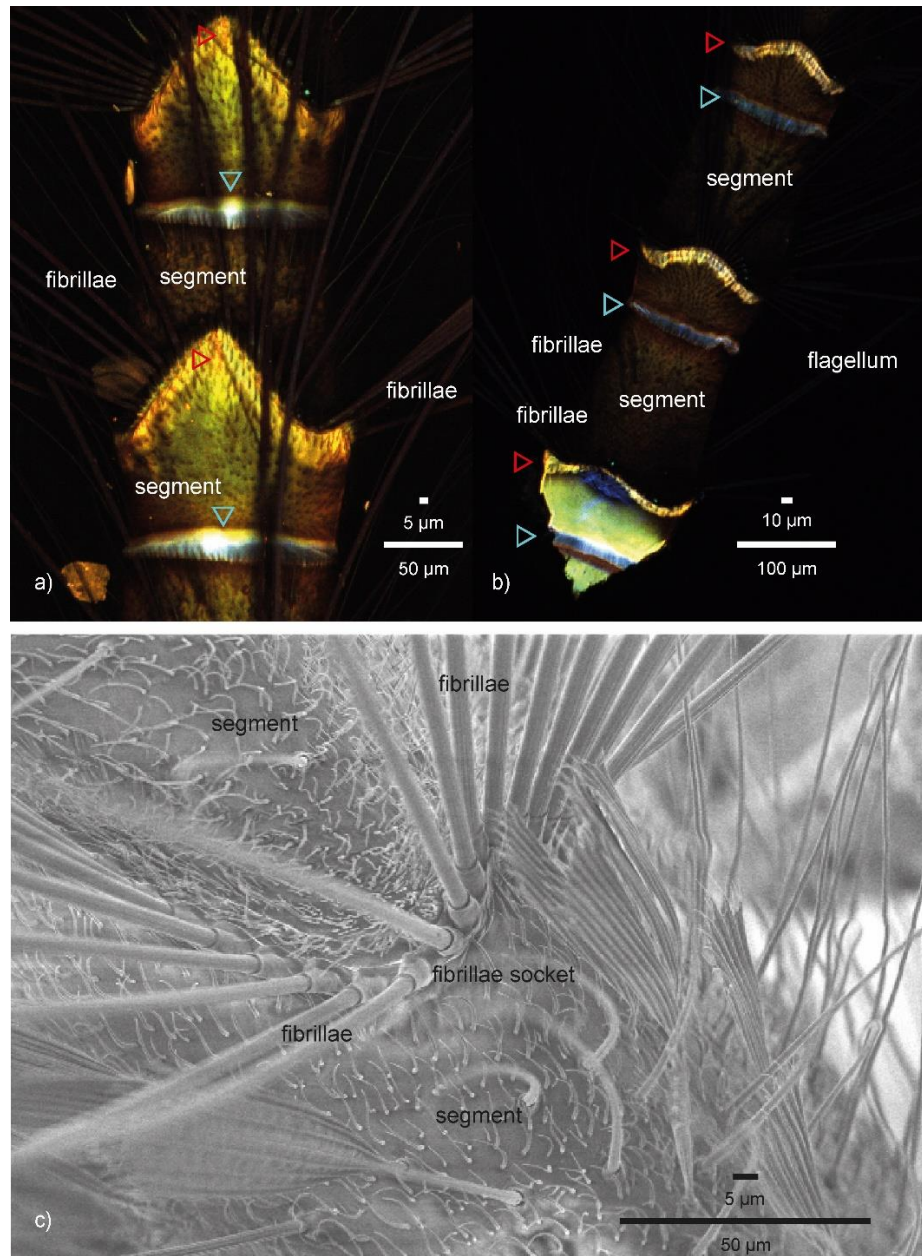


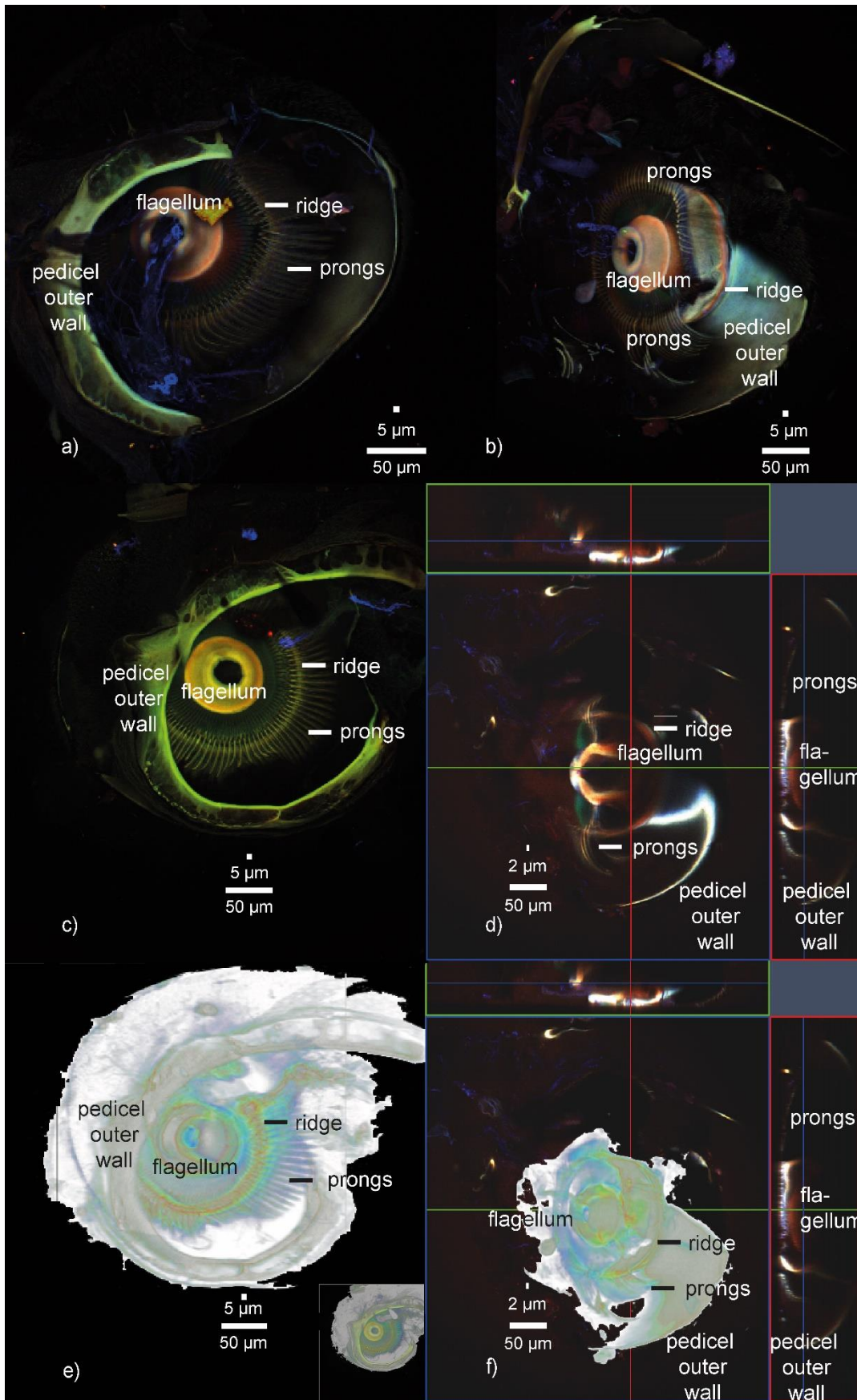
Fig. 3.4: Male *T. brevipalpis* antenna – maximum intensity projection. a) Detail of the 3rd to 4th segment. b) Detail of the 2nd to 4th segment of a different individual. Both highlight that the long fibrillae show no indication of a material gradient. c) Scanning Electron Microscopy image overview. The 10 μ m wide blue (soft band) and hard crown (orange) are visible. a) This panel reveals a large number of seemingly orderless short hairs. b) Allows one to view the inside of the flagellum wall, at the most proximal as the antenna was broken off here. The interior is more strongly fluorescent than the outside (intensive green and blue colouration). While in some optical sections a measurement of wall thickness is possible, this directly shows that the flagellum cuticle is best represented by a hollow cylinder with thin rings of varying stiffness for simulation. c) Scanning Electron Microscopy image showing fibrillae crest and the fibrillae sockets (fbs) in higher anatomical detail.

Fig. 3.5 d), an optical section through the pedicel, helps to see that prongs either run over or attach to a cuticular ridge and their articulation is roughly less than 2 μm thick (Fig. 3.5 d)). In Fig. 3.5 d) some prongs have become detached, allowing an assessment of their attachment at the broad ridge on the flagellum and showing how they bend over the ridge in the pedicel. All these results regarding the pedicel are reproducible within the 3D reconstructions (Fig. 3.5 e, f), which furthermore allow for a more precise measurement of the prongs.

Fig. 3.5 (next page): Details of the male pedicel of *T. brevipalpis*. ac) Maximum intensity projections of opened pedicels, b-c) left and right from the same individual. D) Optical section through the attachment of flagellum and pedicel same specimen as b). e) 3D-reconstructions of the pedicels shown in a) and f) 3D reconstruction of the pedicel shown in b) and d).

The prongs are uniform among each other within each pedicel regarding material stiffness and thickness. The attachment of the flagellum (red cone in the middle of the image) is comparatively hard (a-d), and the prongs run over a harder ridge.

Panels a-d), however, illustrate the variation stemming from inter-individual variation and different CLSM settings, reiterating that one should not compare results between images taken with different experimental settings quantitatively. The attachment of prongs (d) happens in a narrow plane. The blue autofluorescence of the middle indentation (d) indicates that this part is softer than the surrounding cuticle. Panels e) and f) serve primarily as visualisation, helping to solve the optical ambiguity whether prongs bend up or downwards over the ridge, and allow for more detailed measurements than the maximum intensity projection. E) Contains an inset in the same orientation as a). The model in e) is rotated 20° clockwise around the Y axis.



3. 2 *Toxorhynchites brevipalpis* female

Externally the flagellum, compared to the pedicel, shows weak green-dominated autofluorescence (Fig. 3.1 and Fig. 3.6a). The flagellum is non-plumose and composed of 13 segments. The first segment's length is 200 μm and thereby about 10-20% shorter than the 220 to 250 μm length of the more distal segments. The diameter of these segments is roughly constant. Short fibrillae cover each segment irregularly (Fig. 3.1 and Fig. 3.6). In the joint areas, autofluorescence is distinctly stronger. The joints are visible as narrow blue bands of ca. 3 μm (Fig. 3.1 and Fig. 3.6). The round sclerotized structures distal and proximal of the blue ring measure approximately 4-7 μm in length between the first two segments. Further along the flagellum they are not clearly visible, therefore the joints 8 to 9 and 9 to 10 feature an additional blue band distal to the joint, which in itself is about half as wide as the 2nd joint. In a brightness enhanced version (Fig. 3.1) in all lower joints 1-5 three bands are present (indicated by matching colour bars in Fig. 3.1), although we cannot infer material properties in a brightness-enhanced image. While the few long fibrillae at the segment borders of the 4th and more distal segments are invariant in autofluorescence, the short fibrillae on all segments show a material gradient in female *T. brevipalpis*. The fibrillae start off tough but flexible at the base, turning increasingly soft towards the tip – this is indicated by a colour gradient from basal yellow over green-blue, to blue and dark blue at the tip. While no functional similarity is assumed, this optically looks similar to the stiffness gradient in attachment structures of ladybird beetles found by Peisker et al. (2013). Pedicels in females are externally uniform and, internally, prongs passing or attaching to two edges can be seen.

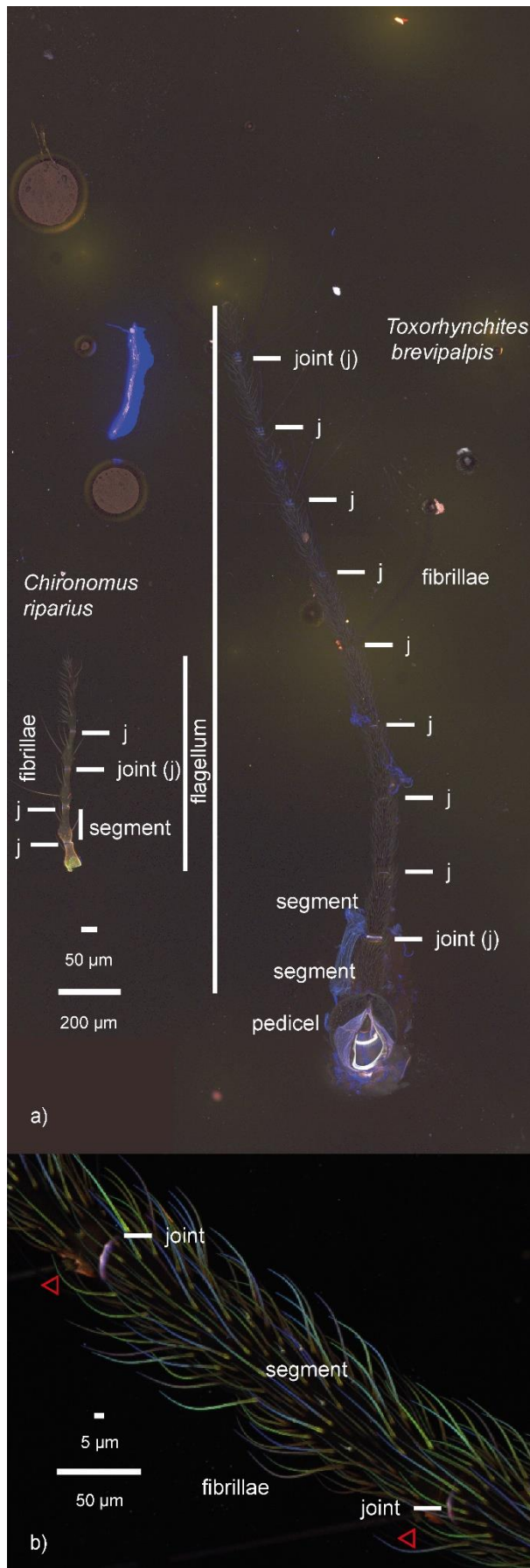


Fig. 3.6: a) Comparison images between females of *T. brevivalpis* (right) and *C. riparius* antenna (left), brightness increased. Most notable is the size difference followed by the fact that 9 of the 12 actually present joints that are imaged in *T. brevivalpis* while in *C. riparius* there are only 4 joints. b) Female *T. brevivalpis* detail image of the 4th antennal segment. b) Shows a material gradient in the short fibrillae and two orange, that is medium hard to hard, sockets (indicated by arrow) of the very few long fibrillae present in female *T. brevivalpis* right after the blue ring structure of each segment.

3.3. Male to female comparison *Toxorhynchites brevialpis*

Externally, in both sexes only the segment joints show distinct autofluorescence. Unsurprisingly joints are consistently flexible as indicated by their materials' blue autofluorescence (Fig. 3.1). Internally, pedicels feature uniform prongs (see Fig. 3.5 a-e)). This however is where similarities stop – female antennae are approximately half as thick (50µm) than male antennae (100µm). While both are covered in fibrillae (Fig. 3.1), in females the fibrillae coverage of the antenna appears even thicker, although the singular fibrillae are much shorter. Parallel joints are a sequence of a red (sclerotized), blue (flexible) and red again structure, however the second sclerotized ring appears to have a higher proportion of less hard chitin in females (making it a bit more flexible). The female structure is evenly rounded, while the male structure is irregularly crown shaped – both entirely circumscribe the flagellum. (Figs. 3.1 and Fig. 3.7). Some differences in blue autofluorescence can be explained by size (e. g. the ring is four to five times thinner in females and the flagellum diameter is half the size). When comparing similar areas for intensity, males exhibit a five times higher median intensity (20) than females (4) for an 8-bit image with an intensity range of 0-255. This means that the intensity of blue autofluorescence is actually about twice as strong in females if corrected for size. The overview image (Fig. 3.1) and the detail image (Fig. 3.7), are taken with different settings rendering material comparison between impossible it is nonetheless confirming that structurally the crown shaped male structure is twice as thick as the female ring structure.

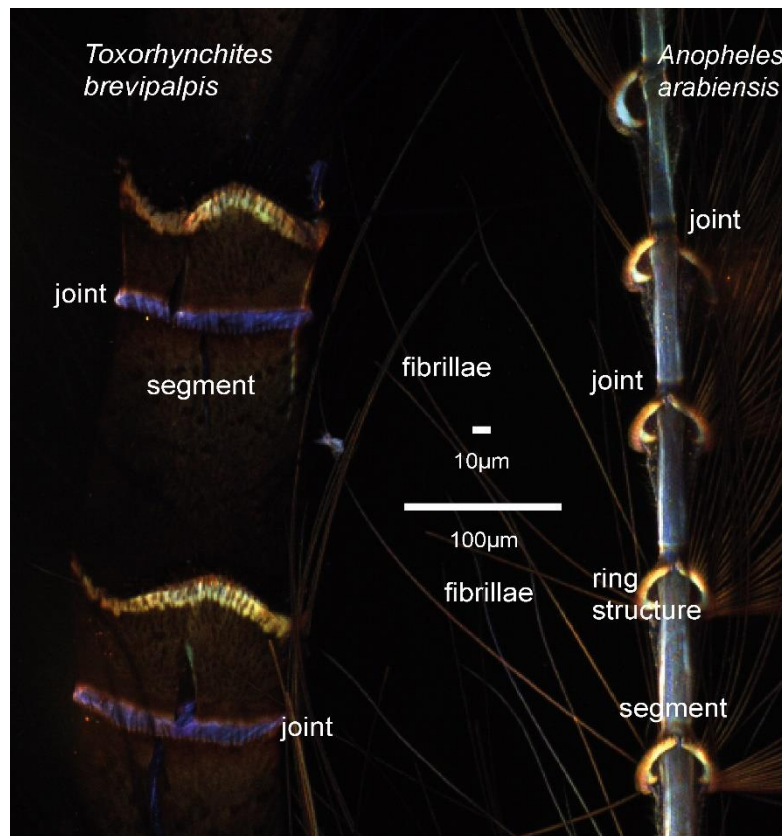
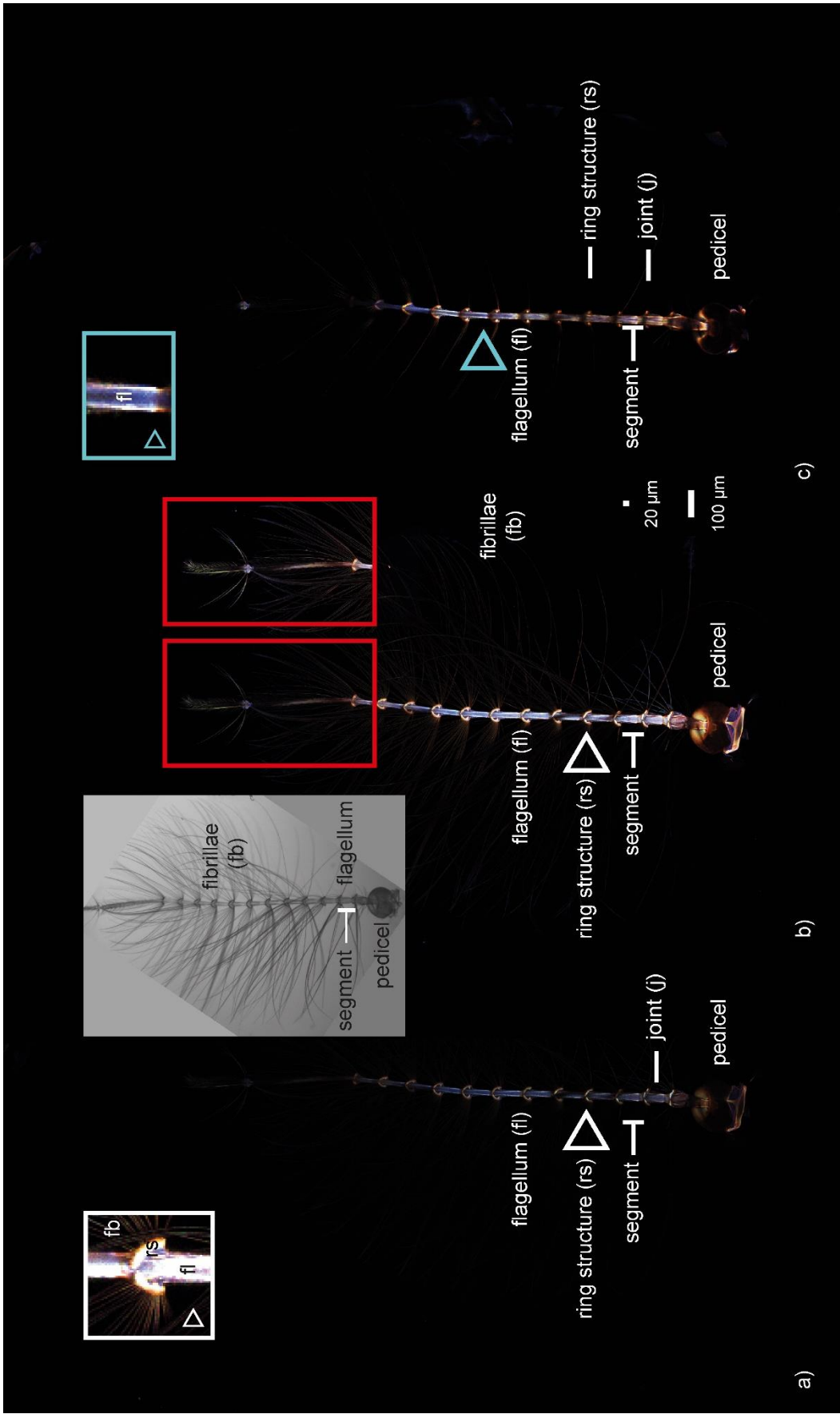


Fig. 3.7: a) Comparison images between the male 2nd segment of *T. brevipalpis* (left) and the 4th to 8th segment of the *An. arabiensis* antenna (right) – brightness-increased maximum intensity projections. The size differs greatly between *T. brevipalpis* and *An. arabiensis*. The *T. brevipalpis* antenna is with 3.3mm about twice as long as in the smaller species with 1.7mm. The diameter is 15µm in *An. arabiensis* and 120µm in the larger *T. brevipalpis*. Together those measurements mean that the volume and thereby the mass of the antenna in *T. brevipalpis* is more than 100 times that of *An. arabiensis*. The composition however is almost inverted with the larger antenna being made up of intermediate hard cuticles and featuring hard and soft bands (blue) while the smaller is mainly made out of flexible cuticle (light blue) and features hard bands (red, orange). A common aspect of both antennae is that the fibrillae are inserting as an orderly crest – each in an individual socket – on the most distal point of a hard band in each segment.

3.4 *Anopheles arabiensis* male

The antenna has 13 segments as seen in Fig. 3.8, while the 2nd to 12th are gradually tapering in diameter the 13th is filamentous and has comparatively low fluorescence (Fig. 3.8b). The 12th segment is about half as wide as the 2nd and the 1st segment is similar to the following eleven, but medially broader than at insertion to the pedicel. The segments in this species are largely flexible (blue autofluorescence) and each except the 13th has two sclerotized ring-like structures (orange-brown-red) which circumvent the flagellum. On the larger and broader of these harder rings the fibrillae crest of each segment do insert (Fig. 3.8c). Giving the ridge appearance of this structure it is reminiscent of a bear spring trap. The individual sockets of the fibrillae are clearly visible in *An. arabiensis* (white arrow Fig. 3.9). Between the two red rings – approximately as wide as the ring structures the flagellum is fluorescent in a deeper-blue (that is it is more strongly dominated by resilin). Proximal to the ring, there is a membranous area lacking in strong autofluorescence, spreading from one end of the ring to the other. It, however, is clearly outlined with orange granules and appears to be a sac of cuticle (Fig. 3.9 – gr below rs).

Fig. 3.8 (next page): Full antenna of *An. arabiensis* male – maximum intensity projection. a) Original, white arrow pointing at ring structure, provided as magnified inset. b) Brightness-increased version of a). For orientation, a light microscopy image is provided as inset. The area inside the red box is reproduced a second time right to its position further increased in brightness. c) Optical section of the flagellum and pedicel, inset shows the magnified cuticular cylinder. Relatively soft and flexible areas make up most of the antenna, interspaced with comparatively hard bands on which fibrillae insert in single sockets. Segments are uniform and slightly tapering with the exception of the 1st, which articulates in the pedicel and the 13th, which is filamentous. In section c), the 10th segment is seen from the outside while segments 8 and 9 are transects allowing to see that the soft flexible cuticle is a thin sheet of no more than 2µm, thereby on both sides together amounts to maybe 10% of the antenna's volume.



Compared to the flagellum the pedicel is more sclerotized and it is approximately hemispherical (Fig. 3.8b). The intricate structure of the articulation is visible from the outside through the translucent outer wall (Fig. 3.8b, c). The prongs attaching to the articulation have a diameter of 2-4 μm . Their attachment is not markedly sclerotized.

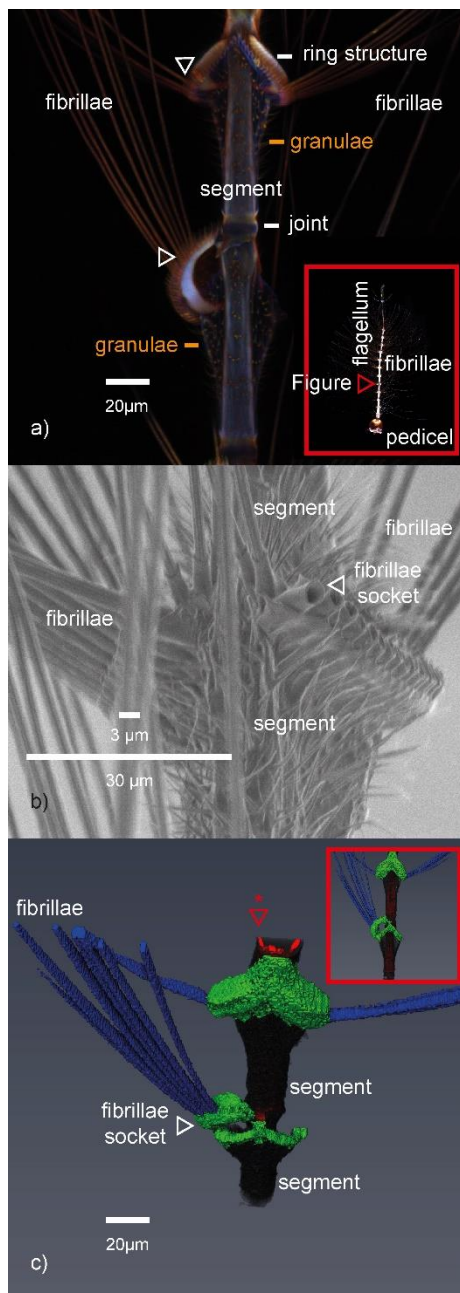


Fig. 3.9: Detail of *An. arabiensis* male. a) Brightness-increased maximum intensity projection. b) SEM detail of the ring structure, white arrow pointing at fibrillae sockets c) 3D model with inset in the original orientation and the main image slightly rotated out of plane to illustrate the thinness of the cuticula wall (red star).

Insertion of fibrillae in singular sockets (arrowheads). Along the hard flagellum circumscribing the ring structure (rs) appears the membranous sac structure below the ring, outlined by hard cuticle granulae (orange). *An. arabiensis* males erect and collapse fibrillae during the diurnal cycle. The combination of the membranous sack and the harder ring above could facilitate this. The fibrillae show no material gradient.

The upper one of the two ring structures is complete, the lower only half and therefore allows assessment of the internal structure. Where the two half rings meet, the flagellum below is – indicated by deep blue colour – even more flexible and durable. This flexible ring is flanked by two small harder rings. Segments, not unlike in bamboo, taper slightly towards distal but broaden again after the ring structure, which serves as a folding mechanism.

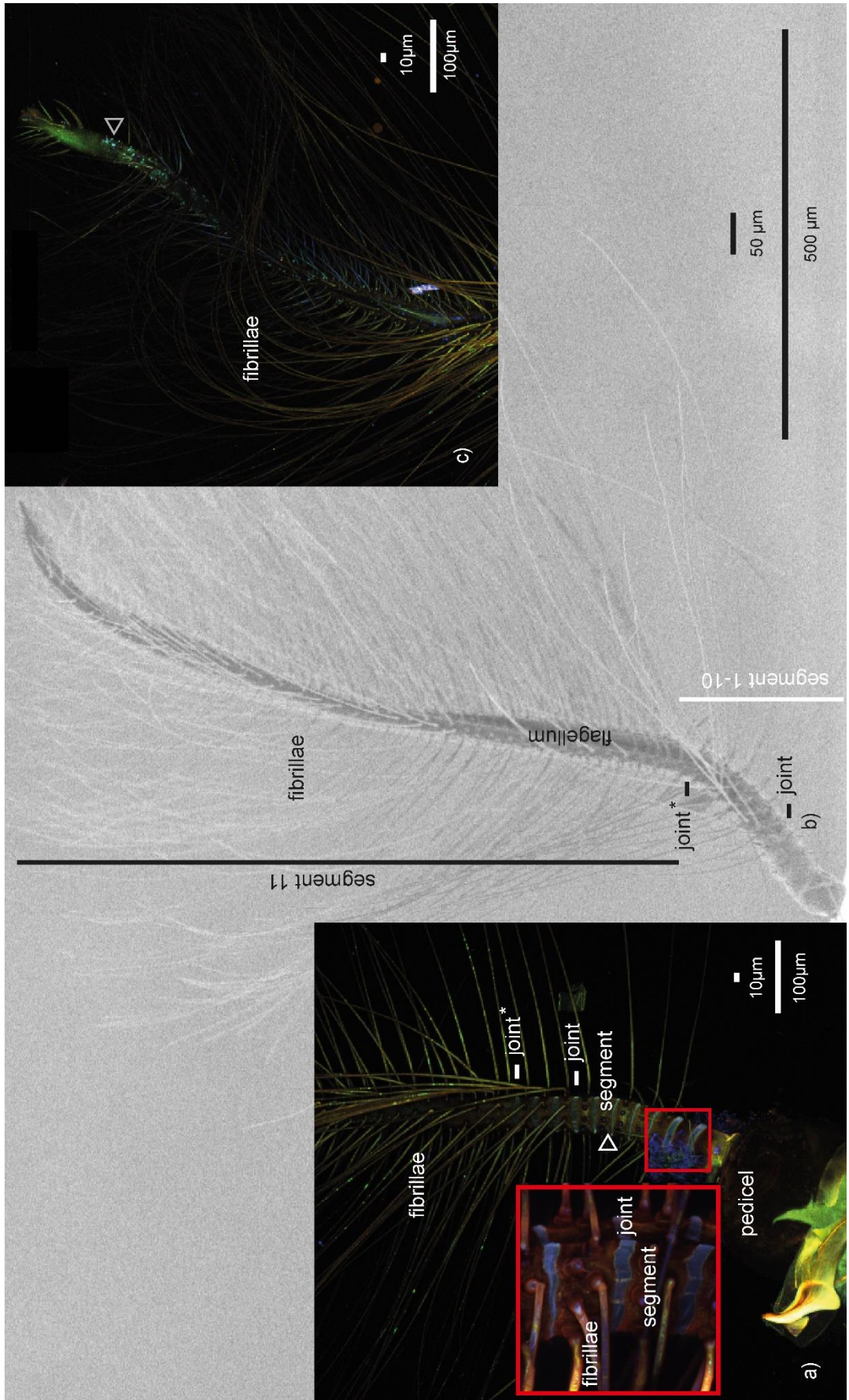
3.5 *Chironomus riparius* male

In the male of *C. riparius*, the pedicel appears black, exhibiting nearly no autofluorescence below the most distal, strongly sclerotized, ring structure (Fig. 3.10). This ring is also, maybe even more prominently so, discernible from the inside (Fig. 3.11). In segments 1 to 10 a singular crest of fibrillae emerges on the sclerotized (red) ring, which except in the 1st segment, follows immediately upon a basal blue ring (flexible) – in this most proximal segment the blue ring might be hidden by the pedicel or merged with the articulation. Red, green and blue cuticle rings follow in a rapid sequence upon each other in those segments. Segment 11, the most distal segment, differs from this pattern as rings are entirely absent and the whole segment is of green autofluorescence with irregularly spaced fibrillae emerging (Fig. 3.11). There is no clear pattern to these fibrillae.

Fig. 3.10 (next page): Male antenna of *C. riparius* as a montage of two maximum intensity projection images of the same individual.

a) Maximum intensity projection of the basal part of the antenna including pedicel. The inset shows a detail of a few segments of a different individual, which, also apparent in the others, features two rows of long fibrillae per segment. b) SEM overview for orientation. c) Detail of the antenna tip from the same individual as a).

The majority of the antenna – last joint marked with * in a) – seems to be made up of the 11th segment ending in a pointed tip. This in consequence means that all shifts between hard and soft elements are located in the lower third to half of the antennae. The strong orange fluorescence of the topmost ridge of the pedicel, which is otherwise low in fluorescence, indicates that the rim is hard. c) Beyond the limited gradient visible along the shorter fibrillae on the last segment appears a field of 1µm wide soft spots, potentially (chemo-)sensillae on the inside of the antennae. As before, long fibrillae do not have a material gradient.



From the 2nd to the 9th, the segments decrease in length – 30, 30, 25, 25, 20, 20, 20, and 20 μm . Also, the proportion of flexible and hard parts changes. The distal segments are similar in length to the sclerotized part of the most proximal ones. Similarly, in distal segments the flexible part decreases in length. At the same time the sclerotized part, which approximately stays similar in length, is less and less dominated by red autofluorescence and becomes entirely green (i.e. tough and partially flexible) with the 5th to the 6th segment.

Overall, the diameter of segments decreases from around 65 μm to 40 μm in the 10th, the 11th segment then continuously tapers towards a pointed tip (Fig. 3.10) – here the autofluorescence decreases. A distal image of a differently positioned antenna also features (in blue Fig. 3.10) an array of sensillae at the tip. The fibrillae shorten along the flagellum axis and also become more irregularly spaced towards the end of segment 11. None of the fibrillae show strong autofluorescence or a material gradient (Fig. 3.10a). Prongs inside the pedicel are of the same size and autofluorescence (similarly stiff) among each other. They show a gradient along their length, being deep blue (flexible) at the attachment turning red to rose (harder) between the central attachment and a cuticle ridge they run over or attach to, and then continue on greenish (Fig. 3.11).

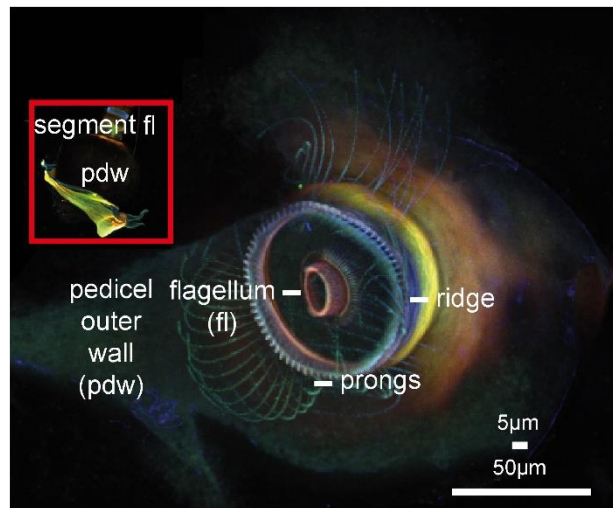
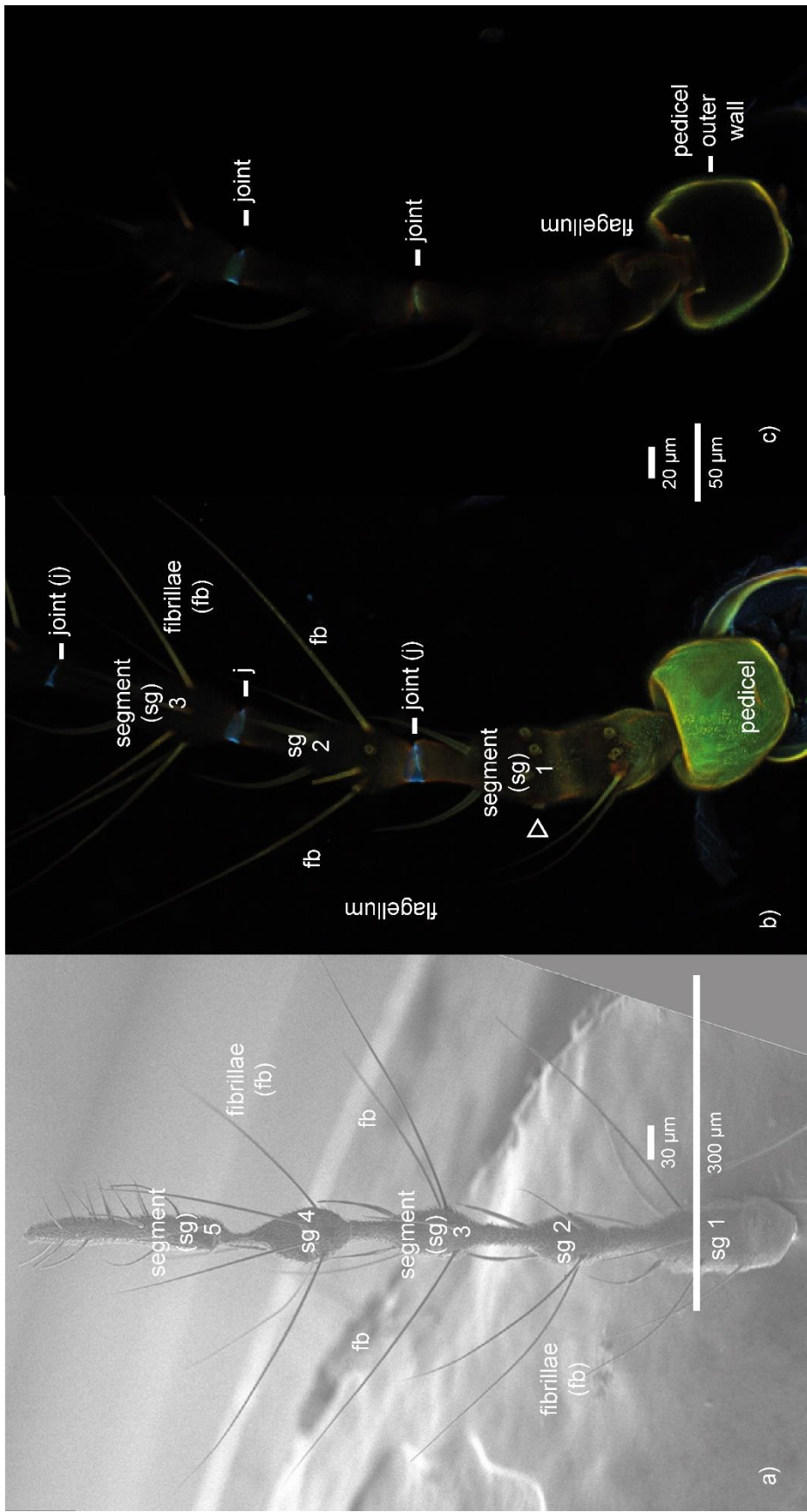


Fig. 3.11: Opened male pedicel of *C. riparius*, maximum intensity projection, the inset shows a pedicel of the same species from the outside for orientation. The end point of the flagellum inserting centrally is comparatively hard (red colour). The prongs attaching on it are not as uniform as in the mosquitoes – starting off centrally in the image more green-yellow, turning via a more blue shade to full green once they passed over the circular ridge. The ridge itself is deep blue and therefore flexible at the top and sharply transitioning to yellow at its lower end, then gradually turning orange red – this orange area can also be seen as the topmost ring in the outside view of the pedicel. There is, however, no visible variation between different prongs, in that respect they are similar to the situation in the mosquitoes.

3.6 *Chironomus riparius* female

Five segments, each with 6-8 separate fibrillae in one to two crests, show no clearly dominant autofluorescence. One of the crests is short and the other is long, emerging on the widest part of each segment before it tapers again (Fig. 3.12).

Fig. 3.12 (next page): Overview of the *C. riparius* female antenna. a) SEM image as overview for orientation in the anatomical detail. b) Maximum intensity projection. c) Optical section. Panels b) and c) are the same scale. In b) the fluorescence in the pedicel is much stronger than in the flagellum. The first 3 of 4 joints of the antenna are visible, compare Fig. 3.6. Furthermore, the two crests of fibrillae inserting in isolated standing sockets per segment are visible. The crests are of different length with the first line of each segment being longer. In c) only the first two segment joints are in the plane and the articulation of the flagellum. The cuticle walls are about 2-4 μm in the pedicel and that half for the flagellum base.



Beyond the two crests there are no further fibrillae present. The segments are separated with a flexible ring (blue) (Fig. 3.12). Noteworthy is that the pedicel exhibits a stronger green fluorescent and is more flat than domed (Fig. 3.12). In the optical sections Fig. 3.12b and Fig. 3.13 one can see how flagellum and pedicel articulate. The central part of the flat articulation is rather flexible (blue).

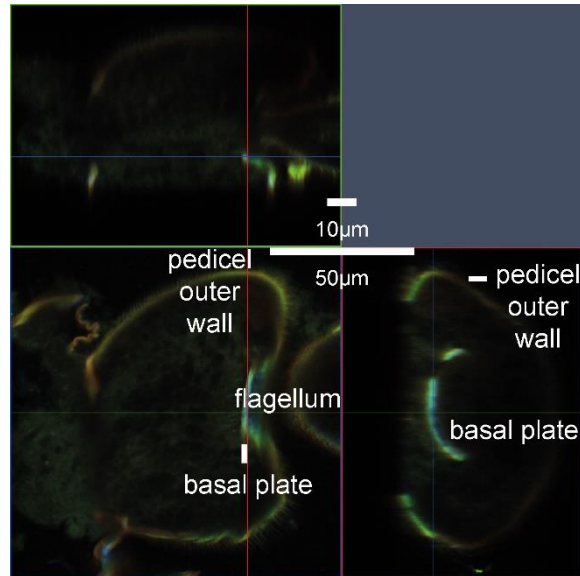


Fig. 3. 13: Female *C. riparius* pedicel, optical section. The attachment plane of pedicel and flagellum is narrow and soft, as well as more square than in males. Basally and internally the flagellum is softer (blue) than the surrounding cuticle (green). Squares of different colour represent different cutting planes and correspond with lines of same colour in the other two cutting planes – e.g. the green line corresponds to the green square, representing one cutting plane.

3. 7 *Chironomus riparius* male to female comparison

While comparison can only be qualitative as images were not taken with exactly the same settings, the pedicel is more strongly fluorescent in females than in males, compared to the flagellum (Fig. 3.10, 3.11, male and Fig. 3.12, 3.13, female). The spherical male pedicel is internally more structured (Fig. 3.10, 3.11), the female one is flatter and more rectangular and has a stronger green fluorescence (Fig. 3.12, 3.13). The same tendency is true for the articulations of the flagellum in both sexes. Along the flagellum the sexual dimorphism is strong, the most prominent difference is that the female flagellum is less covered in fibrillae (Fig. 3.10, male vs. Fig. 3.12, female), it also does not show the rapid frequency of hard, medium, and soft rings seen in males of the species, and only feature 4 instead of 10 joints except the flagellum articulation in the pedicel.

3. 8 *Toxorhynchites brevipalpis* and *Chironomus riparius* female comparison

Between females of those two species one direct comparison image is available featuring both antennae adjacent to each other. In *C. riparius* (Fig. 3.6 and Fig. 3.12a indicated by j) only four joints, compared to the first nine of twelve in *T. brevipalpis* are visible (Fig. 3.6). Further differences include that the 1st flagellomere in *C. riparius* has a more complex substructure, beginning greenish at the base and becoming more orange (that is more sclerotized like the following segments) – in *T. brevipalpis* segments are more similar among themselves.

Furthermore, while *T. brevipalpis* segments are uniformly cylindrical, the first segment in *C. riparius* is widest, 40-50 μm at the bottom, and tapers towards the joint by roughly half. This tendency, albeit less pronounced, is also seen in subsequent segments (Fig. 3.12). The first and second segment in *C. riparius* feature prominent orange-red individual fibrillae sockets at the base of the crest – in the comparison image, *T. brevipalpis* shows no such feature. A differently adjusted detail picture of the fourth segment of another animal confirms a 5 μm wide, orange socket at the base of the larger fibrillae in *T. brevipalpis* (Fig. 3.12 – white arrowhead). However, as settings are different, no material comparison is possible. Fibrillae crests insert just behind the joints in *T. brevipalpis*, and in *C. riparius* where segments are widest. In *C. riparius*, no additional short fibrillae are seen.

3. 9 *Toxorhynchites brevipalpis* and *Anopheles arabiensis* male comparison

While the huge difference in size combined with the plumose nature of both male antenna between *An. arabiensis* and *T. brevipalpis* (Fig. 3.7) made a high-resolution direct comparison image difficult the following paragraph will focus up on the 2nd flagellomere of *T. brevipalpis* and the 6th to 10th of *An. arabiensis* (Fig. 3.7).

To illustrate this, *T. brevipalpis* segments are about 150 μm wide and 200 μm long segments in *An. arabiensis* segments measure 10-20 μm in width (about seven to 15 times less) and with 100 μm are half as long as in the larger species. Notwithstanding the immensely different amounts of material per segment – assuming for both a 10% volume fraction of the outer chitin wall. This can be verified by inspecting e.g. the broken flagellum shown in Fig. 3.4. Combining this volume fraction assumption with the above measurements of the flagellum, less than 1% of chitinous material is used

in the smaller species *An. arabiensis* – nonetheless the autofluorescence is much stronger in *An. arabiensis*. Large parts of *T. brevipalpis* show nearly no signal (neither blue nor yellow-orange) and appear brown to greenish. The more delicate (softer, lighter and smaller) *An. arabiensis* antenna is characterised by alternating long flexible (blue) and sclerotized (orange) areas with no intermediate areas in between.

This makes the antennae almost mirror images of each other insofar as that in *T. brevipalpis* small (ca. 10µm), therefore slightly deeper blue bands separating rather tough and sclerotized segments (ca. 200µm), while in *An. arabiensis* the whole segments (ca 100µm) are light blue and only small proportions are sclerotized.

In both species the long fibrillae (almost only visible as shadows) insert on the orange structure circumventing the flagellum. They lack strong autofluorescence or a visible material composition gradient. In *T. brevipalpis* the most-red, the flagellum-circumscribing structure, is coronal, while it is annular in *An. arabiensis* (both in Fig. 3.7, see also 3.1. and 3.4). It is this structure from which the fibrillae emerge.

An optical cross section (Fig. 3.14) of both antennae – at least if brightness-enhanced – leaves no doubt that it is a thin surface layer that constitutes the highest proportion of – at least – the blue autofluorescence (Fig. 3.14), justifying the low volume ratio attributed to cuticle in Section 4. Also, an optical cross section shows the prongs in both species remain comparatively similarly thin with 2-4µm, while the whole pedicels are roughly twice as large as in the larger *T. brevipalpis*.

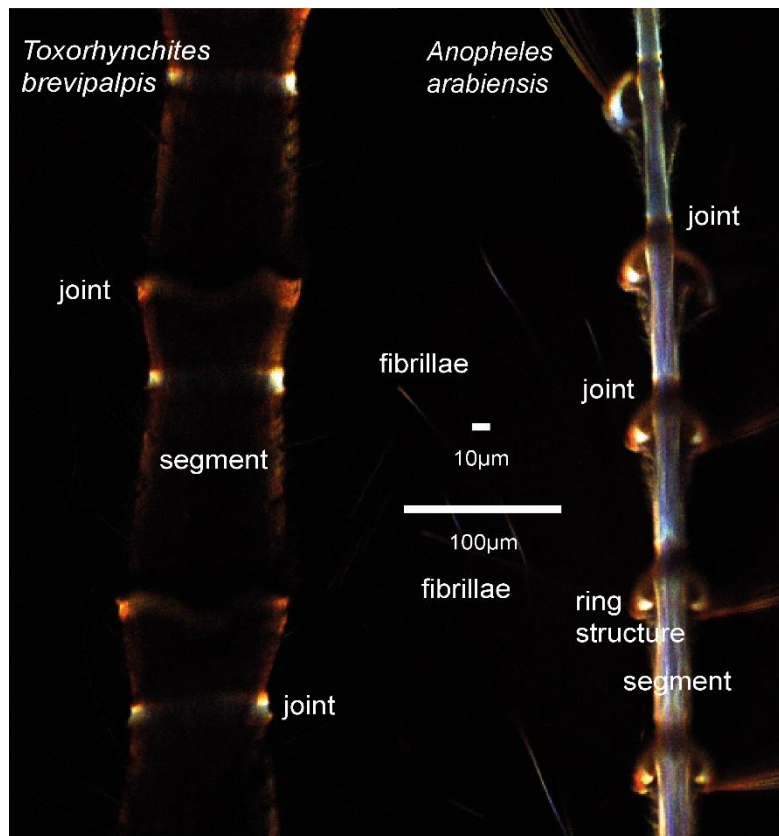


Fig. 3.14 Comparison images between the 2nd segment of *T. brevipalpis* (left) and the 4th to 8th segment of the *An. arabiensis* (right) male antennae – brightness increased optical sections. As with the maximum intensity projection in Fig. 3.7, the size differs greatly between *T. brevipalpis* and *An. arabiensis*. The *T. brevipalpis* antenna is with 3.3mm about twice as long as in the smaller species with 1.7mm. The diameter is 15µm in *An. arabiensis* and 120µm in the larger *T. brevipalpis*. Together those measurements mean that the volume and thereby the mass of the antenna in *T. brevipalpis* is more than 100 times that of *An. arabiensis* even if assuming the same material composition. The composition however is almost inverted with the larger antenna being made up of intermediate hard cuticles and featuring hard and soft bands (blue), while the smaller is mainly made out of flexible cuticle (light blue) and features hard bands (red, orange). The thin cylindrical/conical shape of the antenna can be studied in more detail and cleanliness than in the overview picture 3.8, and is, perhaps not surprisingly, a common feature of both species.

3. 10. Concluding remarks on results and outstanding comments

The *C. riparius* male pedicel has the most complex substructures of all the pedicels investigated (see Fig. 3.5 for *T. brevipalpis* male, Fig. 3.6 for *T. brevipalpis* female, Fig. 3.11, *C. riparius* male, Fig. 3.12, 3.13 for *C. riparius* female, and Fig. 3.15 for *An. arabiensis*). All antennae show a banded pattern, but attribution and localisation (*C. riparius*) are different between species and sexes – no unifying material attributions could be identified.

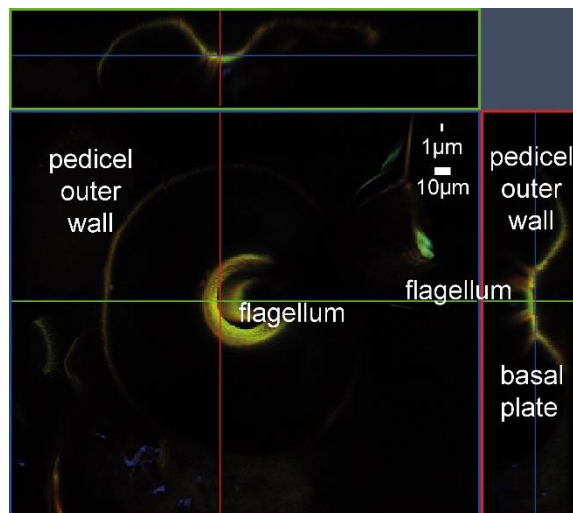


Fig. 3.15 Male *An. arabiensis* pedicel – optical section.
The attachment to the prongs happens in a 2-4μm plane, centrally the flagellum attachment is not sclerotized but made out of flexible cuticle.
The pedicel lacks a defined harder area around the articulation.

3.11 Discussion of CLSM results male

Antennae of all three species investigated were found not to be homogeneous along the flagellum axis. CLSM results show that they consist of hard and soft elements, which alternate in species-specific patterns. As shown in Saltin et al. (2019), to my knowledge this is the first time material differences in mosquito and midge antennae were reported. Allocation and interpretation of colour followed the established method of Michels et al. (2012), in which red corresponds to more sclerotized and blue to more flexible material. In *An. arabiensis* the antenna is chiefly light blue fluorescent and short orange ring elements are distributed in an evenly spread fashion along the flagellum. In the large *T. brevipalpis* antenna, fluorescence is of green colour and low intensity, with blue rings in joint areas and a red ring proximal and distal to the blue ring. This means that the males of the two mosquito species' antennae almost look like mirror images of each other in terms of flexibility. The midge *C. riparius* differs in the location and number of rings – all 10 (instead of 12 in the investigated mosquitoes) are located in the lower third to half of the antenna. This gives them the appearance of a rapidly shifting colour sequence with the last segment being by far the largest and in itself rather uniform.

The largest of the species investigated is *T. brevipalpis*. As both sexes were available, it can be generalised that the overall antenna structure of this species is tough but not sclerotized (as indicated by general green autofluorescence). Also, in both sexes, small flexible and well-sclerotized ring structures are present. The established sexual dimorphism in antenna structure between males and females was shown to extend beyond the diameter (roughly twice in males) and shape (males' antennae are plumose, the females' are not) to the material patterns. Proportion as

well as intensity of red respectively blue autofluorescence differs in the sexes, which further indicates a functional difference of this dimorphism. Details of (Fig. 3.4) confirm the thin shell-like configuration of the flagellum, where the majority of the stiffness is likely conveyed by the outermost part. This is also true for the likely flexible ring structures, observable in blue of (Fig. 3.4).

In the smaller mosquito *An. arabiensis* only males were investigated. They show an inverted distribution compared to *T. brevipalpis*. The documented combination of a sclerotized ring structure, and the area of the membranous sac proximal to this ring, could play a fundamental role in the behaviour of male *Anopheles* antenna collapsing and extending the fibrillae on their antennae by means of hydraulic pressure according to different functional requirements during the daily cycle, which was already reported elsewhere (Nijhout, 1977).

By the very nature of CLSM, imaging the presented figures shows only the situation with extended fibrillae as the whole antenna is suspended in fluid.

The overall antennal structure of the more curved antenna of *C. riparius* is different. The ten proximal segments are short. The distalmost segment follows a 10th soft ring and at 40 μm is already more slender than the antenna base, at 65 μm , it continues to taper (see Fig. 3.10a) ending in a pointed tip (Fig. 3.10). The function of this basal rapid sequence of flexible and sclerotized material remains unclear – it is not seen in other species. Between the pedicels of the different species there is a large variation of autofluorescence intensity, with *C. riparius* females showing the strongest fluorescence and *T. brevipalpis* males the weakest.

Internally and externally they look rather similar between species. An exception to this is that in males of *T. brevivalpis* and *C. riparius*, a hard area on the distal ridge – where the flagellum leaves the pedicel – is visible. Different prongs of the same animal are rather similar in fluorescence, diameter and size in all species.

Comparison between images is hindered by the fact that different CLSM settings are necessary for proper visualisation of the structure and material differences, hence no exact judgement of material properties between different species – or even individuals of the same species – is possible, as they were imaged individually. This is in line with assumptions made by Avitabile et al. (2010) based on previously existing morphological investigations. They constructed a microscopic emergence-based model on how the pedicel might achieve amplification (Avitabile et al., 2010). This model can be viewed as essentially emergence-based, as it explains macroscopically present phenomena e.g. self-oscillation as a result of interactions of microscopic subunits, which each on their own would and do not show the macroscopically observed properties. In this and other (e.g. Nadrowski et al., 2009b and Mhatre, 2015) models, prongs are treated as uniform, rigid, body extensions of the flagellum. The same, however, cannot be said about the flagellum which, although its exact functionality remains unclear for now, appears to be more complexly composed than a simple rocking beam. This internal uniformity on the level of the prongs again hints towards the scolopidia as sources of internal stiffness variation. Windmill et al. (2018), using atomic force microscopy have shown that scolopidia could be the source of the observed twice-frequency forcing. This is also corroborated by electrophysiological results made by Lapshin et al. (2019).

Open questions are: How does the observed material pattern correlate with direct mechanical measurements in this insect antenna? How much of the observed variation between *An. arabiensis* and *T. brevipalpis* antennae is due to size effects? For example, the flagellum of the smaller species' antenna has <1% of the volume compared to that of the larger species. This directly correlates with the mass of the structure, which can be expected to be about 100 times less in the smaller species. Another open question that comes up is how different the antenna functionality between the species might be and how much this owes to the material patterns. For the last question some indication might be gained by the FEM chapter and the inability of *T. brevipalpis* to collapse the fibrillae.

4 Finite Element Modelling (FEM)

Finite Element Modelling is a technique widely used in engineering science and industry (e.g. Eriksson, 1999, Zienkiewicz et al., 2005, Gu, 2017) as it enables to predict the performance of devices or structures with certain parameters without previously having to go through the whole prototyping process in advance.

Furthermore, FEM allows to identify structures or functions not seen or recognised in the experiment, as their absence prevents the model from reproducing the experimental results. In this study, and not for the first time (e.g. Holzapfel et al., 1996, Mackie, 2015, Reid, 2017, Albert et al., 2016), this powerful tool is turned on a biological problem. In contrast to the engineering problem, where the primary aim is to avoid spending time and money on an essentially potentially flawed design, here the objective is to probe nature within digital space where it is much easier to control for example parameters of the antenna than in the real world.

Admittedly, given the relatively recent advent of the CRISPR/Cas9 gene editing technique, the prospect of having experimental animals with artificially more or less complex antenna substructure is much more attainable than a few years before (Tait-Burkard et al., 2018, Khanzadi et al., 2019). However, the effort of real experiments of that sort still is much larger than in a computer model. In the computer, it's a simple matter of assigning the same or different properties to different parts of the model and one can compare different configurations and thereby infer with some confidence whether a given structure has an effect and what that effect could be, while each control condition needs to be individually genetically engineered and bred.

This is what FEM is employed for in this thesis, to allow an estimate for how an antenna with no substructure would vibrate differently from an antenna with the substructure observed under CLSM (Section 3).

4.1 FE modelling of the antenna

The simulations in this chapter are based on aspects of antenna material distribution and hence elasticity variations, as observed in CLSM. The advantage of using COMSOL is that it is an explicit finite element solver.

The following mesh dimensions were used to ensure sufficient accuracy:

Table 4.1: This table summarises the geometry and meshing settings used in all three species. Reproduction of Table 2.4.

Antenna Model	Overall size [mm]	Number of elements	Average element quality	Minimum element quality	Large parts mesh: fine [10^{-4} m]	Small parts setting [$m 10^{-5}$]
<i>Toxorhynchites brevipalpis</i>	3.3	47707	0.455	0.009789	0.33-2.65	Finer 1.32-18.2
<i>Anopheles arabiensis</i>	1.7	249915	0.5763	0.001367	0.17-1.37	Extra fine 0.26-5.99
<i>Chironomus riparius</i>	1.2	85709	0.5694	0.05336	0.14-1.14	Extremely fine 0.03-2.85

Additionally, more simple beam simulations will be discussed here. All reported simulations are frequency-domain studies of vibrational behaviour. Other parameters of the antenna taken into account include “base stiffness” – a compound quality which is defined in Methods – and general geometry based on CLSM images, 3D constructions, and SEM. Parts of the present chapter are based on “Material stiffness variation in mosquito antennae”, published in Royal Society Interface (Saltin et al., 2019) in collaboration with the University of Kiel, Germany.

As, in contrast to the range of stiffness, no great variations of density are known for insect cuticle (Vincent et al., 2004), this value will be considered constant between cuticle with different stiffness values.

4.1.1 Background for the antenna simulations – the simple harmonic oscillator

Without doubt, it could be argued that even a relatively simple structure such as the presented insect antenna is in many ways more complex than the idealised case presented by a simple harmonic oscillator. One does not need to look further than some of the simplifications and assumptions made in 4.1. to reach this conclusion. Nevertheless, the concept of the simple harmonic oscillator is instructive to understand more general vibrational behaviour principles. Every simple harmonic oscillator has a resonant frequency, which is defined by the stiffness of its spring element and the value of the mass at the end of that spring element (see Fig 4.1a). It is important to note that all problems this work is concerned with are purely mechanical, and theory and terminology are tailored to the mechanical version of the harmonic oscillator.

The governing formula is:

$$\frac{F}{m} \cos(\omega t) = \ddot{x} + \frac{b}{m} \dot{x} + \frac{k}{m} x \quad (7)$$

With b : drag coefficient, k : stiffness of the spring, m : mass, and x : the deviation of the system from resting position. For the present study, the resonant frequency of the undamped system ω_0 is important and it is given by the last term of the equation.

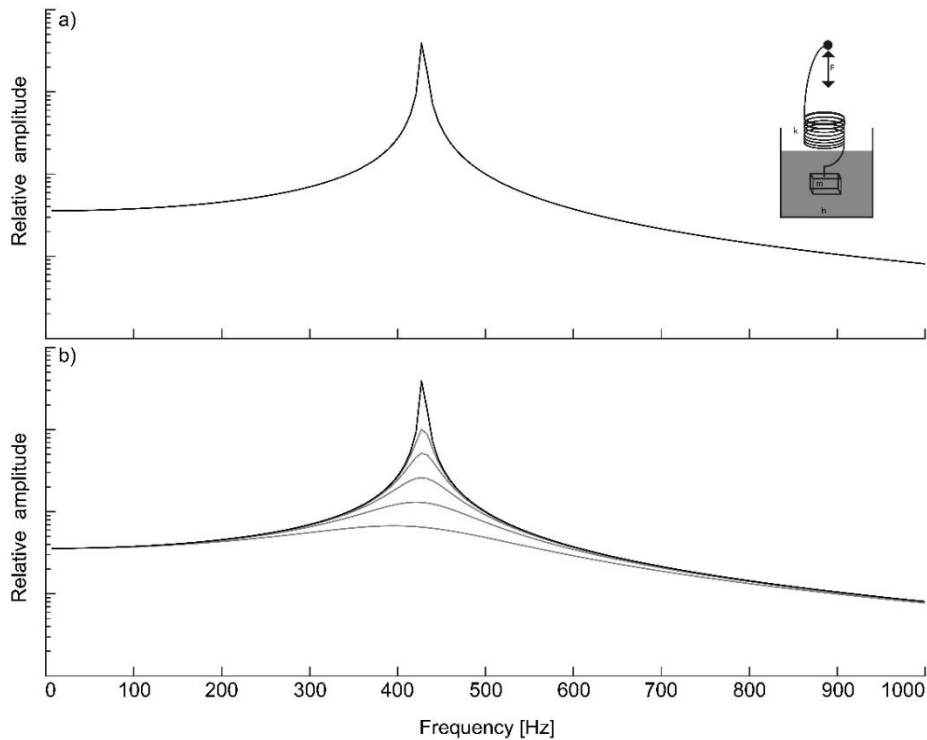


Fig. 4.1: Panel a) shows the frequency response of a simple harmonic oscillator in a linear-log coordinate system and b) the effect of damping on the same harmonic oscillator also in linear-log coordinates.

In figure 4.1, showing the mechanical case of a harmonic oscillator, to the left of the resonant frequency peak the response of the harmonic oscillator is mainly stiffness-dominated, to the right of the peak the inertia of the system takes precedence.

While included for the sake of completeness, the damping of the investigated system is not taken into account in detail, see also section 2.4.1. Note that the peak frequency does not shift but the shape of the peak broadens. This also seems justified by the 3D-vibrometry results shown in Section 6 as the real peaks of the antenna vibration appear very sharp and narrow just like or even sharper than the simulation results. A keen reader will notice that the plateau-like purely stiffness-dominated part of the function is absent in the FEM simulations. This is due to the fact that the base of the antenna is by comparison very soft which in turn means translation movement and momentum have a more pronounced effect in all areas of the more real system.

4.1.2 The simulated geometry

For a more in-depth explanation of the CAD model and the modelling parameter, please refer to (2.4.1 CAD model generation) and physics settings (2.4.2 COMSOL settings). The sole aim of section 4.1.2. is to have the geometry of the simulated antenna readily available when discussing aspects of the results.

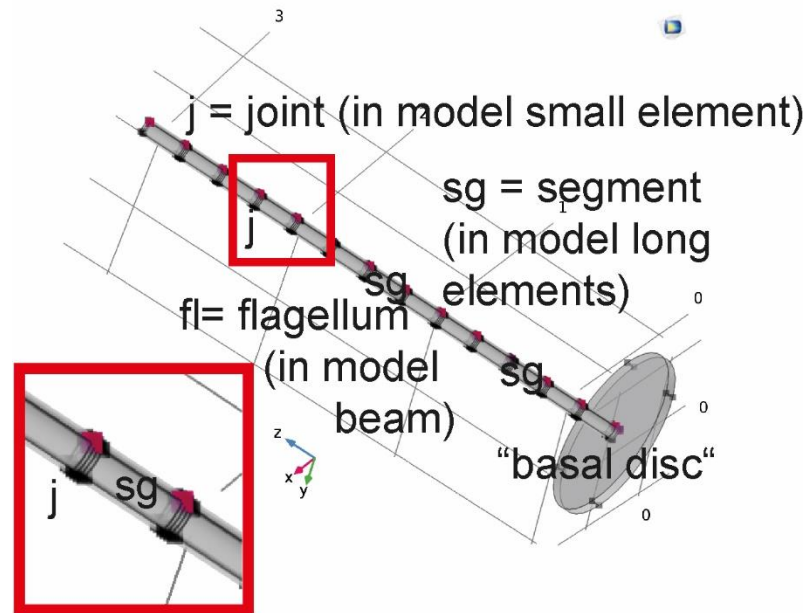


Fig.4.2: is a reproduction of Fig.2.4 from the Methods section. It illustrates the layout of the simplified beam, based on antenna morphology used for COMSOL simulations.

It is comprised of 13 large elements with 12 smaller elements representing segment joints. Joints were assembled, as seen in *T. brevipalpis*, out of three thin discs, or more precisely, ring elements. The beam is medially attached to a basal disc, which conveys the aforementioned basal stiffness, not to be confused with the actual basal plate but rather a compound quality, as described in the main text.

The geometry illustrated by figure 4.2 is slightly varied for the simulations described in sections 4.6 and 4.7. In the first case, the substructure is moved down towards the proximal part of the beam to reflect the situation seen in *C. riparius*. In section 4.7 a uniform beam with no substructure is used and compared to a conical shape of the same length and basal diameter.

4.2 The effect of “basal stiffness” on the antenna vibration

Figure 4.1 illustrates, perhaps to little surprise, that the resonant frequency and overall frequency response of a beam strongly depends upon how and how strong the beam is fixed or articulated in a biological system.

The stiffer the base, the higher the frequency of the resonant peak and the converse is also true. There is, however, a diminishing gain per decade – comparable to the resonant frequency of a clamped beam of the same type. The higher the frequency gets, the more the basal stiffness must be increased to have any appreciable effect. That is to say, within biologically relevant stiffnesses from a certain point defined by beam type (mainly length and stiffness), further increase in basal stiffness has a strongly diminished effect or no effect at all anymore. This demonstrates that the model captures – in relevant aspects and within the range of 90Pa (70Hz resonant frequency) to 100kPa (1520Hz resonant frequency) – a compliantly clamped beam.

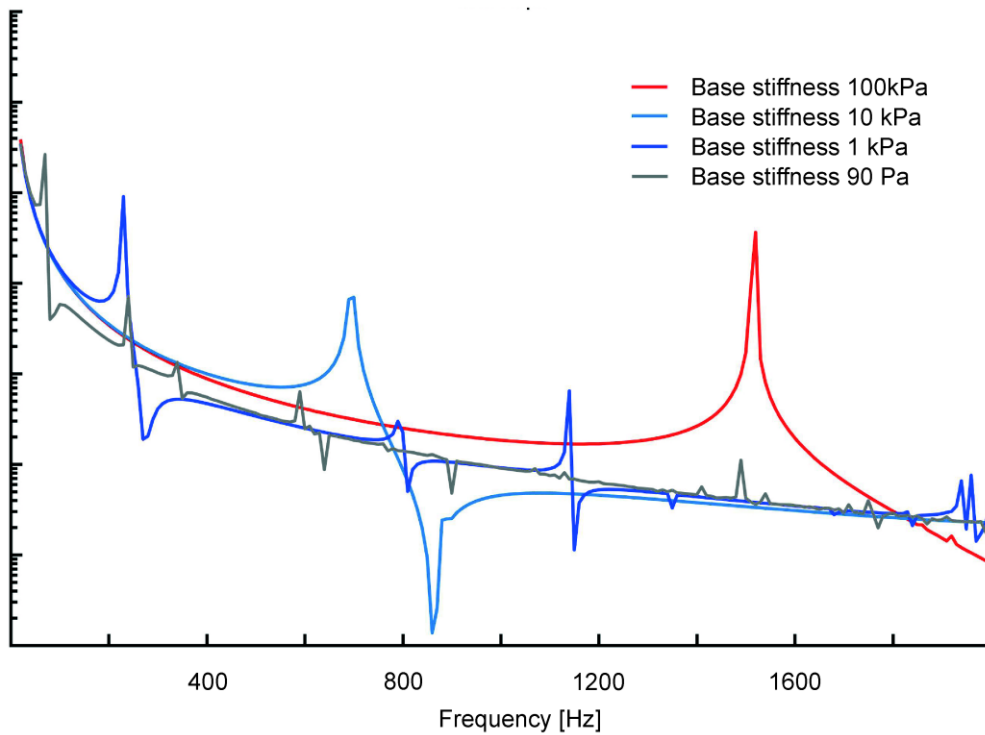


Fig. 4.3: Graphs illustrating some COMSOL simulation results. It deals with the effect of varying the “base stiffness” over four orders of magnitude while keeping the beam itself uniform. Changes in resonant frequency go from 1520Hz (red line), over 690/695 (light blue line) and 220/230 (dark blue) to 70Hz (gray line). The 90Pa model (gray line) is the lowest possible basal stiffness in a *T. brevipalpis*-like model based on considerations of prong diameter and volume percentage of the disc made up by cuticle and tissue material. The 90Pa model (gray line) are a small deviation of the power of ten steps used, based on consideration of prong diameter and volume percentage of the disc made up by cuticle and tissue material, how low could the stiffness in the larger species possibly be.

4.3 The effect of adding small subelements with differing stiffness to a uniform beam

Twelve evenly spread subelements were introduced, qualitatively based on the CLSM results, in a simplified version reproducing the natural distribution in those insect antennae. Again, the effective stiffness of the overall beam can clearly be influenced by such elements (Fig. 4.4). Soft elements, although representing only tiny surface or volume fractions of the whole beam structure, appreciably change the peak frequency to lower frequency values. In numbers that is: With one power of ten softer elements than the beam the frequency drops by 35Hz, with elements a hundred times softer it drops by 240Hz and with elements a thousand times softer even by 525Hz. Adding hard elements also changes the resonant frequency to higher values from about 690-700Hz (between simulated frequencies) up to 700Hz, albeit by a very minute amount (<10Hz).

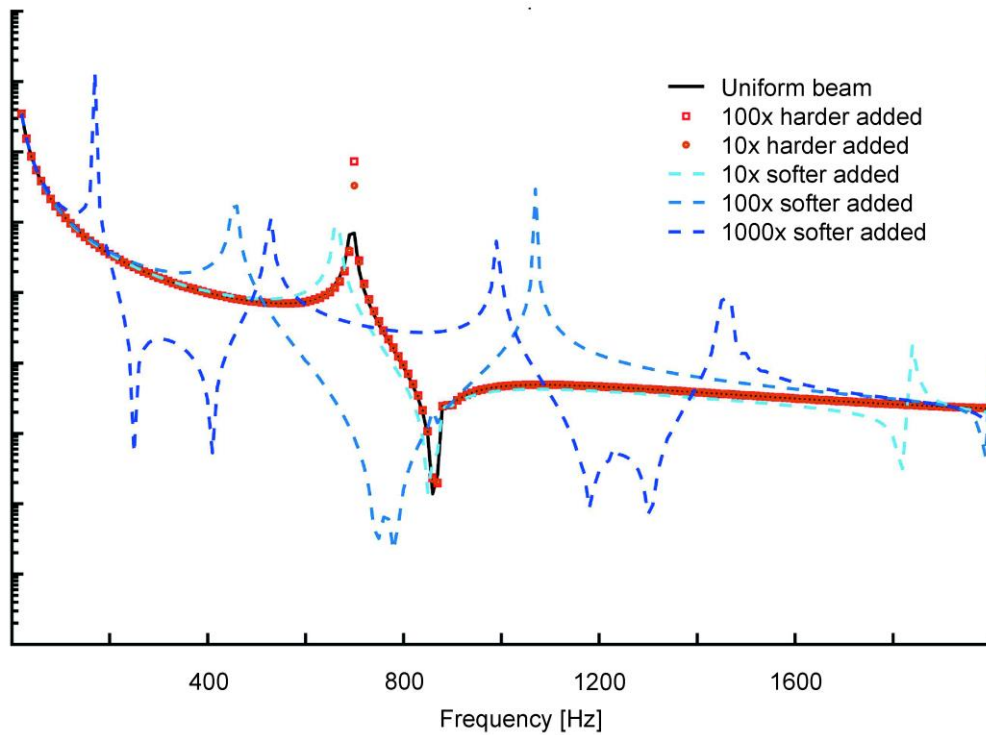


Fig. 4.4: Graphs illustrating some COMSOL simulation results – qualitatively shows that adding variations of stiffness to a beam changes its resonant frequencies. Depicted are the effect of adding hard or soft elements to a uniform beam with base stiffness of 10kPa, represented by a solid black line. The dashed blue lines represent the presence of softer beam elements progressing from light blue – 10x softer – over blue – 100x – softer to dark blue – 1000x softer. Orange circles represent the presence of 10x harder elements and red squares 100x harder elements.

4.4 The effect of the Poisson ratio

A brief test of the effect of varying the Poisson ratio from 0.25 to 0.38 was performed as of Table 4.2 and Fig. 4.5. Shifts are maximal around a beam stiffness of 10MPa (highlighted in bold in Table 4.2) and they differ only by around 3% of the amplitude with no effect on frequency. On average the Poisson ratio affects the amplitude maximum by less than 1% in our model, compared to the 232% shift in amplitude introduced by varying the beam stiffness. Therefore, the simplification of keeping the Poisson ratio at a fixed value is justified.

Table 4.2: Amplitude of the first resonant frequency peak of beams with beam stiffness (Young's modulus) ranging from MPa to GPa at different Poisson ratios. Maximum values denoted in red (in case of a local maximum) and values before reaching a stable value in gray (if monotonously increasing within the investigated range). The column in bold shows the Young's modulus at which the Poisson ratio has the maximum effect on the amplitude. As with the figure, absolute values are of lesser importance compared to the realisation that frequency does not change by changing the Poisson ratio and the amplitude as can be seen is only minutely influenced as well.

Beam stiffness [Pa]	10 ⁶	5x10 ⁶	10⁷	5x10 ⁷	10 ⁸	2.5x10 ⁸	5x10 ⁸	7.5x10 ⁸	10 ⁹
Resonant frequency [Hz]	80	170	240	410	460	490	510	510	510
Amplitude at Poisson ratio 0.25	3,58 x10 ⁻⁴	1,61 x10 ⁻⁴	2,51 x10 ⁻⁴	3,36 x10 ⁻⁴	8,46 x10 ⁻⁵	1,15 x10 ⁻⁵	9,96 x10 ⁻⁶	9,68 x10 ⁻⁵	3,01 x10 ⁻⁵
Amplitude at Poisson ratio 0.3	3,58 x10 ⁻⁴	1,61 x10 ⁻⁴	2,57 x10 ⁻⁴	3,42 x10 ⁻⁴	8,48 x10 ⁻⁵	1,15 x10 ⁻⁵	9,96 x10 ⁻⁶	9,67 x10 ⁻⁵	3,01 x10 ⁻⁵
Amplitude at Poisson ratio 0.32	3,58 x10 ⁻⁴	1,61 x10 ⁻⁴	2,59 x10 ⁻⁴	3,43 x10 ⁻⁴	8,49 x10 ⁻⁵	1,15 x10 ⁻⁵	9,96 x10 ⁻⁶	9,67 x10 ⁻⁵	3,01 x10 ⁻⁵
Amplitude at Poisson ratio 0.35	3,59 x10 ⁻⁴	1,61 x10 ⁻⁴	2,60 x10 ⁻⁴	3,43 x10 ⁻⁴	8,49 x10 ⁻⁵	1,15 x10 ⁻⁵	9,96 x10 ⁻⁶	9,66 x10 ⁻⁵	3,01 x10 ⁻⁵
Amplitude at Poisson ratio 0.38	3,59 x10 ⁻⁴	1,61 x10 ⁻⁴	2,60 x10 ⁻⁴	3,40 x10 ⁻⁴	8,48 x10 ⁻⁵	1,15 x10 ⁻⁵	9,96 x10 ⁻⁶	9,67 x10 ⁻⁵	3,01 x10 ⁻⁵

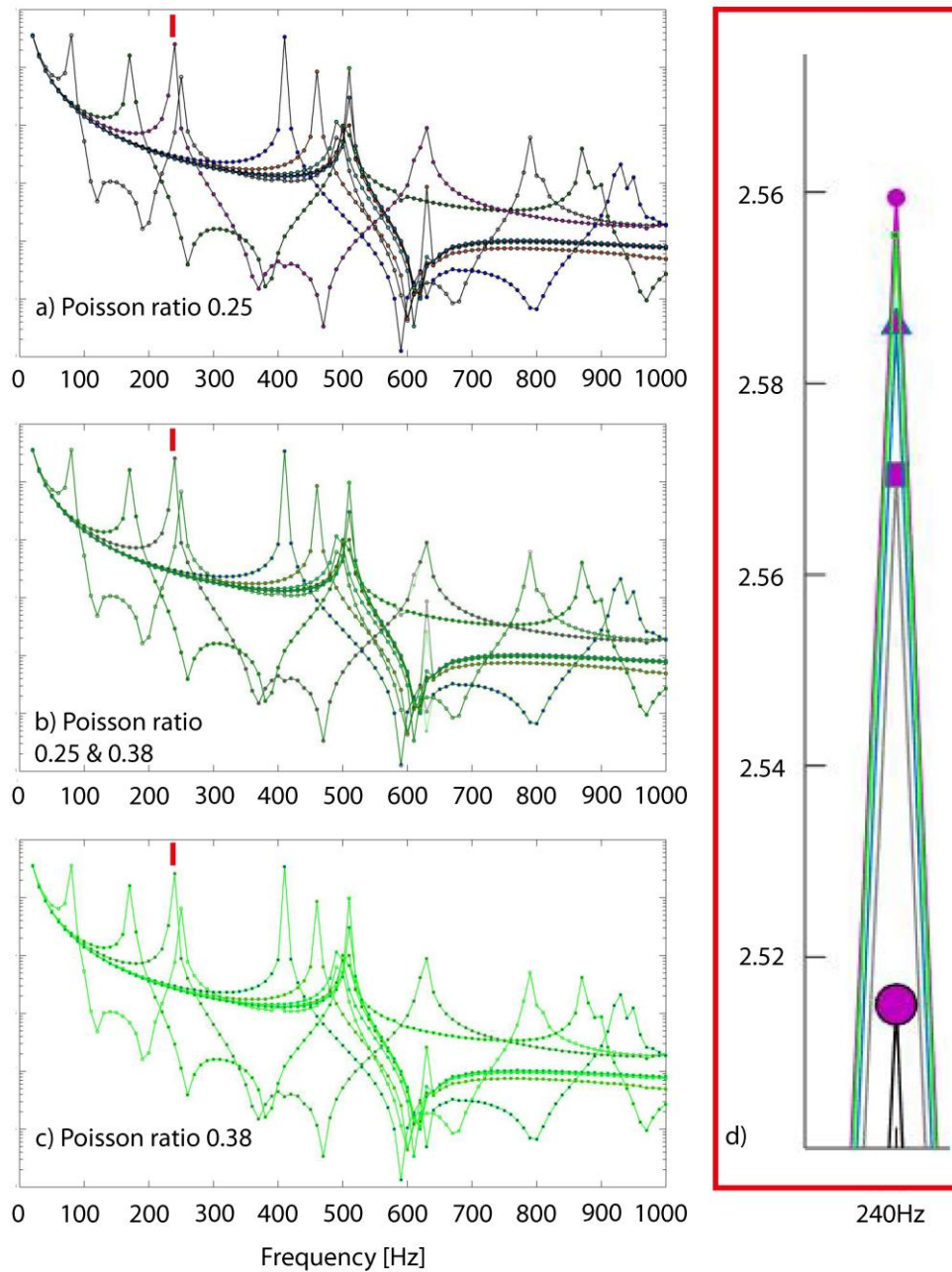


Fig. 4.5: This figure shows that the effect of beam elasticity is more important to the model than the effect of varying the Poisson ratio. Panel a) shows a parametric sweep of beam elasticity ($10^6 - 10^9$ Pa) with a Poisson ratio of 0.25 (lowest Poisson ratio investigated) in black line with coloured circles coding the elasticity in ascending order, left to right as follows: white (10^6 Pa), dark green (5×10^6 Pa), pink (10^7 Pa), dark blue (5×10^7 Pa), orange (10^8 Pa), turquoise (2.5×10^8 Pa), brown (5×10^8 Pa), light green (7.5×10^8 Pa), light blue (10^9 Pa). The red line denotes the 10^7 Pa case used for the detail image d). Panel b) shows an overlay of a parametric sweep of beam elasticity ($10^6 - 10^9$ Pa) with a Poisson ratio of 0.25 and 0.38. The red line denotes the 10MPa case used for the detail image d). Figure text continues on next page.

Figure caption 4.5 continued:

The purpose of this overlay of a light green and black curve to an identical dark green curve is to demonstrate that the effect of changing the Poisson ratio on our model is minimal. Panel c) shows a parametric sweep of beam elasticity ($10^6 - 10^9$ Pa) with a Poisson ratio of 0.38 (highest Poisson ratio investigated) – light green line. d) Example at point of maximum effect of varying Poisson ratio from 0.25 (large circle) over 0.30 (large square), 0.32 (triangle), 0.35 (circle) to 0.38 (square). As with a-c), absolute values do not matter here, the important point is to demonstrate the small range of effect that the Poisson ratio has on our model.

4.5 Qualitative analysis of the *Toxorhynchites brevivalpis* and *Anopheles arabiensis* antenna stiffness distribution

Figure 4.4 shows four cases: (1) uniform beam, (2) uniform beam with added stiff elements, (3) uniform beam with added soft elements, and (4) uniform with both stiff and soft elements added – the latter case being close to the one observed in the antenna of male *T. brevivalpis*. For a mainly hard-to-medium stiff beam like the antenna of *T. brevivalpis* (case 4) it becomes evident that only adding soft elements changes the resonant frequency by a large amount – 300Hz (>45%). Addition of hard elements is insufficient to alter the natural vibration characteristics of a beam of that type, as shown by case 2 where only a shift of < 10Hz is introduced. In this case, the peak becomes more clearly settled on 695Hz. This is does not change with case 3 (only soft elements) and 4 (soft and hard elements) which are totally indistinguishable in the 10Hz step simulation resolution. Figure 4.7 illuminates the situation in male *An. arabiensis*. The two lines represent the behaviour of a uniform small and soft beam (continuous line), and a beam more faithful to the observed situation in *An. arabiensis* to which hard elements have been added (dashed line).

Admittedly, the addition of hard elements has a lesser effect on a soft beam than that shown for soft elements to a harder beam in Fig. 4.6 but it does increase the resonant frequency by 30Hz from 160 to 190Hz.

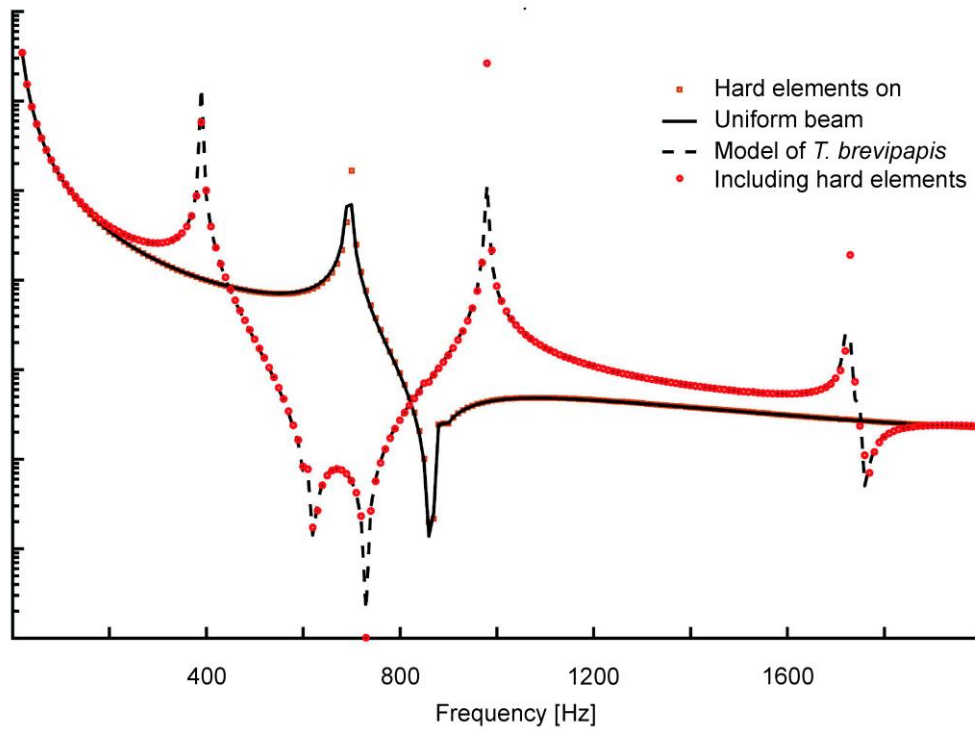


Fig. 4.6: Graphs illustrating the COMSOL simulation comparison of a *Toxorhynchites*-type model with a uniform beam. Starting from a uniform beam in the length of *T. brevipalpis*, successively adding hard elements onto it (orange squares), soft elements (dashed black line) and both soft and hard elements (red circles) approaching the natural situation. Only the addition of soft elements appreciably affects the frequency response. Note that the resonance is consistent with wingbeat frequencies in this species.

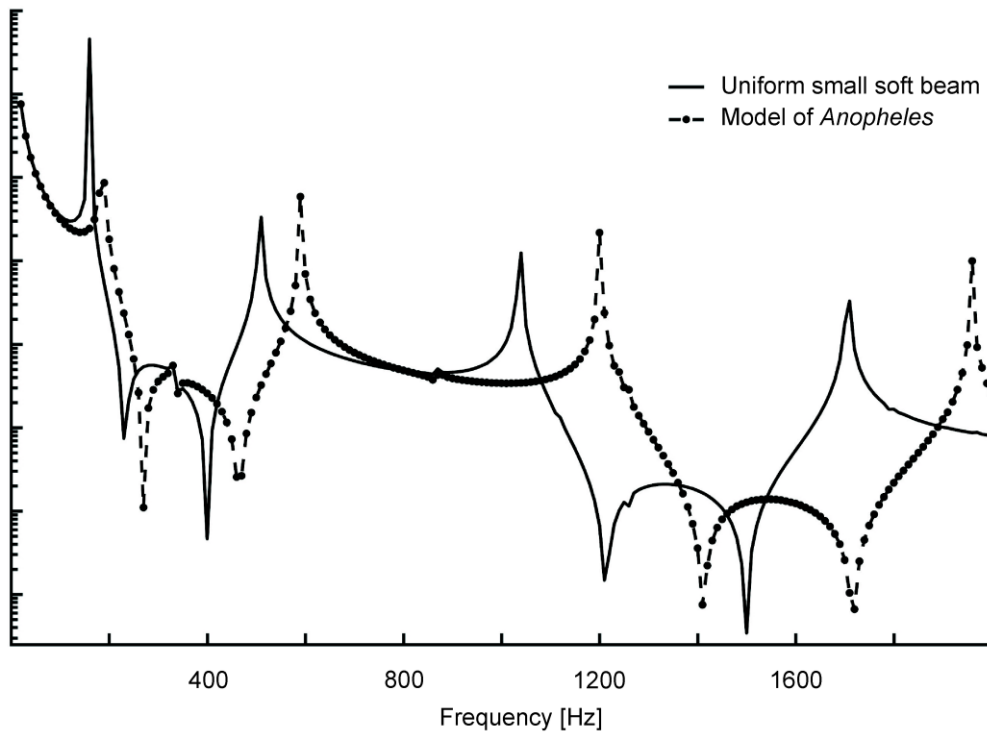


Fig. 4.7: Graphs illustrating of the COMSOL simulation comparison of the *Anopheles*-type model with a uniform beam. Contrary to the situation in an already stiff beam (Fig. 4.4), in a soft beam, adding hard elements does affect the overall beam resonant frequency and shift it up towards the wingbeat frequencies of this species.

4.6 Qualitative analysis of the *Chironomus riparius* or the effect of position

In the midge *C. riparius*, all hard and soft elements are located in the lower third of the antenna and the remainder of the antenna is uniform and of medium stiffness. To investigate how this different spatial distribution affects bending of the beam, this situation was simulated as well and is shown in Fig. 4.8. To exclude size and mass as factors, comparison was done with a uniform beam, with an evenly spread beam (e.g. *T. brevipalpis*) and a beam with the distribution of *C. riparius* – the evenly spread beam was downscaled to match the *C. riparius* size. The resulting graph clearly conveys that the location of elements does matter.

Elements more closely located towards the base as in *C. riparius* have a more pronounced effect in altering the overall resonant frequency. The first resonant peak in a *C. riparius* antenna is at 455Hz – 2Hz higher than 457Hz with evenly spread bands or 4Hz higher than the 459Hz of a uniform beam. To reduce computation time, only the immediate surrounding of the resonant peak was done with 1Hz frequency resolution as the overview simulation – already time-consuming – shows that no relevant frequency behavior can be expected outside of this area.

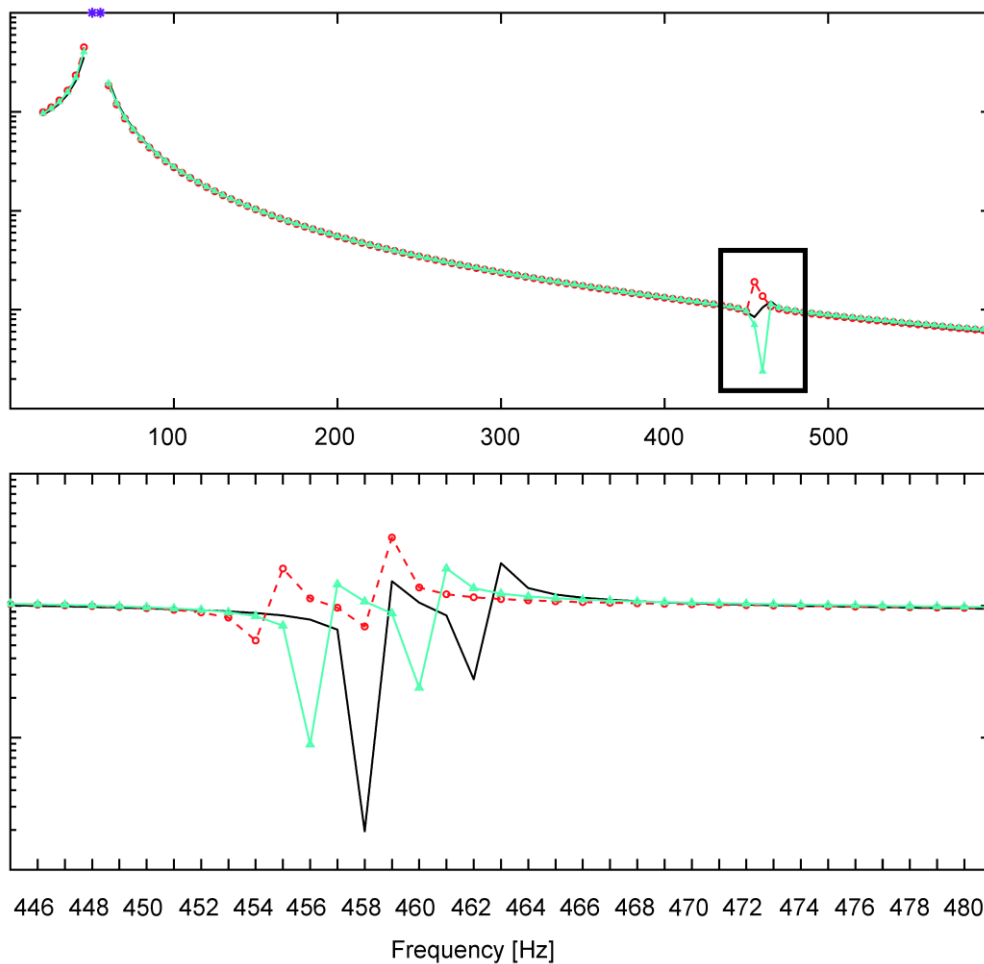


Fig. 4.8: Graphs illustrating COMSOL simulation results, which are the size-independent comparison of a *C. riparius* and a *T. brevipalpis* type distribution of elements and a uniform beam. Panel a) shows the full frequency range from 25 to 600Hz, in 5Hz steps. Panel b) is a 1Hz step version around the non-singular frequency response, see black frame for position. The black line represents the base line of a uniform beam, the red dashed line is the *C. riparius* type with elements at the lower end, and the green line a *T. brevipalpis* type, in *C. riparius* size. The purple stars denote the 45 to 50Hz singularity, which could not be computed. This emphasizes that not only flexibility, but also the position of flexible elements, has an influence. *C. riparius* has all hard-soft bands located in the lower third of the flagellum, in contrast to *T. brevipalpis*, where they are evenly spaced. Soft elements close to the base have less effect on the resonant tuning.

4.7 The effect of straight beam vs. cone shape

As the antenna is plumose, the flagellum cross-section is not considered to have a huge effect on beam bending as such. Nonetheless, a comparison between a cone-shaped tapering antenna of the same length as *T. brevipalpis* and the straight beam model for *T. brevipalpis* was simulated. It was found that keeping length and density the same a cone shape increased the resonant frequency compared to a simple beam by 75Hz (Fig. 4.9).

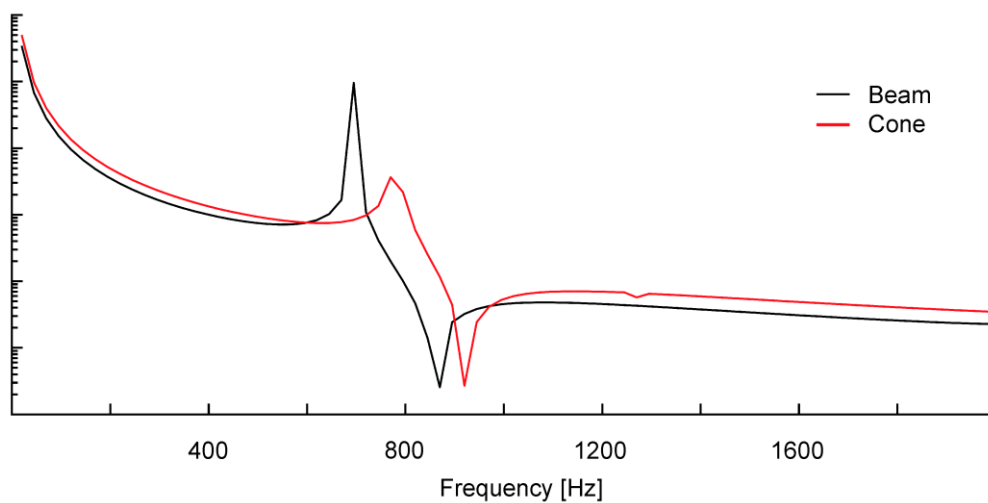


Fig. 4.9: Graphs illustrating the COMSOL simulation results, comparing the effect of a tapering cone shape (red line) of the flagellum to a straight beam of the same size (black line).

As a word of caution, at present it is difficult to assess to what degree the plumose nature of the antenna could alter the vibrational characteristic beyond the shape of the central beam structure by altering the overall antenna shape. Broadening and lowering the peak by adding damping are the most likely effects to be observed.

It is clear that, viewed on its own, the cone shape at the same cross-sectional area, despite having less mass, would increase the resonant frequency.

4.8 Concluding remarks

Appreciating that the performed simulations are basic representations, it is believed to be demonstrated that our simulation captures a compliantly clamped beam (Fig. 4.3). Figures 4.4, 4.6, 4.7 illustrate that shifting the effective stiffness of a beam can be achieved by introducing comparatively tiny elements of either harder or softer material – whereas the stiffness ratio between main beam and introduced elements defines how strong the influence is.

Noteworthy is that within a biologically relevant parameter range, without adding the discovered disc elements to the beam structure, resonant frequencies matching those seen in nature are difficult, if at all possible, to obtain. This contrasts the predictions for a simple compliantly clamped beam, whose resonant frequency is mostly determined by the beam dimensions and the stiffness of the clamp (Rao, 2011). As shown also in Section 4, however, antennae cannot further be considered a simple rocking rod and therefore different mechanical behaviour also seems reasonable to assume.

Furthermore, as it has become clear that not only the presence and absence, but also the location of elements of varying stiffness can have an effect on the vibrational characteristics of the antenna (Fig. 4.8), the situation is in reality even more complicated. Investigating the effect of tapering could also be an interesting future route. In summary, the addition of elements of different stiffness to the beam has the potential to change beam resonant frequency (Fig. 4.2, 4.4, 4.5), as does changing the basal stiffness (Fig. 4.1) and both effects can have a similar order of magnitude.

4.9 Discussion of the FEM modelling of the male antenna of the three species

Results indicate the possibility of resonant tuning by altering the stiffness of elements along the flagellum. This being said, there are a great number of reasons why material variations along the flagellum could be advantageous, for example in constructing a transmission-line structure. While it has not been proven for highly functional structures, metabolic cost might be one of them. In the framework of reduced cost, alternating structures of higher-cost material with the base material might be a way to optimize the balance between functionality and cost – as resilin (conveying flexibility) and sclerotization both should be more energy-expensive than base chitin. “Wear and tear” protection is one of the known functions of resilin in insect cuticle (Mountcastle et al., 2013, Rajabi et al., 2018), so the flexible parts could be necessary to keep it functional rather than having a direct relevance to the function as acoustic sensors. Particularly as exposed sensory organs like insect antennae are potentially under almost continuous mechanical stress – especially considering that they in the investigated species can move autogenously even in the absence of a stimulus.

Another aspect is that, while the strength of the articulation is under the functional constraint to provide reliable support to the system, this is not the case for the beam. Furthermore, modification of element distribution could open another route to realize individual variation, thereby allowing for selectability in the trait.

This biological consideration aside, the fact that differing stiff beam elements should influence the resonant behaviour of the system is somewhat expected from a mechanical point of view.

The frequency a system resonates at (ω_0) is defined as:

$$\omega_0 = \sqrt{\frac{k}{m}} \quad (7b)$$

The contributing factors are: k : stiffness, I : second area moment of inertia, which depends on mass distribution ρ : density, A : cross section, and E : Young's modulus.

Therefore, we can approximate a hollow cylinder mass (m) with:

$$\omega = k^2 \sqrt{\frac{\left(\frac{E}{2} m R^2\right)}{(mVA)}} \rightarrow \omega = k^2 \sqrt{\frac{\left(\frac{E}{2} R^2\right)}{(VA)}} \quad (7c)$$

By replacing V : Volume of the hollow cylinder, and R : radius of the hollow cylinder.

$$V = \pi R^2 L \quad (8)$$

$$A = 2 R L \quad (9)$$

This can be transformed with (8) and cross area (9) to be

$$\begin{aligned} \omega &= k^2 \sqrt{\left(\frac{\left(\frac{E}{2} R^2\right)}{(\pi R^2 L 2 R L)}\right)} \\ &= k^2 \sqrt{\frac{E}{\pi 4 R L^2}} = k^2 \sqrt{\frac{E}{\pi R}} \sqrt{\frac{1}{4 L^2}} \\ &= \frac{k^2}{2 L} \sqrt{\frac{E}{\pi R}} \end{aligned} \quad (7d)$$

The factors affecting the resonant frequency are stiffness (k), which is constant if we are interested in only the first mode, length of the beam (L), and the square root of the Young's modulus (E).

The relevant value here is the effective Young's modulus of the whole beam, be it made up of varying subelements or one material of uniform elasticity.

Therefore, it seems reasonable that by changing the micro distribution of elasticity, a further mechanism to control bending properties by changing the effective stiffness is introduced. This is in line with the findings in the *T. brevipalpis* type model (Fig. 4.6) and the *An. arabiensis* type model (Fig. 4.7), where the overall resonant frequency can be tuned by addition of small elements – whose elasticity varies from the main beam – along the flagellum. This is not to say that the stiffness of the base articulation does not provide a contribution to resonant tuning. The *C. riparius* type model (Fig. 4.8) in addition showed that the position of those elements along the beam matters as well. This difference observed in FEM for *C. riparius* does align with Laser Doppler Vibrometry (LDV) results, which demonstrate a different mechanical behaviour than in the two mosquito species. Both findings combine to form the hypothesis that microstructure and distribution can be a relevant factor in resonant tuning within the frequency range of those animals' hearing. In simulations a weak bending mode is observed at the frequency of first resonance. Considering that in the case of small angular displacements a very weak bending mode is almost indistinguishable from an actual pendulum mode – as in both the displacement is largest at the tip and relatively uniform along the beam axes in these mode shapes – this lines up well with older experiments, performed on other species (Göpfert et al., 1999). They showed a pendulum mode in *Aedes aegypti* antennae (Göpfert et al., 1999 and Sane et al., 2009). The effect of tapering, in other insects shown to be a relevant factor (Rajabi et al., 2018) is not easy to assess in mosquitoes and midges, given their more complex plumose antenna structure. The fibrillae might also change more than the exposed area of the antenna.

4.9.1 Combining CLSM observations and FEM

Following Johnston's (1855) report of the pedicel's astonishing complex nerve and cuticle structure generations of scientists have investigated various functions of the pedicel. In the present study the focus is on its role in acoustic perception. Acoustics plays a relevant role in the mating behaviour of swarming (Downes, 1969, Belton, 1974, Göpfert et al., 1999, Yack, 2004, Cator et al., 2009, Pennetier et al., 2010) and non-swarming mosquito species (Jackson et al., 2006). For example, in *Anopheles* mosquitoes, which are important vectors of human and animal diseases, acoustic perception is deemed essential (Pennetier et al., 2010, Cator et al., 2010). Also, some other workgroups report findings that demand some cautioning on this (Tripet et al., 2004). Similarly, swarming has been reported for various midges, among others *C. riparius* (Downes, 1969, Neems et al., 1992, Puckett et al., 2015), although the relevance of acoustic perception in those animals is as yet (2019) unknown – related frog-biting midges (Corethrellidae), however, can home in on prey by means of acoustics (Bernal et al., 2006, deSilva et al., 2015). In many of those species, a sexual dimorphism in antennae has been known for a long time (Neems et al., 1992). In this chapter, two mosquito species, one swarming (*An. arabiensis*) and one non-swarming (*T. brevipalpis*), are compared for antennal structure. In both species antennal hearing is thought to play a role in males locating females (Downes, 1969, Belton, 1974, Göpfert et al., 1999, Yack, 2004, Jackson et al., 2006, Cator et al., 2009, Pennetier et al., 2010). This comparison revealed, contrary to expectations, no obvious common features between the species beyond the alteration of stiffness along the flagellum and that the prongs inside each single pedicel are rather uniform. The same is true for the midge *C. riparius*, where the acoustic situation is less clear.

The predominantly soft flagellum of *An. arabiensis* is interspaced with hard rings, while in *T. brevipalpis* the flagellum itself is medium-hard and features cuticle rings with higher and lower stiffnesses in a regular pattern.

That those substructures could have a tuning effect on the entire beam was the reason to conduct FEM simulations. The results indicate that this is true. As predicted, hard elements can increase the resonant frequency, while soft elements decrease it. The tapering of the antenna, which has been shown to be the dominant factor in studies of the static case at least in stick insects (Rajabi et al., 2018), is shown to have at least some influence on our model (Fig. 4.9). It is, however, at present unclear, considering the plumosity of the antenna in the much smaller flies, whether this effect would be of similar magnitude and this presents a potentially fruitful avenue for future research. Presently the focus of investigation is the frequency of the largest mechanical response observed in acoustic perception. To help with that the FEM simulations are concerned with understanding the importance of the banded structure seen in these animals.

While an exhaustive list would include the stiffness of the base articulation, the cell attachments to the scolopidia, prongs and scolopidia themselves, geometry, and viscous effects of the setae, amongst other things, it is to be said that it is very difficult to disentangle all those factors that do or at least can contribute to antennal bending. The situation is made even more complicated by the fact that emergent system properties (e.g. Avitabile et al., 2010) are very well possible and even if one manages to investigate some of the factors singularly, they are likely not giving the complete picture unless viewed as a whole.

The present findings and the findings of Rajabi et. al. (2018), as such make clear that a better understanding of the various aspects of antennal structure – including the antenna heart – is needed to fully understand the antenna. I would like to close the discussion on models, COMSOL or otherwise, by referring to Ouellette (2015).

Depending on intentional use of a model one has to agree with him, questioning: “How much does it matter that a model is completely correct?”. If it already allows for example a technical replication it might or might not be enough for engineering purposes without capturing all the biological facts – yet caution has to be applied as simpler models might not be as robust if exposed to complex natural situations (Ouellette, 2015).

This means in our context, that there are at least two possible outcomes: Does the model a) capture how the mechanics could happen and therefore allows technical replication, or b) does it actually capture and therefore explain the process leading to the observed behaviour? There is a semantically sounding, but highly relevant difference to both of these outcomes in terms of explanatory power of the model, which in case a) could be zero, or at least close to zero. It will require further, more in-depth studies of those structures, to make a sound judgement of how well the simulations fit the experimental situation – it has been demonstrated, however, that in *T. brevipalpis*, the resonant peak of experiment and simulation fall into a similar range. Whatever the reason for varying the material stiffness along the flagellum, (static, frequency tuning or aiding one of the other sensory modalities of the antenna), it remains true that adding hard or soft elements does shift the resonant frequency, be it for good or ill or a trade-off in between.

5 Results of 3D Laser Doppler Vibrometry investigation of antenna self-oscillation

The following chapter aims to characterise the observed three-dimensional antenna movement for each of the species investigated. In general, the view on the data – not the data themselves – will be rotated. One might argue for data rotation by pointing out that if directions align with the coordinate system, the data are easier to read. However, after a trial data rotation, the fact that views and axes are attached to the experimental setup is considered more intuitive and useful. Trial data rotation, by Z ($\pi/4$) and Y (ca. $3\pi/10$) to align antenna axis with the system's Z axis, satisfyingly demonstrated that rotated data are the same movement pattern, albeit in differently named planes than when unrotated views are used. By use of an unrotated coordinate system, the movement orientation is kept the same as experienced by the animals.

5.1 Antenna self-oscillation frequency

Focusing on the frequency domain for the moment, the self-oscillation of the male antenna of *Toxorhynchites brevipalpis* and *Anopheles arabiensis* can be described as follows: In *An. arabiensis* males, a clear common peak around $372 \pm 15\text{Hz}$ (see section 5.4.1) is evident, whilst in *T. brevipalpis* multiple sharp peaks exist, but no clear species-specific convergence frequency could be shown. The median frequency, however, is $422 \pm 35\text{Hz}$ (see section 5.2.1.). The female antenna shows a maximum movement at $236 \pm 27\text{Hz}$ in *T. brevipalpis*, thus at a much lower amplitude (see section 5.3). Furthermore, it is noteworthy that while statistically insignificant, the average peak in *An. arabiensis* has slightly different frequencies in

the X, Y, and Z directions, a trend also seen in the individual peaks of both species. Finally, self-oscillation was also found to be present in *Anopheles gambiae* $379 \pm 25\text{Hz}$ (see section 5.5). The presence of different oscillation frequencies in the three directions, which was observed, could indicate a slightly varying stiffness of the system. This variation in turn could be theorized to support out-of-plane movement of the flagellum.

5.2 Self-oscillation of the *Toxorhynchites brevipalpis* male

5.2.1 Fourier domain data analysis of the *Toxorhynchites brevipalpis* male

For the present consideration, the norm of the X, Y, Z displacement is used as a measure for the overall displacement; in later stages the actual 3D pattern will be shown and more closely examined.

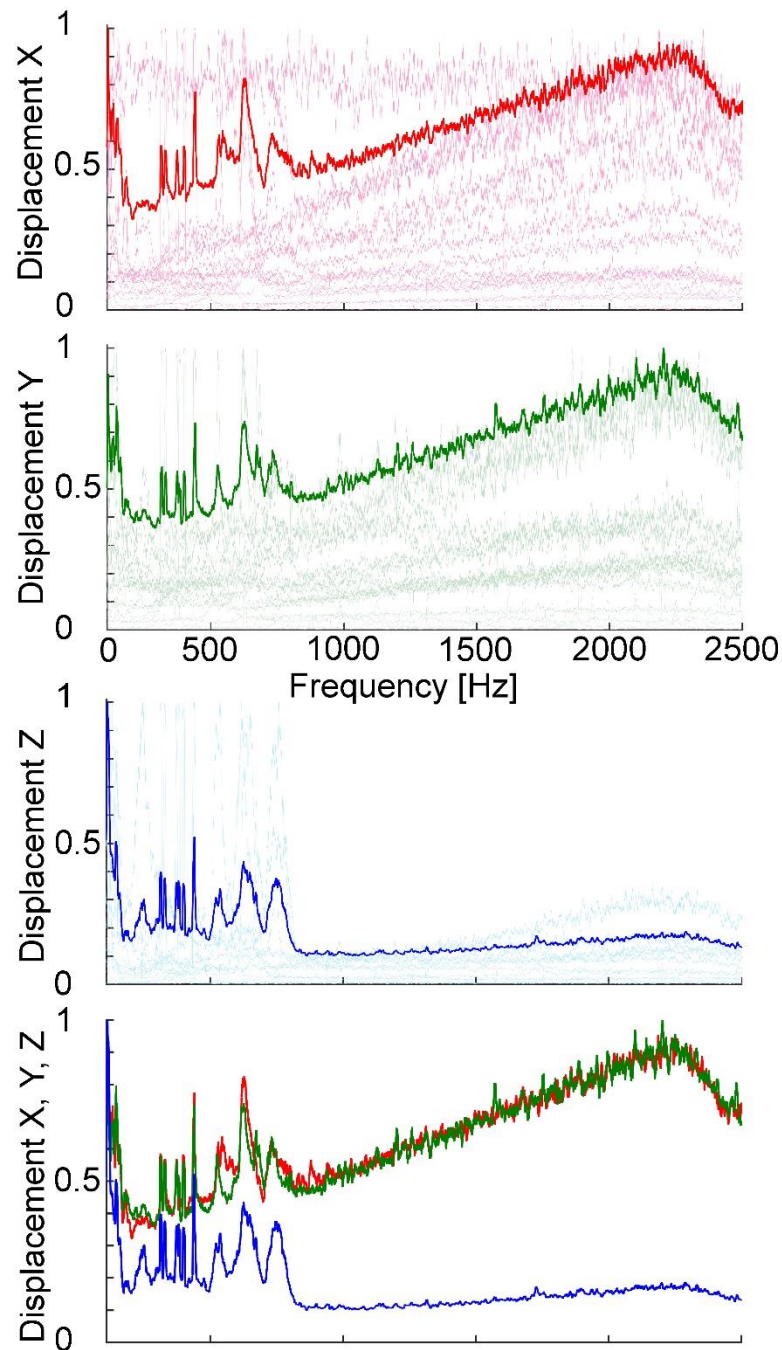


Fig. 5.1: Average frequency overview of self-oscillation in *T. brevivalpis* males – the figure illustrates that while each animal shows a sharp peak, the bandwidth of frequencies in this species is higher than seen in *An. arabiensis* (Fig 5.14) and they are not converging towards one central frequency. a) X direction, red, b) Y direction, green, c) Z direction, blue, d) averages only X (red), Y (green) and Z (blue) direction. All data are smoothed (24 running average) and normalised to their specific maximum to allow viewing all individuals in one image per direction. Dark bold line: species average; thin lines: individuals.

In the case of *T. brevipalpis*, high Q-factors can be reported for all three directions and are given alongside norm displacement and average peak frequency in the below Table 5.1 – for an overview see also Fig 5.1.

Table 5.1: This table shows the mean and median plus-minus one standard deviation for *T. brevipalpis* males. From left to right: Average frequency, directional Q-factor and norm displacement.

<i>Toxorhynchites brevipalpis</i>	Frequency [Hz]	Quality factor by direction			Norm Displacement [nm]
		X	Y	Z	
Male N=16					
Mean	477 ± 33	477 ± 90	539 ± 93	546 ± 84	183 ± 75
Median	422 ± 35	359 ± 94	413 ± 98	459 ± 87	4 ± 87

5.2.1.1 Note: Is age a factor in the self-oscillation frequency?

Fig. 5.2 shows the older age group in red, the younger in blue. While in tendency the red group has higher frequencies, the range of frequencies in the *T. brevipalpis* male overlaps so much that no age effects can be reported either on frequency or peak shape.

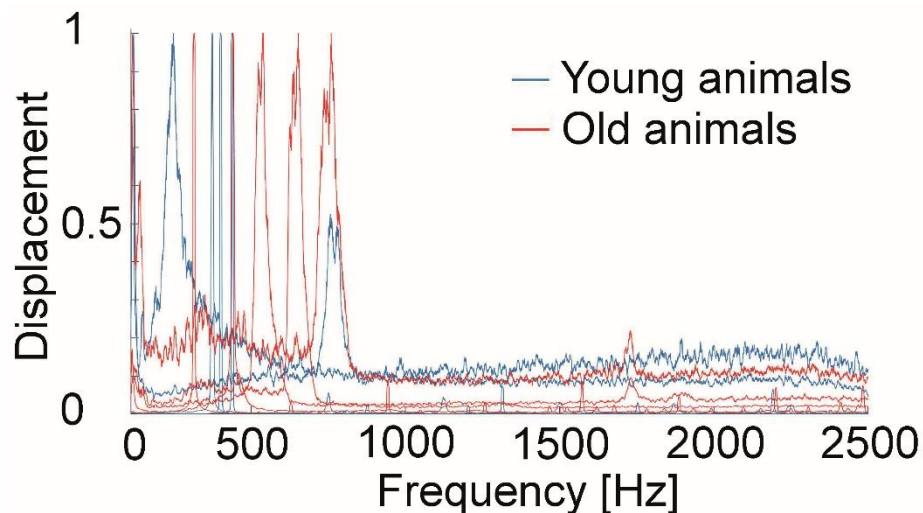


Fig. 5.2: Age difference in *T. brevipalpis* male. The figure indicates strongly overlapping frequency ranges between animals younger (N=5, blue) and older (N=5, red) than eight days. Data are normalised to their respective maximum after conversion to displacement in Fourier domain a) X direction, b) Y direction, c) Z direction.

For all directions the qualitative statement supported by Fig. 5.2 was backed up with a statistical test. The strongly overlapping standard deviation of about $\pm 170\text{Hz}$, while both median and mean between the old and the young are only about 120Hz apart, already indicates that there will be no statistical difference.

The full descriptive statistic for the young age group is as follows: $X=438\pm 81\text{Hz}$ ($401\pm 84\text{Hz}$), $Y=463\pm 89\text{Hz}$ ($439\pm 90\text{Hz}$), $Z=443\pm 85\text{Hz}$ ($401\pm 88\text{Hz}$).

Respectively, for the old age group the statistic is: $X=528\pm 72\text{Hz}$ ($531\pm 73\text{Hz}$), $Y=527\pm 72\text{Hz}$ ($527\pm 72\text{Hz}$), $Z=541\pm 78\text{Hz}$ ($539\pm 78\text{Hz}$). In both cases data are given as mean \pm standard error (median \pm standard error of the median). These two sets of descriptive statistics already indicate what a t-test for each direction confirmed, data in brackets: X (0.4328), Y (0.5894), Z (0.4188), $df=8$, $\alpha=0.05$. That means there is no apparent difference between the age groups in any direction.

5.2.2 Power spectrograms of self-oscillation in the *Toxorhynchites brevipalpis* male

In contrast to Fourier-domain data, spectrograms provide the opportunity to look at the instantaneous frequency behaviour, allowing to classify three different types of self-oscillation behaviour beyond the numerical values. Antenna self-oscillation in male *T. brevipalpis* can either be a single-frequency movement (Fig. 5.3), movement in two unrelated frequencies (Fig 5.4), or in one frequency with its harmonics (Fig 5.5). In the latter case the second, not the first harmonic is the strongest harmonic.

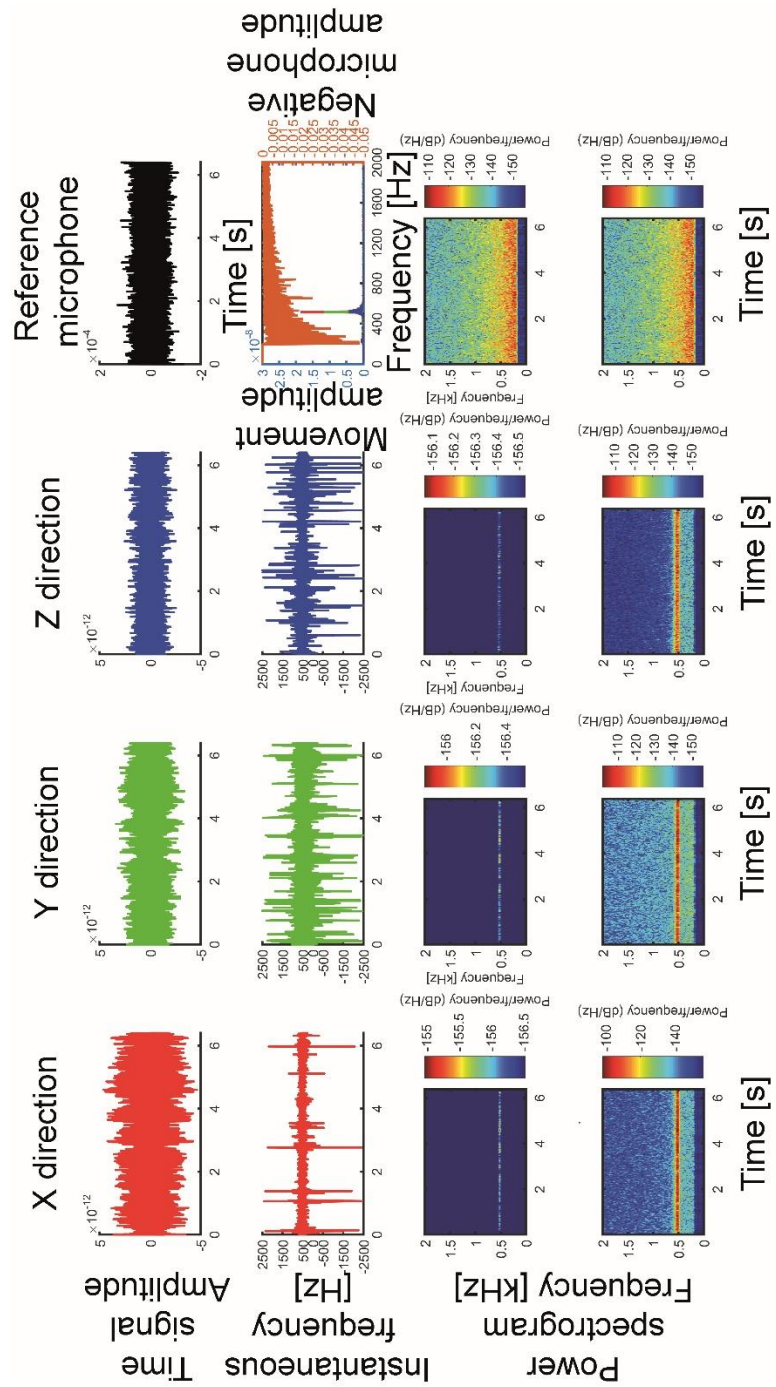


Fig. 5.3: Example of the antenna in a male *T. brevipalpis* self-oscillating in one more or less stable frequency, seen in N=6 (datasets of animals labelled 11, 12, 21, 26, 33, as all *T. brevipalpis* males are numbered continuously). Row one: Time-signal from left to right, X, Y, and Z direction vs. time, followed by reference. Row two: Instantaneous frequency. From left to right, X, Y, and Z direction vs. time, fourth column Fourier-domain signal of the whole time window. Row three: spectrograms of left to right, X, Y, and Z direction vs. time followed by a spectrogram reference microphone. Row four: spectrograms of, from left to right, X, Y, and Z direction vs. time multiplied to improve contrast, followed by reference.

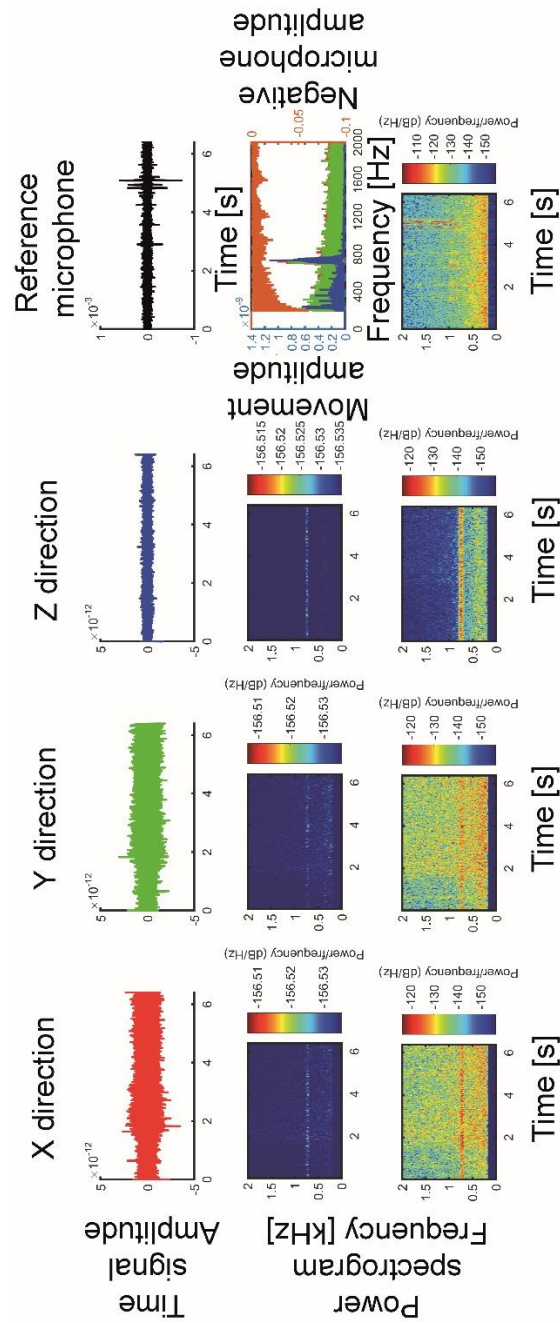


Fig. 5.4: Example of the antenna in a male *T. brevipalpis* self-oscillating featuring two independent frequencies being strongly seen in N=3 (animals labelled 24, 30, and 34) and weakly in N=3 (animals labelled 16, 20, and 31).

Row one: Time-signal from left to right X, Y, and Z direction vs. time, followed by reference. Row two: spectrograms of, from left to right, X, Y, and Z direction vs. time, fourth column Fourier-domain signal of the whole time window. Row three: spectrograms of from left to right, X, Y, and Z direction vs. time multiplied to improve contrast, followed by reference microphone.

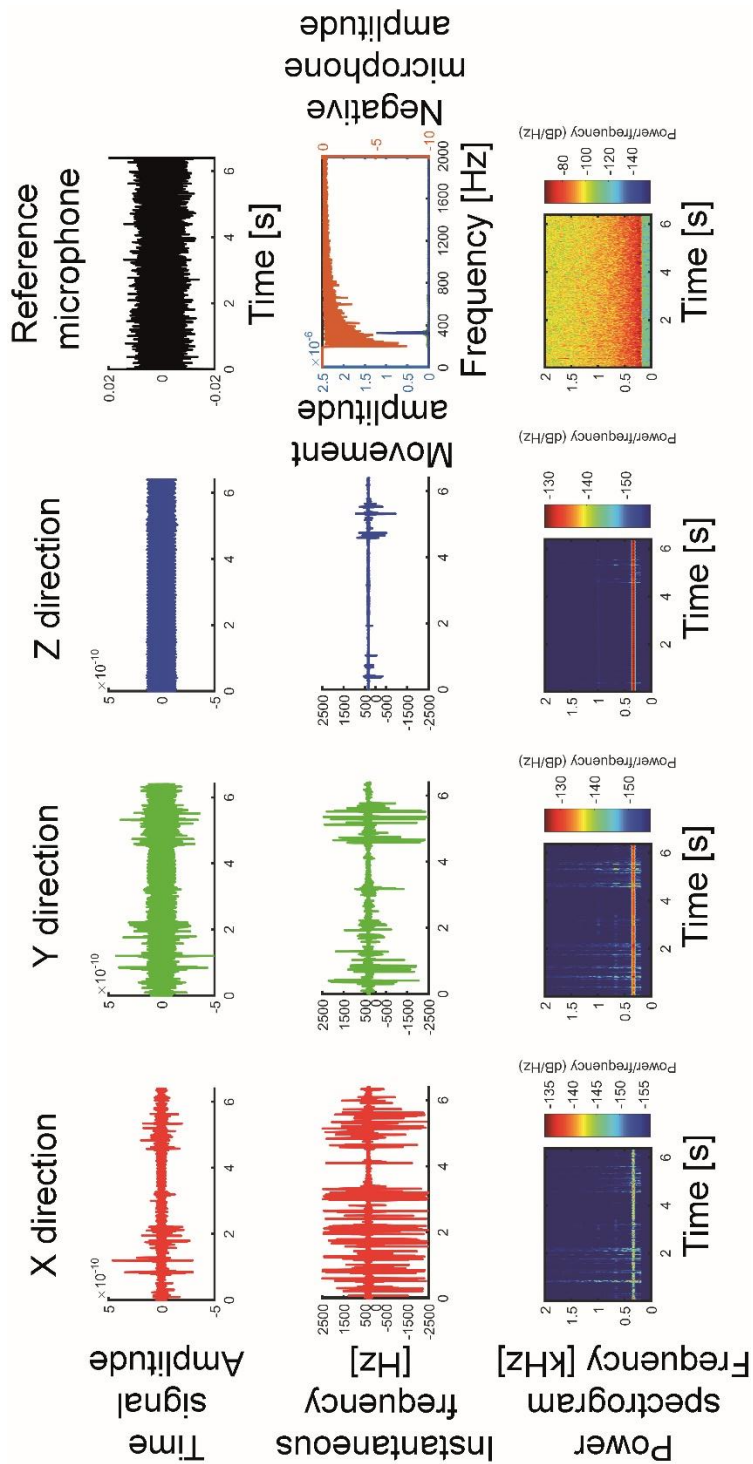


Fig. 5.5: Example of the antenna in a male *T. brevipalpis* self-oscillating in one stable frequency and its harmonics up to at least the 3rd harmonic seen in N=4 (animals labelled 06, 08, 10, and 15). Row one: Time-signal of the X, Y, and Z direction vs. time, followed by reference microphone. Row two: Instantaneous frequency, from left to right, X, Y, and Z direction vs. time, fourth column Fourier-domain signal of the whole time window. Row three: spectrograms of X, Y, and Z direction vs. time followed by reference microphone.

Of the shown types Fig. 5.3-5.5 type Fig. 5.5, which features the harmonics, is stronger than the other types by three orders of magnitude. It is likely that the clear presence of harmonics is due to the much more vigorous antenna movement.

5.2.3 3D-patterns of self-oscillation in the *Toxorhynchites brevipalpis* male

While, as we have seen in 5.2.2, it is possible to distinguish variant types of antenna self-oscillation based on power spectrograms, all self-oscillations are more or less distorted ellipsoid traces in 3D-space. The degree of distortion depends on the amount of contribution to the overall energy by the harmonics and noise.

As can be verified in figure Fig. 5.6, it also depends on the viewed plane whether the trace appears to be crossing itself as a figure of eight. This could be the result of the harmonic carrying the same or more energy than the base frequency – which is not the case in any of the observed self-oscillation. Alternatively, the apparent figure of eight might be a projection of a spatially twisted 3D-motion upon a viewing plane and is actually an ellipsoid (see Fig. 5.7.).

The ellipsoid shown in Fig. 5.7 b & c is most prominently visible with strong self-oscillation but was observed even with picometre self-oscillations. This holds also true for the one other species of mosquitoes investigated in the same manner, *An. arabiensis* (5.4.2). The point of Fig. 5.6 is to illustrate that, while from a spectral point of view the self-oscillation appears to be constant, it can, when viewed in space, shift its primary plane of motion in consecutive time intervals shown in orange, black and blue in Fig. 5.7.

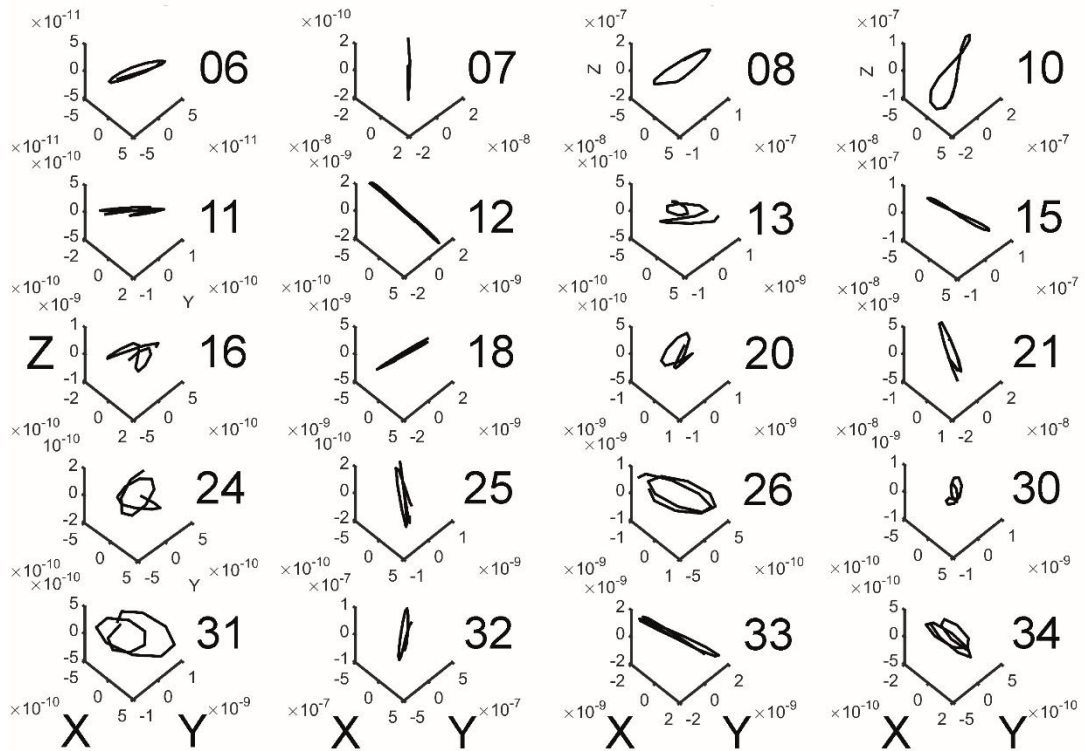


Fig. 5.6: Overview of potential 3D-movement patterns observed in individual recordings of *T. brevipalpis* males. Ranging from linear, e.g. animal labelled 07 (row five, second image) to circular, e.g. animal 08 (row one, third image) or animal 26 (row four, third image), spanning variations of figures of eight, e.g. animal 10 (row one, fourth image) or animal 15 (row five, first image) and rather arbitrary-looking time traces e.g. animal 13 (row five, third image). The main purpose of this image is to illustrate the wide variety of potential movements between individuals. In fact, most of the patterns can be seen in each individual, and even each recording at different points in time.

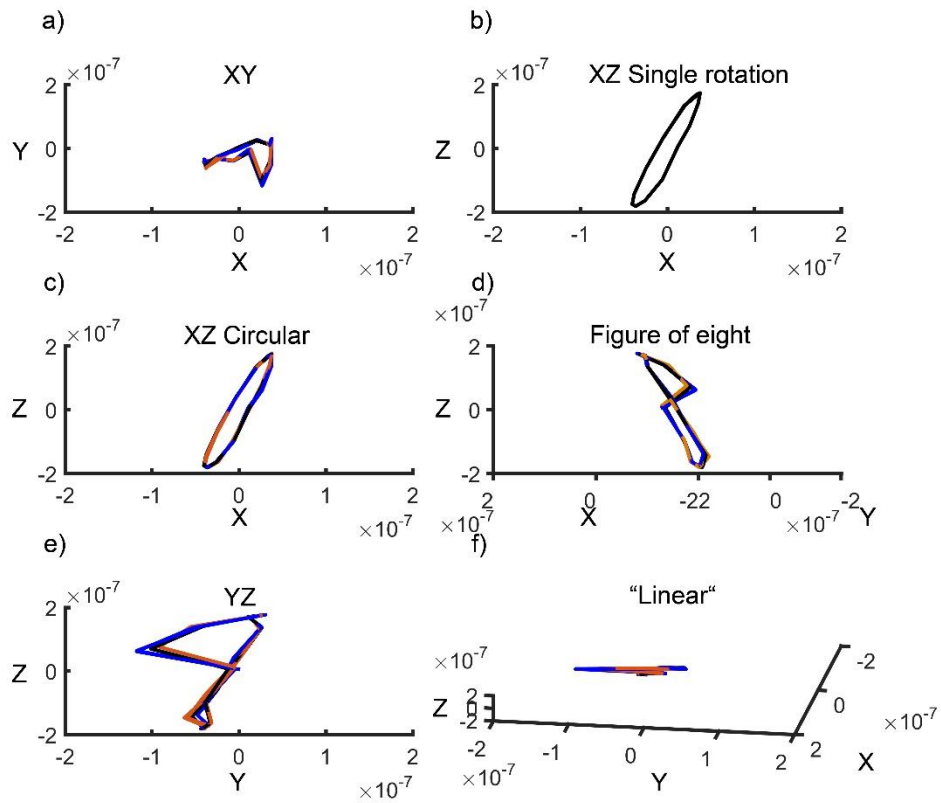


Fig. 5.7: This figure shows the self-oscillation of one *T. brevipalpis* male, labelled animal 08, in multiple viewing planes. a) The top-down view of the Z plane. b) & c) The Y plane, through which the antenna is projecting outwards from the animal. d) An arbitrary viewing plane. e) The X plane and f) again an arbitrary viewing plane. In all except b), which only shows one rotation of the antenna, the colour-code is as follows: Blue is the last movement cycle, black the current movement cycle and orange the temporally next movement cycle. Note that the identical movement of the same animal can appear as linear (f), ellipsoid (b) & c)), or resemble a false figure of eight (d)). By illuminating in part temporal dynamics as three subsequent movement cycles are shown, it becomes clear that the plane of motion can shift ever so slightly from one interval to the next, over time allowing more pronounced nutations of the movement plane.

5.2.4 Male antennal reception of a directly presented female in *Toxorhynchites brevipalpis*

Fig. 5.8-10 below illustrates the time dynamic of a male *T. brevipalpis* antenna vibration in response to the female wingbeat frequency. Most important is that in general the wingbeat recordings include energy in the harmonics and subharmonics. Also, it is shown that the antenna's signal-to-noise ratio is higher than that of the microphone – judging by the larger deep-blue areas in the spectrograms of the antenna compared to the microphone spectrogram. The scale here goes from high sound intensity at a given frequency shown in red to the lowest intensity in deep blue. The left-most plot shows the Fourier domain data of the displacement in the X, Y, and Z directions and on a second top-down orientated Y axis the sound volume recorded by a reference microphone. Here it is notable that the antenna responds strongly to frequencies over 800Hz (e.g. the band in which the female recordings appear to contain the most energy). However, opposed to the microphone, a second strong peak is evident in the male antenna at half of the highest energy band of the wingbeat, coinciding with the frequency range of the regularly observed self-oscillation frequency range (Fig. 5.8-10 – row 1 of the spectrograms).

In most of these spectrograms, a lower and less clearly defined, comparatively high-energy frequency band can be observed. In the case of female 2 (Fig. 5.9), there is even a third peak closely below the subharmonic. This cursory experiment (N=3 females presented to one male) should, however, be read with caution.

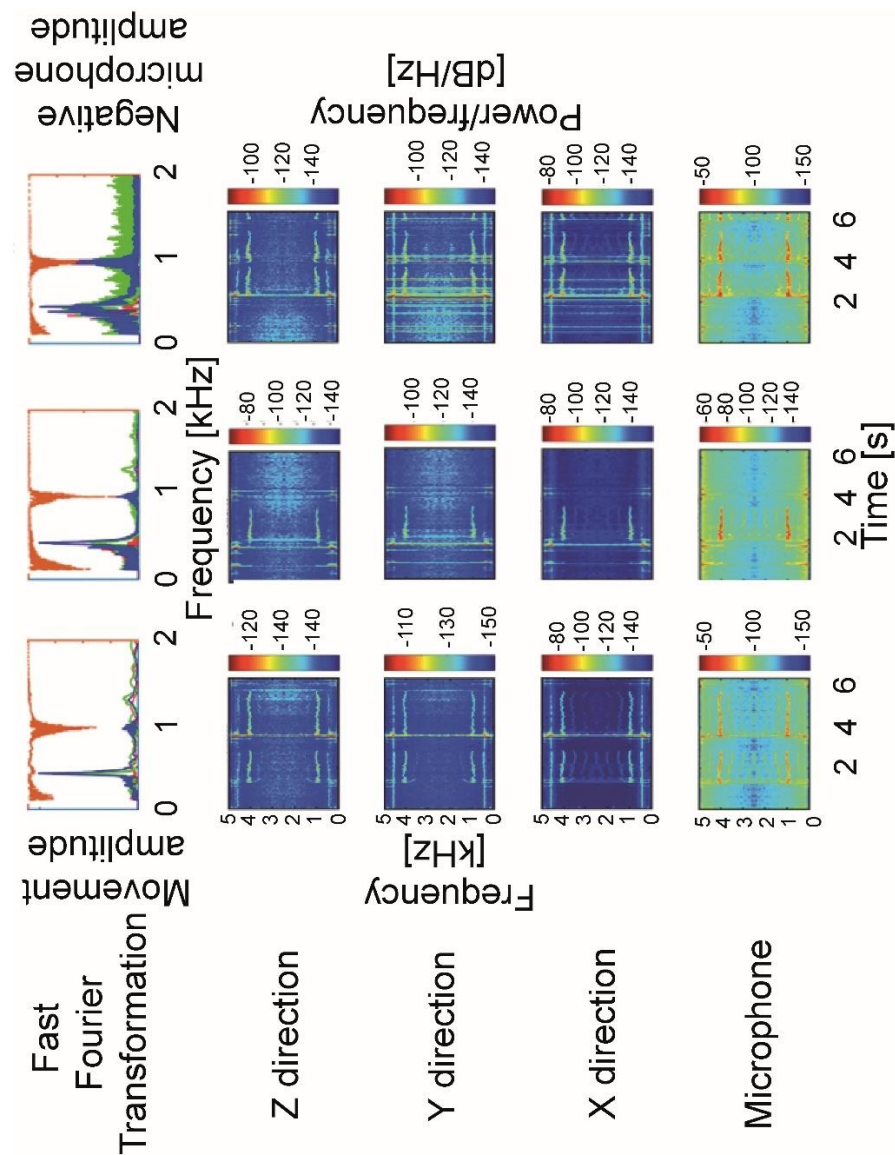


Fig. 5.8: Shows a male *T. brevipalpis* in response to three recordings of one *T. brevipalpis* female, labelled animal 1. In each triplet the first row is the is the Fourier domain representation of the data of the directions X (red), Y (green), Z (blue), and the reference plotted in orange upside down on the same scale, indicating that while in the microphone 977.5Hz contains the highest energy, the antenna responds strongly to the subharmonics.

The following three rows are, from top down, the X, Y, and Z direction spectrograms of the three LDV recordings of the male antenna. The fifth row is the spectrogram of the reference microphone directly recording the female wingbeat.

The spectrogram reveals the relative energy content per frequency, thereby showing even more harmonics in shape and position identical to the microphone recording. Note that the subharmonics almost coincide with the shown self-oscillation (row 1) and that the antennae and LDV have a higher signal-to-noise ratio than the reference microphone.

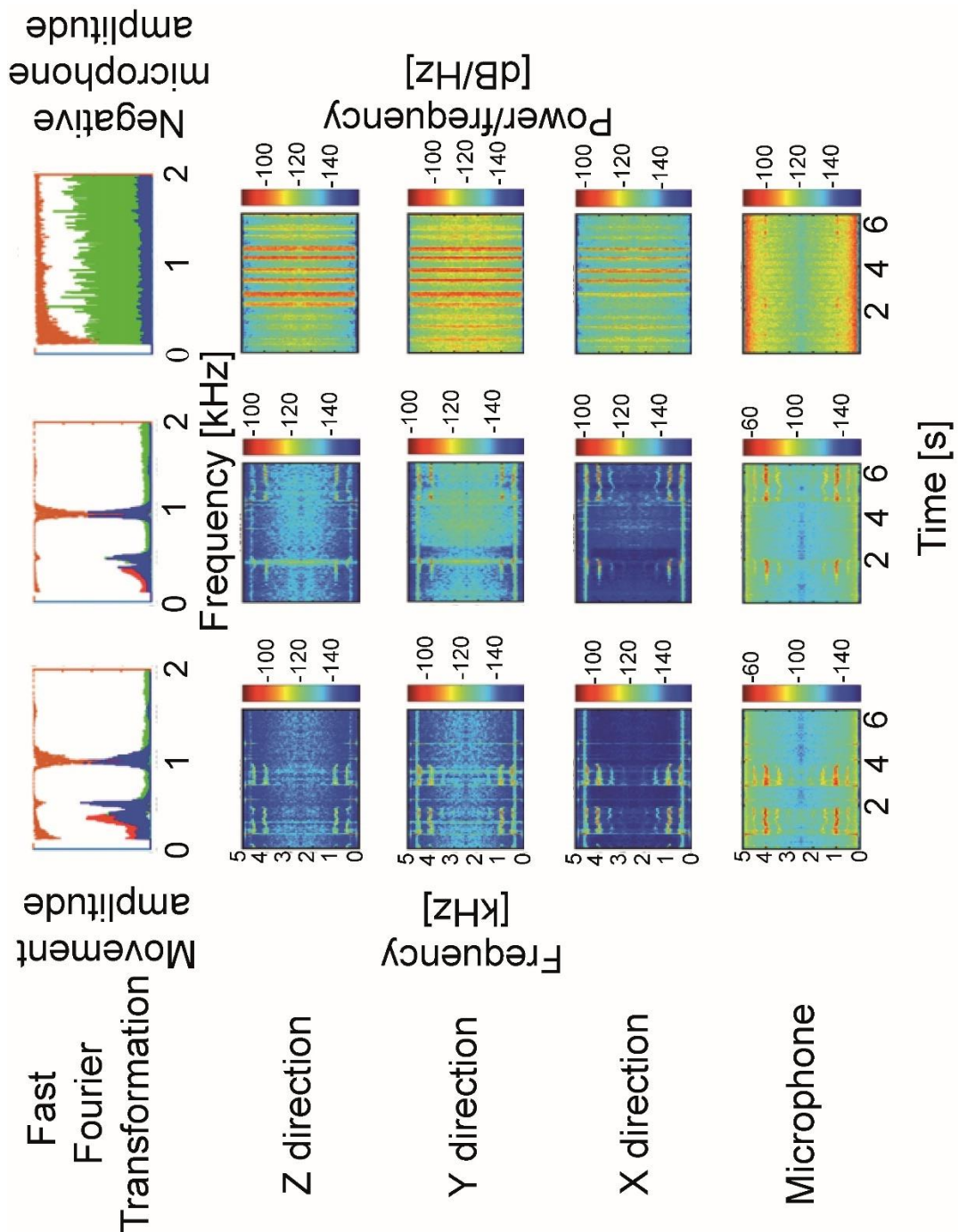


Fig. 5.9: Shows a male *T. brevipalpis* in response to three recordings of one *T. brevipalpis* female, labelled animal 2. Data shown as in Fig 5.8. Wingbeat according to microphone has the highest energy in 977.0Hz. Note that the subharmonics almost coincide with the shown self-oscillation (row 1) and that the antennae and LDV have a higher signal-to-noise ratio than the reference microphone. Here recording 3 did not work out well in the reference spectrogram (column 3) the main frequency is nonetheless present and similar to recording 1&2.

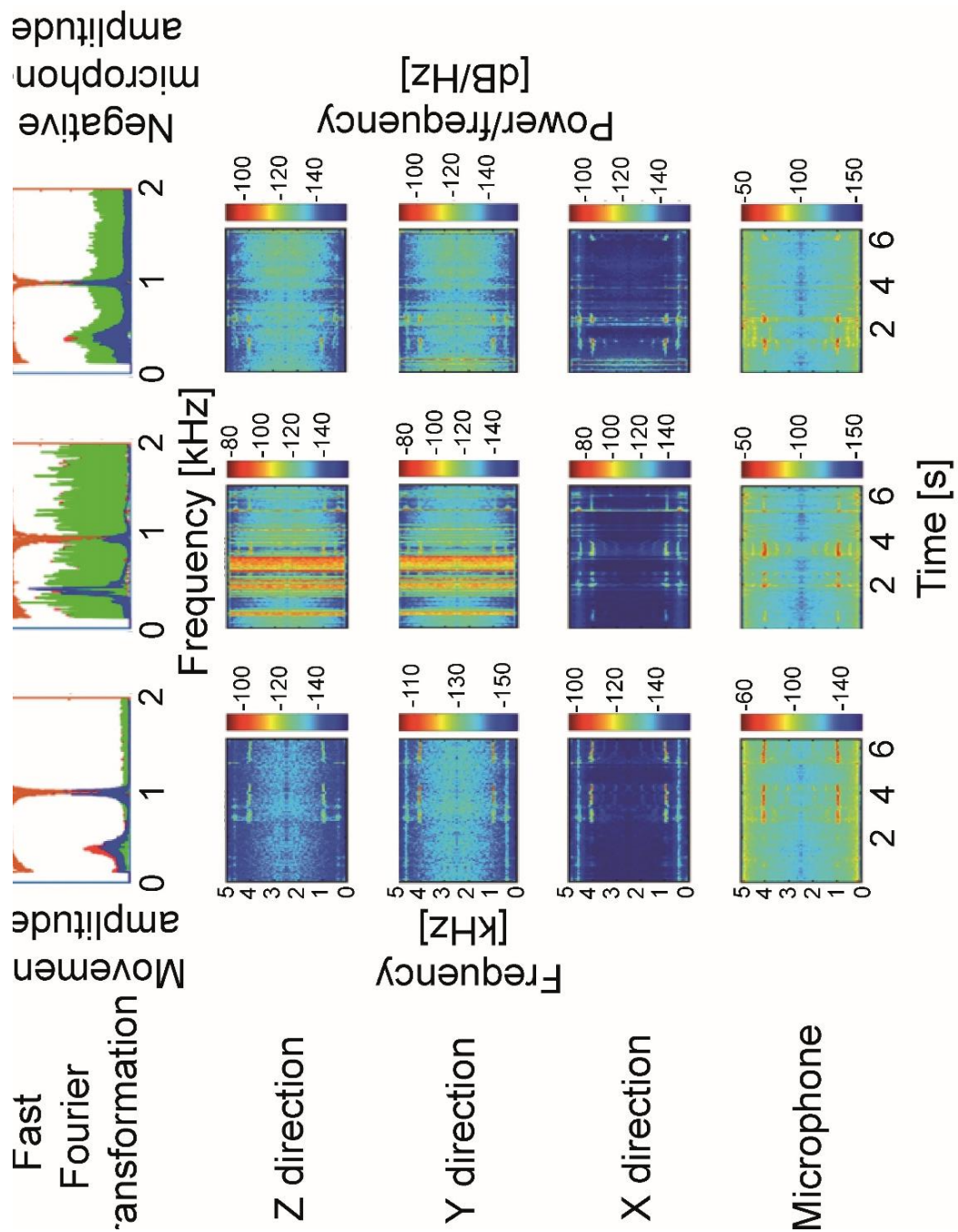


Fig. 5.10: Shows a male *T. brevipalpis* in response to three recordings of one female *T. brevipalpis* labelled animal 3. Data shown as in Fig 5.8. Wingbeat according to microphone has the highest energy in 984.6Hz. Note that the subharmonics almost coincide with the shown self-oscillation (row 1) and that the antennae and LDV have a higher signal-to-noise ratio than the reference microphone.

5.3 Self-oscillation in *Toxorhynchites brevivalpis* female

While only a side note to the overall arc of investigation, less sharp and intense self-oscillation has been recorded from female *T. brevivalpis* (N=5) around 250Hz, see

Table 5.2 below.

Table 5.2: This table shows the mean and median \pm one standard deviation for *T. brevivalpis* females. From left to right: Average frequency, directional Q-factor and norm displacement.

<i>Toxorhynchites brevivalpis</i>	Frequency [Hz]	Quality factor by direction			Norm Displacement [pm]
		X	Y	Z	
Female N=5					
Mean	256 \pm 26	2.4 \pm 0.5	1.9 \pm 0.4	2.1 \pm 0.5	350 \pm 46
Median	236 \pm 28	2.1 \pm 0.5	1.9 \pm 0.40	1.6 \pm 0.6	384 \pm 49

5.3.1 Wingbeat frequency recordings

As the focus of interest was the vibrational characteristics of these insects' antennae and the male antenna is presumably tuned towards the detection of the female wingbeat, the properties of the stimulus were briefly examined. As the recordings were cursory and the exact distance to the microphone unknown, the magnitude of the wingbeat sound is not taken into account just the frequency.

While the N=3 is small, the frequency component containing the most energy in our recordings (see also Figures 5.11-13) was on average to found to be 979.7Hz with a remarkably low standard deviation of 2.99Hz. Interestingly, with all recordings harmonics and subharmonics are present.

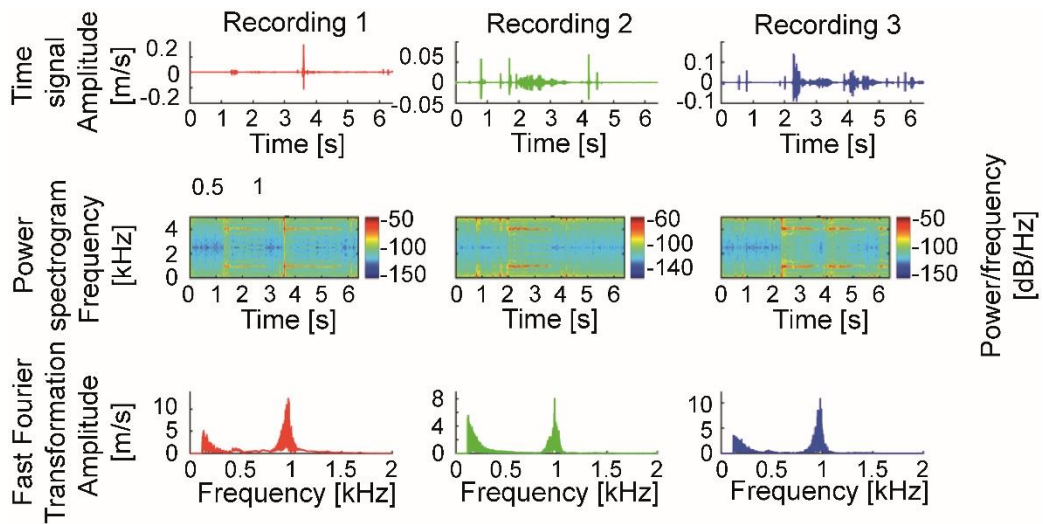


Fig 5.11: This figure shows three recordings of the female *T. brevipalpis* labelled animal 1 as time trace (row 1), instantaneous frequency (row 2), spectrogram (row 3) and frequency domain (row 4). Row 1 and 2 in correlation show the temporal sequence of the flight tone. Row 3 indicates the energy content of the wingbeat burst indicating harmonics and subharmonics. Row 4 shows the frequency domain spectra. Note that the subharmonic appears close to the resonant frequency of the male antenna.

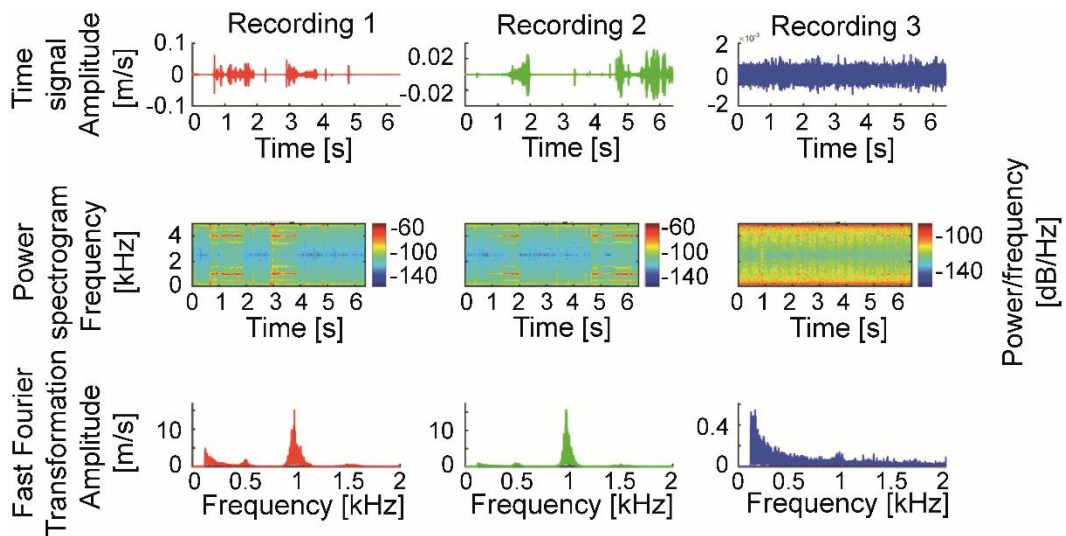


Fig 5.12: This figure shows three recordings of the female *T. brevipalpis* labelled animal 2. Data shown as in Fig. 5.11.

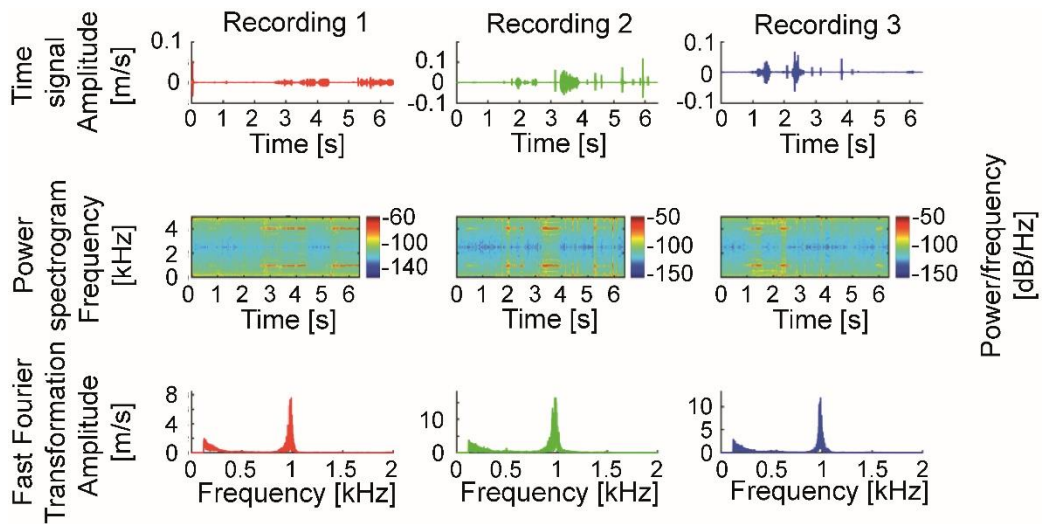


Fig 5.13: This figure shows three recordings of the female *T. brevipalpis* labelled animal 3. Data shown as in Fig. 5.11.

5.4 *Anopheles arabiensis* male

5.4.1 Fourier domain data analysis of *Anopheles arabiensis* male

In the case of *Anopheles arabiensis*, as with *Anopheles gambiae* (5.6), the supply of specimens was limited and clear, noise-free recordings difficult to obtain. For this reason, in order to at least get a benchmark for this species as well, recordings were performed with the “magnitude averaging” setting over three consecutive recordings. While this allows to get an accurate idea of the frequency of self-oscillation in this species, displacements will likely be underestimated and Q-factors are less reliable than in *T. brevipalpis* and likely overestimated. This being said, the values are still robust enough in this species to state tendencies (see Table 5.3) and are orders of magnitude larger than 1 in all three directions. In the below Table 5.3 it is given for all three directions individually alongside norm displacement and average peak frequency.

This can be seen by comparing the five recordings done without averaging (Table 5.4) with the recordings with averaging (Table 5.3). The values shown in Table 5.4, while more varied, show a similar order of magnitude as in those in Table 5.3.

As with *T. brevipalpis*, in the present consideration the norm of the X, Y, and Z displacement is used as a measure for the overall displacement, in later stages the actual 3D-pattern will be shown and more closely looked at.

Table 5.3: This table shows the mean and median \pm one standard deviation for *An. arabiensis* males, from left to right: Average frequency, directional Q-factor and norm displacement.

<i>Anopheles arabiensis</i>	Frequency [Hz]	Quality factor by direction			Norm Displacement [nm]
		X	Y	Z	
Male N=10					
Mean	367 \pm 15	191 \pm 42	171 \pm 46	184 \pm 34	126 \pm 6
Median	372 \pm 15	154 \pm 42	110 \pm 48	198 \pm 32	21 \pm 7

Table 5.4: This table shows the mean and median \pm one standard deviation for *An. arabiensis* males, from left to right: Average frequency, directional Q-factor and norm displacement. The Median error is due to high variation and limited number of non-averaged measurements not trustworthy.

<i>Anopheles arabiensis</i>	Frequency [Hz]	Quality factor			Norm Displacement [nm]
		X-direction	Y-direction	Z-direction	
Male N=5					
Mean	362 \pm 26	108 \pm 23	97 \pm 25	95 \pm 12	88 \pm 53
Median	366 \pm 26	77 \pm 28	109 \pm 26	100 \pm 12	24 \pm 62

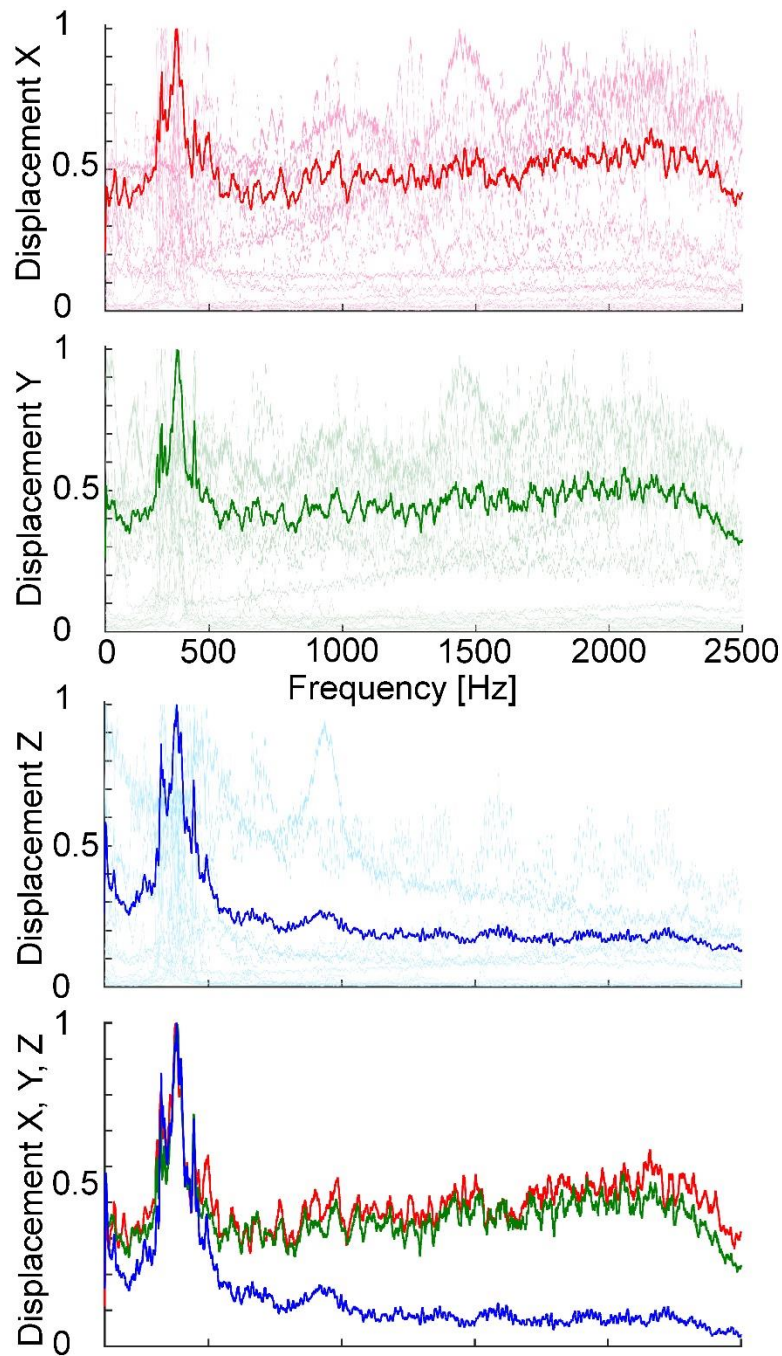


Fig. 5.14: Average frequency overview of self-oscillation in *An. arabiensis* male. The figure illustrates that while each animal shows a sharp peak, the bandwidth of frequencies in the species is higher. a) X direction, red, b) Y direction, green, c) Z direction, blue d) averages only X (red), Y (green) and Z (blue) direction. All data are smoothed (24-point running average) and normalised to their specific maximum – to allow viewing all individuals in one image per direction. Dark bold line: species average in contrast to individual overview *T. brevipalpis* male (Fig. 5.1), the species clearly converges to a central frequency; thin lines: individual data.

5.4.2 3D patterns in *Anopheles arabiensis* males

The 3D-patterns shown here parallel the ones observed in *T. brevipalpis* (5.2.3). Fig. 5.15 shows the apparent elliptical spatial trace in time of self-oscillation in the antenna of *An. arabiensis* males. After establishing the general shape, now to the matter of the motion shifting in the plane of movement over time illustrated in Fig 5.16. As with the other mosquito species, with strong self-oscillation the ellipsoid is more clearly defined but is present in all non-averaged movement recordings of *An. arabiensis* males.

5.4.3. Pulsing of the self-oscillation in *Anopheles arabiensis* males

Power spectrograms of the self-oscillation in multiple individuals (N=3) indicated that in contrast to *T. brevipalpis*, the oscillation might not be constant in *An. arabiensis*, see Fig 5.16. This clearly could also be a by-product of a plane shift (which is in fact happening in some individuals, see Fig. 5.17). The time-traces of the individuals in question were examined to reveal a mixed result. In one of the individuals, as movement in one direction decreases, it is compensated in the other direction, suggesting the plane shift explanation. In the other two, however, while minor phase differences persist, the maxima and minima of the enveloping beating frequency align, indicating the presence of a modulation mechanism.

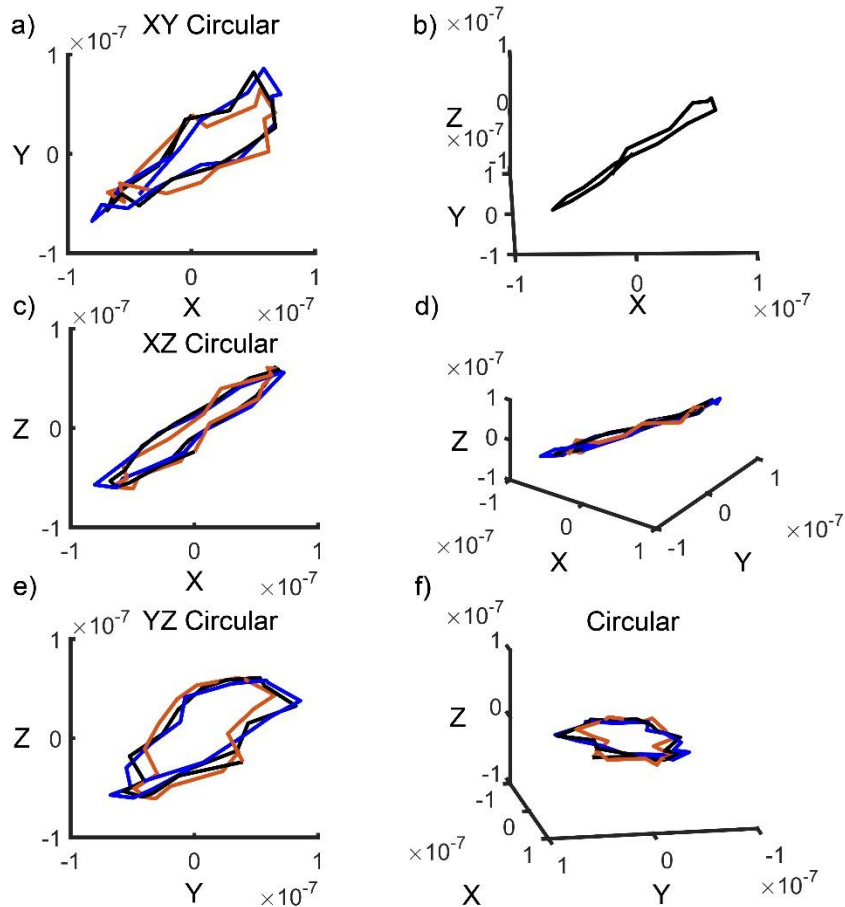


Fig. 5.15: This figure shows the self-oscillation of *An. arabiensis* 26 in multiple viewing planes. a) Top-down view of the Z plane, b) arbitrary viewing plane appearing as figure of eight, c) the Y plane, through which the antenna is projecting outwards from the animal, d) an arbitrary viewing plane, appearing linear, e) the X plane and f) again an arbitrary viewing plane, appearing circular. In all except b), which only shows one rotation of the antenna, the colour-code is as follows: Blue is the last movement cycle, black the current movement cycle, and orange the temporally next movement cycle. Note that the identical movement of the same animal can appear as linear (d), elliptical (a, c, e) or resemble a figure of eight (b)).

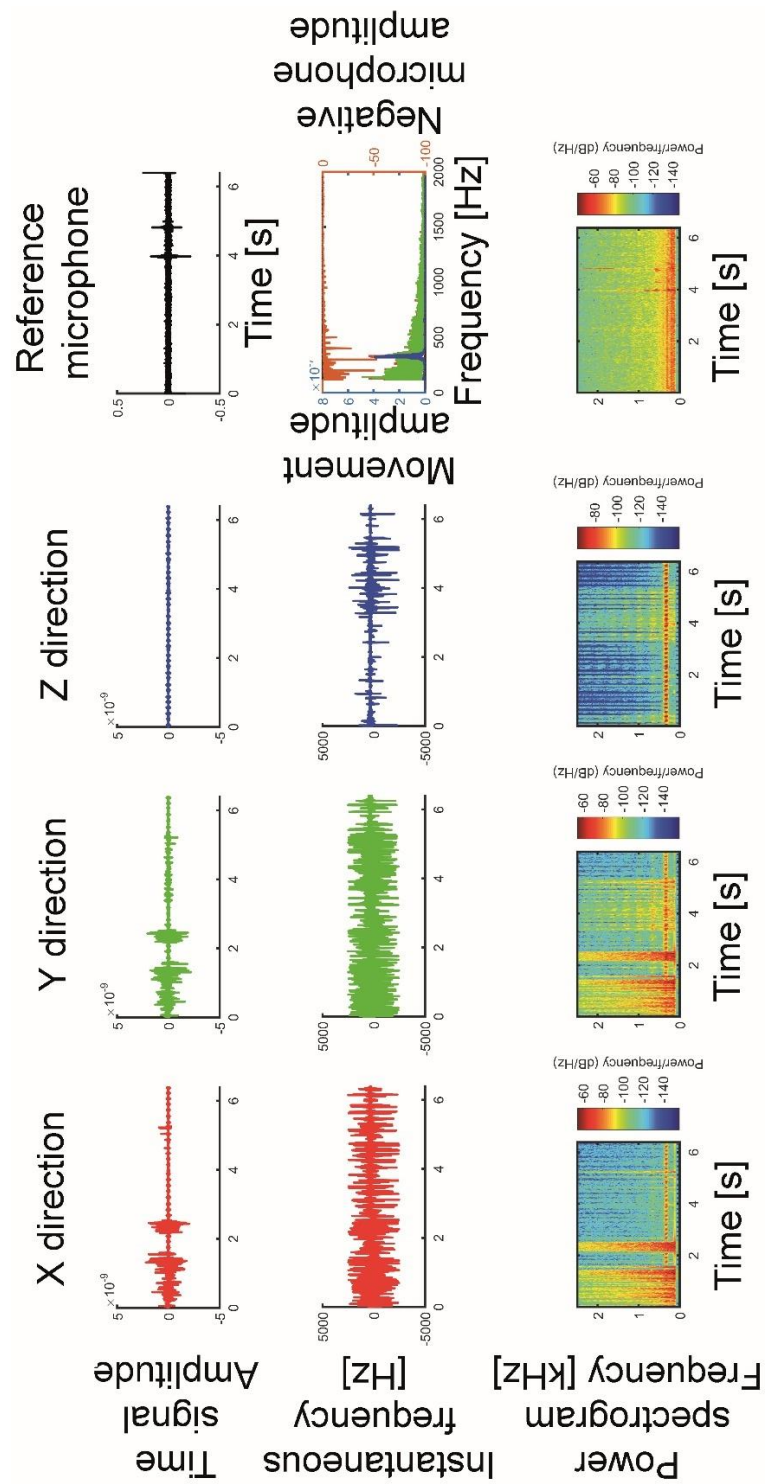


Fig. 5.16: This figure shows an example of the antenna in a male *An. arabiensis* self-oscillating featuring non constant oscillation (N=3). Row one: Time-signal, left to right, X, Y, and Z direction, followed by reference. Row two: instantaneous frequency of, left to right, X, Y, and Z direction, fourth column Fourier-domain signal of the whole time window. Row three: spectrograms of, left to right, X, Y, and Z direction vs. time multiplied to improve contrast, followed by reference.

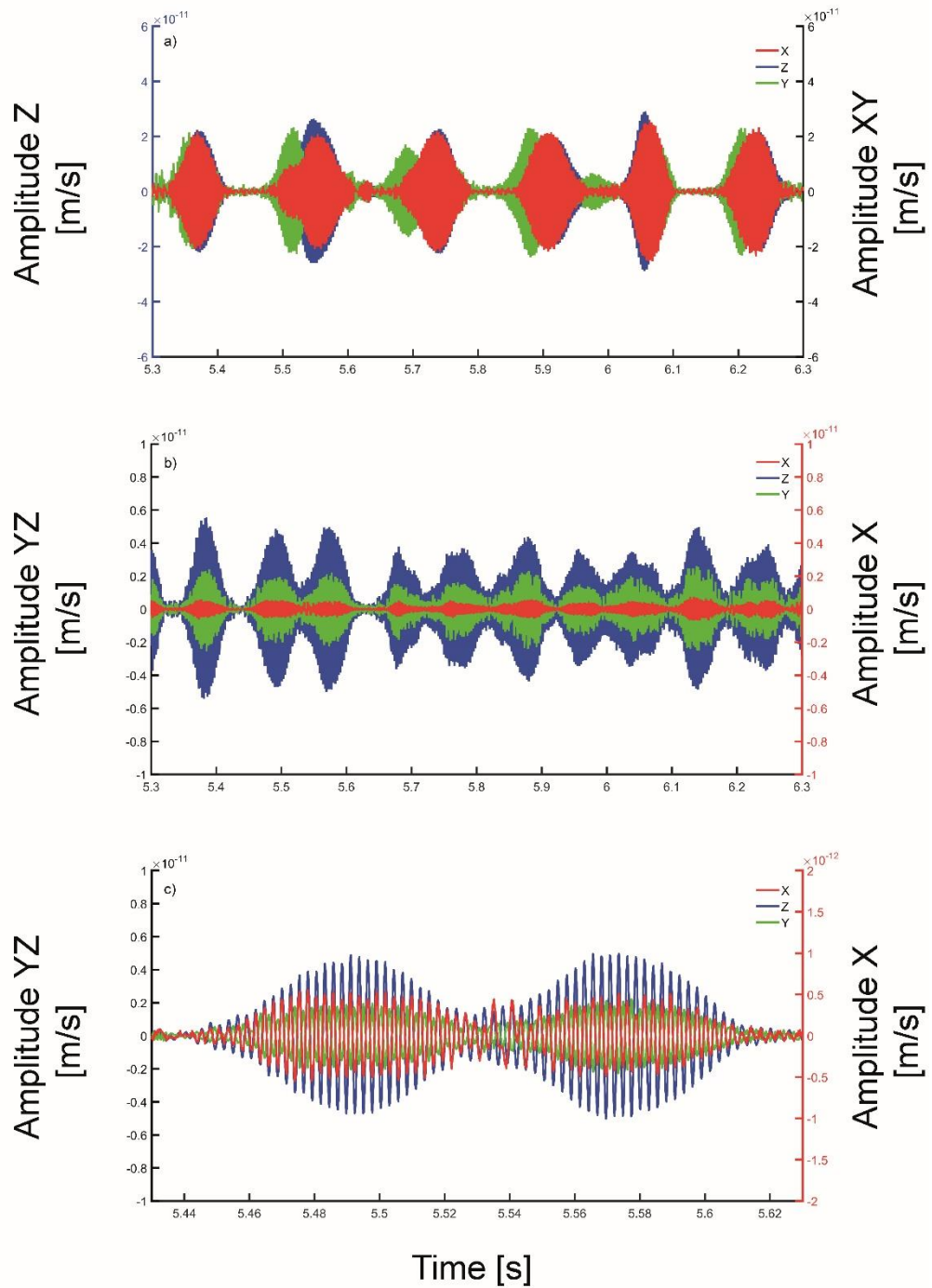


Fig. 5.17: This figure shows the two observed phase behaviours in *An. arabiensis*. While a) could be a by-product of a plane shift of the antenna motion as X seemingly compensates the amplitude of Y and vice versa, in b) and c) it is clear, as amplitudes go to zero in all directions at the same time, that true short-term modulation of the antenna movement is possible in this species at least.

5.5 Comparing three-dimensional movements in *Anopheles arabiensis* and *Toxorhynchites brevipalpis*

With cases of strong self-oscillation, applying the usual 120-2500Hz and 200-2500Hz high-pass filters does not alter the overall shape. The same is true for 120-800Hz and 200-800Hz. This holds to some degree for strong oscillations if the high-pass filter is lowered to 5Hz. Filtering does however straighten out the time-traces, as can be seen most prominently from the weaker self-oscillations. As it is now established that even drastic filtering steps do not fundamentally change the entrained paths, for the remainder of chapter only the 120 or 200Hz respectively up to 2500Hz will be shown. This was necessary to demonstrate that a coherent three-dimensional motion is taking place – as one would expect, since for all included animals Q-factors are high. High Q-factors of self-oscillation mean the movement is coherent. This is only true for a self-oscillating system as in this case the Q-factor in principle measures for how many subsequent cycles the motion persists more or less undisturbed. It can be – as it has been in this case – calculated by dividing the peak frequency by the half intensity peak width in the Fourier domain. Indeed looking at *T. brevipalpis* in 5.7 and *An. arabiensis* in 5.15 it becomes clear that for any given recording with sufficient self-oscillation there is at least one viewing plane, in which the antennae of male *An. arabiensis* and *T. brevipalpis* trace an ellipsoid path in three-dimensional space and in most specimens a rotation of this plane can lead to a false figure-of-eight appearance. Figure 5.15 b) and e) further demonstrates that in both species plane and in-plane direction can shift quickly over time.

5.6 Side note: *Anopheles gambiae* male – approximate values

In the case of *Anopheles gambiae*, the specimen supply was even more limited than for *An. arabiensis* and similarly, clear, noise-free recordings were difficult to obtain. For this reason, in order to get at least a benchmark for this species as well, recordings were performed with the “magnitude averaging” setting over three consecutive recording. While this allows to get an accurate idea of the frequency of self-oscillation in this species, displacements will likely be underestimated and Q-factors of over 400 are less reliable and likely overestimated. This being said, values are still robust enough to state tendencies – see table 5.5 and Fig. 5.18 – and are two orders of magnitude larger than 1 in all three directions. The table furthermore indicates the usual norm displacement and average peak frequency.

As with the other *Anopheles* species and *T. brevipalpis* in the present consideration, the norm of the X, Y, and Z displacement is used as a measure for the overall displacement, in later stages the actual 3D-pattern will be shown and more closely be looked at.

Table 5.5: This table shows the mean and median \pm one standard deviation for *An. gambiae* males. From left to right: Average frequency, directional Q-factor and norm displacement. Note that due to the limited supply of *An. gambiae* and the difficulties of getting good recordings, as opposed to other species “magnitude averaged” recording (averaging 3) are used.

<i>Anopheles gambiae</i>	Frequency [Hz]	Quality factor by direction			Norm Displacement [nm]
		X	Y	Z	
Male N=5.					
Mean	400 \pm 24	447 \pm 181	486 \pm 169	502 \pm 71	31 \pm 13
Median	379 \pm 26	312, \pm 193	493 \pm 169	474 \pm 72	24 \pm 14

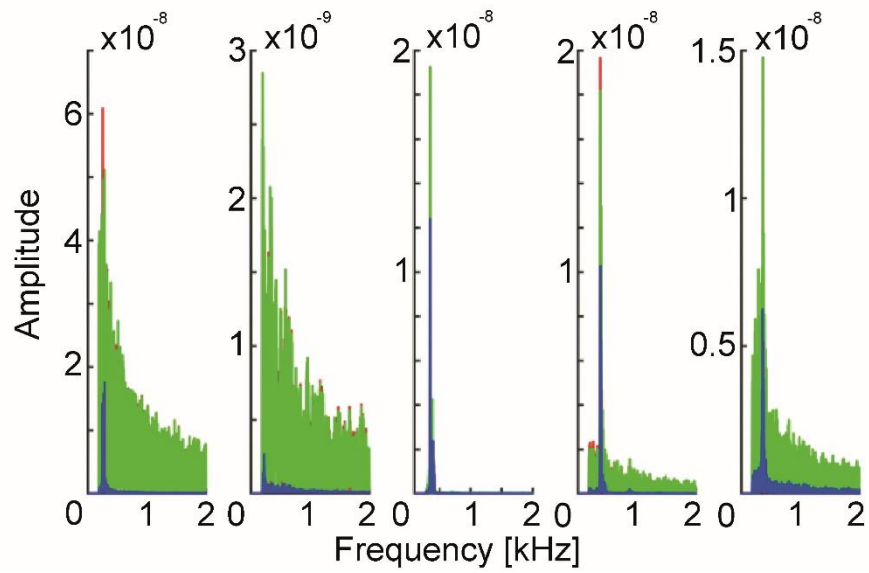


Fig. 5.18: This figure shows the Fourier domain representation of the self-oscillation observed in *An. gambiae*. Compared with recordings of *An. arabiensis* and *T. brevipalpis* the self-oscillations are, even with “magnitude averaging”, less prominent but without question the animals are capable of self-oscillation in three-dimensional space.

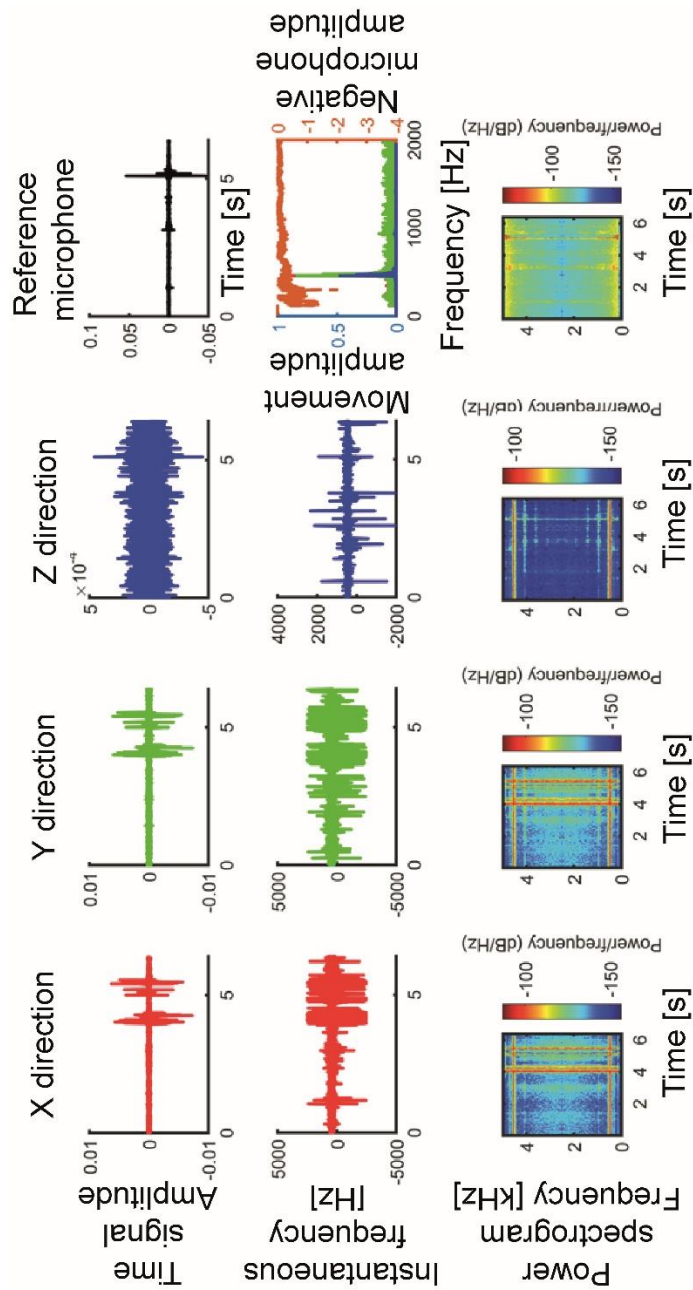


Fig. 5.19: This figure shows the self-oscillation of the antenna of one male *An. gambiae*, chosen for clarity of the recording. The first line represents the time-trace of the recording magnitude averaged over three 6.4-second time intervals. Displayed in red is the X direction, in green the Y direction, in blue the Z direction, and in black the reference microphone. The Fourier domain representation of the data has the same colour-code and the reference plotted in orange upside down on the same scale, indicating a self-oscillation of alternating between 462 and 476Hz, although nothing is picked up in the reference microphone. In the second line the spectrogram reveals the relative energy content per frequency showing the harmonics of the self-oscillation. Note that the values in row 1 and 3, column 1-3 and row 2, column 4 are given in velocity, not displacement.

5.7 *Chironomus riparius* male and female

Usually, no self-oscillation is observed in the males of this species. In females, the situation is less clear, as 50% of the investigated six females showed some motion. However, noise levels are high and while no accurate measurements of the Q-factor were performed, with frequencies around 300Hz and the broad bandwidth of 200Hz the self-oscillation like in *T. brevipalpis* females remains too vague to comment on extensively.

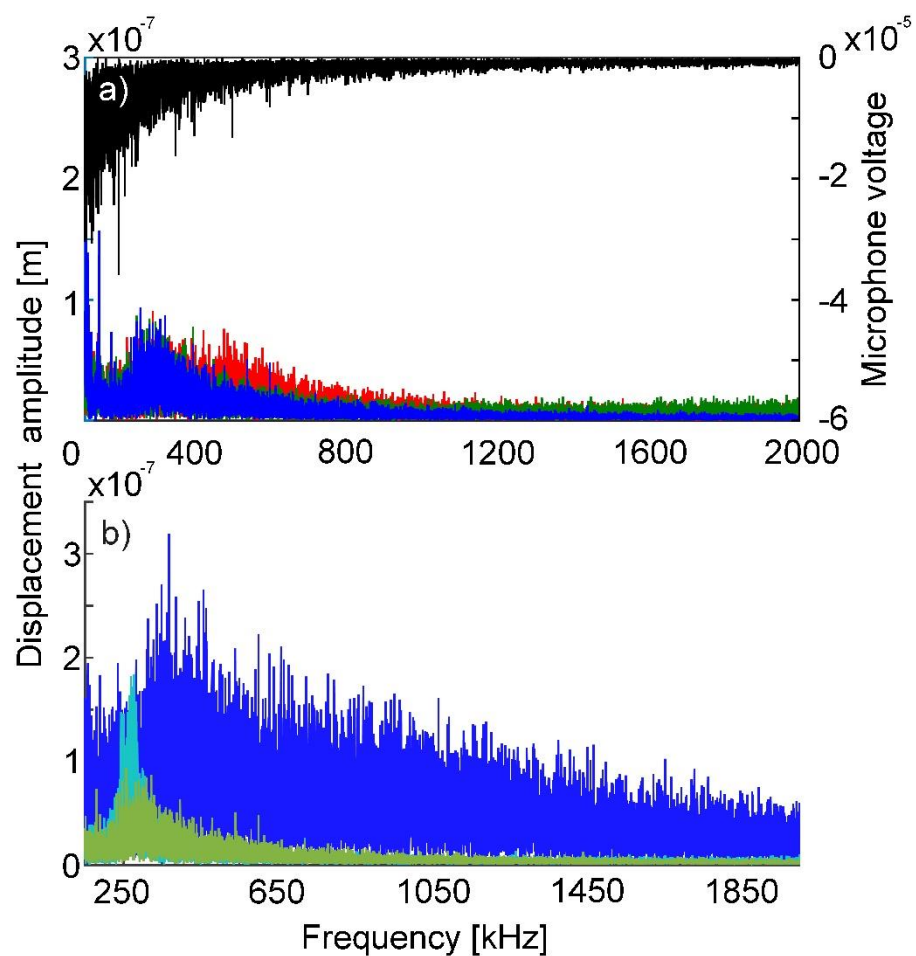


Fig. 5.20: This figure shows *C. riparius* female putative self-oscillation: a) One individual of *C. riparius* female showing a weak case of self-oscillation, chosen for being the most clear example in this species. X direction red, Y direction green, Z direction blue, reference black, b) Z direction component of three individuals plotted on the same axis to illustrate this is not a singular occurrence.

5.8 Further controls on the principle of self-oscillation experiments

The following pages are dedicated to control experiments intended to show that the antenna self-oscillation is a) real and b) independent from any physiological processes further removed in distance than the head.

5.8.1 Electrophysiology control: pedicel potential vs. flight muscle potential

A small electrophysiology experiment series with $N=4$ was performed to test whether there is a visible correlation between wing activity and the antenna self-oscillation measured in the Laser Doppler Vibrometry setup. To this end, two electrodes were inserted into the animal, one in the pedicel the other in the flight muscle.

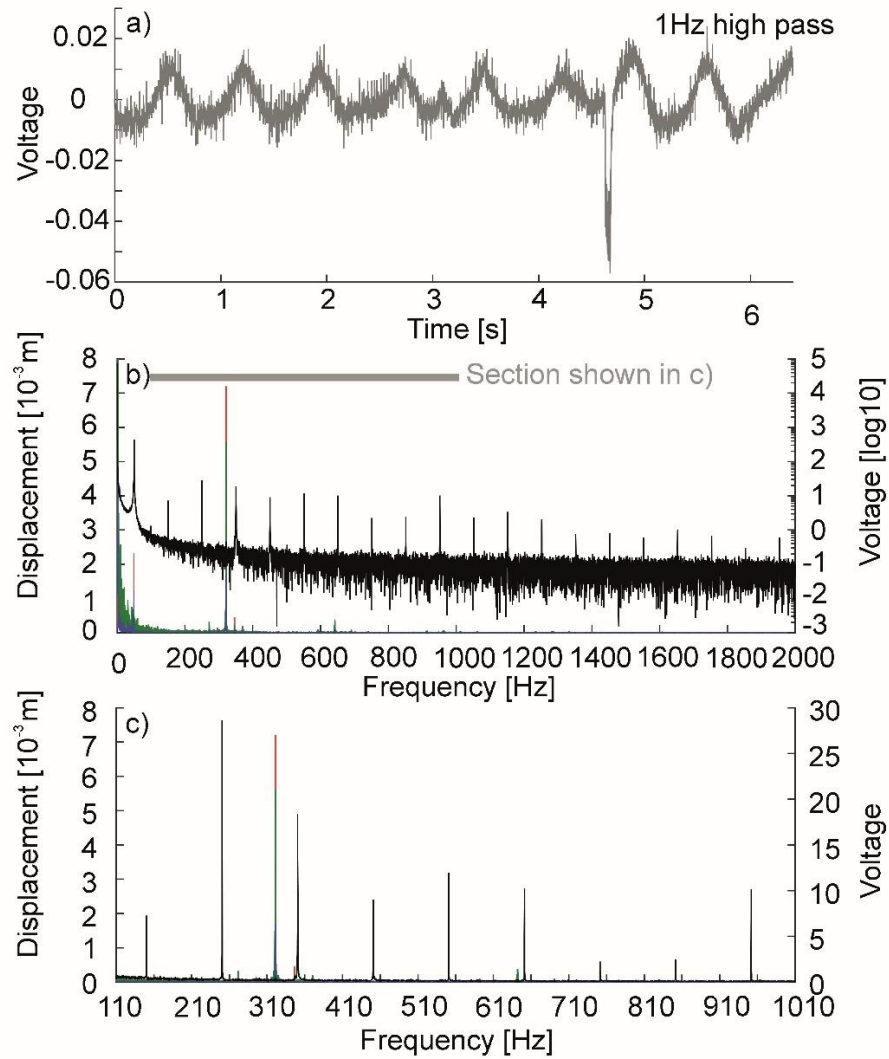


Fig. 5.21: This figure shows *T. brevipalpis* in panel a) that the setup did capture the large nerve impulse in the time domain. Data are filtered as described in methods, but with a 1Hz high-pass filter. Panel b) shows the Fourier domain representation of one representative electrophysiological data set (black line) in log scale set against frequency to facilitate a direct comparison to the vibrational data (X direction: red, Y direction: green, Z direction: blue) acquired at the same time, which are plotted on a second Y axis also in Fourier domain against frequency. Panel c) is a detailed view of the same data set as b). Here electrophysiological (black line) and vibrational data (X direction: red, Y direction: green, Z direction: blue) in linear scale are shown around the self-oscillation frequency. While the image of the female labelled animal 3 (3rd recording) presented is chosen for clarity, the pattern is comparable in all recordings. Except the 50Hz electric noise peak, there are no peaks that are clearly above noise floor, which match between the vibrational and the electrophysiological recording. The vibrational data show clearly that the animal at the given time was performing antenna self-oscillation. The electrical data show further up to the tenth or sometimes even higher harmonic of the 50Hz noise but no other peaks.

Fully acknowledging that comparing muscle potentials of the wings to the delicate structure in the pedicel can be seen as a stretch – the absolute absence of correlated peaks, be it multiples or halves of the vibration frequency and the absence of any kind of intermodulation demonstrates that wing or wing muscle motion is not essential to the self-oscillation, nor is it electrically correlated.

5.8.2 Decapitation control

As a final test of independence, a subset of *T. brevipalpis* specimens was decapitated in order to verify whether the self-oscillation is truly independent of body processes most prominently contraction of the flight muscles. This is important, as flight muscles operate at very similar frequencies, which in this case is beyond the temporal capacity of classical neuronal muscle control. The high frequencies in many insect flight muscles are achieved by a combination of passive restoration force and autogenous muscle activity of those asynchronous muscle – which only occasionally receive neuronal input (e.g. Pringel, 1949, Pringel, 1981, Josephson et al., 2000, Syme et al., 2002). In midges, observation of these superfast contractions goes back to as early as at least 1953 (Sotavalta, 1953). With $N=4$, see the example shown below (Fig. 5.22), it is demonstrated that a decapitated head is capable of self-oscillation of the antenna – ruling out dependency on body processes beyond those located in the head. The fact that antennae attached only to a bodyless head still self-oscillate should be convincing that self-oscillation is truly independent, regardless of the N number.

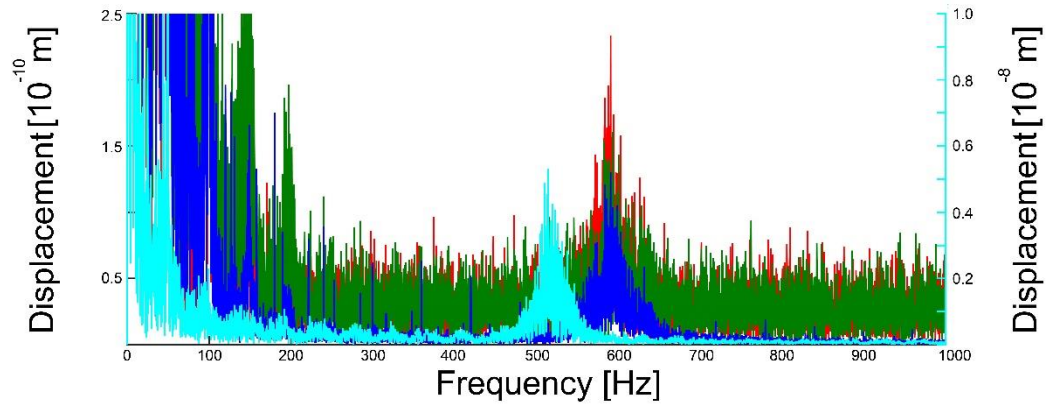


Fig. 5.22: This figure shows the two clearest cases, in which the antenna of a male *T. brevialpis* still shows self-oscillation after the head was removed from the body. The left Y axis is for animal 4 with clear readings in X (red), Y (green) and Z (dark blue). The second Y axis on the right is in the same light blue as the Z movement of animal 1, to which it belongs.

5.9 Concluding remarks on the self-oscillation vibrometry

The present data on *T. brevipalpis* (section 5.1), *An. arabiensis* (section 5.4), and *An. gambiae* (section 5.6) unequivocally support self-oscillation beyond the model system *T. brevipalpis*. This allows research on *T. brevipalpis* to be viewed as more generalisable to at least some other mosquitoes. The ball-socket-like joint of the flagellum in the pedicel is strongly suggestive of the possibility of an elliptical to circular movement path – which in fact has been shown to exist in both of the two species investigated for spatial paths. Median quality factors of self-oscillation are robustly high $\gg 1$ in the order of hundreds in all three mosquito species where male self-oscillation was measured. In *T. brevipalpis* (section 5.2) and *An. arabiensis* (section 5.4) clear tendencies of the antenna to shift the plane of motion during self-oscillation are evident. In *T. brevipalpis* (section 5.2) this seems not to affect the amplitude of oscillation at all while in *An. arabiensis* (section 5.4) some pulsing, likely not only related to plane shift has been reported. Despite dramatic differences in body size and antenna length (*An. arabiensis* ca. 1.7mm, *T. brevipalpis* 3.3mm), frequencies of motion (*An. arabiensis* 372Hz and *T. brevipalpis* 422Hz) and amplitude (*An. arabiensis* mean 124 ± 63 (median 15 ± 73) nm and *T. brevipalpis* mean 183 ± 75 (median 4 ± 87) nm) are remarkably close. For details see section 5.2 for *T. brevipalpis* and section 5.4 for *An. arabiensis*. Decapitation controls (section 5.8.2) in *T. brevipalpis* support the oscillation being if not completely independent in terms of energy then at least not dependent on the wing muscles. Similarly, electrophysiology does not suggest a correlation between muscle activity and antenna oscillation.

In females of *T. brevipalpis* (section 5.3), the picture is less clear, as the amplitudes are low, and the peaks are broad. While Q-factors are above 1, they are lower than in the males of the species. While some acoustic interaction of both sexes has been reported (Gibson et al., 2006, Cator et al., 2009, 2010, 2011), the so far common understanding, dating back to at least Downes (1969), is that the males of at least some species use their antennae to detect and locate females against the acoustically noisy backdrop of the swarm. In this light, it is possible that the more pronounced sharpness of the antenna tuning observed in males than in females – as indicated by two orders of magnitude higher Q factors – serves the purpose of mate finding in these species. Therefore, the presented data align with a higher necessity for an acute sense on hearing in one sex than the other. Multiple *C. riparius* males and females were investigated (section 5.7), but no self-oscillation of any significant amount could be shown for this species.

5.10 Standalone discussion of self-oscillation vibrometry

5.10.1 On the meaning of the Quality factor in *Anopheles arabiensis* and *Toxorhynchites brevipalpis*

The fact that in both investigated mosquito species – one solitary, one swarm-mating – the signal is highly coherent points towards a common engine and function behind the antenna movement of the two mosquito species (Downes, 1969, Charlwood et al., 1979, Steffan et al., 1981, Pennetier et al., 2010).

In contrast, no coherent self-oscillation could be shown in *C. riparius*.

Another point that has to be made is, as self-oscillation is a highly coherent and close to sinusoidal movement, inevitably there will be harmonics present in the system. This – while the meaning is less clear than their existence – could hold implications for harmonic convergence, which is widely reported (Gibson et al., 2006, Cator et al., 2009, Warren et al., 2009, Pennetier et al., 2010, Cator 2011) and the twice-frequency forcing in a strictly mechanical sense. This would be in no way detracting from the importance of neuronal processes described elsewhere (Jackson et al., 2009, Warren, 2010, Windmill et al., 2018). It then would be possible to envision additive and subtractive effects of the first harmonic, which would have the double frequency and increase the amplitude half the time, half the time decrease the amplitude as illustrated in Fig. 5.23. This as such makes no assumption on where the second sinusoidal signal would be generated from. On this note, a final remark that the wingbeat of female *T. brevipalpis* was recorded as a brief (N=3) control experiment. Here it appears that the frequency carrying the dominant amount of energy is about twice of the antenna self-oscillation all by itself. The subharmonic would be very close to the observed self-oscillation in that case.

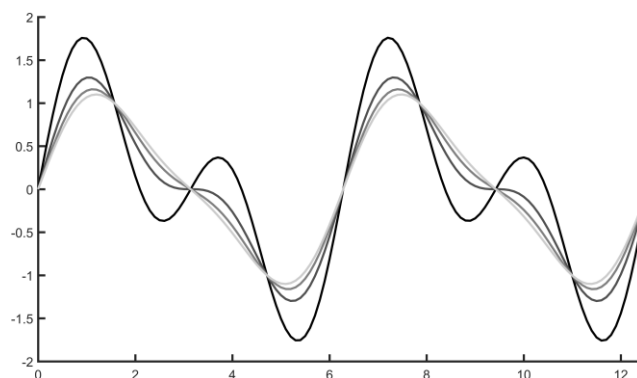


Fig. 5.23: Shows four cases of in-phase sine wave addition of two frequencies, one of which is twice of the other. The scales are relative and show a 4π interval, starting with the black line, where both frequencies have the same amplitude and go towards the lighter gray lines (over 2:1, 3:1, with towards the lightest gray resembling a situation where amplitudes have a 4:1 ratio.

5.10.2 On the meaning of the results in *Anopheles gambiae*

With $N=5$ and the use of magnitude averaging, due to limited availability and noisiness of recordings, the results are to be viewed with more caution than in the other species. However, with the sharp peaks in Fig. 5.18 and mean Q-factor while overestimated between 447 ± 181 in X direction, 486 ± 169 in Y direction and 502 ± 71 in Z direction, which are two magnitudes larger than one, it is clear that beside the species investigated in more depth this species is also capable of self-oscillation, within a frequency range comparable to the female wingbeat. This is also in agreement with wingbeat frequencies results by Pennetier (2010), which put the female wingbeat in this species, depending on population type, between 475Hz (S type) and 489Hz (M type).

5.10.3 Comparing the self-oscillation in male and female *Toxorhynchites brevipalpis* antenna responses.

The self-oscillation frequency in males with a mean of 477 and median 422Hz (N=16) is around one standard error in distance from the resonances reported by others, which range from 404 ± 29 Hz (Jackson, 2006) to 500 Hz (Gibson et al., 2006) with Göpfert's (et al., 2000) value of 420 being the closest. The female self-oscillation is centered on mean 259Hz and median 246Hz (N=5) and thereby about 50-60% lower. The amplitude varies as well by two (mean) or one (median) powers of 10, in males nanometre, in females hundreds of picometres. One could argue that the female self-oscillation amplitude therefore is close to thermal noise level. However, while it is less pronounced and in tendency more than a hundred times weaker than in their male conspecifics, the Q-factors of the female self-oscillation are larger than one.

6 Results in *Toxorhynchites brevipalpis* when adding sound to self-oscillation

While the previous chapter was focused on the native behaviour of an otherwise undisturbed antennal system – and showed that results from *T. brevipalpis* are likely in principle transferrable to if not all, then at least some, other mosquito species – the present chapter deals with how the self-oscillating and quiescent antenna of *T. brevipalpis* males responds to sounds played at it. The main focus will be section 6.1, the response to imposed pure-tone sine waves, before in section 6.2 a quick control experiment is presented, in which one male was directly presented with three different tethered females.

6.1 Response to imposed pure-tone sine waves

Generally speaking, it has to be stated that responses are very varied and no overall trend will be reported but rather, this chapter is describing a catalogue of observed three-dimensional movement patterns. Among other hard-to-control factors, the main reason is that as a sporadically nonlinear self-oscillating system, animals changed their behavioural states too quickly to allow for more vigorous testing.

The four types of behaviour seen most frequently are a) entrainment to a close-by frequency in which all three directions behave differently but not independently (Fig. 6.1 and Fig. 6.2), b) the system sustaining its self-oscillation in parallel to the presented frequency with little to no intermodulation (Fig. 6.3), c) the emergence of a different tone vibration (Fig. 6.4), d) down-modulation in the face of higher energy input in at least one direction (Fig. 6.5).

In many cases it has to be stated that the antennae seem to pick up harmonic frequencies also seen in the microphone, but with a comparatively (although just qualitatively not quantitatively) higher signal-to-noise ratio, albeit at a lower overall amplitude (see range from background to maximum peak in spectrograms) indicating a high frequency selectivity.

6.1.1 Entrainment by close-by frequency in 3D

Column four of the second row in Fig. 6.1 shows the Fourier domain representation of all three movement directions. Two peaks are apparent, one of which matches with the frequency played and recorded by the microphone. Shown in the recording as indicated by row 2 and 3 from the time of playback onset, the antenna moves with a different amplitude (up in the X and Z direction, down in the Y direction, see row 1) and solely on the playback frequency (row 2, column 1 to 3, and row 3). The spectrogram of the reference microphone's pickup of the playback indicates no interfering noise before the playback is started. On the contrary, all spectrograms of the antenna feature harmonics of the self-oscillation before and after the playback and, while the sound is played, also harmonics of the input frequency.

From Fig. 6.2 it is clear that self-oscillation before the signal (blue) is an ellipsoid, the signal (black) changes the dominant direction and after (red) the self-oscillation is circular and yet again in a different plane.

It is noteworthy that none of the directions varies in order of magnitude, meaning that the self-oscillation in a strong case has the same amplitude as a stimulating sound source in each direction within a factor of 2-3.

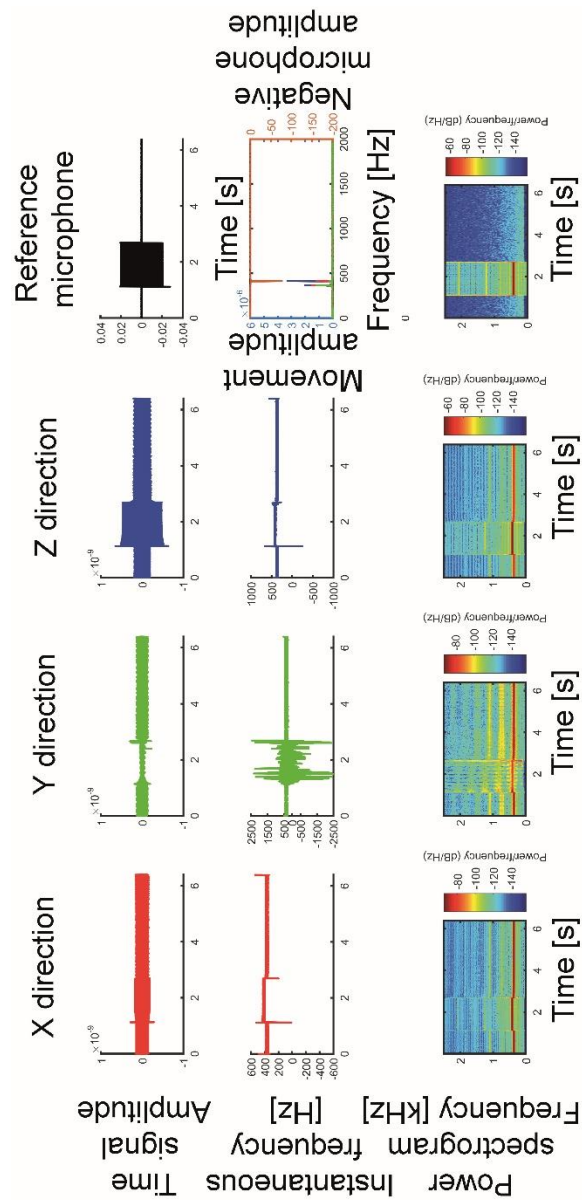


Fig. 6.1: This figure shows the antenna of a male *T. brevipalpis*, animal labelled 31, in the state of complete entrainment to a frequency close to its self-oscillation frequency. Note that the intensities – colour-coded blue = low to red = high, in row three – go up in X and Z, but down in Y. See also time-signal in row one, here the amplitude increases in X and Z and decreases in Y. Harmonics are present in the antenna in self-oscillation even while the speaker (see microphone reading) is completely silent. N=5 (animals labelled 13, 21, 23, 26, 31) show this. Row one: Time-signal, from left to right in the X, Y, and Z direction vs. time, followed by reference. Row two: Instantaneous frequency, from left to right X, Y, and Z vs. time, fourth column Fourier-domain signal of the whole time window. Row three: spectrograms of, from left to right, X, Y, and Z direction vs. time followed by a spectrogram reference microphone.

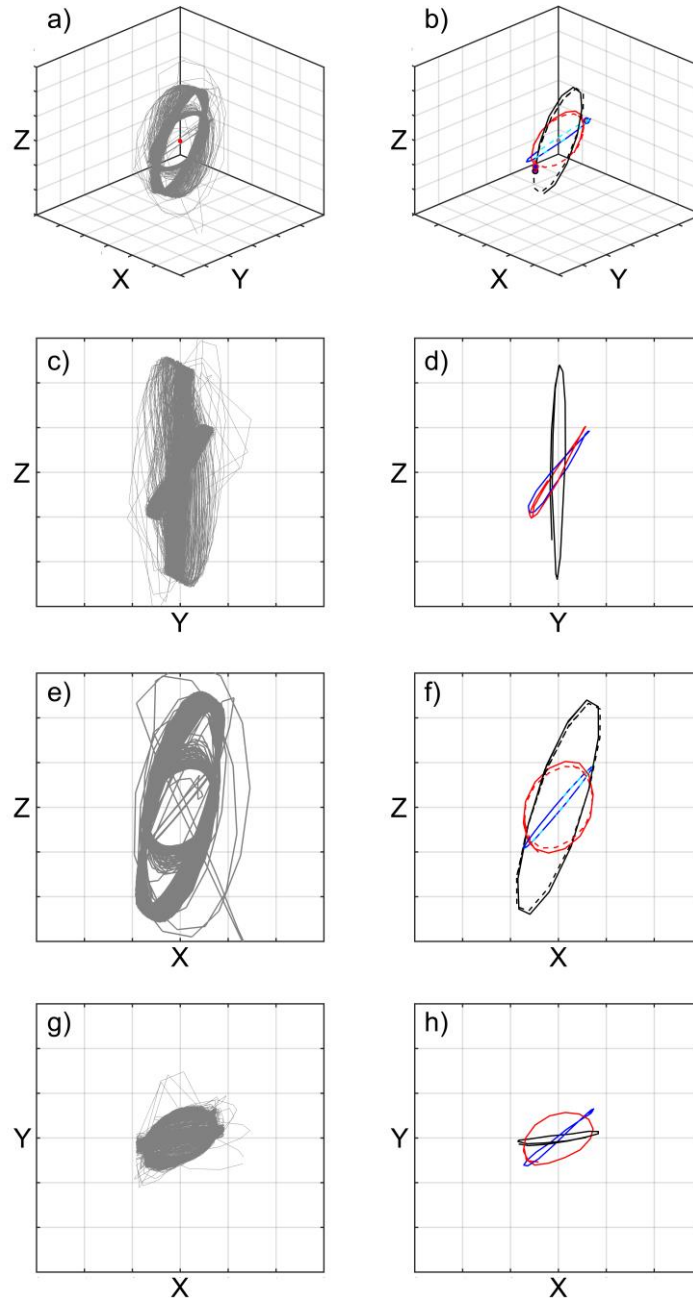


Fig. 6.2: This figure shows the 3D-movement patterns of the antenna in the male *T. brevipalpis* labelled animal 31. The grid equals 0.2nm in each panel. Panels a), c), e), g) show the whole time interval. Panels b), d), f) and h) show one to two individual cycles at any given time. In panels b), d), f) and h) blue indicates a movement cycle in time before a signal is played, see Fig. 6.1, black while a signal is played, see Fig. 6.1, and red after the signal has stopped. Panels a) and b) show the three-dimensional view. The red dot in a) and the gray dot in b) signify the coordinate origin. In b) dots of matching surrounding colour show the first point of the recording interval of their colour. Panels c) and d) show the X plane, e) and f) show the Y plane, g) and h) show the Z plane.

6.1.2 Sustained self-oscillation despite close frequency being played, resulting in two movements with little intermodulation

Figure 6.3 allows one to compare the situation between the antenna and the microphone before a sound playback is started at about four seconds. Like in Fig. 6.1, in the Fourier domain representation of all three movement directions (row 2 column 4) two peaks are apparent, one of which matches with the frequency played and recorded by the microphone. Here, however, the second frequency does not vanish at playback onset, even gets stronger and persists despite the playback, as can be seen in the second row, first to third column, and row three. The spectrogram of the reference microphone's pickup of the playback indicates no interfering noise before the playback is started – which means the antenna is moving on its own. All the spectrograms feature harmonics (row 3) and intermodulations between the playback and the self-oscillation, which from second 4 onwards changes to a lower frequency.

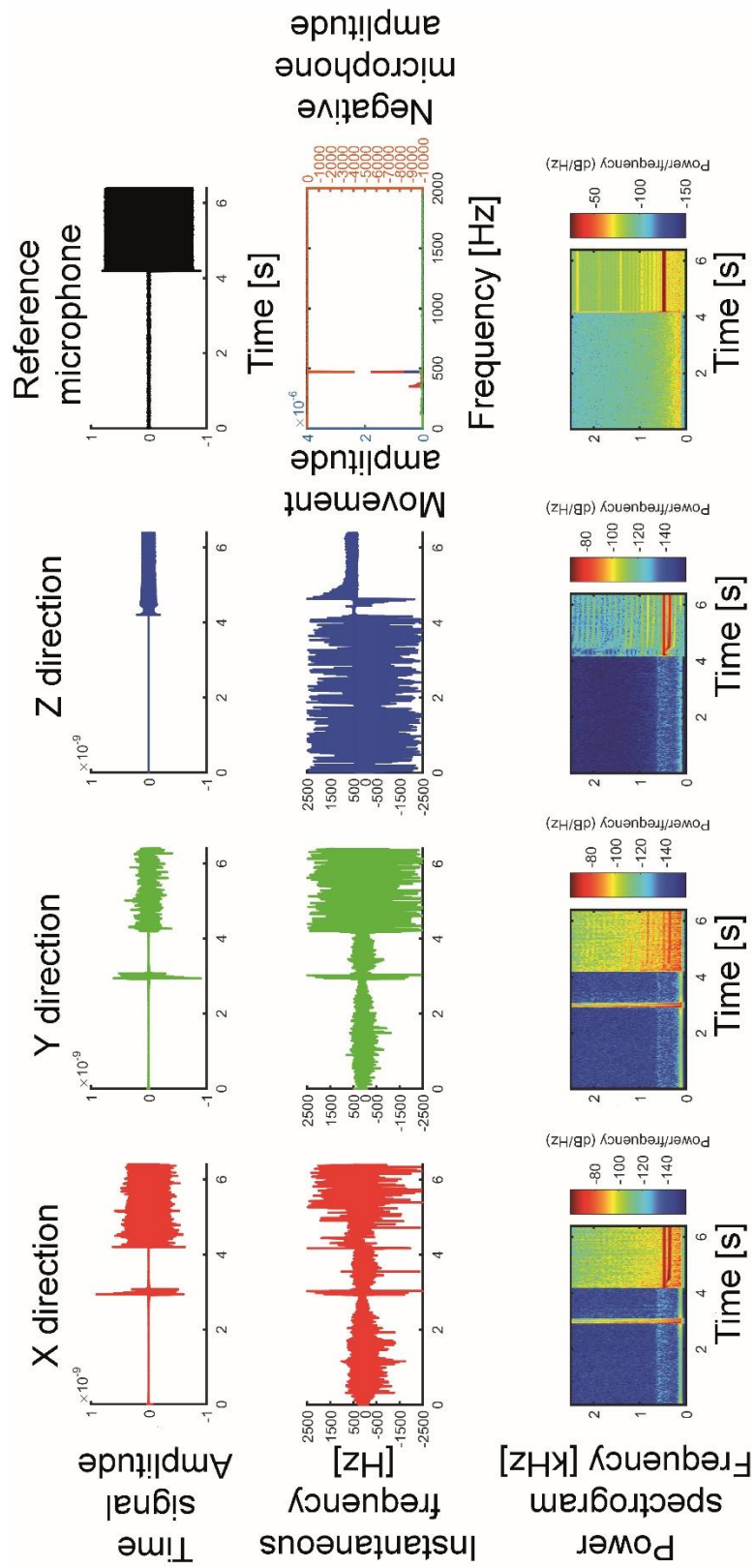


Fig. 6.3: This figure shows the state of two frequencies being presented to the *T. brevipalpis* male labelled animal 24 in the antenna vibration at the same time. N=3 (animals labelled 15, 24, 33) show this. Data shown as in Fig 6.1.

6.1.3 Difference tone vibration

Figure. 6.4 shows the situation where after the onset of a sound playback at about 1.5 seconds, a difference tone vibration emerges. Like in Fig. 6.1 in the Fourier domain representation of all three movement directions (row 2 column 4) multiple peaks are apparent, one of which matches with the frequency played and recorded by the microphone, one represents the self-oscillation and the third the difference tone. Here like in Fig. 6.2, however, the self-oscillation does not vanish at playback onset, instead it persists despite the playback, as can be seen in row 2 column 1 to 3 and row 3. The time domain representation in the first row and the spectrograms' third and fourth rows indicate that the X and Y directions are much more noisy than in the cases shown in sections 6.1.1 and 6.1.2. The spectrogram of the reference microphone's pickup of the playback indicates no interfering noise before the playback is started – which means the antenna motion seen in the spectrograms' 1-3 is self-oscillation. All the spectrograms (row 3 and 4) feature, from 1.5 seconds, harmonics and intermodulations between the playback and the self-oscillation.

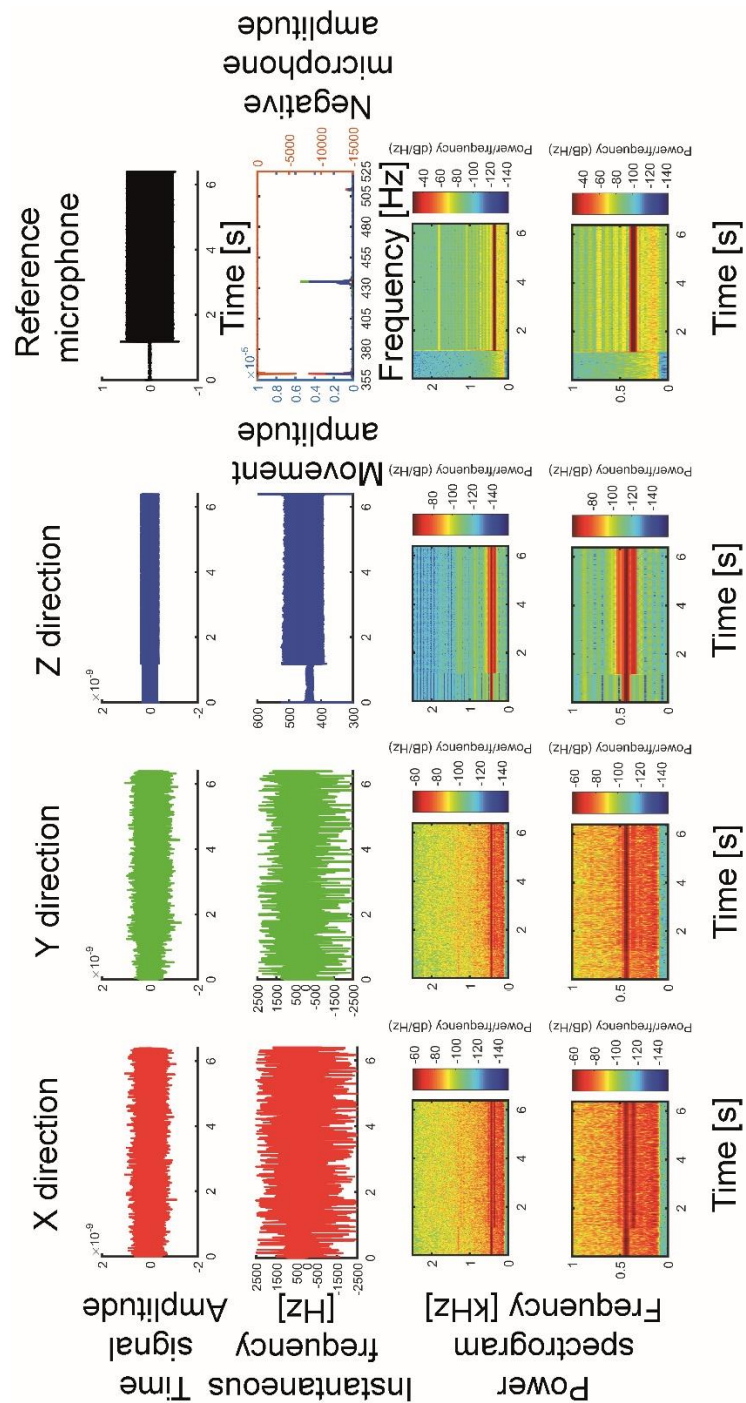


Fig. 6.4: This figure shows the state of the antenna where a difference tone emerges. $N=2$ (animals labelled 06, 08) show this. In the present case the difference tone is at 507Hz (2 times 432 (self-oscillation) – 360Hz (playback)). In row three only a portion of the Fourier domain representation from 355to 525Hz is shown, as this allows a better assessment of the frequencies strongly involved. Row four: detail spectrograms of, from left to right, X, Y, and Z direction vs time followed by a spectrogram reference microphone. Data otherwise shown as in Fig 6.1.

6.1.4 Down-modulation of entraining frequency

In Fig. 6.5 a playback is shown, in which after the start of playback at 5 seconds, the motion of the antenna changes. Like in Fig. 6.1, in the Fourier domain representation of all three movement directions (row 2 column 4), two peaks are apparent, one of which matches with the frequency played and recorded by the microphone. Here, however, the second frequency does not vanish at playback onset, it even gets stronger and persists despite the playback, as can be seen in the second row, column 1 to 3 and row 3. The spectrogram of the reference microphone's pickup of the playback indicates no interfering noise before the playback is started – which means the antenna is moving on its own. All the spectrograms (row 3) feature harmonics and intermodulations between the playback and the self-oscillation, which from second 4 onwards changes to a higher frequency. Amplitude decreases at the same time, as can be seen in row 1, column 1 (X direction), and column 3 (Z direction), at about 4 seconds into the recording, while it increases, albeit to a lesser extent, in column 2 (Y direction).

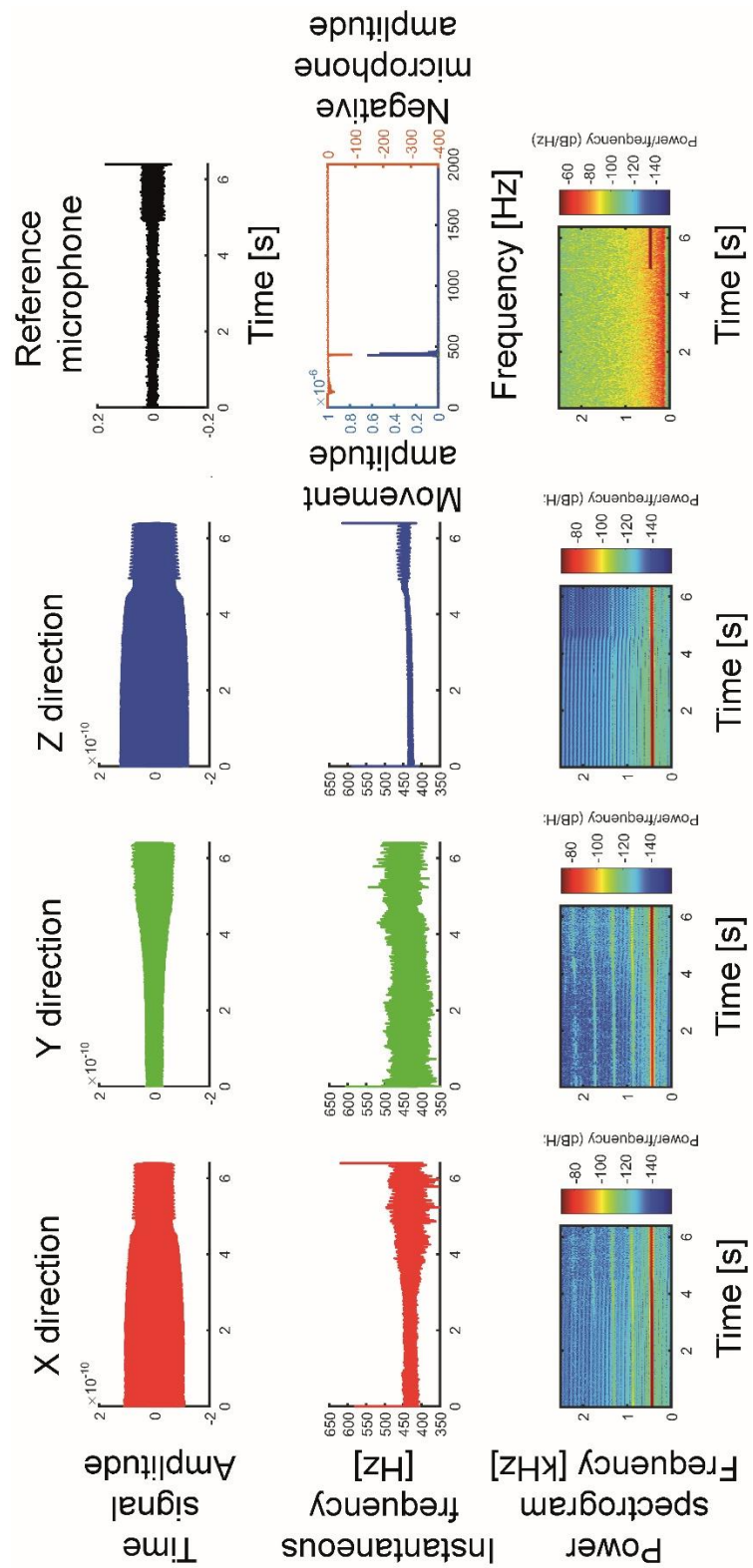


Fig. 6.5: This figure shows down-regulation of self-oscillation in one *T. brevipalpis* male labelled animal 10 in two directions while the overall intensity increases due to played signal. N=2 (animals labelled 10, 13) show this. Data shown as in Fig 6.1.

6.2. Reception of a directly presented female

Figures 6.6-8 below illustrates the time-dynamic of a male *T. brevipalpis* to the female wingbeat frequency. Most important is that in general the wingbeat recordings include energy in the harmonics and subharmonics. Additionally, it is shown that the signal-to-noise ratio in the antenna and LDV is higher than for the microphone – judging by the larger deep-blue areas in the spectrograms. The leftmost plot shows the Fourier domain representation of the displacement in the X, Y, and Z directions and, on a second, top-down orientated Y axis, the reference microphone. Here it is remarkable that the antenna responds strongly to frequencies over 800Hz (e.g. the band in which the female recordings appear to contain the most energy). However, contrary to the microphone a second strong peak is evident in the antenna at half of the highest energy band of the wingbeat, coinciding with the often visible self-oscillation (Figs. 6.6-8 – row 1 spectrograms). In most of these spectrograms a lower and less clearly-defined comparatively high energy frequency band can be observed. In the case of female 2 (Fig. 6.7) there is even a third peak closely below the subharmonic. This cursory experiment (N=3 females presented to one male) should be read with caution.

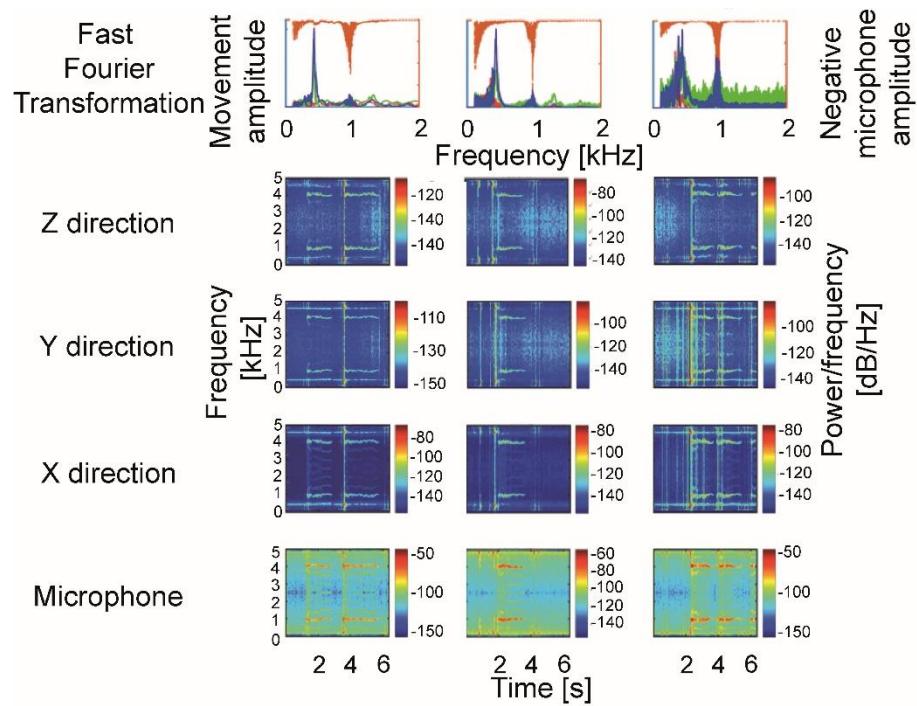


Fig. 6.6: Shows a male *T. brevipalpis* in response to three recordings of one *T. brevipalpis* female, labelled animal 1. In each triplet the first row is the is the Fourier domain representation of the data of the directions X (red), Y (green), Z (blue), and the reference plotted in orange upside down on the same scale, indicating thatn while in the microphone 977.5Hz contains the highest energy, the antenna responds strongly to the subharmonics The following three rows are, from top down, the X, Y, and Z direction spectrograms of the three LDV recordings of the male antenna. The fifth row is the spectrogram of the reference microphone directly recording the female wingbeat. The spectrogram reveals the relative energy content per frequency, thereby showing even more harmonics in shape and position identical to the microphone recording. Note that the subharmonics almost coincide with the shown self-oscillation (row 1) and that the antennae and LDV have a higher signal-to-noise ratio than the reference microphone.

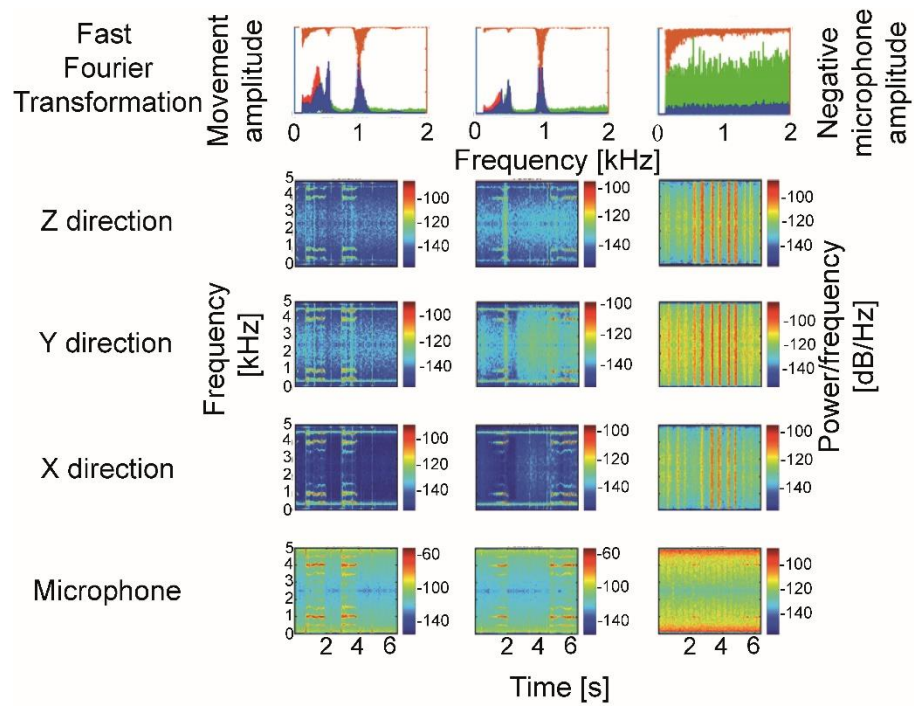


Fig. 6.7: Shows a male *T. brevipalpis* in response to three recordings of one *T. brevipalpis* female, labelled animal 2. Data shown as in Fig 6.6. Wingbeat according to microphone has the highest energy in 977.0Hz. Note that the subharmonics almost coincide with the shown self-oscillation (row 1) and that the antennae and LDV have a higher signal-to-noise ratio than the reference microphone. Here recording 3 did not work out well in the reference spectrogram (column 3) the main frequency is nonetheless present and similar to recording 1&2.

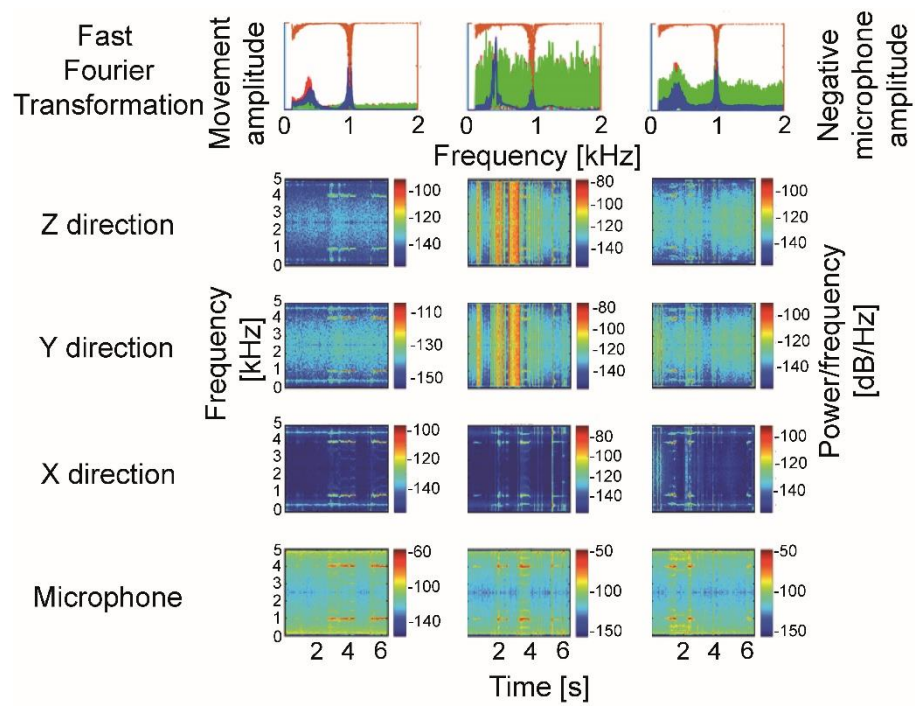


Fig. 6.8: Shows a male *T. brevipalpis* in response to three recordings of one female *T. brevipalpis* labelled animal 3. Data shown as in Fig 6.6. Wingbeat according to microphone has the highest energy in 984.6Hz. Note that the subharmonics almost coincide with the shown self-oscillation (row 1) and that the antennae and LDV have a higher signal-to-noise ratio than the reference microphone.

6.3 Concluding remarks and discussion

6.3.1 Male antenna stimulated with a sine wave sound

The four most frequent cases shown in sections 6.1.1 to 6.1.4 illustrate the variant nature of the mosquito hearing system's responses to sound stimuli. The system as such is therefore capable of entrainment, generation of harmonics and intermodulations between playback and self-oscillation up to self-oscillation persisting in spite of high-intensity playback. While it is possible to class and sort the animals' responses and thereby to generate a catalogue of system states, the present data are not capable of explaining the observed phenomena in terms of either cause or meaning. However, these effects are all well-known as properties of nonlinear systems.

6.3.2 Male *Toxorhynchites brevipalpis* antenna response to the female wingbeat

While the reported results are only based on one male, presented with N=3 female wingbeats, a clear tendency is visible. Like the microphone, the antenna picks up the transient wingbeat. Compared to the microphone the antenna and LDV show a higher signal-to-noise ratio. The subharmonic observed in female wingbeat sounds is close to the self-oscillation of the antenna, this also is evident in the direct presentation with female sounds where the male antenna responds strongly not only to the high energy component but also to the subharmonic.

This also puts the self-oscillation of mean $260 \pm 26\text{Hz}$ (median $236 \pm 28\text{Hz}$) in females in relation to their averaged wingbeat frequency of 979.7Hz.

6.3.3 Last notes on the addition of sound to self-oscillation

As the antenna represents the initial mechanical reception filter, it is interesting to note that the harmonics are present, which tentatively means that as any signal produces them, a selective discrimination of harmonic matchings seems unlikely.

This is because either they are filtered out neuronally (then there would be no perception) or they are always there once the base frequency is present. This would mean that harmonic convergence, independent of whether it happens actively or passively due to the necessity of flying close to each other could be outside the animals' perception.

Ablation of antenna could be used to show whether this is an intentional or physically consequential of mating. However, antenna ablation might, while precluding a purely passive mechanism, not be the best experiment to identify the internal mechanism, as mutilated animals might not engage in close enough interaction to trigger convergence behaviour.

7 General discussion

Before discussing the individual results and returning to the wider field of bioacoustics in mosquitoes, I would like to examine the key observations made in respect to the aims stated in the beginning.

7.1 Comparing the results with the aims

The aims of this study were

- 1) Noting that mechanical baseline data of these insects' antennae were missing, a qualitative overview of the different species is given. Section 3 (CLSM) clearly demonstrates that the antennae are not just unstructured beams. Furthermore, it appears that in each species investigated, a different pattern is seen. Most noticeably, in the two mosquito species, the observed pattern of hard and soft elements along the flagellum is inverted, although both show self-oscillation. The common feature here is the alteration of hard and soft elements.
- 2) Section 4 explores the potential effect of the observed structural features from Section 3, in computer simulations. It was found that the observed pattern can influence the mechanics of the beam. Namely, a beam with additional hard elements has a higher frequency for its strongest mechanical response than a uniform beam, and addition of soft elements has the opposite effect. Not surprisingly, the effect of hard elements is stronger in an overall soft beam and vice versa, soft elements change the response of a harder beam more than of a softer beam. Other observations from the simulations are that the response mode of the base can be moved depending on the qualities of the attached beam.

3) Sections 5 and 6 deliver comparable measurements of more than one mosquito species producing self-oscillation in three-dimensional space.

With 3D LDV it was shown that:

a) No matter whether the system is already self-oscillating or quiescent, a strong enough external stimulus can force the antennae into an elliptical movement pattern.

b) Self-oscillation, however, can have all manner of 3D-patterns. If it is sufficiently strong, it can also approach circular motion.

c) It seems that in *An. arabiensis*, there exists a modulation mechanism that is neither reliant on nor independent of plane shift of the motion – while in *T. brevipalpis* modulation is more rare and seems to relate to plane shift.

7.2 Reflection on the meaning of CLSM and COMSOL results

While this study did not reach the final explanation why structures of different stiffness along the flagellum would be beneficial, the combination of presenting different distribution of materials in the three species investigated and between the sexes of two of them, as the females of *An. arabiensis* were not available, and the simulation results showing that those differences can influence the mechanical response, I could show a tuning effect of these structures and thereby a selectable mechanism for stiffness along the antenna. Factors like antenna shape, for example tapering, shown here in parallel to what has also been demonstrated by Rajabi et al. (2018), and position of elements of different stiffnesses also influence the mechanical response. There remains a huge potential for – in comparison to active and thereby continuously costly – cheap morphological adaptations in antennal hearing, which are for now far from being understood.

7.3 Reflection on the meaning of 3D LDV results

Like Warren (et al., 2010) and Göpfert et al. (1999, 2000) the LDV recordings show self-oscillation in both sexes of *T. brevipalpis*. In a similar manner they reveal that the male self-oscillation is sharper and higher in amplitude than that of the female animal, which is also in line with Warren (et al., 2010) and Göpfert (1999, 2000).

In otherwise consistent conditions, a variety of different animal responses has to be reported, the cause of which is not to be understood from the current experiments.

These responses range from full entrainment over self-oscillation persisting seemingly undisturbed (both at similar, but not the same, amplitudes) to harmonics or different tones appearing when sound is added.

7.4 What does antenna self-oscillation mean for hearing?

Depending on whether one views self-oscillation as a boon, enhancing detection (e.g. Göpfert et al., 2001), or as a consequence of the different receptor fields (e.g. Lapshin, 2011, 2013), different interpretations open up to the different antenna geometries seen in CLSM between midges and mosquitoes. While the latter are somewhat evenly spread in distribution of bands of varyingly stiff elements, midges have all of those bands in the lower third of the antenna (Fig. 3.10) – which could be seen as a damping mechanism, if for midges another antenna function is more important than hearing. The same would be true if the hearing in midges is actually taking place at lower frequencies than the self-oscillation, as proposed by Lapshin (e.g. Lapshin, 2015).

In that case, self-oscillation would in fact become a hindrance. Antennae have been shown to be sensitive to a variety of stimuli covering windspeed, gravity and hearing (Kamikouchi et al., 2009, Kamikouchi, 2013, Matsuo et al., 2013) as well as olfaction (Ismail, 1962, Syed et al., 2008). All authors agree on the existence of twice-frequency forcing, but not necessarily on its function (Jackson et al., 2009, Warren, 2010, Lapshin, 2015, Windmill et al., 2018). If hearing in all these animals depends on the twice-frequency forcing (Jackson et al., 2009, Warren, 2010, Windmill et al., 2018), and the real meaningful movement is not at lower frequencies (e.g. suggested by Lapshin, 2015), the self-oscillation could, however, be beneficial to hearing in itself. It has to be stated that given the results by Göpfert for *Drosophila* and that tympanal hearing evolved multiple times, it is more than merely possible that also not all antennal hearing is completely alike, so both might be true in different species. Based on the observation that even pure tones regularly elicit their harmonics in the antenna, a question on harmonic convergence arises. In contrast to earlier reports (Downes, 1969, Lapshin, 2015), which have attested to acoustic behaviour in midges as well as in mosquitoes, vibrometry data on the investigated midge species do not show anything vaguely like the self-oscillation system observed in mosquitoes. Given that mosquitoes and *Drosophila* seem to have different motor proteins supporting hearing (Warren et al., 2010), and seeing how often types of hearing have evolved in insects, this, however, does not preclude some sort of acoustic behaviour in midges, although it is likely that it is facilitated in a different way.

On the matter of dynein and myosin, it bears mentioning that a) dynein has been implied in *Drosophila* hearing as early as Eberl et al. (2000) and that no matter where the self-oscillation is generated, it would be unable to move the flagellum if the cilia are depolymerised by colchicine.

7.5 What makes it move?

Recapitulating what has been proposed by Hart et al. (2011) based on the works of Risler it seems possible from nowadays point of view, that the more numerous type of scolopidia is involved in self-oscillation while hearing is facilitated by the approximately equally numbered type of scolopidia. My results agree with this consideration and results by Göpfert et al. (1999, 2000). They also report oscillation in both sexes, but with higher amplitudes in the male animals than in the females. In relation to Avitabile's integrate and twitch model, it has to be pointed out that anatomical data from Risler, published by Hart, indicate that not the whole scolopidium but parts thereof are more likely to be involved in vibration (Hart et al., 2011). In Avitabile's defence, it bears mentioning, however, that he never claimed to know which morphological structure represents his mathematical threads, which in synchronous action could move the flagellum (Avitabile et al., 2010). Thirdly, based on Hart et al. (2011) it appears that – despite the mechanical coupling shown by Göpfert et al. (1999) – each individual fibrilla is neuronally connected at least in some *Aedes* species. To my knowledge, however, there is no recent credible claim that the fibrillae are involved in the sense modalities of hearing. The presence and absence of fibrillae does apparently not even influence the electric activity in the pedicel (Hart et al., 2011, quoting Wishart 1962).

7.6 General observations

7.6.1 Movement of the antenna and resonant frequency of the scolopidia

Reports from Lapshin et al. (2015) of different frequency maxima in different directions, taken together with personal communication with Joseph Jackson (April 2018) indicating that once a system is in motion even with equal stiffness in all directions, the smallest perturbation can make it move outside the plane of excitation, and the articulation in a ball socket joint lead to an elliptical/circular movement. This to my knowledge has not been documented before. However, it has been postulated based on the morphology by Albert et al. (2016). In contrast, Lapshin et al. (2019) state for mosquitoes, or more precisely, *Culex* mosquitoes, that units of different tuning would be evenly distributed. Given the overall flexibility of the flagellum and the maybe not frequently but regularly observed plane shifts of the flagellar movement – be it in self-oscillation or driven condition – I would, however, go further and suggest that while the base of the flagellum is approximately locked to a plane by its connection to the flagellum, the whole structure is to a degree able to move in 3D.

The point made by Belton in 1974 that some of the architecture of the mosquito antenna might be more tailored to reject their own wingbeat than to enhance perception of the female wingbeat, while not to be rejected entirely, is questioned by results by Andres et al. (2016), which strongly indicate afferent nerves in the pedicel. Given the presence of neuronal feedback networks, the rejection of the own wingbeat could potentially be part of a neuronal feedback loop rather than a mechanical effect. In this light, it is also important to remember that antennae are multimodal.

One of the other functions is flight control, in which the neuro-architecture is better, although not fully understood, and the integration and counter-balance of antennal wing mechano-receptors and visual cues plays a role (Chan et al., 1998, Bomphrey et al., 2018) – in this context, working at similar frequencies, neuronal feedback mechanisms are crucial, they therefore also could be important in hearing. Furthermore, results by Simoes are even turning Belton’s rationale upside down by demonstrating that the Johnston’s organ is in fact tuned to the difference tone between male and female wingbeat, making the male wingbeat an essential component of acoustic detection instead of a hindrance (Simoes et al., 2016). One has to keep in mind, however, that in *Culex quinquefasciatus*, on which Simoes worked, like in many species the male and female flight tone is dramatically different – $789 \pm 10\text{Hz}$ in males vs. $474 \pm 10\text{Hz}$ in females (Simoes et al., 2016). While in other species, for example *T. brevipalpis*, both sexes fly at similar frequencies (Gibson et al., 2006) this means there could be different mechanisms involved in different species. In this mindset, looking afresh at the four to five model classes reviewed by Mhatre (2015), it is conceivable that maybe more than one model is true in the sense of capturing the situation in different animal groups. The role of effectively passive mechanisms, for example variation in cuticular properties – as shown in this work – in this context is only beginning to be understood.

7.6.2 Behavioural implications of mosquito hearing range

While there is a point to be made for behavioural experiments that show multi-metre hearing in mosquitoes (Menda et al., 2019) and that I also observed previously undocumented picometre antenna motions that are over noise level, some words of caution are indicated. The first concern is even with the good signal-to-noise behaviour observed in antenna vibration, that the natural environments where swarming occurs are not free of sounds and other vibrational noises. In fact, not in mosquitos but for substrate-borne vibrational communication, for example in leafhoppers (Mazzoni et al., 2009, Nieri et al., 2018), disrupting communication with noise is explored as management strategy – the work by Dieng (et al., 2019) uses a similar approach for mosquitoes.

There are some reservations against the use of acoustic trapping especially with airborne sounds, mainly revolving around the cost of equipment and the fact that, for example in the case of mating signals, only adults of one sex are likely to respond (e.g. Mankin, 2011). Nonetheless, Mankin (2011) concedes that in special cases, for example Hemiptera, vibrational communication is being successfully targeted, see also Mazzoni et al. (2009). Furthermore, there are considerations of environmental disturbance and unforeseen side-effects depending on the sound intensity used for trapping. With noise-cancelling technology developing and becoming cheaper, using sound-based devices might become a viable, toxin-free approach for mosquito control within human houses. The second is noise of a different, more fundamental kind, as everything that is not at 0K temperature, be it a building (alas, on this scale there would be little visible effect) or even a laser beam, is subject to thermal noise.

The picometre movements observed in the present study and given the cubic intensity drop per distance doubling for sound velocity – which in the past led to sound velocity hearing being characterised as near-field hearing – make especially females hearing male swarm aggregation, which can be approximated as sound source with the added power output of all the individuals, at least less likely. One has to keep in mind that similar claims were made for the vertebrate cochlea in the 70s because it is just the active processes in our ears that enable among others a process called active cooling generating a system that behaves in some respects as if unaffected by thermal noise. The fact that active processes have been shown in mosquitoes among other insects (Göpfert et al., 2001), so has the previously doubted efferent control (Andres, 2016), means they could potentially circumvent limitations posed by thermal noise on acoustic perception.

The third issue with the multimetre-reaching perception in mosquitoes is that, as for example Bompfrey et al. (2018), who is chiefly interested in the antenna's role in flight control, and others before (Kamikouchi et al., 2009, Nadrowski et al., 2010, Matsuo et al., 2013) pointed out, that insect antennae are multimodal sensory organs covering humidity, smell, windspeed, gravity, heat, hearing (Pielou, 1940, Schadova et al., 2009, Kamikouchi et al., 2009, Nadrowski et al. 2010, Matsuo et al., 2013), and in some cases (not relevant to the current issue) sense of touch (Staudacher et al., 2005, Harley et al., 2009, Dirks et al., 2011, Krause et al., 2012).

If the insect behaviour is apparently unchanged by covering the eyes to exclude visual stimuli for orientation, this makes it very difficult to adequately exclude the sense of smell in real swarm interactions to contribute to orientation.

In principle there are the two approaches: Firstly, ablation, but without antenna there is no hearing and smelling at the same time – that is, if in this species not the palps can perform some smell tasks as well, which would mean we got rid of hearing but the sense of smell we wanted to exclude could still be partially functional. Secondly, having animals respond to playbacks with no other animals being present. This can range from using speakers to stimulating animals with recorded or generated sounds (Göpfert, 1999, Jackson, 2006, Gibson et al., 2018, to name but a few current examples) to extreme examples like the virtual fish swimming arena by Stowers et al. (2017) – which in turn can have implications in terms of control optimisation and miniaturisation for the collective behaviour implementation for robots and the improvement of small robots (Bonnet et al., 2019) or flapping wing robots (Bomphrey et al., 2018). With especially the virtual approaches having some perks, for example in controllability, but also pitfalls in that if each individual is recorded individually, interactions (based on feedback) will not happen. However, if a natural swarm for example is recorded, one would need to solve the very same problem of other senses influencing the behaviour prior to the recording instead of prior to the experiment. Furthermore, one needs to be clear that all relevant parameters are collected for a projection/playback to be biologically relevant. This is a similar issue as has been described for simulations (Oulette, 2015). In short, there are a host of issues with experimental control here, none of which can really be solved prior to understanding what stimulus makes the animal actually display a given behaviour. Warren (2010) reported – as did earlier works, for example Belton (1974) – observing two frequency peaks in self-oscillation.

Here, in my experience, one has to distinguish two situations: either both frequencies are real and exist in parallel, or they are the product of temporal or spatial summation. It is a) possible that two peaks result from temporal summation, as the animals are capable of shifting the oscillation frequency – which was also observed in the present study –, b) it can be a product of either the different resonance frequencies in different directions (Lapshin, 2015), or of the twice-frequency forcing reliably observed for example by Windmill et al. (2019) and Lapshin et al. (2019). It could also be the same phenomenon that enables waves of different frequencies to simultaneously travel with different speeds and different directions in plants (Kovacica et al., 2017, Kovacica et al., 2018) or even, as also observed in the present study (Section 5 & 6), that spectrograms opposed to the formerly mentioned temporal summation case reveal two frequencies being present at the same time. This could be two in self-oscillation or with up to three frequencies, which are at least neither a set of harmonics nor the $2f_1-f_2$ intermodulation, resulting in different tones or harmonics of each other (Fig. 6.3-5).

7.7 The evolutionary perspective

For many Diptera (a Phylogeny can be found in Appendix 2), hearing plays a part in two fundamental tasks every living creature has to solve – the first one is locating food, as seen in frog-biting midges (Cortellidae) (Bernard et al., 2006, Menda et al., 2019, Virgo et al., 2019), the second locating and identifying mating partners, as seen in many mosquitoes (Gibson et al., 2006, Cator et al., 2009, 2011, Nadrowski et al., 2010, Menda et al., 2019). Therefore, it should come as no surprise that effective and versatile acoustic sensory organs have evolved – even if one limits oneself, as I

have, to antenna-based hearing. In this context it also does not matter whether the principle underlying hearing is difference-tone perception (e.g. Warren et al., 2009, Simoes et al., 2016) or harmonic convergence (e.g. Gibson et al., 2006, Cator et al., 2009, Aldersley et al., 2016), all described in mosquitoes but in different species. Aldersley (2016) confirmed with playback experiments that both participants in harmonic convergence play an active part independent from sex – therefore must be able to perceive – and that at least male-male interaction are more varied than the principal avoidance behaviour that was originally described by Gibson et al. (2006). Results by Tripet et al. (2004) show that wingbeat recognition cannot explain reproductive isolation in *Anopheles gambiae*. This together indicates that while important acoustic recognition on its own might not be sufficient for mating and speciation to occur.

It is known that tympanal hearing in insects evolved multiple times (Kirstensen, 1981, Robert, 2007, Strauß et al., 2015) – the same could be true for antennal hearing. At the same time, it has been shown that the chordotonal organs are conserved (Yack 2004, Strauß et al 2015) on an even broader evolutionary level as, for example, pointed out by Hoy (2006) scolopidia and hair cells in vertebrate ears are both ciliary sensory receptors. This deep convergent evolution has implications for the understanding of hearing in general and differences as well as similarities have been repeatedly reviewed in 2012 (Montealegre-Z et al.) and 2016 (Albert et al.). Furthermore, the role of loss function is not entirely clear and can obscure the number of times hearing has evolved. This issue is for example explored by Bailey et al. (2018), they also address the interesting aspect of the coevolution of host and

parasite, see also Gesto et al. (2018). The coevolution of predator and prey was for acoustics addressed for example by Windmill et al. (2006).

Like Darwin himself needed his broad database to see and understand the governing principles – which of course have been refined, but in essence do still stand – it will be necessary to collect comparable data from as many species as possible to solve the details of function and evolution of hearing, which is why it is so vexing that so many interesting findings are made in a single species, then at best generalised without further investigation and at worst forgotten as a side note of science.

7.8 Concluding Remarks

All in all, the exciting last 50 to 60 years, which have first been termed the Von-Békésy period, followed by the post-Von-Békésy period of hearing research (Dallos, 1992), have shown that given the complexity of the hearing system (in this example the vertebrate one) a lot of unexpected and interesting findings have been made since the first description of the cochlea amplifier (Kemp 1978, Rhode, 1978). The singular insect system might not be as complex, which is good from the perspective of using them as model systems. Insects have been suggested as an accessible model system for hearing in general (Boekhoff-Falk, 2005, Christie et al., 2014). There is, however, an astonishing number of different hearing solutions, for a review see (e.g. Yack, 2004). And there have been a lot of changes to our perception of their peripheral receiver system already (efferent control, active processes, and directional hearing while being small, to name but a few) there are a lot more hitherto unexplained phenomena waiting to be discovered.

The discovered patterning of hard and soft cuticle can play a part in the tuning of natural and artificial beam structures and highlight the potential importance of material properties for the function of these acoustic systems. While my vibrometry experiments rather describe the varied possibly three-dimensional responses – previously hidden from our eyes and attention – than deliver an explanation on how they are achieved and what they mean, the hope is that by adding to our catalogue of knowledge about the system, they will enable the design of future experiments that will explain their origin and meaning.

8. Reference List

- Akhtar R., Sherratt M. J., Cruickshank J. K., Derby B., 2011. Characterizing the elastic properties of tissues. *Materials today* 14 (3).
- Albert J. T., Nadrowski B., Göpfert M. C., 2007. Mechanical signatures of transducer gating in the *Drosophila* ear. *Current Biology* 17, 1000–1006. doi: 10.1016/j.cub.2007.05.004.
- Albert, J. T., Kozlov, A. S., 2016. Comparative aspects of hearing in vertebrates and insects with antennal ears. *Current Biology* 26, R1050–R1061, R1051. doi:10.1016/j.cub.2016.09.017.
- Aldersley A., Champneys A., Homer M., Robert D., 2016. Quantitative analysis of harmonic convergence in mosquito auditory interactions. *Journal of the Royal Society Interface* 13 (117), 20151007. doi:10.1098/rsif.2015.1007.
- Andres M., Seifert M., Spalhoff C., Warren B., Weiss L., Giraldo D., Winkler M., Pauls S. and Göpfert, M.C., 2016. Auditory efferent system modulates mosquito hearing. *Current Biology*, 26 (15), 2028-2036. doi: 10.1016/j.cub.2016.05.077.
- Archie-west.ac.uk. (2020). *ARCHIE-WeSt | Academic and Research Computer Hosting Industry and Enterprise in the West of Scotland*. [online] Available at: <https://www.archie-west.ac.uk/> [Accessed 15 Jan. 2020].
- Armitage P. D., Pinder L. C., Cranston P. S., eds. 2012. *The Chironomidae: Biology and ecology of non-biting midges*. 1st edition. Springer Science & Business media, Berlin/Heidelberg.
- Avitabile D., Homer M., Champneys A. R., Jackson J. C., Robert D., 2010. Mathematical modelling of the active hearing process in mosquitoes. *Journal of the Royal Society Interface* 7 (42), 105–122. doi:10.1098/rsif.2009.0091.
- Bailey N.W., Pascoal S., Montealegre-Z. F., 2018. Testing the role of trait reversal in evolutionary diversification using song loss in wild crickets. *Proceedings of the National Academy of Sciences* 116 (18), 8941–8949. doi: www.pnas.org/cgi/doi/10.1073/pnas.1818998116.
- Bartussek J., Lehmann F.-O., 2018. Sensory processing by motoneurons: a numerical model for low-level flight control in flies. *Journal of the Royal Society Interface* 15 (145): 20180408. doi: <http://dx.doi.org/10.1098/rsif.2018.0408>.
- Belton P., 1974. An analysis of direction finding in male mosquitoes. In: *Experimental analysis of insect behaviour* (139-148). Springer, Berlin, Heidelberg. doi:10.1007/978-3-642-86666-1_10.
- Benelli G., 2016. Spread of Zika virus: the key role of mosquito vector control. *Asian Pacific Journal of Tropical Biomedicine*, 6 (6), 468-471.
- Bender J. A., Dickinson M. H., 2006. A comparison of visual and haltere-mediated feedback in the control of body saccades in *Drosophila melanogaster*. *Journal of Experimental Biology*, 209 (23), 4597-4606.
- Bennet-Clark H. C., 1971. Acoustics of insect song. *Nature* 234. 255-259.
- Bennet-Clark H. C., 1998. Size and scale effects as constraints in insect sound communication. *Philosophical Transactions of the Royal Society of London. Series B: Biological Sciences*, 353 (1367), 407-419.
- Berg, M. B., Hellenthal, R. A., 1992. The role of Chironomidae in energy flow of a lotic ecosystem. *Netherland Journal of Aquatic Ecology* 26 (2-4), 471-476.

- Bergmann P., Richter S., Glöckner N., Betz O., 2018. Morphology of hindwing veins in the shield bug *Graphosoma italicum* (Heteroptera: Pentatomidae). *Arthropod structure & development*, 47 (4), 375-390. doi: 10.1016/j.asd.2018.04.004.
- Bernal X.E., Rand A.S., Ryan M.J., 2006. Acoustic preferences and localization performance of blood-sucking flies (*Corethrella Coquillett*) to túngara frog calls. *Behavioral Ecology* 17 (5), 709-715.
- Boekhoff-Falk G., 2005. Hearing in *Drosophila*: development of Johnston's organ and emerging parallels to vertebrate ear development. *Developmental dynamics: an official publication of the American Association of Anatomists* 232 (3), 550-558.
- Bomphrey R. J., Godoy-Diana R., 2018. Insect and insect-inspired aerodynamics: unsteadiness, structural mechanics and flight control. *Current opinion in insect science* 30, 26-32.
- Bonnet F., Mondada F., 2019. Shoaling with Fish: Using Miniature Robotic Agents to Close the Interaction Loop with Groups of Zebrafish *Danio rerio*. Springer Tracts in Advanced Robotics, Springer Nature Switzerland AG, Cham, Switzerland. Doi: <https://doi.org/10.1007/978-3-030-16781-3>
- Boo K. S., Richards A. G., 1975. Fine structure of the scolopidia in the Johnston's organ of male *Aedes aegypti* (L.) (Diptera: Culicidae). *International Journal of Insect Morphology and Embryology*, 4 (6), 549-566.
- Brogdon, W. G., 1998. Measurement of Flight Tone Differentiates Among Members of the *Anopheles gambiae* Species Complex (Diptera: Culicidae). *Entomological Society of America* 35 (5), 0022-2555/98/0681-0684\$02.00/0.
- Broza, M., 2008. Chironomids as a Nuisance and of Medical Importance. In: Capinera J.L., ed., *Encyclopedia of Entomology*. Springer, 2008.
- Butail S., Manoukis N. C., Diallo M., Ribeiro, J. M., Paley, D.A., 2013. The dance of male *Anopheles gambiae* in wild mating swarms. *Journal of medical entomology* 50 (3), 552-559.
- Buunen T. J. F., Vlaming, M. S. M. G., 1981. Laser-Doppler velocity meter applied to tympanic membrane vibrations in cat. *Journal of the Acoustical Society of America* 69, 744. doi: 10.1121/1.385574.
- Capanna E., 2006. Grassi versus Ross: who solved the riddle of malaria? *International Microbiology*, 9 (1), 69-74.
- Carpenter S., Wilson A., and Mellor P.S., 2009. *Culicoides* and the emergence of bluetongue virus in northern Europe. *Trends in Microbiology* 17 (4). DOI: <http://dx.doi.org/10.1016/j.tim.2009.01.001>
- Cator L. J., Arthur B., Harrington L. C., Hoy, R. R., 2009. Harmonic convergence in the love songs of the dengue vector mosquito. *Science* 323, 1077–1079, doi:10.1126/science.1166541.
- Cator L. J., Ng'Habi K. R., Hoy R. R., Harrington L. C., 2010. Sizing up a mate: variation in production and response to acoustic signals in *Anopheles gambiae*. *Behavioral Ecology*, 21 (5), 1033-1039.
- Cator L. J., Harrington, L. C., 2011. The harmonic convergence of fathers predicts the mating success of sons in *Aedes aegypti*. *Animal Behaviour* 82, 627–633. doi:10.1016/j.anbehav.2011.07.013.
- Chan W. P., Dickinson M. H., 1996. Position specific central projections of mechanosensory neurons on the haltere of the blow fly, *Calliphora vicina*. *Journal of Comparative Neurology*, 369 (3), 405-418.

- Chan W. P., Prete F., Dickinson M. H., 1998. Visual input to the efferent control system of a fly's 'gyroscope'. *Science* 280, 289–292. doi:10.1126/science.280. 5361.289
- Charlwood J. D., Jones M. D. R., 1979. Mating behaviour in the mosquito, *Anopheles gambiae* s. 1. save: I. Close range and contact behaviour. *Physiological Entomology*, 4 (2), 111-120.
- Choochote W., Jitpakdi A., Teerayut Suntaravitun T., Junkum A., Rongsriyam K., Chaithong U., 2002. A note on laboratory colonization of *Toxorhynchites splendens* by using an artificial mating technique and autogenous *Aedes togoi* larva as prey. *Journal of Tropical Medicine and Parasitology* 25, 47-50.
- Christie K.W., Eberl D. F., 2014. Noise-induced hearing loss: new animal models. *Current opinion in otolaryngology & head and neck surgery*, 22 (5), 374-383. doi:10.1097/MOO. 0000000000000086.
- Clements A. N., 1963. *The physiology of mosquitoes*. New York, USA, Pergamon Press.
- COMSOL Reference Manual. 2007.
- Dallos P., 1992. The active cochlea. *Journal of Neuroscience*, 12 (12), 4575-4585.
- Darwin C., 1959. *The Origin of Species*. The Temple Press, 1928, reprinted 1934.
- Demtröder W., 2008. *Experimentalphysik, I. Mechanik und Wärme*, 401-402. Springer, Heidelberg, 5ed. doi: 10.1007/978-3-540-79295-6.
- de Silva P., Nutter B., Bernal X. E., 2015. Use of acoustic signals in mating in an eavesdropping frog-biting midge. *Animal Behaviour* 103, 45-51. doi: <http://dx.doi.org/10.1016/j.anbehav.2015.02.002>.
- Dévai , Györgi, 1990. Ecological background and importance of the change of chironomid fauna (Diptera: Chironomidae) in shallow Lake Balaton. In: Dumont, H. J. (Ed.), *Developments in Hydrobiology*, vol. 53. Springer, Heidelberg, 189-198.
- Dieng H., The C. C., Satho T., Miake F., Wydiamala E., Kassim N. F. A., Hashim N.A., Vargas R. E. M., Morales N.P., 2019. The electronic song “Scary Monsters and Nice Sprites” reduces host attack and mating success in the dengue vector *Aedes aegypti*. *Acta tropica* 194, 93-99. doi: <https://doi.org/10.1016/j.actatropica.2019.03.027>.
- Dirks J. H., Dürr V., 2011. Biomechanics of the stick insect antenna: damping properties and structural correlates of the cuticle. *Journal of the mechanical behavior of biomedical materials* 4 (8), 2031-2042. doi:10.1016/j.jmbbm.2011.07.002.
- Domingo-Roca R., 2018. PhD Thesis. 3D-Printing Technology Applied to the Development of Bio-Inspired Functional Acoustic Systems (Department of Electronic and Electrical Engineering University of Strathclyde).
- Doppler C., 1842. Über das farbige Licht der Doppelsterne und einiger anderer Gestirne des Himmels. Calve.
- Downes J. A., 1969. The swarming and mating flight of Diptera. *Annual review of entomology* 14 (1), 271–298. doi:10.1146/annurev.en.14.010169.001415.
- Ebenstein, D.M. and Pruitt, L.A., 2004. Nanoindentation of soft hydrated materials for application to vascular tissues. *Journal of Biomedical Materials Research Part A: An Official Journal of The Society for Biomaterials, The Japanese Society for Biomaterials, and The Australian Society for Biomaterials and the Korean Society for Biomaterials*, 69(2), pp.222-232. doi: 10.1002/jbm.a.20096.

- Eberl D. F., Duyk G. M., Perrimon, N. 1997. A genetic screen for mutations that disrupt an auditory response in *Drosophila melanogaster*. *Proceedings of the National Academy of Sciences* 94 (26), 14837-14842.
- Eberl D. F., Hardy R. W., Kernan M. J., 2000. Genetically similar transduction mechanisms for touch and hearing in *Drosophila*. *Journal of Neuroscience* 20 (16), 5981–5988.
- Eriksson M., 1999. Finite element analysis and design of experiments in engineering design. Division of machine design, department of design science, faculty of engineering LTH, Lund University.
- Fedorova M.V., Zhantiev R.D., 2009. Structure and function of the Johnston's organ in *Fleureia lacustris* Kieff. males (Diptera, Chironomidae). *Entomological review* 89 (8), 896-902. Original Russian Text © M. V. Fedorova, R. D. Zhantiev, 2009. *Entomologicheskoe Obozrenie* 88 (3), 521–528.
- Feugère L., Gibson G., Roux O., 2019. How far away can female mosquitoes hear the flight tones of their conspecific male-swarm? 1MIVEGEC, IRD, CNRS, Univ. Montpellier, Montpellier, France.
- Field, L. H., Matheson, T., 1998. Chordotonal Organs of Insects. *Advances in Insect Physiology* 27.
- Gibson G., Russell I., 2006. Flying in tune: sexual recognition in mosquitoes. *Current Biology* 16, 1311–1316. doi:10.1016/j.cub.2006.05.053.
- Gibson G., Warren B., Russell I., 2010. Humming in tune: sex and species recognition by mosquitoes on the wing. *Journal of the Association for Research in Otolaryngology* 11 (4), 527-540.
- Gibson J. S., Coccoft R. B., 2018. Vibration-guided mate searching in treehoppers: directional accuracy and sampling strategies in a complex sensory environment. *Journal of Experimental Biology* 221, jeb175083. doi:10.1242/jeb.175083.
- Göpfert M. C., Briegel H., Robert D., 1999. Mosquito hearing: sound-induced antennal vibrations in male and female *Aedes aegypti*. *Journal of Experimental Biology* 202, 2727–2738.
- Göpfert M. C., Robert D., 2000. Nanometre-range acoustic sensitivity in male and female mosquitoes. *Proceedings of the Royal Society of London. Series B: Biological Sciences* 267, 453-457.
- Göpfert M. C., Robert D., 2001. Active auditory mechanics in mosquitoes. *Proceedings of the Royal Society of London. Series B: Biological Sciences* 268, 333-339.
- Göpfert M. C., Robert D., 2001b. Turning the key on *Drosophila* audition. *Nature* 411 (6840), 908.
- Göpfert M. C., Robert D., 2003. Motion generation by *Drosophila* mechanosensory neurons. *Proceedings of the National Academy of Sciences* 100 (9), 5514-5519.
- Göpfert M. C., Robert D., 2008. *Active Processes in Insect Hearing in Active Processes and Otoacoustic Emissions*. Springer, New York.
- Gesto J. S. M., Araki A. S., Caragata E. P., de Oliveira C. D., Martins A. J., Bruno R. V., Moreira L. A., 2018. In tune with nature: *Wolbachia* does not prevent pre-copula acoustic communication in *Aedes aegypti*. *Parasites & Vectors* 11 (109). doi: <https://doi.org/10.1186/s13071-018-2695-x>
- Greenfield M. D., 2016. Evolution of acoustic communication in insects. In: Pollack G. S. et al. (eds.), *Insect Hearing. Springer Handbook of Auditory Research* 55, Springer, Berlin. doi: 10.1007/978-3-319-28890-1_2.
- Gu S., 2017. Application of finite element method in mechanical design of automotive parts. IOP Conf. Series: *Materials Science and Engineering* 231 (2017), 012180. doi:10.1088/1757-899X/231/1/012180.

- Harley C. M., English B. A., Ritzmann R. A., 2009. Characterization of obstacle negotiation behaviors in the cockroach, *Blaberus discoidalis*. *Journal of Experimental Biology* 212, 1463–1476. doi: 10.1242/jeb.028381.
- Hart M., Belton P., Kuhn R., 2011. The Risler Manuscript. *Mosquito Bulletin* 29 (2011), 103-113.
- Heisenberg, M., Wolf, R., 1988. Reafferent control of optomotor yaw torque in *Drosophila melanogaster*. *Journal of Comparative Physiology A* 163, 373-388.
- Holzapfel G. A., Eberlein R., Wriggers P., Weizsäcker H. W., 1996. Large strain analysis of soft biological membranes: Formulation and finite element analysis. *Computer methods in applied mechanics and engineering*, 132(1-2), 45-61.
- Hoy A., 2006. A boost for hearing in mosquitoes. *Proceedings of the National Academy of Sciences* 103 (45), 16619-16620, www.pnas.org/cgi/doi/10.1073/pnas.0608105103.
- Hudspeth A. J., 1997. Mechanical amplification of stimuli by hair cells. *Current Opinions in Neurobiology* 7, 480-486.
- Hudspeth A. J., Choe Y., Mehta A. D., Martin P., 2000. Putting ion channels to work: Mechano-electrical transduction, adaptation, and amplification by hair cells. *PNAS* 97 (22), 11765–11772.
- Hudspeth A. J., 2008. Making an Effort to Listen: Mechanical Amplification in the Ear. *Neuron* 59 (4), 530-545.
- Hurn A.D., Wallace J.B., 1986. A method for obtaining in situ growth rates of larval Chironomidae (Diptera) and its application to studies of secondary production 1. *Limnology and Oceanography*, 31 (1), 216-222.
- Ismail I. A. H., 1962. Sense Organs in the Antennae of *Anopheles maculipennis atroparvus* (v. Thiel), and their Possible Function in relation to the Attraction of Female Mosquito to Man. *Acta Tropica* 19 (1), 1-58.
- Jackson J. C., (2006) 2012. PhD Thesis. Experimental and theoretical investigations into the active nonlinear processes of mosquito audition (Doctoral dissertation, University of Bristol).
- Jackson J. C., Robert D., 2006. Nonlinear auditory mechanism enhances female sounds for male mosquitoes. *Proceedings of the National Academy of Sciences* 103 (45), 16734-16739. doi:10.1073/pnas.0606319103
- Jackson J. C., Windmill J. F. C., Victoria G., Pook V.G., Robert, D., 2009. Synchrony through twice-frequency forcing for sensitive and selective auditory processing. *Proceedings of the National Academy of Sciences* 106 (10), 177–10 182. doi:10.1073_pnas.0901727106.
- Jennings, D.M., and Mellor P.S., 1988. The Vector Potential of British *Culicoides* species for Bluetongue Virus. *Veterinary Microbiology* 17 (1988), 1-10
- Johnston C., 1855. Original communications: auditory apparatus of the *Culex* mosquito. *Journal of Cell Science*, 1(10), 97-102.
- Kamikouchi A., Inagaki H. K., Effertz T., Hendrich O., Fiala A., Göpfert M. C., Ito K., 2009. The neural basis of *Drosophila* gravity-sensing and hearing. *Nature* 458, 165-171.
- Kamikouchi A., Albert J. T., Göpfert M. C., 2010. Mechanical feedback amplification in *Drosophila* hearing is independent of synaptic transmission. *European Journal of Neuroscience* 31, 697–703.
- Kamikouchi A., 2013. Auditory neuroscience in fruit flies. *Neuroscience Research* 76, 113–118.

- Khanzadi M.N., Khan A.A., 2019. CRISPR/Cas9: Nature's gift to prokaryotes and an auspicious tool in genome editing. *Journal of Basic Microbiology* 2019, 1-12. DOI: 10.1002/jobm.201900420
- Kemp D. T., 1978. Stimulated acoustic emissions from within the human auditory system. *Journal of the Acoustical Society of America* 64, 1386. doi: 10.1121/1.382104.
- Kernan M., Cowan D., Zuker C., 1994. Genetic Dissection of Mechanosensory Transduction: Mechanoreception-Defective Mutations of *Drosophila*.
- Keppler M., 1958. Zum Hören von Stechmücken. *Zeitschrift für Naturforschung (B)* 13, 280-284.
- Kössl M., Coro F., Seyfarth E.-A., Nässig W. A., 2008. Otoacoustic emissions from insect ears having just one auditory neuron. *Journal of Comparative Physiology A*, 193 (8), 909–915. doi: 10.1007/s00359-007-0244-8.
- Kovacica I., Radomirovic D., Zukovica M., Pavel B., Nikolic M., 2018. Characterisation of tree vibrations based on the model of orthogonal oscillations. *Scientific reports*, 8 (1), 8558. doi:10.1038/s41598-018-26726-5.
- Kovacica I., Radomirovic D., Zukovica M., 2018. Tree vibrations: Determining oscillatory properties by using infra-red marker-tracking system. *Urban Forestry & Urban Greening* 34, 114–120. doi: https://doi.org/10.1016/j.ufug.2018.06.010.
- Krause A. F., Dürri V., 2012. Active tactile sampling by an insect in a step-climbing paradigm. *Frontiers in behavioral neuroscience*, 6, 1–17. doi:10.3389/fnbeh.2012.00030.
- Kristensen N. P., 1981. Phylogeny of insect orders. *Annual review of entomology*, 26 (1), 135-157.
- Kuzenkov O., Morozov A., 2019. Towards the Construction of a Mathematically Rigorous Framework for the Modelling of Evolutionary Fitness. *Bulletin of Mathematical Biology*, 1-26. doi: https://doi.org/10.1007/s11538-019-00602-3.
- Lankheet, M. J., Cerkenik, U., Larsen, O. N., van Leeuwen, J. L., 2017. Frequency tuning and directional sensitivity of tympanal vibrations in the field cricket *Gryllus bimaculatus*. *Journal of The Royal Society Interface*, 14 (128), 20170035.
- Lapshin D. N., 2011. Mosquito bioacoustics: auditory processing in *Culex pipiens pipiens* L. Males (Diptera, Culicidae) during flight simulation. *Entomological review* 92 (6), 605-621.
- Lapshin D. N., Vorontsov D. D., 2013. Frequency tuning of individual auditory receptors in female mosquitoes (Diptera, Culicidae). *Journal of Insect Physiology* 59, 828-839.
- Lapshin D. N., 2015. Directional and frequency characteristics of auditory receptors in midges (Diptera, Chironomidae). *Entomological Review* 95 (9), 1155-1165.
- Lapshin D. N., Vorontsov D. D., 2019. Directional and frequency characteristics of auditory neurons in *Culex* male mosquitoes. bioRxiv preprint first posted online Apr. 13, 2019; doi: http://dx.doi.org/10.1101/608778.
- Liu J., Heng H., Poh P. S. P., Machens H.-G., Schilling A. F. H., 2015. Hydrogels for engineering of perfusable vascular networks. *International journal of molecular sciences* 16 (7), 15997-16016. doi: 10.3390/ijms160715997.
- Lu Q., Senthilan P. R., Effertz T., Nadrowski B., Göpfert M. C., 2009. Using *Drosophila* for studying fundamental processes in hearing. *Integrative and comparative biology* 49 (6), 674-680.

- Mackie, D. J., 2015. PhD thesis. Biologically inspired acoustic systems: from insect ears to MEMS microphone structures. (Department of Electronic and Electrical Engineering University of Strathclyde).
- Malkin R., McDonagh T.R., Mhatre N., Scott T.S., Robert D., 2014. Energy localization and frequency analysis in the locust ear. *Journal of the Royal Society Interface* 11, 20130857. doi:10.1098/rsif.2013.0857.
- Mankin R. W., 2012. Applications of acoustics in insect pest management. *CAB Reviews*, 7 (001), 1-7.
- Manley G., 2000. Cochlear mechanisms from a phylogenetic viewpoint. *Proceedings of the National Academy of Sciences* 97, 11736–11743.
- Manley F. A., Fay R. R., Popper A. N. Springer Handbook of Auditory research, 2008, ISBN 978 0387 714677.
- Manson P., 1900. Experimental proof of the mosquito-malaria theory. *British medical journal* 2 (2074), 946-951.
- Martin P., Mehta A. D., Hudspeth A. J., 2000. Negative hair-bundle stiffness betrays a mechanism for mechanical amplification by the hair cell. *Proceedings of the National Academy of Sciences* 97 (22), 12026–12031.
- Masters B. R., 2010. The Development of Fluorescence Microscopy. In: Encyclopedia of Life Sciences (ELS). John Wiley & Sons, Ltd: Chichester. doi: 10.1002/9780470015902.a0022093.
- Matsumura Y., Michels J., Appel E., Gorb S. N., 2017. Functional morphology and evolution of the hyperelongated intromittent organ in *Cassida* leaf beetles (Coleoptera: Chrysomelidae: Cassidinae). *Zoology* 120, 1–14. doi:10.1016/j.zool.2016.08.001.
- Matsuo, E., Kamikouchi, A., 2013. Neuronal encoding of sound, gravity, and wind in the fruit fly. *Journal of Comparative Physiology A*, 199 (4), 253-262. doi: 10.1007/s00359-013-0806-x.
- Mazzoni V., Lucchi A., Čokl A., Prešern J., Virant-Doberlet M., 2009. Disruption of the reproductive behaviour of *Scaphoideus titanus* by playback of vibrational signals. *Entomologia experimentalis et applicata*, 133 (2), 174-185. doi: 10.1111/j.1570-7458.2009.00911.x.
- McIver S., Siemicki R., 1978. Fine structure of antennal sensilla coeloconica of adult *Toxorhynchites brevipalpis* (Diptera: Culicidae). *Journal of Medical Entomology* 14 (6), 673-676.
- Menda G., Nitzany E. I., Shamble P. S., Wells A., Harrington L. C., Miles R. N., Hoy R. R., 2019. The long and short of hearing in the mosquito *Aedes aegypti*. *Current Biology* 29 (4), 709-714. doi: https://doi.org/10.1016/j.cub.2019.01.026.
- Mercer C., 2006. Prosig Signal Processing Tutorials, Acceleration, velocity and Displacement Spectra- Omega Arithmetic. prosig.com/wpcontent/uploads/pdf/blogArticles/OmegaArithmetic.pdf www.prosig.com – last accessed 16.09-2019
- Mhatre N., Robert D., 2013. A tympanal insect ear exploits a critical oscillator for active amplification and tuning. *Current Biology*, 23 (19), 1952–1957. doi: http://dx.doi.org/10.1016/j.cub.2013.08.028
- Mhatre N., 2015. Active amplification in insect ears: mechanics, models and molecules. *Journal of Comparative Physiology A* 201 (1), 19-37.
- Michels J., Gorb S. N., 2012. Detailed three-dimensional visualization of resilin in the exoskeleton of arthropods using confocal laser scanning microscopy. *Journal of microscopy*, 245 (1), 1-16. doi:10.1111/j.1365-2818.2011.03523.x.

- Michelsen A, Larsen ON. 1985. Hearing and sound. In: Kerkut GA, Gilbert LI, editors. *Comprehensive insect physiology, biochemistry, and pharmacology*. New York: Pergamon Press., USA, p 495–556.
- Michelsen A, Löhe G. 1995. Tuned directionality in cricket ears. *Nature* 375, 639, doi:10.1038/375639a0.
- Michelsen A, Popov AV, Lewis B. 1994. Physics of directional hearing in the cricket *Gryllus bimaculatus*. *J. Comp. Physiol. A* 175, 153–164, doi:10.1007/BF00215111.
- Michelsen A: Biophysics of sound localization in insects. In: *Comparative Hearing: Insects*. Edited by Hoy RR, Popper AN, Fay RR. New York: Springer; 1998:18-62.
- Minsky, M., 1961. Microscopy apparatus. US3013467
- Mitchell, D. R. 2007. The evolution of eukaryotic cilia and flagella as motile and sensory organelles. *Adv. Exp. Med. Biol.* 607, 130–140. (doi:10.1007/978-0-387-74021-8_11).
- Montealegre-Z F., Jonsson T., Robson-Brown, K. A. Postles, M., Robert D., 2012. Convergent evolution between insect and mammalian audition. *Science* 338 (6109), 968-971.
- Mountcastle A. M., Combes S. A., 2013. Wing flexibility enhances load-lifting capacity in bumblebees. *Proceedings of the Royal Society B: Biological Sciences*, 280 (1759), 20130531. doi:10.1098/rspb.2013.0531.
- Nadrowski B., Göpfert M. C., 2009. Level-dependent auditory tuning: transducer-based active processes in hearing and best-frequency shifts. *Communicative & integrative biology*, 2(1), 7-10.
- Nadrowski B., Göpfert M. C., 2009b. Modelling auditory transducer dynamics. *Current Opinion in Otolaryngology & Head and Neck Surgery* 2009, 17, 400–406.
- Nadrowski B., Effertz T., Senthilan P. R., Göpfert M. C., 2010. Antennal hearing in insects. New findings, new questions. *Hearing Research* 273, 7-13, doi: 10.1016/j.heares.2010.03.092.
- Neal, H.V. & Rand, H.W. *Comparative anatomy*. Philadelphia, USA, P. Blakiston's Son & CO., Fig. 497, p. 600.
- Neff D., Frazier S. F., Quimby L., Wang R.-T., Zill S., 2000. Identification of resilin in the leg of cockroach, *Periplaneta americana*: confirmation by a simple method using pH dependence of UV fluorescence. *Arthropod Structure and Development* 29, 75–83. doi:10.1016/S1467-8039(00)00014-1.
- Neems R. M., Lazarus J., Mclachlan A. J., 1992. Swarming behavior in male chironomid midges: a cost-benefit analysis. *Behavioral Ecology*, 3 (4), 285-290.
- Nijhout H. F., 1977. Control of antennal hair erection in male mosquitoes. *The Biological Bulletin*, 153 (3), 591-603.
- Nieri R., Mazzoni V., 2018. Vibrational mating disruption of *Empoasca vitis* by natural or artificial disturbance noises. *Pest management science*, 75 (4), 1065-1073. doi 10.002/ps.5216.
- Ogawa K., Sato, H., 1993. Relationship between male acoustic response and female wingbeat frequency in a chironomid midge, *Chironomus yoshimatsui* (Diptera: Chironomidae). *Japanese Journal of Sanitary Zoology*, 44, 355-355.
- Ouellette N. T., 2015. Empirical questions for collective-behaviour modelling. *Pramana —journal of physics* 84(3), 353–363, doi: 10.1007/s12043-015-0936-5.

- Peisker H, Michels J, Gorb S.N., 2013 Evidence for a material gradient in the adhesive tarsal setae of the ladybird beetle *Coccinella septempunctata*. *Nature communications*, 4, 1661. doi:10.1038/ncomms2576
- Pennetier C., Warren B., Dabire K. R., Russell, I. J., Gibson, G., 2010. ‘Singing on the wing’ as a mechanism for species recognition in the malarial mosquito *Anopheles gambiae*. *Current Biology* 20(2), 131–136. doi:10.1016/j.cub.2009.11.040.
- Pielou, D. P., 1940. The Humidity Behaviour of the Mealworm Beetle, *Tenebrio Molitor* L. *Journal of Experimental Biology*, 17 (3), 295-306.
- Polytec Scanning Vibrometer Theory Manual, Software 9.1.
- Polytec Software Quick Start Guide.
- Polytec Accessories for Stand Based Systems guide.
- Polytec Micro System Analyzer MSA-100-3D Operating Instruction.
- Polytec Scanning Vibrometer MSA-100-3D Acquisition, version 9.4.
- Polytec Scanning Vibrometer MSA-100-3D Presentation, version 9.4.
- polytec.com/int/vibrometry/technology/\$laser-doppler-vibrometry/ last accessed 2019.10.31
- Puckett J. G., Ni R., Oullette N. T., 2015. Time-Frequency Analysis Reveals Pairwise Interactions in Insect Swarms. *Physical Review Letters* 114, 258103.
- Rajabi H., Shafiei A., Darvizeh A., Gorb S. N., Dürr V., Dirks J.-H., 2018. Both stiff and compliant: morphological and biomechanical adaptations of stick insect antennae for tactile exploration. *Journal of the Royal Society Interface* 15, 20180246, doi:10.1098/rsif.2018.0246.
- Rao S. S., Yap F. F., 2011. *Mechanical vibrations* (vol. 5). Prentice Hall. London.
- Reid A. B., 2017. PhD Thesis. Directional Hearing at the Micro-Scale: Bio-inspired Sound Localization. (Department of Electronic and Electrical Engineering, University of Strathclyde).
- Riemann, B., 1851. *Grundlagen für eine allgemeine Theorie der Functionen einer veränderlichen complexen Grösse* (Basis of a general theory of function of a variable complex quantity. Doctoral dissertation University Göttingen).
- Ristroph L., Bergou A. J., Ristroph G, Coumes K., Berman G. J., Guckenheimer J., Wang Z. J., Cohen I., 2010. Discovering the flight autostabilizer of fruit flies by inducing aerial stumbles. *Proceedings of the National Academy of Sciences* 107, 4820–4824. doi:10.1073/pnas. 1000615107.
- Ritz W., 1909. Über eine neue Methode zur Lösung gewisser Variationsprobleme der mathematischen Physik. *Journal für die reine und angewandte Mathematik* 135, 1861-1909.
- Regen, J., 1913. Über die Anlockung des Weibchens von *Gryllus campestris* L. durch telephonisch übertragene Stridulationslaute des Männchens. *Pflügers Archiv European Journal of Physiology*, 155 (1), 193-200.
- Rhode W. S., 1978. Some observations on cochlear mechanics. *Acoustic Society of America* 64 (1).
- Robert D., Göpfert M. C., 2002. Novel schemes for hearing and orientation in insects. *Current opinion in neurobiology* 12 (6), 715-720.

- Robert D., 2007. Insect hearing and nanoscale mechanoreception. 3rd International Symposium on Plant Neurobiology.
- Robert D., Hoy R. R., 2007. Auditory Systems in Insects. *Cold Spring Harbor Monograph Archive*, 49, 155-184.
- Rothberg S. J., Allen M. S., Castellini P., Di Maio D., Dirckx, J. J. J., Ewins D. J., Halkon B. J., Muysshondt P., Paone N., Ryan T., Steger H., 2017. An international review of laser Doppler vibrometry: Making light work of vibration measurement. *Optics and Lasers in Engineering*, 99, 11-22. doi: <https://doi.org/10.1016/j.optlaseng.2016.10.023>
- Salim Z.T., Hashim U., Arshad M. K. Md., Fakhri M. A., Salim E. T., 2017. Frequency-based detection of female Aedes mosquito using surface acoustic wave technology: Early prevention of dengue fever. *Microelectronic Engineering* 179 (2017) 83–90, <http://dx.doi.org/10.1016/j.mee.2017.04.016>.
- Saltin B. D., Matsumura Y., Reid A., Windmill J. F., Gorb S. N., Jackson J. C., 2019. Material stiffness variation in mosquito antennae. *Journal of the Royal Society Interface*, 16 (154), p.20190049.
- Sane S. P., McHenry M. J., 2009. The biomechanics of sensory organs. *Integrative and Comparative Biology*, i8-i23, 411 doi:10.1093/icb/icp112.
- Su M.P., Andrés M., Boyd-Gibbins N., Somers J., Albert J. T., 2018. Sex and species specific hearing mechanisms in mosquito flagellar ears. *Nature Communications*. doi: 10.1038/s41467-018-06388-7
- Sawadogo S.P., Diabaté A., Toé H.K., Sanon A., Lefevre T., Baldet T., Gilles J., Simard F., Gibson G., Sinkins S., Dabiré R.K., 2013. Effects of age and size on Anopheles gambiae as male mosquito mating success. *Journal of medical entomology*, 50 (2), 285-293.
- Sehadova H., Glaser F. T., Gentile C., Simoni A., Giesecke A., Albert J. T., Stanewsky R., 2009. Temperature entrainment of Drosophila's circadian clock involves the gene nocte and signaling from peripheral sensory tissues to the brain. *Neuron* 64, 251-266.
- Simões P. M. V., Robert A., Ingham R. A., Gibson G., Russell I. J., 2016. A role for acoustic distortion in novel rapid frequency modulation behaviour in free-flying male mosquitoes. *The Company of Biologists Ltd | Journal of Experimental Biology* 219, 2039-2047 doi:10.1242/jeb.135293.
- Simões P. M. V., Ingham R., Gibson G., Russell I. J., 2018. Masking of an auditory behaviour reveals how male mosquitoes use distortion to detect females. *Proceedings of the Royal Society B: Biological Sciences*, 285 (1871), 20171862. <http://dx.doi.org/10.1098/rspb.2017.1862>.
- Spitzen J., Takken W., 2018. Keeping track of mosquitoes: a review of tools to track, record and analyse mosquito flight. *Parasites & Vectors* 11, 123.
- Staudacher E.M., Gebhardt M., Dürr V., 2005. Antennal movements and mechanoreception: neurobiology of active tactile sensors. *Advanced Insect Physiology* 32, 49–205. doi:10.1016/S0065-2806(05)32002-9.
- Steffan W. A., Evenhuis N. L., 1981. Biology of Toxorhynchites. *Annual Review of Entomology* 26, 159-181.
- Stowers J. R., Hofbauer M., Bastien R., Griessner J., Higgin P., Farooqui S., Fischer R. M., Nowikovsky K., Haubensak W., Couzin I. D., Tessmar-Raible K., 2017. Virtual reality for freely moving animals. *Nature methods*, 14(10), 995. doi:10.1038/nmeth.4399.

- Strauß J., Stumpner A., 2015. Selective forces on origin, adaptation and reduction of tympanal ears in insects. *Journal of Comparative Physiology A*, 201(1), 155-169.
- Syed Z., Leal W.S., 2008. Mosquitoes smell and avoid the insect repellent DEET. *Proceedings of the National Academy of Sciences* 105 (36), 13598-13603 doi/10.1073/pnas.0805312105.
- Tait-Burkard C., Doeschl-Wilson A., McGrew M.J., Archibald A.L., Sang H., M. Houston, R.D., Whitelaw, C.B., and Watson, M., 2018: Livestock 2.0 – genome editing for fitter, healthier, and more productive farmed animals. *Genome Biology* 19:204 doi:10.1186/s13059-018-1583-1
- Thurm U., 1965. An Insect Mechanoreceptor Part I: Fine Structure and Adequate Stimulus. In: *Cold Spring Harbor symposia on quantitative biology* 30, 75-82. Cold Spring Harbor Laboratory Press.
- Tischner H., 1954. Das Hören von Stechmücken. *Attempto* 4, 23-26.
- Todi S. V., Sharma Y., Eberl D. F., 2004. Anatomical and molecular design of the Drosophila antenna as a flagellar auditory organ. *Microscopy research and technique*, 63 (6), 388-399.
- Tripet F., Dolo G., Traoré S., Lanzaro, G. C., 2004. Tripet, F., Dolo, G., Traoré, S. and Lanzaro, G.C., 2004. The "wingbeat hypothesis" of reproductive isolation between members of the Anopheles gambiae complex (Diptera: Culicidae) does not fly. *Journal of medical entomology*, 41 (3), 375-384.
- Uga S., Kuwabara M., 1965. On the fine structure of the chordotonal sensillum in antenna of Drosophila melanogaster. *Journal of Electron Microscopy* 14, 173-181.
- Von Békésy G., 1960. *Experiments in hearing* (Vol. 8). New York: McGraw-Hill.
- Vincent, J. F. V., Wegst, U. G. K., 2004. Design and mechanical properties of insect cuticle. *Arthropod Structure and Development* 33, 187–199, doi:10.1016/j.asd.2004.05.006.
- Virgo J., Ruppert A., Lampert K. P., Grafe T. U., Eltz T., 2019. The sound of a blood meal Acoustic ecology of frog-biting midges (Corethrella) in lowland Pacific Costa Rica. *Ethology* 125 (7) 465–475. doi: 10.1111/eth.12871.
- Vigoder F. M., Souza N. A., Peixoto A. A., 2011. Acoustic signals in the sand fly Lutzomyia (Nyssomyia) intermedia (Diptera: Psychodidae). *Parasites & Vectors* 4 (1) 76
- Warren, B., 2011. *Hearing and acoustic interaction in mosquitoes* (Doctoral dissertation, University of Sussex).
- Warren B., Gibson G., Russell I. J., 2009. Sex recognition through midflight mating duets in Culex mosquitoes is mediated by acoustic distortion. *Current Biology* 19, 485–491. doi:10.1016/j.cub.2009.01.059.
- Warren B., Lukashkin A. N., Russell I. J., 2010. The dynein–tubulin motor powers active oscillations and amplification in the hearing organ of the mosquito. *Proceedings of the Royal Society B: Biological Sciences*, 277 (1688), 1761-1769. doi:10.1098/rspb.2009.2355.
- Wegst U. G. K., Ashby M. F., 2004. The mechanical efficiency of natural materials. *Philos. Mag.* 84, 2167–2181. Doi: 10.1080/14786430410001680935
- Wenk P., 1965. Über die Biologie blutsaugender Simuliiden. *Zeitschrift für Morphologie und Ökologie der Tiere* 55, 671-713.
- Whitear M., 1960. Chordotonal organs in Crustacea. *Nature* 187, 522-523.
- Wickramarachi P., 2003. Effects of windowing on the spectral content of a signal. *Sound and Vibration*, 37 (1), 10-13.

Wiederhold M. L., 1976. Mechanosensory transduction in " sensory" and " motile" cilia. *Annual review of biophysics and bioengineering*, 5 (1), 39-62. doi:10.1146/annurev.bb.05.060176.000351.

Windmill J. F. C., Jackson J. C., Tuck E. J., Robert D., 2006. Keeping up with Bats: Dynamic Auditory Tuning in a Moth. *Current Biology* 16, 2418–2423, doi: 10.1016/j.cub.2006.09.066

Windmill, J.F., Jackson, J.C., Pook, V.G. and Robert, D., 2018. Frequency doubling by active in vivo motility of mechanosensory neurons in the mosquito ear. *Royal Society open science* 5 (1), 171082. doi: <http://dx.doi.org/10.1098/rsos.171082>.

Wishart, G. and Riordan, D.F., 1959. Flight responses to various sounds by adult males of *Aedes aegypti* (L.) (Diptera: Culicidae). *The Canadian Entomologist*, 91(3), pp.181-191.

Wishart G., van Sickle G. R., Riordan, D. F., 1962. Orientation of the males of *Aedes aegypti* (L.) (Diptera:Culicidae) to sound. *The Canadian Entomologist* 98, 613-626.

World Malaria Report, 2018, Geneva: World Health organization; 2018 ISBN 978 92 4 156565 3, CC-BY-NC-SA 3.0 IGO

Yack Y. E., 2004. The structure and function of auditory chordotonal organs in insects. *Microscopy Research and Technique* 63, 315–337. doi:10.1002/jemt.20051

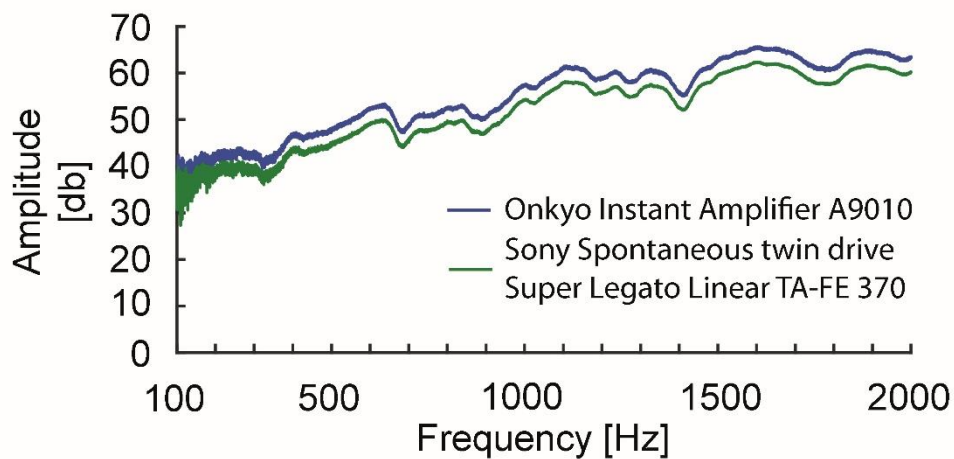
Zhantiev R. D., Fyodorova M. V., 1999. Fine Structure of Male Johnston's Organ in *Chironomus plumosus* L. (Diptera, Chironomidae). *ENTOMOLOGICAL REVIEW C/C OF ENTOMOLOGICHESKOE OBOZRENIE*, 79, 148-155.

Zienkiewicz O. C., Taylor R. L., Zhu J. H., 2005. The finite element method: its basis and fundamentals. Elsevier Butterworth-Heinemann Linacre House, Jordan Hill, Oxford.

9. Appendix

9.1 Speaker Characterisation

In order to verify reproducibility the response of the used speaker in combination with both used amplifiers was recorded with the calibrated B&K microphone (see microphone calibration). The below figure illustrates this between 0.1kHz and 2kHz. Please note that for each experiment also a reference microphone recorded the sound field right next to the animal, hence it is only of limited concern that the response, while not entirely flat, has a less than 2% component, which is outside twice the standard variation. The averages are Onkyo 55dB Sony Legato 52dB, The median values 57dB for the Onkyo Amplifier and 54 for the Sony Legato.



FigA1: Speaker and amplifier response between 0.1-2kHz of the Onkyo-(blue) and Sony Legato-amplifier (green). For equipment description see section 2.

9.2 Phylogeny of Diptera

This page is dedicated to illustrating the phylogenetic relation of the genera investigated as well as the distance between some groups, which have the ability to perceive sound. *Toxorhynchites brevipalpis*, *Anopheles arabiensis*, and *An. gambiae* are all Culicomorpha, *Chironomus riparius* is part of Chironomidae. The phylogenetic tree by Wiegmann (et al., 2011) was chosen as base.

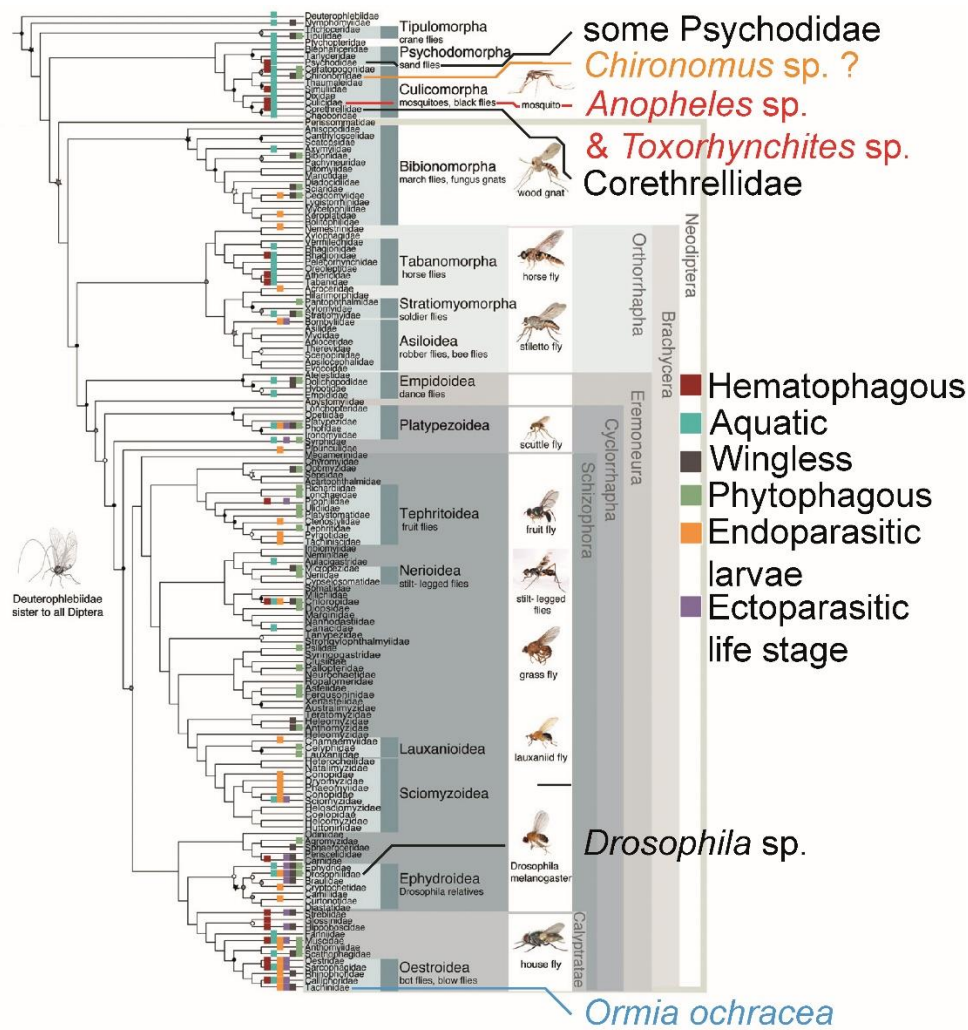


Fig. A2: The basic tree is from Wiegmann (et al., 2011). It already contained mapped on the tree some larval characters and hematophagy. For the thesis I added groups or species in larger font – were hearing is proven or implied in at least some species. *Ormia ochracea* – the only known Diptera with sophisticated pressure-based hearing – is shown in blue. For tree statistics (bootstrap values etc) and detail see Wiegmann (et al., 2011).

Research



Cite this article: Saltin BD, Matsumura Y, Reid A, Windmill JF, Gorb SN, Jackson JC. 2019 Material stiffness variation in mosquito antennae. *J. R. Soc. Interface* **16**: 20190049. <http://dx.doi.org/10.1098/rsif.2019.0049>

Received: 26 January 2019

Accepted: 23 April 2019

Subject Category:

Life Sciences – Engineering interface

Subject Areas:

biomechanics, biophysics, biomaterials

Keywords:

Anopheles, mating behaviour, *Toxorhynchites*, confocal laser scanning microscopy, finite-element modelling, antennal hearing

Author for correspondence:

B. D. Saltin
e-mail: brian.saltin@gmx.de

Electronic supplementary material is available online at <https://dx.doi.org/10.6084/m9.figshare.c.4492862>.

Material stiffness variation in mosquito antennae

B. D. Saltin¹, Y. Matsumura², A. Reid¹, J. F. Windmill¹, S. N. Gorb² and J. C. Jackson¹

¹Centre for Ultrasonic Engineering, Department of Electronic and Electrical Engineering, University of Strathclyde, 204 George Street, Glasgow G1 1XW, UK

²Department of Functional Morphology and Biomechanics, Zoological Institute of the University of Kiel, Am Botanischen Garten 9, 24118 Kiel, Germany

id BDS, 0000-0001-6668-962X; YM, 0000-0002-3438-2161; AR, 0000-0003-0511-4640; JFW, 0000-0003-4878-349X; SNG, 0000-0001-9712-7953; JCI, 0000-0001-9302-8157

The antennae of mosquitoes are model systems for acoustic sensation, in that they obey general principles for sound detection, using both active feedback mechanisms and passive structural adaptations. However, the biomechanical aspect of the antennal structure is much less understood than the mechano-electrical transduction. Using confocal laser scanning microscopy, we measured the fluorescent properties of the antennae of two species of mosquito—*Toxorhynchites brevipalpis* and *Anopheles arabiensis*—and, noting that fluorescence is correlated with material stiffness, we found that the structure of the antenna is not a simple beam of homogeneous material, but is in fact a rather more complex structure with spatially distributed discrete changes in material properties. These present as bands or rings of different material in each subunit of the antenna, which repeat along its length. While these structures may simply be required for structural robustness of the antennae, we found that in FEM simulation, these banded structures can strongly affect the resonant frequencies of cantilever-beam systems, and therefore taken together our results suggest that modulating the material properties along the length of the antenna could constitute an additional mechanism for resonant tuning in these species.

1. Introduction

The exquisite sensitivity of animal sensory organs has been noted many times [1–6]. However, little attention has been paid to the mechanical properties that shape a sensor's response as much, if not more, as the neuronal filters [7]. The mosquito antenna is a well-known example of a highly sensitive particle-velocity receptor [2,3,8,9], and in many species, the key function of the antenna is to locate the flying conspecific mate [2,10–12]. Different models on how they achieve complex mechanical behaviour, for example, active amplification, have been proposed and are reviewed by Mhatre [13]. While knowledge of mechanical behaviour, for some sensory organs, has increased in the last decade [7], rather little is known about the material composition and properties underlying these complex behaviours in terms of the geometry-defining distribution of stresses and strains within the sensor [7].

The mosquito antenna comprises three parts—scape, pedicel and flagellum [1] (figure 1). Control of the antennal direction is done in part by the scape, but the scape is not relevant to the present study. The pedicel houses some 16 000 sensory neurons [14], the majority of which are used for acoustic detection. These neurons connect to radially distributed prongs, attaching the neurons to the base of the flagellum. The flagellum itself is the physical sensor—it consists of 13 sequential flagellomeres that project distally. These act as viscosity sensors, undergoing oscillatory displacement in the presence of

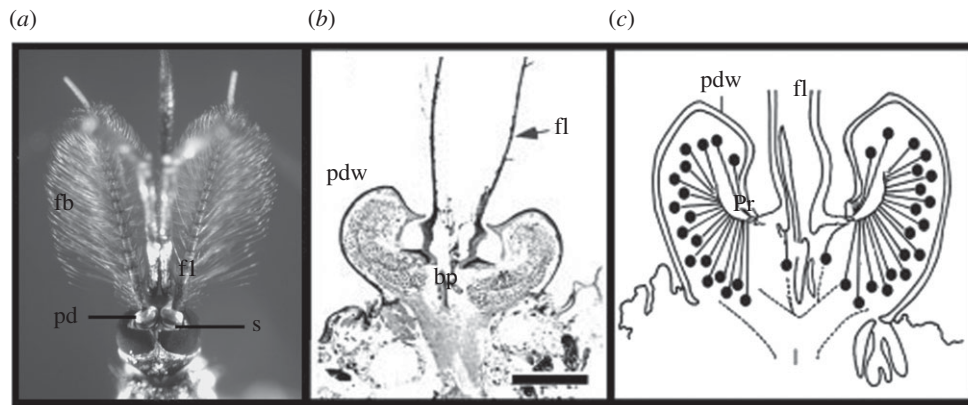


Figure 1. Schematic of antenna morphology. (a) Head of *T. brevipalpis*. (b) Cross section of the pedicel scale bar 0.1 mm. (c) Schematic of the inside of the pedicel (b,c) from Yack [15], simplified and modified. Image abbreviations: bp, basal plate; fb, fibrillae; fl, flagellum; pd, pedicel; pdw, pedicel wall; pr, prongs; s, scape.

acoustic fluid flow. The flagellum is covered in hair-like structures known as fibrillae (or setae) in which case the antenna is considered *plumose*—these fibrillae serve to increase the viscosity of the sensor improving its performance [2]. It has been shown that for biologically relevant sounds, the flagellum moves like a paddle [2]. Taken together, the whole system is resonantly tuned to respond maximally at the wingbeat frequencies of flying conspecifics and is the key sensor in the animal's phonotactic mating behaviour [11].

Most research into mosquito audition focuses on the biophysical basis for mechano-electrical transduction that endows these sensors with high sensitivity and often assumes that the flagellum is simply a stiff rod in which the material properties are of negligible importance. However, we consider material properties to be an overlooked and potentially important factor in the biophysics of acoustic perception. As the resonance of the whole system will undoubtedly be determined by some contribution of the flagellum and the effective stiffness of the pedicel attachment, it is possible that the way in which the flagellum is built may be significant for resonance tuning, and thus mating behaviour. Therefore, with no *a priori* expectation on the spatial distribution of material properties, we investigated the stiffness distribution in mosquito antennae with confocal laser scanning microscopy (CLSM).

The use of CLSM for obtaining information about general types of cuticle present is well established (e.g. [16–24]). It enables us to visualize the insect exoskeleton using autofluorescences and to estimate material properties of structures. Michels & Gorb formulated that it is capable of estimating material properties, since well-sclerotized, flexible and resilin-dominated regions are visualized differently [16]. It has also been previously cross-validated using three-point bending tests, AFM nanoindentation and compression tests [17,22,23]. Merits of CLSM are that the technique allows one to take sharp images of narrow sample planes by restriction of light entering the camera. This is achieved by the appropriate choice of pinhole size depending on the wavelength of the light, creating optical sections of the object. This image stack in turn then can be combined to create maximum intensity projections—in one image—showing the structure without loss of depth resolution (electronic supplementary material, table S1). One can therefore image the whole intact surface structure in great detail. In addition, the varying excitability of different unknown cuticle compounds with different laser wavelengths provides an estimation of material properties of the cuticle.

In many mosquito species, acoustic communication is essential for mating [10–12,15] and many are vectors for animal and human diseases, such as malaria, yellow fever or the zika virus [12,25]—indicating how important it is to understand their biology.

Antennae of two mosquito species of different size and ecology—*Toxorhynchites brevipalpis* and *Anopheles arabiensis*—were examined here. Many *Anopheles* species are swarming mosquitoes in which acoustics is crucial during mating [10,11,26,27]. However, *T. brevipalpis* is a solitary non-swarming species, in which their behaviour is scarcely documented [28,29].

There is significant interest in the *Toxorhynchites* genus for mosquito population control as its larvae predate on other mosquito larvae, many of which are species that have global importance [28,29]. As this mosquito is large, robust and non-biting, it has been previously used as an amenable model system in earlier studies of insect auditory systems [8,9,26,30]. According to Gibson & Russell [30], the wingbeat frequency of males and females synchronize during aerial mating [12,26]—and this is termed distinct flight/wingbeat frequency-matching during the mating display. As antennal ears are part of detecting the mating partner, and beam-like structures are most sensitive around their resonance, it is beneficial to have the resonance of the sensory organ close to the acoustic stimulus (the wingbeat frequency) [31]. Similar acoustic behaviour has been observed in *Anopheles*, which are responsible for the spread of diseases in cattle and humans, and therefore play a substantial social and economic role [27].

Neither of the two species mentioned above have, to our knowledge, been studied for the potentially varying stiffness along the length of the flagellum. As we will show, CLSM proves to be very useful in demonstrating changes in material stiffness along the flagellum. From the results of the CLSM work detailed later, we used finite-element modelling (FEM) to determine the effect of the measured stiffness profiles along the antenna on a compliantly clamped beam.

2. Material and methods

2.1. Specimen preparation

Animals were deeply anaesthetized with CO₂, and dissected in PBS (Carl Roth GmbH & Co KG, Karlsruhe, Germany). The antennae were treated with the surfactant Triton X-100 (Sigma-

Aldrich Chemie GmbH, Steinheim, Germany), to ensure wetting of the entire surface, a necessary step as the fibrillae of plumose antennae easily trap air bubbles. Triton X-100 was washed off in triple steps with PBS. Antennae or their parts were transferred to glycerine (Carl Roth GmbH & Co. KG, Karlsruhe, Germany), which is a suitable medium as it has a similar refractive index to glass [16].

In the present study, only males are included. There are three main reasons for this: (1) due to strong structural sexual dimorphisms, morphological sex comparisons are difficult. (2) While acoustics is important to both sexes (e.g. [30,32]), the male antenna is the most studied with respect to their acoustic response, lending itself to easier comparison. (3) CLSM as relative method benefits more from comparing two separate, but structurally similar objects. Four individuals of each species were used for the present study, not all of which were CLSM-imaged, but it was confirmed the structures imaged are typical, either under the CLSM Zeiss LSM 700 (Carl Zeiss Microscopy GmbH, Jena, Germany) or a fluorescence microscope (Zeiss Axioplan).

2.2. CLSM operation

Following an established standard method [16], which is applied for many insect exoskeleton studies (e.g. [33–35]), antennae were visualized using autofluorescences using the same excitation wavelengths and emission filters applied in the referenced studies. Michels & Gorb [16] demonstrated that the resilin autofluorescence is excitable at the wavelength of around 405 nm. Moreover with a combination of different excitation wavelengths, the method can estimate differences of material properties within a properly adjusted image or images taken with same settings, because in general well-sclerotized, flexible and resilin-dominated regions are visualized differently [16]. The stack construction was performed with ZEN 2009 (6.0 SP2) (Carl Zeiss MicroImaging GmbH), which automatically corrects for wavelength-dependent slice thickness and resulting in varying overlap between stacks taken with different wavelengths.

After adjustment of excitation level according to existing standards [16], the specimens were exposed sequentially to four different excitatory wavelengths (405, 488, 555 and 639 nm), and emitted lights were filtered using a band-pass emission filter of 420–480 nm and long-pass emissions filters transmitting light with wavelengths ≥ 490 , ≥ 560 and ≥ 640 nm, respectively.

Each sample was imaged only once to avoid the photobleaching which could alter the resulting visualization of the material, as different compounds are not similarly susceptible to this effect. This is important for our case, since relatively high laser power (up to max. 30%) was used in order to allow weakly fluorescent structures to be imaged. High laser power can lead to pronounced bleaching if the sample were to be imaged multiple times with the same laser [16].

2.3. Image colour coding

Confocal laser scanning micrographs were colour-coded according to Michels & Gorb [16]. Blue, green and two red image colours were assigned for each micrograph corresponding to excitation wavelengths 405, 488, 555 and 639 nm, and filters 420–480, ≥ 490 , ≥ 560 and ≥ 640 nm, respectively. The two 'red' channels, which provide similar results, were each set to 50% saturation and combined into one red channel to compensate for the double acquisition, a process required as otherwise the red autofluorescence would unduly dominate the image making assessment difficult. According to [16], material properties were interpreted based on resultant micrographs as follows—in superimposed images of insect exoskeletal parts: (1) well-sclerotized structures are usually red, (2) tough-flexible cuticular structures

are typically yellow-green, (3) relatively flexible parts containing a relatively high proportion of resilin are light blue and (4) resilin-dominated regions appear deep-blue. Note that the image colours represent autofluorescence and code the intensity of light in specific channels.

This interpretation was confirmed by observation of corresponding samples under a stereomicroscope. Since assessment of material based on CLSM are relative, not absolute, the comparison is only valid if images are taken with the same settings (electronic supplementary material, figure S1 and table S1), or if two structures are imaged in one single scan (figure 3*b,c*).

Therefore, when necessary we scanned multiple samples simultaneously. Images are reproduced here with increased brightness and contrast, to improve clarity (unaltered images are available in the electronic supplementary material). The exact imaging settings can be seen for each image in electronic supplementary material, table S1.

2.4. Finite-element modelling

FEM with COMSOL 5.3a (Comsol Inc., Stockholm, Sweden) was conducted in the frequency domain to investigate the vibrational characteristics of the antennae using the Solid Mechanics module. Simulations were performed on both desktop computers and the ARCHIE-WeSt supercomputer.

The objective of these simulations was to ascertain the relevance of the observed banded structure of the flagellomeres on the overall frequency response of an idealized compliantly clamped beam. We have reduced the mosquito antenna to a simple system, and thus the simulations are solely to observe the frequency-response changes due to the presence of hard and soft rings in the flagellomeres.

Control simulations were done on uniform cylinders whose expected resonant frequencies are well established from Euler–Bernoulli beam theory. Once established that control simulations yield appropriate results, a subdivided ringed structure seen in the CLSM images was simulated (figure 3).

The fibrillae were not included in the model—they are apparently stiffly coupled to the beam, so that for biologically relevant frequencies, the fibrillae and flagellum move as one [2]. From a mechanical perspective, these fibrillae add damping, but little mass, and thus broaden the response of the whole antenna but do not shift the resonance frequency appreciably. Additionally, the densities of the materials modelled are identical, since remarkable density differences are not known despite the range of stiffnesses in chitinous structures [36].

The geometry of the model antenna was informed by the images that indicated that the cuticle of the flagellum is a thin sheet compared to the absolute volume, hence the flagellum is represented by a 10%*v* wall hollow cylinder filled with tissue (90%*v*, Young's modulus 1 kPa), which we will describe as a beam, to avoid confusing it with the biological structure. The tissue was assumed to have a fraction of the literature value for soft tissue as those values are given for pulling on tissue assemblies in the direction of maximum resistance.

This beam, illustrated in figure 2, was subdivided into 13 long elements of constant size separated by 12 triplets of small elements, to represent the segment joint areas of the antenna. Size of the individual elements was 1/13 of the antenna length (3.3 mm for *T. brevipalpis* and 1.7 mm for *An. arabiensis*) and the diameter was 120 μm for *T. brevipalpis* and 15 μm for *An. arabiensis*. Of importance for the present study is ensuring the spatial distribution of elements of different stiffnesses was matched to the results of the CLSM imaging.

The articulation in the pedicel, which unquestionably contributes to the mechanical behaviour of the antenna, is represented by the round disc (figure 2) for simplicity and is modelled with an effective stiffness that takes into account the

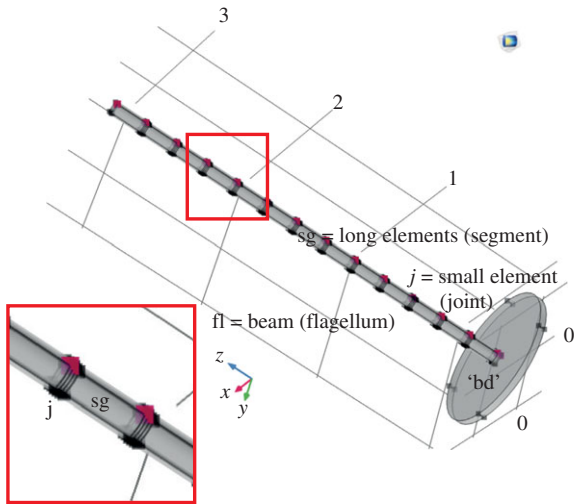


Figure 2. Three-dimensional representation of our antenna model. This figure correlates modelling terminology with morphological terms. The antenna comprises 13 segments with 12 joints. In a model for *T. brevipalpis*, the antennal structure is a sequence of relatively hard long elements, interspersed with a series of three small elements of one soft material sandwiched between two hard small elements (figure 3*a,b*). In contrast in *Anopheles*, the antennal structure is a sequence of soft elements, separated by thin discs of hard material (figures 3*c,d* and 4). Points used for simulations in figure 6 are shown in red. To simulate an impinging sound field, a load was applied perpendicular to the beam axis in the +X direction on elements 2–13. Image abbreviations, with morphological terms in brackets if applicable: ‘bd’ basal disc (approximating the pedicellar articulation); fl, beam (flagellum); j, three small elements (joint); sg, long element (segment).

diameter of the prongs and an approximation of their stiffness. This compound quality of the pedicel articulation is later on referred to as ‘basal stiffness’. It is important to note that our ‘basal disc’ is not matched in size or any other way to the basal plate, but its allometric relation to the beam length and diameter ensures it stays constant in relative size between species.

As estimations of Young’s modulus of insect cuticle vary greatly between different reports (see [36,37] as examples), only the ratio of Young’s moduli between the materials was used for simulations, while keeping values in the natural range. The large and small segments were allocated stiffnesses within the range of the material property estimation according to CLSM images and literature values [36].

Taken together, the model beam is as follows: for *T. brevipalpis* the large elements are of medium stiffness (0.5 GPa) and the triplet of small elements is a stack of hard (5 GPa), soft (1 MPa) and hard element (5 GPa), followed by the next ‘large element’. For *An. arabiensis* the large elements are soft (1 MPa) and all three of the triplet of small elements are hard (5 GPa). Vibrational characteristics of the modelled antennae were simulated in 10 Hz steps (figure 6) over the frequency range of 10–2720 Hz, which includes the typical hearing range of these insects. Only the range 20–2000 Hz is shown.

3. Results

Results are presented separately for each species and highlight differences and similarities in antennal structure as well as its putative material properties. According to the colour scheme of [16], areas shown in blue are likely to be resilin-dominated structures, relatively soft structures will

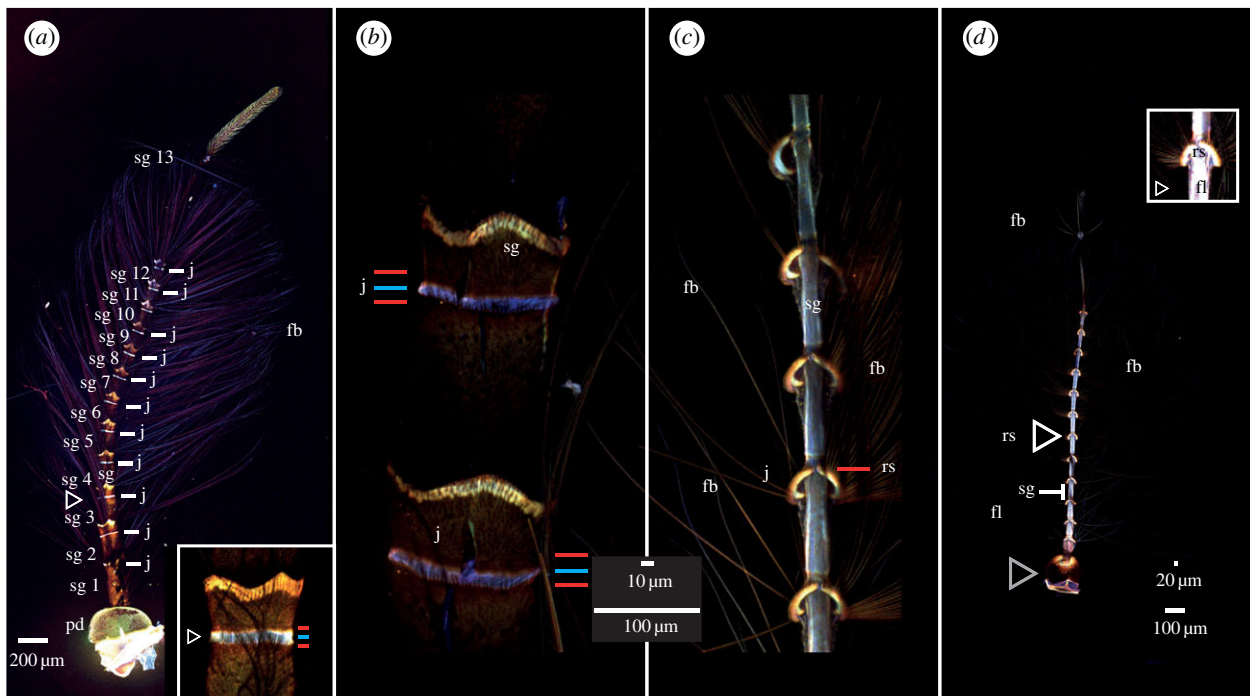


Figure 3. CLSM-based maximum intensity projections of the male antennae of *T. brevipalpis* (*a,b*) and *An. arabiensis* (*c,d*). Higher resolution images available in the electronic supplementary material. (*a*) Antenna, with increased brightness, showing the 12 more-or-less regular subunits and a varying 13th one. Inset: Zoomed image of bands of a different individual. (*b,c*) Comparison image of (*b*) *T. brevipalpis* (2nd segment) and (*c*) *An. arabiensis* (4th to 8th segment), with increased brightness. The antenna of *T. brevipalpis* is larger and thicker. It is made up of relatively stiff cuticle with small, relatively flexible (blue) and hard (red/orange) rings, while *An. arabiensis* antenna is made up of relatively soft (light blue) cuticle interspaced with hard rings. In both species, the area where the fibrillae emerge is hard (orange). In (*a,b*) (*T. brevipalpis*), the image shows two red-orange discs sandwiching a blue disc at the base of the segments (white arrow). (*d*) Overview of *An. arabiensis* with increased brightness. The overall anatomy is dominated by relatively soft and flexible areas, interspaced with comparatively hard bands where fibrillae insert. Image abbreviations: fb, fibrillae; fl, flagellum; j, joint; pd, pedicel (grey arrowhead in (*d*)); rs, ring structure; sg, segment.

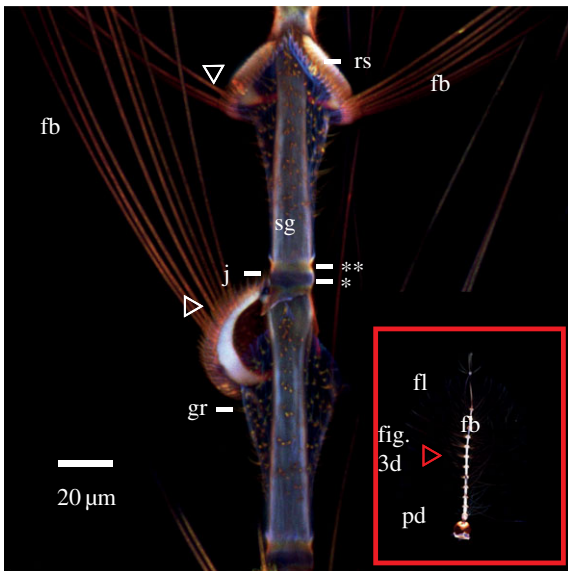


Figure 4. Maximum intensity projection of *An. arabiensis*, with increased brightness, showing detail of two flagellomeres and the insertion position of fibrillae. Males of this species can erect the fibrillae depending on diurnal cycle and activity, due to the presumably soft, sac-like structure that is outlined by the granulae (**gr**) below the hard ring structure (**rs**). The combination of these two structures can potentially provide the mechanical basis to inflate by hydraulic pressure and erect the fibrillae. Fibrillae sockets on the ring structure (white arrowheads) are where the fibrillae insert. Image abbreviations: fb, fibrillae; fl, flagellum; gr, granulae; j, joint; pd, pedicel; rs, ring structure; sg, segment. *Deep-blue fluorescent small band, **yellow-orange fluorescent band.

appear light blue, tough structures in yellow-green and sclerotized structures in red.

3.1. *Toxorhynchites brevipalpis* male

The flagellum consists of 13 segments, each of which, except the first that articulates in the pedicel and therefore cannot be observed directly, has a blue ring followed by a yellow-reddish arrowhead or coronal structure that appears to be more sclerotized. At the tip of this structure, fibrillae emerge in a pattern shown in figure 3*a,b*. Distal to the coronal structure, a comparatively weakly fluorescent material is located. The thin final ring-like structure, observable in detail in red, is interpreted as being part of the lower segment (figure 3*b*), and the next segment therefore begins with a blue ring structure. The segments continuously decrease in length and diameter from proximal to distal locations.

By contrast, the fibrillae have a relatively uniform length and autofluorescence along the flagellum. The long fibrillae are absent on the 13th segment, giving the antenna a somewhat rounded appearance (figure 3*a*). The 13th segment is different from the others; it continues for five to six times the length of the 12th, is noticeably thinner, and shows little tapering.

The 13th segment only sprouts a limited amount of much-shorter fibrillae (figure 3*a*). Externally, the pedicel autofluorescence is rather uniformly green, except the uppermost ridge, where the flagellum emerges (figure 3*a*). Where the pedicel and flagellum join, the material appears orange, due to a higher contribution of red autofluorescence compared to the pedicel's outer wall (figure 5 red arrowhead and electronic supplementary material, figure S1*a*).

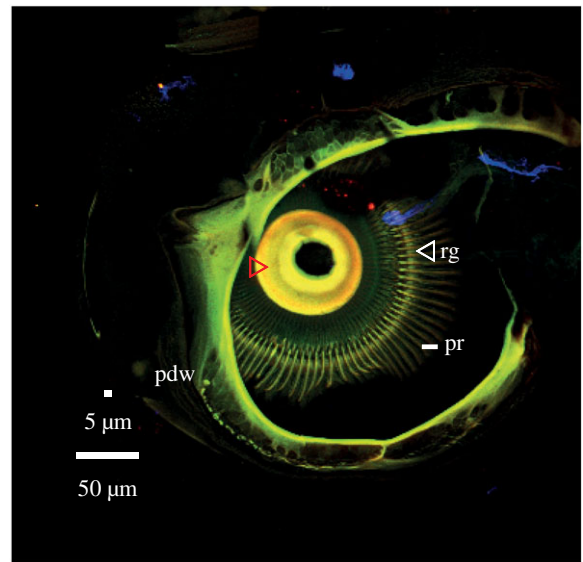


Figure 5. CLSM images of a *T. brevipalpis* male that shows a maximum intensity projection of an opened pedicel. This attachment is comparatively hard (red arrowhead) and the prongs run over a ridge (white arrowhead), which appears as hard as the prongs themselves. Image abbreviations: pdw, pedicel outer wall; pr, prongs; rg, ridge (white arrowhead).

The inside of the pedicel is dominated by centrally attached prongs. Note that the prongs are uniform in their green autofluorescence (and thickness) with their neighbours, as far as can be assessed (figure 5 and electronic supplementary material, figure S1), indicating that prongs are of uniform stiffness.

An optical section (electronic supplementary material, figure S1*a*) of the pedicel indicates that the prongs either attach to, or pass over, a cuticular ridge. The thickness of the whole articulation point is less than approximately 2 μm (electronic supplementary material, figure S1).

However, it should be noted that across individuals and depending on experimental settings, the colour of autofluorescence varies—the difference in settings between experiments makes comparison across individuals difficult.

3.2. *Anopheles arabiensis* male

Segments 2–12 are very similar, albeit gradually tapering to about half the initial diameter by segment 12. Each segment consists of a blue part (figures 3 and 4), followed by a broadened ring-like sclerotized structure in orange-brown-red circumventing the flagellum from which the fibrillae crest of each segment emerges (figure 3*d* white arrowhead figure 4). The first segment is of similar structure, but along the flagellum axis, the segment first tapers after insertion, then becomes medially swollen (figure 3*d*). The 13th segment is filamentous (figure 3*c*), showing overall low autofluorescence.

Details of the more strongly orange-red fluorescent ring structure include the socket that each individual fibrilla inserts into (figure 4 white arrowheads). At the site where the ring joins the flagellum, a deep-blue fluorescent small band of similar width as the ring is present (figure 4*), followed by a more yellow-orange fluorescent band (figure 4**) before the segment continues to show a light blue material fluorescence. Note that the area proximal to the ring structure and surrounding the flagellum is lacking autofluorescence, with the exception of scattered orange fluorescent granulae which outline the cuticle

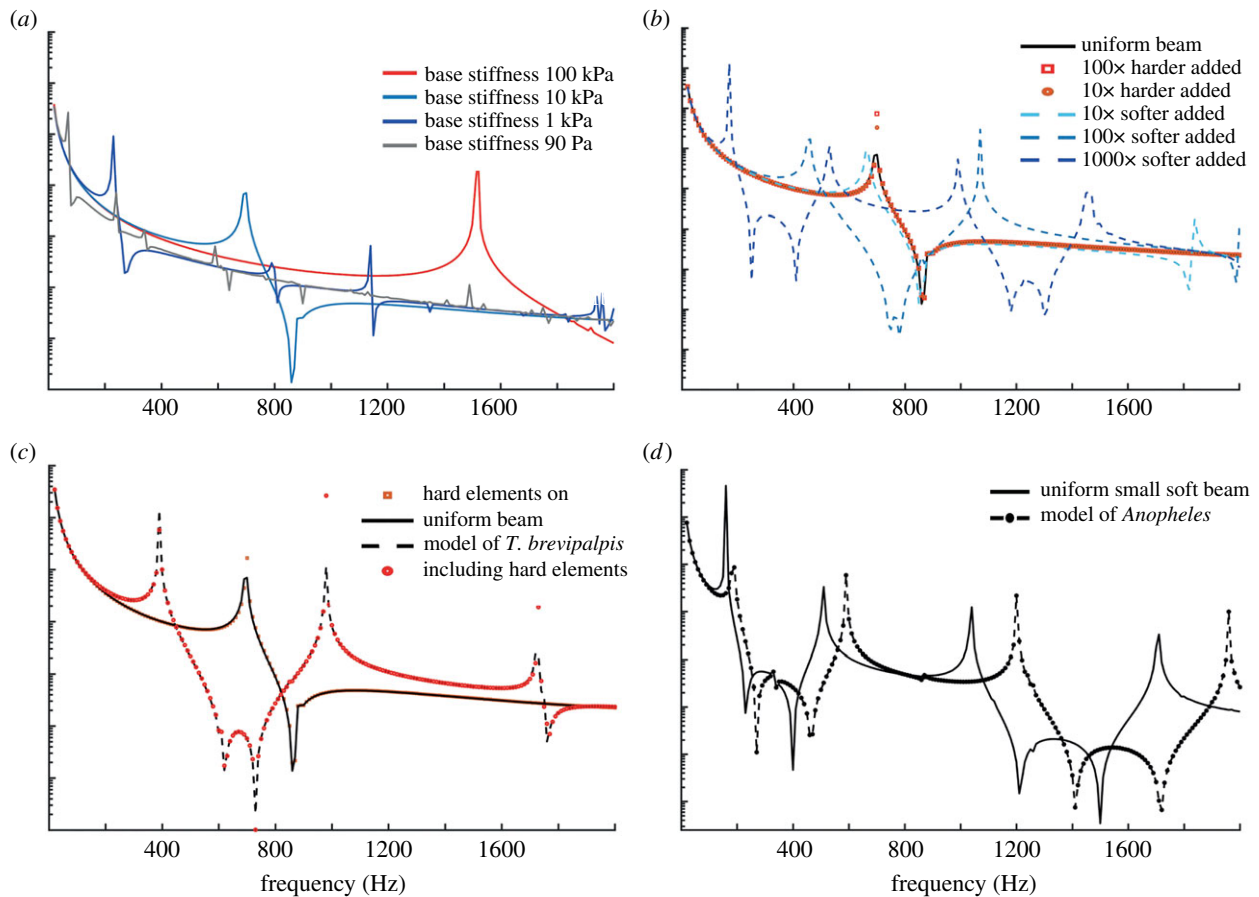


Figure 6. Simulation results. For a modelled beam, (a) shows the change of frequency response over four orders of magnitude of base stiffness, and (b) shows the effect of adding hard or soft elements to a uniform beam with base stiffness of 10 kPa as in figure 2. Overlaid are dashed curves indicating simulations where both hard and soft elements are added—in this case 10× harder elements in combination with 10×, 100× and 1000× softer elements—colour-coded as for soft elements. (c) Comparison of a *Toxorhynchites*-type model with either uniform stiffness, or hard and/or soft elements added. Only the addition of soft elements appreciably affects the frequency response. Note that the resonance is consistent with wingbeat frequencies in this species. (d) Comparison of the *Anopheles*-type model with either uniform stiffness or the addition of hard elements. Hard elements increase the resonant frequency.

sac area (figure 4, gr below rs). The rather sclerotized articulation of the flagellum in the pedicel is approximately hemispherical and at the upper end of the distalmost part of the pedicel (figure 3d grey arrowhead). With CLSM, further internal structure, except the crest of uniformly fluorescent prongs, cannot be visualized (electronic supplementary material, figure S1b).

3.3. *Toxorhynchites brevivalpis* and *Anopheles arabiensis* male comparison

Comparison of the second segment in *T. brevivalpis* (figure 3b) to the sixth to 10th segments of the antenna in *An. arabiensis* (figure 3c) shows a noticeable difference in size. These segments in *T. brevivalpis* are 120–150 μm wide and 200 μm long. The antenna of *An. arabiensis* is much smaller with each segment about 100 μm long, and only 10–20 μm wide. The long fibrillae inserting on the orange structure circumventing the flagellum lack an autofluorescence gradient and are barely visible in both species as autofluorescence is overall low in the fibrillae.

Whereas large parts of *T. brevivalpis* show nearly no signal in contrast autofluorescence in *An. arabiensis* is in general stronger, every part of the antenna is either likely flexible (blue) or putatively sclerotized (orange) with no areas of intermediate properties. As a further difference, it can be stated that the most red part in *T. brevivalpis* is a coronal

structure, while it appears more annular in *An. arabiensis* (figure 4). Both antennae are almost mirror images in the respect that in *T. brevivalpis* a rather small band (ca 10 μm) of a slightly deeper shade of blue is in between each segment, while the whole 100 μm long segment in *An. arabiensis* shows light blue autofluorescence. An antennal cross section shows that a rather thin surface layer constitutes the highest proportion of the blue autofluorescence (electronic supplementary material, figure S2) in both species.

Furthermore, the optical sections (electronic supplementary material, figure S1) show that the articulation structure remains uniformly thin (ca 2–4 μm) and comparable in size between the two species, despite the fact that the pedicel of *An. arabiensis* is roughly half as large as the pedicel of *T. brevivalpis*.

3.4. FEM of the male antenna

Frequency-domain studies were performed in COMSOL to observe the effect of the various segmental structures seen in CLSM experiments, as well as other standard parameters of an antennal system such as ‘base stiffness’ and geometry. Figure 6a demonstrates the effect of changing ‘base stiffness’ on the frequency response of a simulated beam. It is clear that increasing basal stiffness leads to an increase in the frequency of the resonant peaks. As expected, further increases in basal stiffness yield diminishing changes in the frequency response as predicted by equation (4.1). In the investigated stiffness

range for the base of 90 Pa (70 Hz)–100 kPa (1520 Hz), a diminishing gain per decade stiffness increase is observed.

In Figure 6b, elements of different elasticity were added to a beam, distributed in agreement with the CLSM results. It is clear that the stiffness modification of segmented structures in the antennal model influences resonant frequencies.

For the beam simulated in Figure 6b, softer segments are shown to reduce the peak frequencies by 35, 240 and 525 Hz as we decrease the stiffness by powers of 10. By contrast, the addition of harder elements leads to an increase in the peak frequencies, although to a lesser extent. Without hard elements the resonant frequency is between 690 and 700 Hz and with hard elements the resonant frequency shifts up to 700 Hz.

While figure 6a,b is already dimensionally matched to *T. brevipalpis*, figure 6c,d shows simulations of frequency responses in male *T. brevipalpis* and *An. arabiensis*, respectively. The graph in figure 6c shows four lines associated with four cases: (1) uniform beam, (2) uniform beam with added stiff elements, (3) uniform beam with added soft elements and (4) uniform with both stiff and soft elements. The latter case is the most morphologically accurate. Clearly, the addition of soft elements is the only case which allows for significant changes in resonant frequencies, from approximately 695 Hz down to 390 Hz. By contrast, the addition of hard elements is insufficient to affect the natural vibration characteristics substantially, resulting in under a 10 Hz shift from approximately 695 Hz. In figure 6d, the two lines represent: (1) a uniform small and soft beam of the same size as the *An. arabiensis* antenna and (2) the same beam but with added hard elements. The latter case is most faithful to the antenna of *An. arabiensis*. The frequency shift appears to be less than the 305 Hz shift shown in figure 6c for soft elements in a harder beam. The addition of hard elements increases the resonant frequency of the overall softer beam from 160–190 Hz. While figure 6a demonstrates the model representing the situation in a compliantly clamped beam, figure 6b–d demonstrates that distribution of varying material properties can have a strong effect on the overall resonant frequency. By contrast, in a simple compliantly clamped beam, the resonant frequency is mostly determined by the beam dimensions and the stiffness of the clamp [38].

Figure 6c,d shows simulations based on stiffness ranges obtained from CLSM autofluorescences in the two species, as well as appropriate geometry. The example of *T. brevipalpis* demonstrates how it is possible to reduce the resonant frequency of a beam to match the observed frequencies seen in the insects studied (i.e. in *T. brevipalpis* and *An. arabiensis* resonant frequencies are 420 ± 5 Hz [39] and 380 ± 46 Hz (new experimental data not shown) for the males, respectively). It is worth noting that within biologically relevant parameter ranges for antenna stiffness *without* adding disc elements to the beam, it is difficult to obtain resonant frequencies in simulation that match those seen in nature. Taken as a whole, the addition of elements of different stiffness in comparison to the main beam can change beam resonant frequency to a similar order of magnitude as changing the basal stiffness (figure 6a).

4. Discussion

The goal of this work was to investigate the material properties of the mosquito antenna. We performed a CLSM study of

mosquito antennae and found that autofluorescence is not homogeneous along the antenna, but instead these antennae comprise repeating bands of harder and softer elements. In general, the presence of harder and softer elements in the antenna is similar between the two mosquito species—however, their distribution is inverted: *An. arabiensis* has large rather flexible bands interspaced with harder ring elements, while *T. brevipalpis* is medium-hard overall and has short flexible ring elements wedged between two hard rings. Given the nature of the results, we also simulated these geometrical configurations to determine whether these material changes and spatial distribution has any effect on the overall resonant frequency of the antenna, a property of significant importance to the animal, as sensitivity of these ears is best around the resonant frequency and acoustic perception is essential for mating [10,11,26,27,30,31]. It is possible that the different sizes of the animals studied may influence the material properties of the antennae, as the larger antennae perhaps have different mechanical constraints to ensure robustness and structural stability. It is not clear in general whether the observed geometrical differences are driven by behavioural or other constraints unique to each species. These questions could be answered with studies on similarly sized and more behaviourally similar species, and are not addressed here. Some interpretation on how the observed stiffness distribution along the modelled beam could play a role in the resonant characteristics, and the implications of this, might be inferred from FEM simulations discussed below.

4.1. Confocal laser scanning microscopy

In *T. brevipalpis* males, the larger of the species investigated, the overall structure is relatively tough and there exist small flexible to well-sclerotized ring structures. In *An. arabiensis* males, the combination of a sclerotized ring structure, on which the fibrillae are present in each segment, and the area of the membrane sac proximal to it is believed to play a role in the behaviour of male *Anopheles* antenna, in which they collapse and extend their fibrillae at different times of the day using hydraulic pressure [40]. Our images are taken after suspension in fluid and show only antennae with extended fibrillae. This position in nature is only assumed during the active swarming phase [40] and therefore is directly related to the detection of conspecifics. Pedicels both internally and externally look similar in structure, but in *An. arabiensis* the intensity of autofluorescence is higher. In male *T. brevipalpis*, a hard area (figure 5 red arrowhead) is visible, where the flagellum leaves the pedicel. The prongs on the inside appear similar in the two species regarding fluorescence and dimensions compared with prongs of the same animal in the same image. Comparison between images demonstrates that different CLSM settings are necessary for proper visualization of material differences this does not allow judgement of material properties between species imaged individually. However, we can say with some confidence that the prongs are neither particularly flexible nor stiff and are all consistent in their autofluorescence and dimensions within the animal.

This is in agreement with Avitabile *et al.* [41], in that the prongs act more or less as rigid-body extensions of the flagellum. Possible variations inside the pedicel would likely be due to the scolopidia, which have recently been shown, by direct measurement using atomic force microscopy, to be motile [42], having long been suspected as the source of stiffness

gating. Further studies have shown the importance of the scolopidia for both power gain of the antenna, and the intra- and interspecific variations seen in antennal mechanics [32].

However, the present study demonstrates that the flagellum itself cannot be approximated as a rigid beam of uniform stiffness, but that it consists of repeating units of stiff and soft elements. A limitation of the present study is the lack of direct correlation of CLSM-based autofluorescence analysis with mechanical measurements, which is to be tackled in follow-up investigations.

4.2. Significance of material property differences in antennae

Since Johnston (1855) [1], the nerve and cuticle structure inside the pedicel has been investigated regarding its auditory and general function. In this study, we visualized the antenna of *An. arabiensis*, a species where males form swarms and females fly into the swarm and are acoustically located by the males. *Toxorhynchites brevipalpis* is a solitary mosquito, where acoustics also plays a role in mating [30]. Within individuals, consistency of the uniform prongs inside the pedicel has been found across both species, and remarkable differences in material distributions were found in the flagellum.

A sensory organ exposed to the environment such as an insect antenna (that can move autogenously without stimulus) is potentially under continuous mechanical stress. This may explain the presence of resilin, a protein known to be used to protect from 'wear and tear' in insects [43,44].

The FEM results indicate a potential for resonant tuning by alteration of material distributions along the flagellum. This is perhaps not that surprising, as the influence of differently stiff elements partially can be expected as the resonant frequency ($\omega/2\pi$) of a beam [38] is dependent on Young's modulus through

$$\omega = k^2 \sqrt{\frac{EI}{\rho A}}, \quad (4.1)$$

where k is the wavenumber, I is the area moment of inertia, ρ is the density, A is the cross section of the beam, and E is Young's modulus. In a composite beam, Young's modulus would likely be an effective Young's modulus of the whole beam, which will be different when elasticity is not uniform. Furthermore, the non-homogeneous material distribution as suggested by CLSM results along the antenna could affect the area moment of inertia. Given the densities are suspected to be similar, the likelihood of this being important is low. Regardless, by changing the distribution of stiffnesses, a further mechanism to control the resonant frequency of the antenna is possible. There are potential benefits to this mechanism in conserving structural integrity in comparison to changing the material.

FEM models of material property distributions in the antennae of the studied insects have been compared to a uniform beam structure. This shows different mechanical behaviours, suggesting that a more rigid antenna, presumably like that of *T. brevipalpis* (figure 6a), and a soft antenna, like that of *An. arabiensis* (figure 6b), can both be tuned significantly by basal stiffness and distribution of stiffness along the beam. However, the effect of hard elements in soft beams seems less than that of soft elements in hard beams. How this different tuning affects behaviour requires further research.

Interestingly, in order to make our model show resonant frequencies that are found in these insects, the addition of the triplet rings was essential. We found it difficult to reproduce the resonant frequencies found in *T. brevipalpis* and *An. arabiensis* (420 ± 5 Hz [39] and 380 ± 46 Hz (data not shown) for the males, respectively) using only the known geometry and typical biological values for material properties—it was somewhat surprising that only the addition of the triplet rings allowed one to bring down the resonant frequencies in *T. brevipalpis* to observed values. The deviation in *An. arabiensis* is due to the other contributing factor—basal stiffness.

Our FEM model shows a very weak first bending mode at the main resonant peak and a pendulum mode at lower frequencies. In particular, in the case of a small angular displacement, the weak bending mode can easily be perceived as a pendulum mode, as while tip displacement is largest, displacement overall is fairly uniform in both of these mode shapes. This is in line with earlier experiments in different species reporting a pendulum mode [2,7].

Generally speaking, there are many factors that may contribute to the antennal mechanical behaviour. An exhaustive list would include the stiffness of the base articulation, the cell attachments to the scolopidia, prongs and scolopidia, geometry, and viscous effects of the fibrillae, among other things. For example, it has been shown in stick insects that tapering of their non-plumose antennae has the largest tuning effect, at least in the static case [44]. The current study suggests that the configuration of spatial distribution of flexibility along the antenna does influence the antenna's mechanical behaviour within the frequency range of the animal's hearing. More in-depth experimental and theoretical investigations of antenna bending are required, which will add to our understanding of mechanical properties of insect hearing systems.

5. Conclusion and outlook

Generally, the highly variable and interesting material properties of insect cuticle have not gone unnoticed (e.g. [21,45,46]). However, in the field of insect auditory systems, the fine detail of material properties and distribution is overlooked. The primary goal of this work was to observe and describe morphological and material differences and similarities in antennal hearing organs of the investigated species. While it is possible to consider the antenna as a simple beam, we have shown that the actual material properties of these antenna are more complex. We also show that these material complexities have the potential to modify the frequency responses of the acoustic sensors, providing a different mechanism to the animal to evolve and direct—mating-critical—frequency selectivity. The addition of soft elements to a hard beam shifts the resonant frequencies to lower values, while adding stiff elements to a soft beam does the opposite and shifts the frequency of resonant upwards. The study of varying material distribution of insect hearing organs with CLSM has a high potential for improving our understanding of the evolution and development of acoustic sensors in nature, especially if combined with FEM and possibly mechanical tests of materials and laser vibrometry, to characterize native system behaviour. The very high variability of mechanical and therefore acoustic properties in these insects studied suggests a potential for many interesting future findings and biomimetic engineering exploitation.

Data accessibility. Additional images, all original images and image values (electronic supplementary material, table S1) are available on (<https://figshare.com>) via Interface. Additionally, data is freely available from the University of Strathclyde KnowledgeBase at <https://doi.org/10.15129/8ec4ac84-3040-4c4d-854e-07e50786a68a>.

Authors' contributions. B.D.S. and Y.M. carried out preparations and CLSM imaging. A.R. and B.D.S. conducted FEM simulations. B.D.S., J.F.C.W., S.N.G. and J.C.J. designed the study. B.D.S., A.R., S.G.N., Y.M., and J.C.J. wrote the manuscript. All authors gave final approval for publication.

Competing interests. We have no competing interests.

Funding. This work was partially supported by the European Research Council under the European Union's Seventh Framework Programme FP/2007-2013/ERC under grant agreement no. 615030 to J.F.C.W. by the EPSRC (J.C.J., EP/H02848X/1) and by the German Research Foundation (Y.M., DFG grant no. MA 7400/1-1).

Acknowledgements. We thank Dr Jan Michels (University of Kiel) for CLSM training, Dr Alexander Kovalev (University of Kiel) for discussion and advice, Dr Jeremy Gibson, members of the Centre for Ultrasonic Engineering (University of Strathclyde) for their support and Dr Francesco Baldini (Vector Biology and Disease Group, University of Glasgow) for providing *Anopheles* specimens. We thank Shahida Begum (London School of Hygiene and Tropical Medicine) for the provision of *T. brevipalpis*.

References

- Johnston C. 1855 Auditory apparatus of the *Culex* mosquito. *Q. J. Microsc. Sci.* **3**, 97–102.
- Göpfert MC, Briegel H, Robert D. 1999 Mosquito hearing: sound-induced antennal vibrations in male and female *Aedes aegypti*. *J. Exp. Biol.* **202**, 2727–2738.
- Nadrowski B, Effertz T, Senthilan PR, Göpfert MC. 2010 Antennal hearing in insects. New findings, new questions. *Hear. Res.* **273**, 7–13. (doi:10.1016/j.heares.2010.03.092)
- Malkin R, McDonagh TR, Mhatre N, Scott TS, Robert D. 2014 Energy localization and frequency analysis in the locust ear. *J. R. Soc. Interface* **11**, 20130857. (doi:10.1098/rsif.2013.0857)
- Albert JT, Kozlov AS. 2016 Comparative aspects of hearing in vertebrates and insects with antennal ears. *Curr. Biol.* **26**, R1050–R1061. (doi:10.1016/j.cub.2016.09.017)
- Greenfield MD. 2016 Evolution of acoustic communication in insects. In *Insect hearing* (eds GS Pollack, AC Mason, AN Popper, RR Fay). Springer Handbook of Auditory Research 55. Berlin, Germany: Springer.
- Sane SP, McHenry MJ. 2009 The biomechanics of sensory organs. *Integr. Comp. Biol.* **49**, i8–i23. (doi:10.1093/icb/icp112)
- Jackson JC, Robert D. 2006 Nonlinear auditory mechanism enhances female sounds for male mosquitoes. *Proc. Natl Acad. Sci. USA* **103**, 16 734–16 739. (doi:10.1073/pnas.0606319103)
- Warren B, Gibson G, Russell IJ. 2009 Sex recognition through midflight mating duets in *Culex* mosquitoes is mediated by acoustic distortion. *Curr. Biol.* **19**, 485–491. (doi:10.1016/j.cub.2009.01.059)
- Downes JA. 1969 The swarming and mating flight of diptera. *Annu. Rev. Entomol.* **14**, 271–298. (doi:10.1146/annurev.en.14.010169.001415)
- Belton P. 1974 An analysis of direction finding in male mosquitoes. In *Experimental analysis of insect behaviour* (ed. L Barton-Browne). Berlin, Germany: Springer.
- Cator LJ, Arthur B, Harrington LC, Hoy RR. 2009 Harmonic convergence in the love songs of the dengue vector mosquito. *Science* **323**, 1077–1079. (doi:10.1126/science.1166541)
- Mhatre N. 2015 Active amplification in insect ears: mechanics, models and molecules. *J. Comp. Physiol. A* **201**, 19–37. (doi:10.1007/s00359-014-0969-0)
- Boo KS, Richards AG. 1975 Fine structure of the scolopidia in the Johnston's organ of male *Aedes aegypti* (L.) (Diptera: Culicidae). *Int. J. Insect Morphol. Embryol.* **4**, 549–566. (doi:10.1016/0020-7322(75)90031-8)
- Yack YE. 2004 The structure and function of auditory chordotonal organs in insects. *Microsc. Res. Tech.* **63**, 315–337. (doi:10.1002/jemt.20051)
- Michels J, Gorb SN. 2012 Detailed three-dimensional visualization of resilin in the exoskeleton of arthropods using confocal laser scanning microscopy. *J. Microsc.* **245**, 1–16. (doi:10.1111/j.1365-2818.2011.03523.x)
- Peisker H, Michels J, Gorb SN. 2013 Evidence for a material gradient in the adhesive tarsal setae of the ladybird beetle *Coccinella septempunctata*. *Nat. Commun.* **4**, 1661. (doi:10.1038/ncomms2576)
- Appel E, Heepe L, Lin CP, Gorb SN. 2015 Ultrastructure of dragonfly wing veins: composite structure of fibrous material supplemented by resilin. *J. Anat.* **227**, 561–582. (doi:10.1111/joa.12362)
- Willkommen J, Michels J, Gorb SN. 2015 Functional morphology of the male caudal appendages of the damselfly *Ischnura elegans* (Zygotera: Coenagrionidae). *Arthropod. Struct. Dev.* **44**, 289–300. (doi:10.1016/j.asd.2015.04.002)
- Filippov AE, Matsumura Y, Kovalev AE, Gorb SN. 2016 Stiffness gradient of the beetle penis facilitates propulsion in the spiraled female spermathecal duct. *Sci. Rep.* **6**, 27608. (doi:10.1038/srep27608)
- Michels J, Appel E, Gorb S. 2016 Functional diversity of resilin in Arthropoda. *Beilstein J. Nanotechnol.* **7**, 1241–1259. (doi:10.3762/bjnano.7.115)
- Matsumura Y, Kovalev AE, Gorb SN. 2017 Penetration mechanics of a beetle intromittent organ with bending stiffness gradient and a soft tip. *Sci. Adv.* **3**, 5469–5477. (doi:10.1126/sciadv.aao5469)
- Schmitt M, Büscher TH, Gorb SN, Rajabi H. 2018 How does a slender tibia resist buckling? Effect of material, structural and geometric characteristics on buckling behaviour of the hindleg tibia in stick insect postembryonic development. *J. Exp. Biol.* **221**, 173047. (doi:10.1242/jeb.173047)
- Büsse S, Gorb SN. 2018 Material composition of the mouthpart cuticle in a damselfly larva (Insecta: Odonata) and its biomechanical significance. *R. Soc. open sci.* **5**, 172117. (doi:10.1098/rsos.172117)
- Beutel RG, Friedrich F, Yang XK, Ge SQ. 2014 *Insect morphology and phylogeny: a textbook for students of entomology*. Berlin, Germany: Walter de Gruyter.
- Cator LJ, Harrington LC. 2011 The harmonic convergence of fathers predicts the mating success of sons in *Aedes aegypti*. *Anim. Behav.* **82**, 627–633. (doi:10.1016/j.anbehav.2011.07.013)
- Pennetier C, Warren B, Dabire KR, Russell IJ, Gibson G. 2010 'Singing on the wing' as a mechanism for species recognition in the malarial mosquito *Anopheles gambiae*. *Curr. Biol.* **20**, 131–136. (doi:10.1016/j.cub.2009.11.040)
- Steffan WA, Evenhuis NL. 1981 Biology of *Toxorhynchites*. *Annu. Rev. Entomol.* **26**, 159–181.
- Collins LE, Blackwell A. 2000 The biology of *Toxorhynchites* mosquitoes and their potential as biocontrol agents. *Biocontrol News Inform.* **21**, 105N–116N.
- Gibson G, Russel I. 2006 Flying in tune: sexual recognition in mosquitoes. *Curr. Biol.* **16**, 1311–1316. (doi:10.1016/j.cub.2006.05.053)
- Jackson JC, Windmill JFC, Victoria G, Pook VG, Robert D. 2009 Synchrony through twice-frequency forcing for sensitive and selective auditory processing. *Proc. Natl Acad. Sci. USA* **106**, 10 177–10 182. (doi:10.1073/pnas.0901727106)
- Su MP, Andrés M, Boyd-Gibbins N, Somers J, Albert JT. 2018 Sex and species specific hearing mechanisms in mosquito flagellar ears. *Nat. Commun.* **9**, 3911. (doi:10.1038/s41467-018-06388-7)
- Bergmann P, Richter S, Glöckner N, Betz O. 2018 Morphology of hindwing veins in the shield bug *Graphosoma italicum* (Heteroptera: Pentatomidae). *Arthropod. Struct. Dev.* **47**, 375–390. (doi:10.1016/j.asd.2018.04.004)
- Matsumura Y, Michels J, Appel E, Gorb SN. 2017 Functional morphology and evolution of the hyperelongated intromittent organ in *Cassida* leaf beetles (Coleoptera: Chrysomelidae: Cassidinae). *Zoology* **120**, 1–14. (doi:10.1016/j.zool.2016.08.001)
- Neff D, Frazier SF, Quimby L, Wang R-T, Zill S. 2000 Identification of resilin in the leg of cockroach, *Periplaneta americana*: confirmation by a simple

- method using pH dependence of UV fluorescence. *Arthropod. Struct. Dev.* **29**, 75–83. (doi:10.1016/S1467-8039(00)00014-1)
36. Vincent JFV, Wegst UGK. 2004 Design and mechanical properties of insect cuticle. *Arthropod. Struct. Dev.* **33**, 187–199. (doi:10.1016/j.asd.2004.05.006)
 37. Wegst UGK, Ashby MF. 2004 Design and mechanical properties of insect cuticle. *Philos. Mag.* **84**, 2167–2181.
 38. Rao SS, Yap FF. 2011 *Mechanical vibrations*, vol. 5. London, UK: Prentice Hall.
 39. Göpfert MC, Robert D. 2000 Nanometre-range acoustic sensitivity in male and female mosquitoes. *Proc. R. Soc. Lond. B* **267**, 453–457.
 40. Nijhout HF. 1977 Control of antennal hair erection in male mosquitoes. *Biol. Bull.* **153**, 591–603. (doi:10.2307/1540608)
 41. Avitabile D, Homer M, Champneys AR, Jackson JC, Robert D. 2010 Mathematical modelling of the active hearing process in mosquitoes. *J. R. Soc. Interface* **7**, 105–122. (doi:10.1098/rsif.2009.0091)
 42. Windmill JFC, Jackson JC, Pook VG, Robert D. 2018 Frequency doubling by active *in vivo* motility of mechanosensory neurons in the mosquito ear. *R. Soc. open sci.* **5**. 171082. (doi:10.1098/rsos.171082)
 43. Mountcastle AM, Combes SA. 2013 Wing flexibility enhances load-lifting capacity in bumblebees. *Proc. R. Soc. B* **280**, 20130531. (doi:10.1098/rspb.2013.0531)
 44. Rajabi H, Shafei A, Darvizeh A, Gorb SN, Duerr V, Dirk J-H. 2018 Both stiff and compliant: morphological and biomechanical adaptations of stick insect antennae for tactile exploration. *J. R. Soc. Interface* **15**, 20180246. (doi:10.1098/rsif.2018.0246)
 45. White ZW, Vernerey FJ. 2018 Armours for soft bodies: how far can bioinspiration take us? *Bioinspir. Biomim.* **13**, 041004. (doi:10.1088/1748-3190/aababa)
 46. Pennisi E. 2016 Bendy bugs inspire roboticists. *Science* **351**, 647. (doi:10.1126/science.351.6274.647)